INVESTIGATIONS ON CAVITATING HYDROFOILS

Thesis by
Richard B. Wade

In Partial Fulfillment of the Requirements
for the Degree of
Doctor of Philosophy

California Institute of Technology
Pasadena, California

1965

(Submitted April 27, 1965)

ABSTRACT

Experimental and theoretical results are presented for the non-cavitating and cavitating performances of a plano-convex hydrofoil in both the isolated and cascade configurations.

In the isolated hydrofoil tests special emphasis is placed on the unsteady region of cavitation separating the partially cavitating region from the fully cavitating region. The detailed behavior of the oscillating cavity together with the magnitude of the force vibrations that occur in this region are investigated from both a qualitative and a quantitative viewpoint. The dependence of the reduced frequency of these oscillations on the angle of attack, cavitation number and flow velocity is also discussed.

The performance of the hydrofoil under steady conditions in both the cavitating and non-cavitating regions is also presented. Details of the test equipment and procedures used and various data corrections made are given.

A linearized partially cavitating theory for this plano-convex hydrofoil is also developed which includes camber and thickness effects. The results from this theory are compared with the experimental data obtained.

In the cascade experiments a feasibility study is undertaken to determine the possibility of using the high speed water tunnel at the California Institute of Technology as a cascade tunnel for investigating the cavitating performance of compressor and turbine cascades.

A comprehensive design study is given of the modifications made to the existing tunnel to achieve this aim. The experimental procedures used in conducting the experiments are then discussed. Tests are performed on two compressor cascades of plano-convex hydrofoils having solidities of 1.25 and 0.625 and cascade angle of 45 degrees, for all conditions of cavitation from the fully wetted to the fully choked conditions. A study is also made of a turbine cascade of solidity 1.25 for the same cascade angle in the non-cavitating region only. Comparisons of the experimental data with several theories indicate that the cascade tests are indeed fulfilling their purpose in proving the methods used in simulating cascade conditions in the tunnel.

Proposals for modifying the system used to avoid several experimental difficulties are presented. Finally, a linearized theory for a cascade of partially cavitating flat plate hydrofoils is developed which is compared with the data obtained.

ACKNOWLEDGMENTS

The author wishes to express his sincere thanks and gratitude to Dr. A. J. Acosta without whose help, guidance and constant encouragement this program could not have been completed.

During the course of this work all members of the Hydrodynamics Laboratory have given unselfishly of their time and many-faceted skills - the author is indeed indebted to all of these gentlemen: Messrs. T. Kiceniuk, C. Eastvedt, H. Hamaguchi, J. Kingan, G. Lundgren, L. Whitcanack, R. Wilson and J. Wilson.

This study would not have been possible without the awards of Institute scholarships during the years 1960-65 and the assistance of the Ford Foundation grants made available to the author. Thanks are due to the Office of Naval Research for supporting this work and providing Research Assistantships during the years 1961-65.

For the preparation of the manuscript the author expresses his thanks to Mrs. Phyllis Henderson, Miss Cecilia Lin and Mrs. Laura Gaard. The programs and computations for the numerical calculations carried out in the course of the research are due to Mrs. Zora Harrison whose help is gratefully acknowledged.

Finally, the author wishes to express his deepest gratitude for the understanding and encouragement given him by his wife and the many sacrifices she gladly made during the period of this study to help in its final accomplishment.

TABLE OF CONTENTS

Page

PART II - CASCADE STUDY

INVESTIGATIONS ON CAVITATING HYDROFOILS

INTRODUCTION

1. Preliminary Remarks - The field of hydrodynamics abounds in many interesting problems not the least of which is that of cavitation. This topic deals with the effects caused by the occurrence of vapor or gas-filled cavities (bubbles) in a fluid. These cavities are formed when the pressure in the fluid is lowered to below a certain critical value (approximately that of the vapor pressure). The subsequent development of these cavities as the local pressure is further reduced has a pronounced influence on the flow field in the vicinity where they occur. These effects lead to a considerable change in the pressure forces exerted by the fluid, causing alterations in the performance characteristics of any lifting surfaces subjected to this type of phenomenon.

The study of cavitation and its effects on stationary and moving surfaces has, for a long time, been of interest to workers in the field of hydrodynamics. This interest has been greatly stimulated over the last few years by the ever-increasing demands placed on the designer of turbo-machinery. These demands necessitate the operation of pumps and turbines at higher rotational speeds, thus giving rise to cavitating conditions. The present day interests in the high speed performance of other types of lifting surfaces, such as those used in hydrofoil boats and modern ship propellers,

has further given an impetus to the study of the behavior of such lifting surfaces under various conditions of cavitation.

The cavitation occurring on hydrofoils or lifting surfaces is usually divided into several distinguishable regimes. Incipient cavitation occurs when at some point on the hydrofoil section bubbles first become apparent. On further decrease in local pressure, which in most practical applications is brought about by an increase in flow velocity, more bubbles are formed until the aggregate of these bubbles may be considered as a single cavity which is frothy in appearance. This cavity starts at the point of lowest pressure on the foil and terminates on the body at some point further downstream where the pressure rise in the fluid is sufficient to collapse the bubbles. This type of cavitation is thus usually referred to as partial cavitation, since the cavity length is less than the chord length. If the pressure is still further decreased, the cavity grows in length until it becomes longer than the chord. Concurrently with this growth the nature of the cavity changes in that the upstream portion of the cavity becomes clear and glassy in appearance and the flow is divided into two distinct regions by a well-defined streamline. The rear end of the cavity, however, remains frothy in nature; a considerable amount of mixing and circulating flow occurs in this area and in the subsequent region downstream from the end of the cavity (the wake). This flow regime is referred to as the fully cavitating region.

All the above types of cavitation may be characterized by the

cavitation number K , which is defined as

$$K = \frac{p - p_c}{\rho V^2/2} \quad ,$$

where p is the free stream static pressure, p_c the cavity pressure and $\rho V^2/2$ the dynamic head. This dimensionless parameter is a measure of the dynamic conditions under which cavitation is taking place; its physical significance may be seen from the foregoing discussion - the smaller the cavitation number, the longer is the cavity obtained. The definition of this cavitation index, however, depends on the ability of defining a cavity pressure. Experimental results indicate that the pressure throughout the cavity may be regarded as constant and hence such a pressure has a well-defined meaning.

As already mentioned the flow field undergoes a significant change during this process of cavitation and the forces on the hydrofoil change accordingly. The study of such flows is thus a necessity and the theoretical treatment of cavitating flows has been dealt with fairly extensively over the last one hundred years. These theoretical studies, however, have been concerned almost exclusively with single bodies under cavitating conditions. Techniques developed in studying these flows have not, until very recently, been applied to the more general problem of cavitating cascades or multi-vane systems. The importance of studying cascades lies in their ability to predict the performance of turbo-machines. The analogy between the flow

through a cascade and that through an axial flow machine can best be illustrated as follows: The axial flow machine may be considered as made up of two basic components - a rotating impeller, and an outer casing. For purposes of analysis the flow through this impeller is divided into three velocity components, viz., a radial component which causes a radial divergence of the streamlines, an axial component responsible for the mass flow through the impeller, and a tangential flow arising from the rotation of the impeller. Usually the radial component of flow is small compared with the other two and the stream surfaces may be assumed to be cylindrical. If, therefore, the blades of the impeller at any cylindrical stream surface are developed into a plane, one obtains a lattice of lifting surfaces and the resulting flow pattern is that of a two-dimensional cascade. The accuracy with which such cascade flows represent the performance of turbo-machines has been amply brought out in the field of classical aerodynamics where the non-cavitating performance of turbines and compressors can be very well predicted by the results obtained from cascade investigations. Both from a theoretical and experimental point of view the cascade is far more amenable to study than is the impeller it is intended to represent. Thus the development of the design of turbo-machines and the understanding of the phenomena occurring in such machines has been due to a large extent to the study and successful application of the cascade concept to these more complicated flows.

Concurrently with the development of theoretical techniques

for coping with cavitating flows, experimental studies have been carried out to understand better the mechanics of these flows and also to check the theories developed. These experimental investigations have again been almost exclusively concerned with the isolated hydrofoil and have not dealt with the case of the cavitating cascade. Here again it is most certain that a study of cavitating cascades will lead one to a far better understanding of the mechanisms taking place under these conditions in a turbo-machine, than would otherwise be obtained from a study of an isolated foil. With these preliminary remarks a survey of the development of cavitation will now be given.

2. Historical Development - The concept of flows bounded partly by solid surfaces and partly by constant pressure surfaces or free streamlines was first formulated by Helmholtz (1)* and Kirchoff (2). Kirchoff considered the potential flow about a flat plate lamina with an infinite "dead water" region occurring behind the plate. This region was separated from the main flow by two free streamlines extending from the body out to infinity. This idealized picture of the wake occurring behind an object was the first step in the development of more physically credible models for representing this type of separated or cavitating flow.

The subsequent analytical treatment of cavity flows may be divided into two types: that of the non-linear theory, and the

---

*Numbers in parentheses refer to the references at the end of the text.

linearized techniques. Both these schemes, however, treat the problem as one in potential flow in which the flow around the body-cavity system is assumed to be inviscid. The possibility of treating these problems in this way is directly dependent on choosing a suitable potential flow model to reproduce the viscous dissipation which actually occurs at the end of the cavity and in the subsequent wake. The fact that it is possible to select certain meaningful physical models to fulfill this aim is due largely to the observed fact that the forces on the body are determined in the main by the local flow field around the body and to a much smaller degree by the detailed behavior of the ultimate wake.

Several models have been proposed for treating cavity flows in the non-linear theory. These models all differ from each other in physical concept and mathematical complexity. In 1921 Riabouchinsky (3) proposed a model wherein the dissipative wake was replaced by an image body at the rear end of the cavity. The force exerted on this image body alone was a measure of the drag experienced by the cavitating fore-body. This proposal was followed by one made by several authors, for example, Efros (4) and Kreisel (5), who considered a "re-entrant jet" model for representing the flow. In this model the free streamlines forming the boundaries of the cavity turn back on themselves at the end of the cavity to form a jet which moves in an upstream direction behind the body. The momentum contained in this jet is then considered as the momentum loss due to drag. This model is very close to what is observed

physically and in fact a re-entrant jet structure is frequently evident in cavitating flows.

Still later, viz. in 1954, Roshko (6) proposed a model in which the wake is considered bounded by two streamlines parallel to the flow direction. The pressure along these streamlines increases from its value in the cavity to that of the free stream. This model is considerably easier to handle mathematically than the previous ones. Finally, Wu (7) has proposed a model somewhat more general than Roshko's in which the wake is again bounded by two streamlines in which, however, the directions of the latter are not determined a priori but given from the theory. Here again pressure recovery occurs along the streamlines. The advantage of the latter two models over those proposed earlier is the ability of these last two to enable one to treat both fully and partially cavitating flow - that is where the cavity is either longer or shorter than the chord length of the body. This then gives the complete spectrum of behavior of the forces and the cavity from the fully wetted condition to the fully cavitating condition.

The mathematical difficulties inherent in these non-linear theories stimulated the development of a linearized cavity theory. This linearized technique is due to Tulin (8) and is basically similar to thin airfoil theory. Here the cavity-body system is considered as a slender body and the flow field due to this system is considered as a small perturbation on the main flow. Further, the boundary conditions are not applied along the actual boundaries, which in the

case of the cavity are unknown, but along a slit representing the system. In Tulin's linear theory the cavity closure and the dissipative wake are represented by a point singularity which is placed at the end of the cavity. The force exerted on this singularity may be viewed as a measure of the energy dissipation. An excellent review of this linearized theory has been given by Parkin (9).

From the experimental viewpoint many works have appeared on the cavitating performance of single hydrofoils. It suffices here to mention but a few of these. In 1932 Walchner (10) investigated the cavitating performance of several hydrofoil sections determining their lift and drag characteristics as a function of the cavitation number. These profiles, subsequently called "Walchner profiles", are a close relative of the Karman-Trefftz airfoils. In his investigations cavitation numbers were based on vapor pressure. This excludes any possible formal comparison with his data at lower cavitation numbers, since as was pointed out by Reichart (11) the cavity pressure as measured is the only meaningful pressure on which to base the cavitation number under these conditions.

Balhan (12) carried out a series of cavitating tests on a family of Karman-Trefftz hydrofoils. His experiments, however, were made over a limited range of cavitation numbers and the region of long cavities or, alternatively, low cavitation numbers, was not investigated. Some correlations between Balhan's results and those obtained from the linearized theory of a partially cavitating flat plate were made by Acosta (13). Over the range of valid

comparison fair agreement was obtained.

In 1953 a program of hydrofoil research was undertaken at the Hydrodynamics Laboratory at the California Institute of Technology. Several reports resulted from this work, principal of which were those of Kermeen (14) and Parkin (15). Kermeen undertook a formal calibration of the then new two-dimensional working section in the high speed water tunnel and further studied the performance of an NACA 4412 hydrofoil and also a Walchner type section in both non-cavitating and cavitating flow. Comparisons made between Kermeen's results and those of Walchner were sufficiently divergent as to lead Kermeen to state that: "If the results obtained in different facilities are to be compared, they must be compared on the basis of the measured cavity pressure wherever possible". Parkin undertook an investigation of a flat plate and a circular arc hydrofoil. Comparison of his results in both cases with a non-linear theory worked out by Wu (16) using the Roshko model were made. Agreement proved to be very good over the range of validity of the theory, namely, for fully cavitating flows.

Some experimental work on partial cavitation was carried out by Meijer (17), in Holland, on bi-convex and plano-convex hydrofoils of small thickness ratios. Correlation between his experimental cavity lengths and those predicted by Geurst (18) using a linearized theory was found. This correlation, however, was limited to the bi-convex foil. For the plano-convex shape a systematic discrepancy was found due no doubt to camber effects, not accounted for in the

theory. In the linearized theory as has already been mentioned the cavity is closed by means of a singularity. Meijer made some measurements of the pressure at the end of the cavity and found that indeed there was a high pressure zone situated there, but of the order of only half the stagnation pressure and not the full stagnation pressure as implied by the theory.

In the experimental investigations of Kermeen, Parkin and Meijer it was found that the transition from partially cavitating flow to fully cavitating flow was accompanied by extreme vibrations in the flow and that the cavity itself was not steady. No detailed investigations were carried out in this regime of cavitation due to the inadequacies of the measuring instrumentation. A somewhat similar unsteady phenomenon was reported by Knapp (19) in which partial cavitation was being observed on cylindrical bodies with hemispherical noses and on thick two-dimensional non-lifting bodies with circular noses. This region of unsteady cavitation, however, is still far from being understood. All the proposed models for describing cavitating flows do not account for this phenomenon as they are all formulated on the basis of a steady flow.

In all the above comparisons between theory and experiment it has generally been borne out that the theory represents a good description of the actual processes taking place in fully cavitating flows with the exception of the unsteady regime mentioned. Needless to say the non-linear theory agrees closer with the experimental results than does the linearized theory. This latter theory usually

overestimates the forces, especially for large angles of attack above about 10 degrees (20). For the smaller angles, though, a fairly good agreement exists although this agreement between linearized theory and experiment is adversely affected by camber and thickness effects of the hydrofoil.

Before reviewing the field of cavitating cascades it is opportune at this juncture if a brief survey is made of fully wetted cascades. Theoretical and experimental work in this field has been extremely comprehensive and only a few relevant works will be mentioned.

Pistolesi (21) dealt with the problem of a cascade of thin slightly cambered blades by the use of an extension to the method developed by Glauert in solving the isolated thin airfoil problem. He established expressions for the lift and moment on the blades by using the first three terms in the Glauert expansion. He also illustrated that a quarter chord point approximation (viz., Weissinger's approximation) can be set up for predicting the circulation around blades of this type in cascade. No numerical work was carried out, however.

In 1944 Garrick (22) published a paper treating the problem of the potential flow past a cascade of arbitrary shaped airfoils. Essentially the method utilized the well-known method of Theodorsen used in isolated airfoil theory in conjunction with a conformal mapping. The use of this technique, however, is relatively arduous and time-consuming. In an effort to cut down on the numerical labor Katzoff et al (23) proposed an interference method which breaks the

problem down into the solution of the flow past an isolated foil together with an interference flow due to all the other blades of the cascade. By the use of certain graphical data the method is made more tractable than the previous ones. Comparison with Garrick's method shows excellent agreement. Although this method achieves a certain amount of simplification it is still quite cumbersome and the numerical labor involved is still considerable.

Subsequently, Schlichting (24) developed a method using thin airfoil theory results which also included thickness effects. The camber and thickness functions, which are represented by vorticity and source distributions, were expanded in a Birnbaum series and the coefficients determined by satisfying the boundary conditions at various points on the profile. By truncating the series after three terms and meeting the boundary conditions at three specific points on the airfoil, he obtained a good and fairly rapid determination of the cascade lift and pressure distribution on the foil. This procedure greatly facilitated the computational aspects of cascade work. Finally in 1959 Mellor (25) obtained the coefficients of the vorticity and source distributions by making use of the orthogonality of the trigonometric functions. The coefficients were obtained as double integrals which were evaluated numerically by means of a very ingenious method. Results from this method are given in graphical form, clearly illustrating the relative effects of angle of attack, camber and thickness on the lift. The effects of solidity and stagger on each of these parameters is also illustrated. The

computation is given for circular arc camber and 65-series camber lines, but the results are applicable without alteration to any symmetrically cambered airfoil. This paper has indeed reduced the fully wetted cascade problem to one that is easily handled numerically and is ideally suited to the designer.

The ability of obtaining reliable experimental data in the field of cascades has been fraught with many difficulties. The effects of end-wall and side-wall boundary layers were such that two-dimensionality of the flow was lost causing erroneous measurements for pressure distributions and turning angles (26). Methods of obviating these difficulties were devised by the use of boundary layer control slots in conjunction with boundary layer suction. This control enabled flow two-dimensionality to be achieved with correspondingly better experimental results. These techniques are described in detail in Reference 27. Comparison of results obtained in this fashion with theory are found to be in very good agreement (28). With this technique of cascade testing, the National Advisory Commitee of Aeronautics undertook a comprehensive program of cascade tests in 1951 (29) covering a wide variety of 65-series compressor blades with varying solidities and stagger angles.

All the above theoretical approaches treat the flow as incompressible and inviscid. Real fluid effects, however, are greatly emphasized in cascade flows, not only with respect to boundary layer growths on the foils together with their corresponding wakes but in the form of other secondary flow losses occurring as a consequence

of the influence of one foil on the other. The real fluid effects associated with the boundary layer growth on the blades has been treated by Schlichting (30). Comparisons of calculated and measured loss coefficients show good agreement. Lieblein (31), (32), (33), (34) has developed a semi-empirical theory to account for these effects from either wake measurements near the body or from the maximum diffusion ratio on the body. The losses associated with the secondary flows have been considered by many authors. A review article of these works is given in Reference 35, together with a comprehensive bibliography.

The field of cavitating cascades is in no way nearly as well covered as that of the fully wetted flows. The work in this area, on the contrary, is relatively sparse and few analyses have appeared in the literature. As examples, Betz and Petersohn (36) applied the model of Helmhotz and Kirchoff to the flow through a series of flat plates. They conducted a series of experiments at zero stagger to verify their theory for these fully choked flows and found fair agreement. The next development in this field was not until 1958 when Cohen and Sutherland (37) treated the case of a cascade of arbitrary foils by means of Tulin's linearized theory. Their results apply only to the fully cavitating region. Numerical results for the flat plate are presented in their paper. Subsequently Acosta and Hollander (38) dealt with the partial cavitation in a cascade of semi-infinite flat plates. This problem was recently treated using non-linear theory with the Roshko model by Stripling and Acosta (39),

but no formal comparison of the two methods was made. Acosta (40) also considered the case of the fully choked cascade of circular arc hydrofoils using linearized techniques. Comparison between this theory (when camber is zero) and that of Betz and Petersohn are fairly good for a wide range of solidity and stagger. Again the linearized theory tends to overestimate the forces.

Experimental work on cavitating cascades has been sparse indeed and only the work of Numachi (41) is known to the author. This work covers tests performed in a high speed water tunnel on various profiles in a quest for an optimum profile from the point of view of cavitation performance. The tests have been carried out for both accelerating and decelerating cascades. The emphasis of the tests, however, seems to have been mainly concerned with arriving at this optimum profile. Detailed investigation of the flow behavior and a thorough explanation of the experimental techniques used are not available and make it somewhat difficult to interpret the results obtained in a systematic and meaningful way.

II. OBJECTIVES OF THE INVESTIGATION

As can be appreciated from the previous section, there exists a lack of information in the area of cavitating cascade tests. This regrettable state of affairs is due in large part to two basic factors: Firstly, very few high speed water tunnel test facilities are available with the required working section dimensions to accommodate such tests without the risks of large wall boundary effects occurring.

Secondly, the conditions which must be fulfilled under cavitation to ensure cascade performance are by no means clear. Thus it is evident that apart from the desirability of obtaining performance characteristics of hydrofoil sections under cascade conditions, basic questions have to be answered as to the best methods suitable for representing these cascade conditions in a water tunnel. The questions of the relative effects of side wall boundary layers, boundary layer interactions, and secondary flow losses are also completely unanswered under these conditions.

As a preliminary to undertaking a cascade investigation it was decided to study anew the characteristics of a hydrofoil in the isolated case. This investigation was motivated by several important reasons: Since the experimental work on cascades is comparatively time-consuming, it was anticipated that the initial scope of the tests would be somewhat limited in range and that the study of the flow characteristics about the isolated foil would provide one with some idea of the salient features to expect and look for in the cascade flow. Moreover tests of this nature are in themselves important in providing data for the designer. An added incentive in studying the isolated foil was the opportunity provided for undertaking a study of the unsteady region of cavitation, as previously mentioned, occurring in the transition from partial to full cavitation. As the only data available in this regime of cavitation was that of Knapp (19) it was deemed a worthwhile endeavor. The results obtained from the partially cavitating region would provide a check on the applicability

of a linearized theory developed for this region of cavitation which accounts for the camber and thickness effects of the profile. Furthermore, this investigation would provide data concerning the behavior of the cavity length as a function of the cavitation number. Precise measurements of cavity length have been relatively few, and these would provide a check for some of the non-linear theories already developed for the range of full cavitation.

These tests would further provide an opportunity of becoming familiar with the various test procedures used in water tunnel work as well as providing a means of developing certain measuring techniques. This phase of the experimental program was thus considered more than just a preliminary investigation to the cascade work but a study which would produce results in its own right.

As already mentioned, since little is known about the behavior of cavitating cascades, these investigations were carried out more as a feasibility study to determine whether or not a consistent procedure could be developed to simulate cascade conditions throughout the entire range of cavitation and to investigate qualitatively and quantitatively the flow behavior under these conditions. The questions regarding the influence of guiding walls on the downstream conditions and on the cascade forces were also of importance. The ability to conduct the tests under fully wetted and fully choked conditions provided a means of determining whether the test procedure used was fulfilling the above requirements.

Another feature of importance was the question as to whether

the unsteady cavitating effects observed in isolated hydrofoils occurred in cascades and if so, whether the phenomenon had the same behavior as the isolated case or would give rise perhaps to a condition similar to that of propagating stall experienced by turbomachines.

The answers to the above questions would no doubt help in determining a suitable procedure for further work on cavitating cascade tests and bring to light some unanswered questions in this field of experimentation. Furthermore, the accuracy and ability of such tests in predicting machine performance could be gaged, thus giving the designer a further tool with which to work.

The present investigation deals mainly with the study of the non-cavitating and cavitating performance of a hydrofoil section in both the isolated and cascade configurations. The model chosen for these tests was a plano-convex section having a flat pressure side with a circular arc suction surface. The reason for deciding on such a model was threefold: Extensive use has been made of this section, and variations thereon, in propeller work. Furthermore, accurate foils of this type can be manufactured at relatively low costs with conventional machines. An added but not essential requirement is that simple shapes such as this lend themselves more readily to analytical study. The details of the models used will be taken up in a later section.

The presentation of the above studies is set out in two sections: Part I covers the experimental procedure and analysis of

the isolated tests. This section covers the detailed explanation of the water tunnel together with its ancillary equipment such as the force measuring equipment and pressure measuring devices. The various experimental techniques used in conducting the tests and obtaining the data as well as the corrections applied to these data are presented. The test results are discussed in three parts: (1) the non-cavitating performance, (2) the cavitating characteristics, and (3) the behavior in the unsteady region of cavitation. Conclusions drawn from these investigations are then presented at the end of the dissertation.

Part II concerns itself with the experimental program undertaken to analyze the performance characteristics of cavitating cascades. The scope of the investigations is somewhat limited by the necessary procedures adopted. Two compressor cascades of different solidities and a turbine cascade are considered. The emphasis of these tests is placed on determining the feasibility of using the water tunnel as a cascade tunnel. The alternative methods considered for modifying the tunnel to accommodate such tests with the subsequent design and manufacture of the component parts to effect this modification are presented. The methods used in conducting the tests such that cascade conditions are simulated are then discussed, as are various procedures used in recording the data together with necessary corrections made. Comparison of the results obtained with available theory is then undertaken with the view of checking whether in fact meaningful results can be expected

with these procedures. These theoretical results are those taken from the fully wetted cascade theories developed by Schlichting (24) and Mellor (25) and from the fully choked theory of Betz and Petersohn (36). For the partially cavitating region a comparison is made with a linearized cavitating theory previously developed by the author and presented in Appendix IX. Finally the conclusions to be drawn from this experiment, including further modifications for extending the versatility of the experimental set-up and improving the flow conditions are considered.

PART I - ISOLATED HYDROFOIL STUDY

III. TEST EQUIPMENT

1. Water Tunnel - The tests were conducted in the high speed water tunnel in the Hydrodynamics Laboratory of the California Institute of Technology. The detailed features of this water tunnel, together with its component parts, are described in Reference 42, and it therefore suffices to mention but a few of the main characteristics.

The tunnel is a closed circuit type, the path of travel of the water being 340 feet. It is provided with a resorber which is essentially a large vertical steel tank 58 feet long by 11 feet 6 inches diameter divided into four ducts. The water makes four circuits through this tank and is thus subjected to large hydrostatic pressures at the bottom of the tank which is 84 feet below the center line of the working section. This large pressure assures complete absorption of any air bubbles in solution before the water reflows through the working section. The tunnel is powered by a direct current 350 horsepower shunt wound motor. This motor is vertically mounted and drives a 48 inch propeller pump.

The maximum velocity attainable in the working section used is approximately 65 feet per second. An added feature of the tunnel is the ability to control the pressure, independently of the flow velocity. This is essential for cavitation studies. The range of

pressure control is from about 100 psi to vapor pressure.

The flow through the working section is made uniform by passing the water through a honeycomb situated just upstream of the tunnel nozzle. This nozzle then reduces the flow area to that of the working section, in this case a reduction of about 67 to 1. The resulting flow distribution entering the working section has been shown to be quite uniform with small side wall boundary layers (14). On passing through the working section, the flow energy is reconverted into pressure energy in a long diffuser. A diagrammatic sketch of the general layout of the tunnel is shown in Figure 1.

2. Working Section - The original high speed water tunnel working section is a 14 inch diameter axially symmetric one. For the purposes of the present study this section is converted into a two-dimensional working section by bolting into place in the tunnel two nozzle castings that convert this circular section into an approximately 14 inch by 3 inch two-dimensional channel. The castings are continued in the working section by flat vertical brass side walls and terminated by a short diffusor casting. This modification is illustrated in Figure 2 and the inserts are seen in position in Figure 3. The modified working section is provided with a lucite window 3 inches wide by 10 inches in length located in one of the brass walls opposite the model mounting location. Further lucite windows are provided at the top and bottom of the section giving a three-way view of the model when it is mounted in the tunnel. The net length of the working section is 20 7/8 inches.

3. Force Balance - The forces on the hydrofoil are measured by means of an external type force balance. This balance measures the lift force, drag and pitching moment on the model under test. These forces are transmitted from the model to a force table which is mounted, by three flexure struts at 120^{o} to one another, to a base plate fixed to the balance frame. These struts effectively ground out any yawing and rolling moments on the model. The required forces are transferred to the balance spindle through three force transmitting flexure struts connecting this spindle to the force table. This entire mechanism is mounted in an oil-filled housing which is always maintained at the tunnel working pressure to avoid any axial thrusts on the system. The balance spindle is pivoted on a wire support and the forces are thus transmitted to three hydraulic force sensing devices. The above is shown schematically in Figure 4.

The balance is so designed that it can be used in a horizontal or vertical position. For the present study the former set-up was used as indicated in Figure 5. Means are provided in the balance for changing the angle of attack of the model by a worm gear drive. This is made possible as the spindle to which the model is attached is mounted in two preloaded ball bearings which permit rotation but hold radial motions to a very small amount, even under maximum loading conditions. The design loads for the balance are ± 150 lbs for both lift and drag and ± 560 lbs in for the moment.

The detailed description, construction and calibration of this

balance is described in Reference 43.

4. Model - As previously mentioned the model was a plano-convex hydrofoil. This foil, a member of the Karman-Trefftz airfoil series, has sharp leading and trailing edges with a flat bottom surface and a circular arc upper surface. The model is integrally machined with a base-plate as shown in Figure 6 and is manufactured from stainless steel. It is provided with a pressure tap located 0.2 inches behind the leading edge on the suction surface of the hydrofoil at approximately mid-span. This orifice enables one to measure the cavity pressure. A semi-conductor half bridge strain gage is mounted at the root of the model flush with the flat surface. The strain gage is located at the center of the hydrofoil and is bonded in place with an epoxy cement, which also acts as a waterproofing agent. The strain gage provides a means of recording fluctuating forces on the hydrofoil which otherwise would be unobtainable by using the force balance since the response of the latter is far too inadequate for this purpose. The model has a thickness ratio of 7 percent with a chord length of 2.77 inches, a span of 2.85 inches and a maximum thickness of 0.19 inches. These dimensions together with the sign convention used in calculating the forces on the model, are shown in Figure 6(b).

5. Instrumentation

A. Force Measurements - The forces recorded by the force sensing elements on the balance are measured by means of balances which automatically balance the forces applied by the

hydraulic system. These force balances consist essentially of a beam supported on a Cardan pivot, with a carriage running along the beam. The position of this rider is controlled electrically, depending on whether the beam is balanced or not. The range of each balance can be increased by the use of pan weights. The position of the rider is indicated by a counter which is calibrated to read directly in pounds for the case of lift and drag and directly in pound inches in the case of the moment. The least count of these counters is 0.01 pounds (or 0.01 pound inches for the moment).

The readings of these force balances are recorded on film during a run by photographing the force console using a 35 mm. recording camera. This system of recording the forces lends itself to a very rapid method of taking data and enables all the forces on the model to be read at the same instant of time.

B. Pressure Measurements - The static and differential pressures in the tunnel are all recorded by means of mercury manometers, with the exception of the differential pressure across the tunnel nozzle. In this instance a balance similar to that used for recording the forces is employed. The hydraulic system is connected to the tunnel through two interface pots where for safety reasons the oil-water interface may be monitored. This balance is so calibrated that it reads out the differential pressure in pounds per square inch with a least count of 0.001 psi. It is recorded photographically along with the force readings.

The mercury manometers used for differential pressure

readings are standard two limb type manometers having vernier scales capable of reading differences of 0.001 feet of mercury. The static pressure in the tunnel is recorded on a well-type mercury manometer which records the absolute pressure in the tunnel, again to within 0.001 feet of mercury.

Measurement of the cavity pressure presents somewhat of a problem. Due to the frothy nature of the cavity, water tends to enter the tubing connecting the cavity orifice with the manometer, thus causing false readings. To ensure correct readings of the cavity pressure the line is kept clear of water by constant purging with a small amount of bleed air. The resulting error in pressure using this procedure is always less than 0.8 inches of water, which corresponds to an error of about one percent or less in the worst case in the determination of the cavitation number. This method of measuring pressure has also been proposed by Gadd (44), but his report was not available at the time this portion of the work was carried out.

C. Cavity Length Measurements - For each data point taken the model is photographed both in plan view and from the side, using two 35 mm. recording cameras. These cameras are remotely controlled and coupled to the camera recording the forces, thus ensuring that the cavity length so recorded is taken at the instant the forces are being recorded. The cavity lengths, both in the partially and fully cavitating regions, are then determined from these films by direct measurement.

D. Unsteady Measurements - In the unsteady region of

cavitation the fluctuating force component normal to the hydrofoil chord is recorded by measuring the output of the solid state strain gage mounted on the model. This strain gage forms part of a simple bridge network. The output from this bridge is recorded by a direct writing recording oscillograph, using photosensitive paper. The strain gage used is a temperature compensated P.N. type silicon gage, with a total internal mounted resistance of 750 ohms and a gage factor of 230. The bridge network is so designed that the maximum energy dissipation in the strain gages is always below the recommended maximum of 0.1 watt, and the current in the gages is essentially constant over the range of interest. The bridge impedance is made equal to the correct loading impedance of the recording galvonometer to achieve critical damping. The galvonometer used has a flat response for 0 - 60 cps with a 6.12 microampere/inch sensitivity. This system behaves extremely well giving good response and adequate sensitivity for the unsteady measurements taken with essentially no non-linearity occurring.

For the unsteady runs the cavity oscillations are also recorded. This is achieved by the use of a 16 mm. high speed movie camera. The camera is run at approximately 1900 frames per second and may be set up to record both plan and side views of the oscillating cavity. The output of the strain gage may also be photographed, if desired, by displaying the trace of the galvonometer on a small mirror which reflects it into the camera's field of view.

Figure 7 shows the working section of the tunnel together with some of the measuring equipment. To the left of the photograph is seen the manometer for measuring the cavity pressure. Mounted below the working section and directly in front of it are the 35 mm. recording cameras for determining the cavity length. At the right of the picture can be seen two of the force balances on the force console.

Figure 8 illustrates one of the test set-ups used in the non-steady investigation. The 16 mm. high speed camera is seen in the foreground mounted on a tripod. The recording oscillograph which houses the galvanometer is seen mounted immediately in front of the working section in a vertical position. Just above the viewing window the small narrow mirror which deflects the light trace of the galvanometer into the field of the camera can be seen held at 45 degrees. The mounted model is just visible through the viewing window.

IV. EXPERIMENTAL PROCEDURE

The model was mounted to the balance spindle by means of three bolts. Shims were used so that the base plate could be set flush with the tunnel wall. A circular gap of 0.020 inches was left between the model attachment piece and the surrounding tunnel wall. The horizontal mounting of the model was chosen so as to eliminate hydrostatic pressure gradients along its span which would give rise to uneven cavitation over the model. No check was made to

determine the flow direction and uniformity in the tunnel since a detailed calibration had already been carried out on this section by Kermeen (14), indicating that the flow is very uniform.

The end gap between the model and the facing wall of the two-dimensional test section was adjusted to 0.005 inches and kept at this value throughout the experiment. This adjustment was made possible by loosening or tightening two bolts holding the wall supporting struts. Although the end gap did vary slightly throughout the experiment, it was found that the variation of the forces on the model with end gap for fully wetted flows over a range of 0.005 inches to 0.0105 inches was less than 5 percent for the lift and drag and negligible for the moment. During a run the variation in end gap was never greater than 0.004 inches, hence this effect was sufficiently small to be considered negligible. Similar results to this were obtained in Reference 14 although somewhat larger drag variations were obtained, due probably to the greater thickness of the model. These changes in the forces with end gap clearance were due to flow taking place through the gap from the pressure side of the hydrofoil to the suction side. The tendency was for the lift to decrease with increase in end gap, together with an increase in drag.

Since the leading and trailing edges of the hydrofoil are sharp, an infinitely negative pressure occurred at the leading edge for positive angles of attack, and normally a cavity would spring from there. This, however, does not always occur. At low angles of attack, below 4 degrees for the section tested, the cavity

appeared down stream of the leading edge on the low pressure surface. In fact, for some of these lower angles two cavities were observed simultaneously; one, very short, springing from the leading edge and the other from a point near the maximum thickness of the hydrofoil. At and above 4 degrees the cavity started at the leading edge for all conditions of cavitation. The emphasis of the present study was placed on angles of attack larger than 4 degrees. Thus the cavity detachment point remained fixed at the leading edge giving a readily anticipated flow pattern and a more straightforward interpretation of the experimental results than would otherwise have been the case. One outcome of this restriction was that the profile behaved essentially like a flat plate for cavities larger than the chord, a configuration previously tested by Parkin (15).

In general the experiment was conducted in two phases to obtain the steady force readings. Fully wetted data were obtained at constant tunnel speed and pressure by varying the angle of attack over the region of interest, in the present case -4^{o} to 15^{o}, in increments of 15 minutes of arc. This was repeated for several velocities to give a range of Reynolds numbers. However, the cavitating experiments were made at constant angle of attack and tunnel speed, whilst the working section static pressure was varied to obtain the full range of cavitation. These tests covered a range of angles of attack of 4^{o} to 10^{o} and velocities from 15 to 40 feet per second.

The readings of the force gages were corrected for no-load

readings, for the effect of tunnel static pressure variation on these no-load readings and for the viscous forces exerted on the model mounting disk. The former corrections were obtained by recording a series of no-load readings at various pressures over the range of interest and applying these readings as corrections to the actual forces. The tare forces on the mounting disk were obtained by mounting the model from the opposite wall of the tunnel with a blank disk fastened to the force spindle. The forces on this disk were then recorded for all conditions covered in the experiment. The details of this method are described in Reference 14. These tare forces, although small in the case of lift and negligible in the case of moment, comprised under certain circumstances as much as 30 percent of the total drag force. The results of these tests are shown in Appendix II.

The dynamic head $\rho V^2/2$, and hence the tunnel speed V, were determined by measuring the pressure drop between the piezometer ring at the 5 foot diameter circular section of the tunnel upstream of the tunnel nozzle and the two-dimensional section itself. This pressure difference was recorded on the force read-out console, as previously mentioned. The cavity pressure was measured with respect to the working section static pressure with a mercury manometer. The method used was that already described in the previous section.

Due to the dimensions of the working section all pressure measurements made in this section were subject to the influence of

the model. The question then arose as to what to call the true working section static pressure or ultimately, what is the pressure corresponding to a point far away from the model. It is usually impractical to have a two-dimensional section of sufficient length to measure the pressure prevailing at an infinite distance upstream - even though this is what is required in the reduction of the force coefficients and cavitation numbers. In the present case the static pressure in the working section was measured at a point 2.25 chords upstream from the center of the model and 1.4 chords above the level of the hydrofoil. A different orifice only 1.8 chords from the model center line and on the center line of the flow was used as the working section static pressure reference for the cavity pressure measurement. It was, therefore, found necessary with the experimental procedure used, to correct all the above pressure measurements for the model effects. The method adopted for applying this model interference correction is given in Appendix III.

The system used for carrying out the unsteady runs was quite similar to the method used in the cavitating tests. At a constant angle of attack and tunnel speed, the tunnel pressure was varied. For each setting the force on the hydrofoil was recorded on the oscillograph. In addition, for the region where the oscillations occurred, the cavity pulsations were photographically recorded in conjunction with the strain gage output by means of the 16 mm. high speed movie camera. This latter reading afforded a means of obtaining the relationship between the changing cavity geometry and

the varying force. Several film strips were assembled into a short sound motion picture* which illustrates this non-steady cavitation process. The above data were obtained for three angles of attack, viz., 4^{o}, 6^{o} and 8^{o}, and for various tunnel speeds.

No attempt was made to analyze separately the effects of moment, drag and lift force on the output of the strain gage. It was assumed that this output would be proportional to the lift force and that this proportionality would be the same for static as well as dynamic conditions. The strain gage was then calibrated by comparing its output with the output of the external force balance when the flow was steady.

V. EXPERIMENTAL RESULTS

For each data point lift, drag and moment coefficients were calculated. Apart from those already mentioned, no corrections were made for tunnel interference effects such as wall blockage, wake blockage and longitudinal pressure gradient. All these effects are small for the present experiment except possibly for the fully cavitating flow.

The force coefficients are defined in the usual manner, viz.,

---

*The film, entitled "Some Non-steady Effects in Cavity Flows", Report No. E-79.5, is obtainable from the Hydrodynamics Laboratory, Karman Laboratory of Fluid Mechanics and Jet Propulsion, California Institute of Technology, Pasadena, California.

$$C_L = \frac{L}{A\rho V^2/2} \quad ; \qquad C_D = \frac{D}{A\rho V^2/2}$$

$$C_M = \frac{M}{Ac\rho\ V^2/2}$$

where the sign convention illustrated in Figure 6(b) is adopted. The cavitation indices, based on measured cavity pressure and on vapor pressure, are

$$K = \frac{p - p_k}{\rho V^2/2} \quad ; \quad K_V = \frac{p - p_v}{\rho V^2/2}$$

respectively. The notation used is given in Appendix I.

1. Fully Wetted Results - First, let us consider the fully wetted characteristics of the hydrofoil. In Figure 9, the lift, drag and moment coefficients are plotted versus angle of attack. The points are shown for a Reynolds number range of from 0.46×10^6 to 0.75×10^6 based on chord length. Over this range there is very little significant change.

It is seen that about 1^o angle of attack there is a slight stalling effect in the lift curve with a corresponding increase in the drag. This effect is characteristic of certain sharp nose aerofoils and is due to the type of boundary layer separation occurring on the foil (45, 46, 47). This wave in the lift curve comes about because of the type of laminar separation of the boundary layer at the leading

edge and its subsequent turbulent reattachment. This hump can be removed by increasing the Reynolds number to approximately 6×10^6 or by increasing the nose surface roughness. These effects are discussed in detail in the above references. According to airfoil theory the zero lift angle of attack of this foil is $-4^\circ 10'$ and the lift coefficient at $\alpha = 0$ is 0.479. From the experimental curve it will be seen that although the zero lift angle is very close to the theoretical one the lift slope is very much lower, being about 83 percent of its theoretical value. This lift slope, less than 2π below the hump, decreases further above it.

Figures 10 and 11 show respectively the variation of the lift-to-drag ratio and the center of pressure location with angle of attack, the kinks in these curves being due, once again, to the boundary layer separation.

2. Cavitating Performance - To determine how consistently the cavity pressure, or cavitation number, could be recorded and how this reading compared with that based on vapor pressure, a plot of K against K_v was made for varying velocities and angles of attack. As is seen in Figure 12, this reading is quite repeatable. The discrepancy between the two readings increases with increasing cavitation number. It will be noted that the cavity pressure is always higher than the vapor pressure. This result is to be expected as the gases in solution contribute to the pressure within the cavity.

For cavitating flow the values of the force coefficients as a function of the measured cavitation number are shown in Figures 13,

14, 15 and 16, each graph being for a different angle of attack. The subsequent photographs indicate the degree of cavitation occurring on the hydrofoil at a few different cavitation numbers which are marked on the graphs. It will be seen from these graphs that as cavitation occurs there is an initial increase in lift with a corresponding decrease in drag for all the angles tested. As the cavity length approaches the chord length, however, the drag increases sharply and the lift begins to decrease. On further decrease in cavitation number both lift and drag decrease. The moment on the hydrofoil remains fairly constant over the partially cavitating range and decreases thereafter. The results obtained in the fully cavitating regime agree well with those of Parkin (15). The lift curves have been extrapolated, by dashed lines, to zero cavitation number where the values of lift shown are those given by the well known Rayleigh formula.

Figures 17, 18, 19 and 20 show graphs of the cavitation number divided by angle of attack as a function of cavity length. The solid points are those occurring in the unsteady flow regime. As can be seen this unsteady region occurs over a range of approximately 0.6 ℓ/c to 1.2 ℓ/c, regardless of the angle of attack. This region of unsteadiness has been indicated on the graphs of the force coefficients as well. Here the forces are fluctuating violently and the points shown plotted are "average" forces recorded by the balance. Although it is believed these average forces are representative of the true time average, no systematic investigation of

this point was made.

Theoretical curves obtained from linearized free-streamline theory in the regions of full cavitation (20) and partial cavitation (13) on a flat plate hydrofoil are also shown in Figures 17-20. We see that for the fully cavitating flow the agreement is better than for the partial cavitating case. This, however, is to be expected since in the former case the hydrofoil acts exactly like a flat plate whereas in partial cavitation, camber and thickness effects play a role. In order to determine the effects of camber and thickness on the partially cavitating performance of a hydrofoil of this type, a linearized solution was developed including these effects. The details of this solution are given in Appendix IV. It will be seen that the effects of profile shape give rise to even larger discrepancies between theory and experiment. The results of Meijer (17) on 4 percent thickness ratio hydrofoils show much better agreement with the present theory. However, his cavitation numbers are based on vapor pressure and not on measured values. If this procedure is adopted in the present case better agreement between theory and experiment is also found. It is known from airfoil experiments that if the theoretical lift is arbitrarily adjusted to the experimental value, the theoretical pressure distribution on the foil agrees with the experimental one. This artifice achieves two purposes. First, it endeavors to some extent to account for real fluid effects and secondly, it affords a means of checking whether the experimental data are self consistent. This approach was utilized here. The

theoretical lift coefficient was adjusted to the experimental value for the same cavity lengths and the corresponding theoretical cavitation number was adjusted accordingly. These adjusted cavitation numbers are shown plotted in Figures 17-20 as are the corresponding uncorrected values. It is seen that the corrected values are in very good agreement with the experiment.

In Figure 21 the polar diagram for the section is plotted. Experimental results on a similar section are reported for non-cavitating and cavitating conditions, for angles of attack of up to 5^{o}, in Reference 10. The cavitation number in these experiments is based on vapor pressure and hence a direct comparison with the present data cannot be made exactly. The thickness of the profile is also slightly different. Nevertheless, quite a favorable agreement is found in the common region covered by both investigations.

3. Non-Steady Cavitation - As mentioned previously oscillations in cavity length and hydrodynamic force developed when the cavity was about sixty percent or so of the chord and persisted until the cavity was at least 1.2 times the chord. A description of the development of this process seems now in order. The general behavior for all angles of attack equal to or greater than 4^{o} is similar, and the general development of the non-steady process is the same for all angles.

From the fully wetted condition to a cavity length of sixty percent chord, the cavities are steady in the mean; the cavity is not glassy clear, however, but is filled with a frothy mixture of air and

water and has no definite structure such as a re-entrant jet, for example. Incidentally, at the very first stages of cavitation when the cavities are no longer than 2-3 percent of the chord, a relatively high-pitched oscillation and noise develop with a frequency of about 270 cps. This is thought to be associated with one of the fundamental vibratory modes of the hydrofoil itself. Although audible noise is generated, the resulting force oscillations are small as measured by the imbedded strain gage. The cavity retains its frothy character until just before oscillation commences, at which point the portion of the cavity near the leading edge becomes clear and glassy. Shortly thereafter the cavity begins to oscillate. These initial oscillations are of small magnitude, both in extent and force, and are relatively high in frequency. For the present tunnel conditions these frequencies may range from 50-60 cps. This stage of oscillation seems to be rather transitory and with a slight decrease in tunnel pressure the oscillation changes over into a more characteristic low frequency, large amplitude disturbance. The oscillations then typically have a double amplitude of about one-half chord. Typical frequencies in this stage under the conditions of the tests were about 12 to 25 cps depending upon velocity and angle of attack. The oscillations would persist with further lowering of tunnel pressure until the cavity was about one-fourth longer than the chord. Generally, the amplitude of the cavity and force oscillation decreased. The flow then became quite steady with proper full cavitation developed. During this entire process the forces, average and non-steady, first increased and then

decreased. The maximum average force and non-steady force occurred at or near the condition of maximum oscillation in the cavity.

One cycle of the cavity oscillation is shown in Figure 22. This figure shows the plan form of the developing cavitation at an angle of attack of 6^{o}. The flow is from top-to-bottom with the leading edge being at the top in both rows. The sequence starts at the upper left and time increases from left-to-right. These are selected from a test film strip taken at 1200 frames per second. Starting at the minimum cavity length, the cavity grows smoothly and as it approaches the end of the hydrofoil a re-entrant jet is seen to form and gradually fill the rearward portion of the cavity. On reaching the end of the foil, the cavity surface becomes uneven and irregular and small vortices may be shed from the end of the cavity causing small fluctuations in the force on the hydrofoil. The flow within the cavity appears then to become unstable and a large volume of cavity is abruptly shed into the stream and the cycle is then repeated. This sequence of events is similar to that of non-steady cavitation reported by Knapp (6). However, there are important differences: The cavity is not completely filled by the re-entrant jet - although oscillations from incompletely filled cavities are reported by him. In the present case, and as can be seen in Figure 22, there is always a cavity at the leading edge of the hydrofoil. The general stages of the oscillation are certainly very much as described by Knapp: "(a) formation and growth, (b) filling, and (c) breakoff". The other difference in our view is that when

breakoff occurs a large change in force ensues and there is a large corresponding change in circulation. This would lead one to suspect that the dynamics of the present phenomenon are related to the time-varying circulation.

The traces of the strain gage (to be presently discussed) were used to measure the frequency of the "strong" cavitation oscillations. These are shown for various angles of attack and tunnel velocities in Figure 23. The frequencies are reported in terms of a dimensionless Strouhal number, chord times frequency over tunnel speed. The range of this parameter is from about 0.07 for 4^{o} angle of attack to about 0.14 at 8^{o} angle of attack. Although there is some variation with speed at the lowest angle, the reduced frequency is relatively constant at the highest angle. This would suggest that the frequency of oscillation is not strongly dependent on the rigidity of the surrounding tunnel structure. There is the basic question, however, of the effect of the tunnel and flow "compliance" on such transient cavity flows as described herein. For example, if the tunnel were perfectly rigid and if there were no free surfaces other than that of the cavity itself, then an infinite pressure difference (in an incompressible medium) would be required to create the changing cavity volume. The tunnel is compliant, however; numerous pockets of vapor collect in the diffusor and from the photographs of Figures 13(b) to 16(b) it can be seen that there are entrained vapor-air bubbles in the flow. All of these effects evidently provide a cushion for the fluctuating cavity volume.

It is interesting to note that the frequencies observed by Knapp are much higher than those of the present work; in his work they ranged from 51 to 200 cps. Calculations of the reduced frequency based on the length of the cavity of these oscillations are about twice the present values. Again, the reduced frequency of his observations is substantially independent of tunnel speed.

It was mentioned that the output of the strain gage was photographed on the motion picture film such as shown in Figure 22. Unfortunately, the trace was too dim to be reproduced in this sequence of prints from the 16 mm. film. Measurements could be readily made from the original film, however, by projecting the film frame by frame on a screen. By this means measurements of force and cavity length were made and a typical example of such a measurement is shown in Figure 24. There it is seen that the double amplitude of the force oscillation is about 20 percent of the mean. The maximum force occurs at the maximum cavity length and the minimum force at the minimum cavity length. Generally speaking there is no substantial phase change between the oscillations of cavity length and the oscillations of force. The lack of an appreciable phase change between the force and cavity oscillations suggests that possible inertial effects of the fluid in the tunnel circuit are not large, as has been already indicated, and that the tunnel boundaries are in effect not rigid.

In Figure 25, these effects are presented in a slightly different form. There the percentage force change, from its minimum value

during the oscillation is presented as a function of cavity length to chord ratio for an angle of attack of 6^{o}. The arrows indicate the direction in which the curve is traversed during a cycle. The outer loop represents the main cycle of events while the inner loop corresponds to a secondary oscillation which sometimes occurs as the cavity grows.

Oscillograph recordings of the force are shown in Figure 25 for one angle of attack (6^{o}) and varying tunnel pressure at constant speed. The sequence of events previously described is borne out by this figure. For example, the high frequency oscillations can just be discerned in the top trace and as the pressure is lowered the small amplitude fast oscillations develop. These lead into the characteristic large oscillation shown in the fourth trace. This trace is near the point of maximum oscillation and maximum lift force as can be verified from Figure 14. Finally, the oscillations die away with further reduction in pressure.

We have already mentioned the relative independence of reduced frequency upon tunnel speed for the large oscillations. The higher frequency oscillations (the second and third traces in Figure 26) are, however, more or less independent of tunnel speed. This raises the possibility that they are related to the dynamics of the force balance or of the tunnel. To investigate this point the force balance with model attached was shock excited but no evidence of the 50-60 cps oscillations seen in Figure 25 were observed. In fact, the lowest well defined structural frequency observed was about 100 cps.

Typical traces of the decay of the vibration when the balance was excited in this way are shown in Figure 27.

The unsteady cavitation behavior is by no means restricted to single hydrofoils. A similar phenomenon occurs in the case of cavitating cascades as borne out by experiments described in Part II.

PART II - CASCADE STUDY

VI. BASIC DESIGN

1. Introduction - With the installation of a recently completed two-dimensional working section in the high speed water tunnel, the possibility of conducting cascade tests became a reality. One of the basic requirements necessary for undertaking such tests is that of having a large enough working section in which to operate the cascade so that the flow turning induced by the hydrofoils can be accommodated. Prior to the completion of the new section the tunnel was incapable of being used for such an investigation.

The dimensions of the new two-dimensional working section are 30 inches high by 6 inches wide. The length of the section is 50 inches. A large "picture window" made of lucite forms one wall of the channel thus ensuring excellent visualization of the flow. The working section is so designed that it can be used in both vertical and horizontal positions. For the present tests the horizontal position was used. This orientation was decided upon to avoid the hydrostatic pressure gradient that would exist across the cascade blades if a vertical position were used, causing uneven cavitation of the various foil surfaces. The horizontal position means, however, a necessary pressure gradient across the span of each blade and possible uneven cavitation occurring, but it was felt that this effect was more tolerable than the alternative set-up.

The basic tunnel circuit remains unchanged except for the installation of a new transition nozzle, the working section, and a new diffuser section. This new leg of the water tunnel is shown in Figure 28. The design and installation of this addition to the high speed facility together with a few preliminary calibrations is described in Reference 48.

Certain modifications had to be made to the tunnel working section in order to accomplish a suitable set up for carrying out cascade tests. These modifications and the basic design and construction involved in achieving them will now be considered:

One of the basic problems to be faced in cascade tests is how one should cope with the flow turning. Clearly, if the cascade is tested in a straight channel, large reaction forces will be experienced by the walls due to this flow turning. Direct measurement of the forces on the foils then becomes impossible as does the ability to obtain uniform cavitation on each blade. In airfoil cascade experiments the exit stream is usually simply discharged to atmosphere and no serious problems arise. However, in water tunnel work discharging the flow into a large reservoir, although not unfeasible, is somewhat impractical. This is particularly true with the existing tunnel configuration. Two alternative methods of treating the discharge flow were considered. Both of these methods involve the installation of inserts in the tunnel contracting nozzle to reduce the working section inlet height. These inserts are extended into the working section forming an inlet channel to the cascade. They are then

terminated at the cascade axis. The flow through the cascade can then be allowed to exit as a submerged jet, or alternatively, movable side walls hinged at the ends of the insert pieces can be used to guide the exit flow.

To investigate the relative merits of each of these systems a test was conducted on a one-sixth scale replica of the tunnel nozzle, working section and diffuser, motivated by the fact that the submerged jet - similar to air tests - would be very cheap.

2. Model Tests (One-Sixth Scale) - The tests on the sub-scale nozzle and working section assembly were conducted in the Hydraulic Machinery Laboratory of the California Institute of Technology. The test model was connected to one of the supply pumps through a 10-inch diameter pipeline, and the discharge from the working section was guided into one of the collecting sumps available. Manometers were provided for recording the differential pressure across the nozzle and recording the static pressures at various locations in the working section on the side and horizontal walls. The model working section was made of lucite and flow observation was possible using a dye solution as a tracer fluid. Nozzle inserts were mounted in the test nozzle converting the one-sixth scale model* (six-inch by one-inch throat dimensions) to a 3.05 inch by one inch rectangular section, corresponding to a six inch by 18.3 inch section in the actual tunnel. These nozzle inserts were so contoured to give a smooth transition

*Incidentally, this was the same test section as used to proof the original tunnel design.

from the nozzle to the straight working section. The inserts were continued in the working section for distances of 3.84 inches and 0.84 inches corresponding approximately to the anticipated geometry to be used in the main tunnel. The line through the termination points of these inserts was at 45 degrees to the flow direction representing a planned 45 degree cascade axis. Two views of this experimental arrangement are illustrated in Figure 29.

The first test conducted in the model experiments was aimed at determining the behavior of the flow through the working section with the inserts terminating abruptly to form a submerged jet of the working stream. These tests were conducted at flow speeds of the order of 10 to 20 feet per second. It was found that under these conditions an extremely irregular flow pattern was obtained - the streamlines were not stationary and large differential pressures of the order of 14 percent of the dynamic head occurred across the jet. In addition to these adverse effects, it was found that the regions immediately downstream of the inserts were stagnant areas where air bubbles had a tendency to collect. At lower pressures, as would arise under tunnel test conditions, these regions would doubtlessly cavitate causing greater distortion of the flow. In an effort to achieve some control of these effects it was decided to install several water inlet lines just downstream of the inserts along the vertical sides of the working section. The flow in these lines could be monitored on a flow rator. By adjusting the relative flow rates of the water in these lines, it was hoped that a uniform flow could be achieved with no

differential pressures occurring across the jet. Although it was found that the pressure distributions across the working section could indeed be controlled in this way, the volume flow necessary to obtain the above conditions was far too great to make this procedure feasible in the main tunnel. The required flow injection was found to be approximately 1/30th of the main flow volume. Furthermore, and more importantly, although the reattachment points of the jet were controllable by injection of external fluid, the main stream direction could not be made very uniform. At the higher speeds it was noticed that some instability occurred in the flow causing a fluctuation in the main flow direction similar to the phenomenon of the stall arising in wide angle diffusers. The drawback regarding the possibility of cavitation occurring behind each insert, at lower pressures, was also still present. In view of these results this method was deemed to be inadequate.

The alternative technique of having guide walls hinged at the termination points of the inserts was next investigated for various wall angles. The length of these walls was made such that they ended at the entrance to the diffuser. This arrangement gave a range of turning of ± 10 degrees. From these tests it would found that a very uniform flow was obtained even downstream of the walls. No vibrations in the working portion of the test section were apparent due to any kind of vortex shedding or mixing occurring from the end of the walls in the diffuser. This result was not surprising as the flow speeds were low. At higher speeds, however, this effect would no

doubt become apparent. The spaces behind these walls were filled with stagnant water and very little flow, if any, was observed in these regions. The pressure difference across the guiding walls was quite substantial, being of the order of 0.1 of the dynamic head. Thus fairly large forces could be expected to act on these walls in the actual tests. The results of this study, however, were sufficiently encouraging to make it acceptable for use in the main tunnel.

3. General Aspects of the Design - The basic geometry and general dimensions of the cascade configuration are determined by several factors. Some of the more important ones are the consideration of the dimensions and size of the working section, the cost and ease of manufacture of the component parts and the requirement that the cascade parameters chosen are, to some extent, representative of the values likely to occur in practice. With these basic concepts in mind the general design of the cascade was undertaken.

The primary problem presenting itself was the determination of the size of the models to be used and the method most suitable for mounting them in the tunnel. Furthermore the number of blades to be utilized was also undetermined. The forces in the cascade were to be measured on the center foil, as the force balance was located on the center line of the tunnel. The force readings obtained by this method would also be less subject to the possible effects of the end walls. The center foil was, therefore, to be mounted on the force balance. The manner of mounting the remaining foils, however, was still unresolved. Numerous methods were considered, but finally it was

decided to support the foils as cantilever beams from the lucite window. This method presented itself as the simplest and most easily achieved with the least modification to the tunnel. This arrangement necessitated drilling a number of holes in the lucite window and the design of a system for holding and locking the hydrofoils, together with a simple but effective angle-of-attack-changing mechanism. As the foils were to be mounted as cantilevers, there was a problem regarding the bending strength of the models. Due to the high cost of vane manufacture, the idea of fabricating the models from stainless steel was abandoned and instead a high strength heat-treated aluminum (7570 T651) was employed. It was required that the models have basically the same geometry as the isolated hydrofoil. However, due to the use of aluminum and to the mounting technique finally used (to be discussed in a later section), the hydrofoil thickness ratio was increased from 7 percent (the value of the isolated foil) to 8 percent. This thickness ratio was required to achieve the necessary strength, when the basic chord length of four inches was adopted. The choice of a 4-inch chord was partly dictated by the above considerations and partly by the solidity ratio required.

The cascade parameters, viz., the cascade angle (the angle between the cascade axis and the oncoming flow direction), and the solidity (the chord to spacing ratio) were chosen to give a configuration within the range frequently used in practical applications. Further, the choice of these parameters was dictated by the physical limitations of the working section and the versatility of the set up. After

considerable thought a basic solidity of 1.25 and a cascade angle of 45 degrees were chosen. With these values it was possible to arrange a cascade having five blades in the tunnel with sufficient space available for the installation of inserts and guiding walls. A consequence of having five blades was the ability to alter the solidity of the cascade by one half by simply removing two of the foils, thus giving added scope to the experiment.

It was not known at the beginning what the influence of the guiding walls would be on the cascade performance of a limited number of blades, and hence it was not clear where to locate the walls with respect to the hydrofoils. Placing these walls a full spacing from the outer foils would require them to simulate a hydrofoil. Alternatively, they could be located on a stream line surface. Since under cavitating conditions these walls would not behave as a foil, the latter arrangement would have been preferred; however, due to space limitations the former was used. In the case of half solidity, though, they became streamline surfaces. The walls were arranged to have a maximum turning angle of ± 10 degrees. It was thus possible to run the cascade in both the compressor and turbine configurations by simply rotating the hydrofoils 180 degrees. These movable walls were hinged to the tunnel inserts and were actuated by two jack screws passing through the tunnel side walls and attached to the guiding walls by means of a two-pin pivot system.

This entire layout is shown schematically in Figure 30. With this brief outline of the general aspects of the cascade design a few of

the more specific details can now be discussed.

4. Design Details

A. Models and Mounting Technique - The manufacture of the hydrofoil sections did not present too great a difficulty since circular arc surfaces are easily generated. Each foil was machined from an aluminum plate one and one-half inches thick. This plate was mounted on a bracket attached to the face plate of a lathe and the circular arc top side was machined. The radius of this arc was made 6.817 inches. The lower flat side was then milled. For the blades mounted from the lucite window, the design required (for reasons of strength) that they be integrally machined from the plate with a shaft one and one-quarter inches diameter. This shaft was 6 15/64 inches long and it provided the mounting fixture. The shaft passed through a nickel-plated brass bushing which was attached to the lucite window. The shaft was sealed with an "O" ring so that a differential pressure could occur across the window. A step in the shaft was provided to make an axial bearing, to adjust the model end-gap clearance and absorb axial thrust. The details of the foil manufacture are shown in Figure 31. The clearance-adjusting device is shown in Figure 32. Alignment of the shaft was provided by a tapered keyway which was referenced to the flat surface of the blade. This keyway provided a means of indexing the zero angle of attack position of the blades and made it possible to rotate the blades 180 degrees.

An advantage of machining the surfaces of the vanes in the fashion described is that once the machine is set up and tooled the

process can be repeated identically on several blades without further set up time, which increases the speed of production, lowers the costs involved in the manufacture of the blades, and provides a set of geometrically similar blades. The machining properties of the aluminum alloy used were such that the leading and trailing edges of the foils were somewhat rough. This was overcome by providing the foils with a small leading and trailing edge radius, viz., one-half percent of the chord.

As the center hydrofoil was mounted to the balance spindle it was not necessary to have it machined with an integral shaft as were the cantilevered blades, but simply with a rectangular base which was then bolted to a base plate and finally potted in position by means of a low-temperature-melting alloy. This foil was also provided with a pressure tap located at center span and just behind the leading and in front of the trailing edges to enable measurements to be made of the cavity pressure. The orifice at the trailing edge was used when the models were inverted and utilized in the turbine configuration. When either orifice was being used, the one at the trailing edge was sealed off with wax.

The span of the hydrofoils was made so that a nominal end-gap clearance of 0.020 inches was provided with the facing wall. The blades mounted from the lucite window also had end clearances at the root of the foil. These were kept to a very small value, however, viz., 0.002 inches. No noticeable flow could be seen through these end gaps during the course of the experiment. All the foils were

anodized after machining to minimize the corrosion effects of the water.

B. Angle Changing Mechanism - This component of the design was made as simply and directly as possible. Radius bars were clamped on the ends of the shafts of each of the foils. This clamping located the final axial position of the models. The angular position of the radius bars was fixed with respect to the flat surface of the foils by means of the keyway previously mentioned located in the shaft. The radius bars were rotated by two bolts which were located on a metal plate bolted to the window frame of the tunnel. Attached to this metal plate were graduations for measuring the angle of the radius bars. Pointers fixed to the ends of these bars facilitated the readings of the angles. This assembly system is shown in Figure 32, which also shows clearly the method of locating the axial position of the models and the push-pull device for adjusting the end gaps.

C. Nozzle Inserts - The throat dimensions of the working section were reduced from a 6 inch by 30 inch section to the required 6 inch by 13.58 inch by the two inserts, as mentioned. These inserts were so designed that they gave a smooth transition from the existing nozzle to the new working section, and were contoured to a cubic equation with a small parallel segment leading into the working section. A cubic equation was chosen since it has a zero second derivative at its origin, hence zero curvature there. This choice of contour, it was hoped, would avoid having a pressure undershoot at

the entrance to the working section. It was important that no large undershoot occur, as then cavitation would occur at the nozzle throat and not on the blades.

The inserts were manufactured in three steps: Firstly, four pieces of one-eighth inch aluminum sheet were hand filed to the desired contour to form four templates. These were then mounted to an aluminum base forming the supporting structure as seen in Figure 33(a). These backbone frames were bolted to the tunnel and used as skeletons around which high density polyurethane foam was poured. This process was done in situ as shown in Figure 33(b). Polyethelene sheet was used to protect the nozzle surface and to form a parting agent. On setting, the inserts were withdrawn and excess foam was sanded off to a final level of approximately one-eighth inch below the template line as can be seen in Figure 33(c). The surface of the inserts was then coated with fiber glass which was sanded down to the contour of the templates. The final finish consisted of several coats of polyester resin sanded down with wet and dry paper. The completed inserts were then fitted into the nozzle and waxed into place. This set up is shown in Figure 33(d).

The nozzle inserts were terminated at the nozzle throat and were continued in the working section by two lucite blocks 8.21 inches by 18.79 inches, and 8.21 inches by 5.21 inches, as shown in the schematic diagram, Figure 30. These blocks were machined and bolted in place. The joint between the nozzle insert pieces and the continuations were waxed. Two piano hinges for pivoting the movable

guide walls were recessed one-eighth inch below the surface at the downstream edges of the lucite blocks.

D. Guide Walls - The movable walls were fabricated from extruded aluminum 5 by 2 inch rectangular box section, to give the walls rigidity against twisting. The walls were widened to 6 inches by the addition of two strips of lucite one-half inch thick along the edges of the aluminum structure. A groove running the entire length of the walls was milled into the lucite to house a rubber O-ring. This O-ring served both as a sliding contact surface and as a seal, and also proved to be essential in preventing wall vibrations.

The actuating mechanism used was a very simple device. A link which consisted of two stainless steel pins mounted in teflon bearings housed in a fork-shaped aluminum connecting piece, attached the end of a one-inch diameter stainless steel rod to a housing bolted in the walls, as seen in Figure 34. This stainless steel rod passed through an O-ring seal in a bushing mounted on the side walls of the working section. This rod was an integral piece of the jack screw. The movement of this rod was effected by revolving a nut which was housed in a steel tube. This nut was retained by two ground steel washers fixed to the steel tube and provided bearing areas to which were fitted teflon pads. A locking nut was provided for locking the system once the wall angle had been set.

The downstream end of the walls were tapered to allow a maximum angle of turning of ± 10 degrees to be obtained. The lengths of these walls were 44 3/4 inches and 19 1/2 inches respectively. The

walls were hinged to the inserts by the two piano hinges already mentioned. The hinges were covered by one-eighth inch neoprene rubber pads which were cemented into place. These pads had a two-fold purpose as they not only provided a smooth surface over the hinges at all wall angles but also eliminated any leakage flow through the hinge joints.

5. Concluding Remarks - The above description of the design aspects is necessarily brief, but an endeavor has been made to stress the main features of interest. The final arrangement of the cascade and the various components described above is best illustrated in Figures 35 and 36. Figure 35 shows the center foil only mounted on the balance spindle. The lucite inserts and the movable walls can also be seen together with the pin-jointed links of the actuating mechanism. Figure 36 illustrates the four foils mounted from the lucite window before the latter has been installed in the tunnel. The final photograph, Figure 37, shows the entire assembly in position with the tunnel filled. The angle of attack mechanism can be clearly seen in this view.

VII. INSTRUMENTATION

1. Force Measurements - The forces on the center hydrofoil only were recorded. The force balance previously described in Part I was used, the only difference being that it was now mounted in a vertical position. No serious problems arose from having the balance in this orientation, as it was originally designed for vertical

mounting. The same readout equipment was used for recording the forces and the same technique of recording the data on film was adopted.

2. Pressure Measurements - The differential pressure and the static pressure of the tunnel working section were recorded at a pressure orifice located in the tunnel nozzle. This orifice was calibrated prior to the main experiment. The details of this calibration will be dealt with later. The static pressure was recorded on a well-type mercury manometer, as before, with readings obtainable to within 0.001 feet of mercury. The nozzle differential pressure was recorded by a seven-foot oil manometer. The manometer fluid was a synthetic oil having a nominal specific gravity of 2.00. This type of manometer was used as the pressure drops recorded at the nozzle orifice were always less than 0.5 feet of mercury, therefore the percentage error in reading this manometer would be reduced by a factor of approximately 13 from that obtained in reading the available mercury manometers. This manometer was calibrated against a mercury manometer to ensure that the nominal specific gravity quoted by the manufacturers was accurate, and not affected by temperature change. From this calibration it was found that this figure was indeed accurate over the range of temperatures likely to be encountered in the tunnel.

A multi-tube mercury manometer was used to measure static pressures in the calibration tests of the modified working section. This multi-tube manometer was referenced to the static pressure in

the settling chamber of the tunnel just prior to the honeycomb. The scale of the manometer was illuminated from behind a ground glass screen enabling the manometer to be photographically recorded. The quality of the recording film was such that readings could be obtained to within 0.002 feet of mercury. During the cascade tests this manometer was left in circuit and recorded the static pressures at various orifices in the tunnel working section.

The same method of cavity measurement was again used with one important modification. The cavity pressure was recorded with respect to atmospheric pressure. The barometric pressure was also recorded and the difference in these two readings gave the cavity pressure.

3. Turning Angle Measurements - The angle of the exit flow from the cascade was obtained in two ways. Since the walls were set according to a scheme based on the theoretical turning from cascade equations, this angle was a measure of the flow direction. The geometric angle of the walls was in turn obtained by a calibration measurement carried out on the actuating mechanism. These angles were related to the distance between the end of the jack screws and a reference point fixed on the tunnel. By measurement of this distance the angles of the walls to the upstream flow could be obtained. This calibration was carried out for both walls since they are not identical.

The second method of measuring the downstream flow direction was by using a Conrad type directional probe. This probe was mounted on the center line of the tunnel 24 inches or six chord lengths

downstream from the axis of the center foil. The probe was held in a probe holder mounted to the tunnel which was capable of measuring the probe angle to the nearest 5 minutes of arc. The two sides of the probe were connected across a sensitive differential pressure transducer (± 1.0 psid); which in turn was connected to a Baldwin amplifier and bridge network. The flow direction was obtained by rotating the probe until a nul reading was obtained. To obtain the zero reference angle of the probe, a six inch chord flat plate hydrofoil was mounted in the tunnel with the walls parallel. The angle of attack of the plate was varied from +2 degrees to -2 degrees by increments of 15 minutes of arc. The probe reading was taken for each point, as was the lift on the plate. This procedure was repeated for several tunnel speeds.

Two items of information were gained from this test. From a plot of the lift coefficient versus the angle of attack of the plate as determined by the angle setting mechanism on the balance, it was found that the zero lift point did indeed correspond to zero indicated angle of attack. Thus it was confirmed that the flow direction through the modified section was parallel to the tunnel axis (and therefore that the inserts were symmetric). This result held for all the velocities tested. The probe angle at zero lift was also plotted as a function of the tunnel speed. It was found that this angle varied slightly with Reynolds number. The tendency was for the zero angle to decrease with increase in speed. This decrease was slightly less than one percent or 20 minutes of arc for a range of tunnel speeds from 15 ft/sec to 35 ft/sec.

The use of the probe as a flow direction indicator, however, was limited to the fully wetted and partially cavitating regions. When full cavitation develops, the probe stem begins to cavitate, thus affecting the probe reading and on further decreasing the pressure, the cavities from the foils enveloped the probe and rendered its reading meaningless.

4. Cavity Length Measurements - Cavity lengths were recorded for each data point. These cavity lengths were recorded by a remote controlled 35 mm. recording camera. Since the tunnel working section was horizontally mounted these cavity length readings were photographed through a first-surface mirror mounted above the tunnel. This mirror was held at approximately 45 degrees enabling the camera to be fixed in a horizontal position. This horizontal mounting was necessary since the field of the camera was inadequate to cover the flow region when it was positioned directly above the lucite window. The mirror was rigidly attached to an overhead cross beam, thus also affording a means of seeing the cascade in operation without having to climb onto the tunnel. The cavity lengths so recorded were then determined from the films. Due to the obstruction of the view of the hydrofoils by the angle-changing mechanism, only cavity lengths greater than the chord were obtainable in this way. For the partially cavitating region cavity lengths were measured by direct observation at the time of the test.

5. Unsteady Measurements - No extensive measurements were made in this region of cavitation. However, the frequencies

of the fluctuations together with the growth and collapse of the cavity were recorded. As in the case of the isolated hydrofoil study, a high speed sound movie was taken of the oscillating cavity with a high speed movie camera mounted directly above the tunnel. Sequences were taken at speeds of 65 frames per second and 1500 frames per second.

During this phase of cavitation the outputs of several differential pressure transducers were recorded on a recording oscillograph. These transducers were connected at various points in the tunnel both upstream and downstream from the cascade. One side of each transducer was referenced to a common manifold maintained at a suitable reference pressure.

The general layout of the working area is shown in Figure 38. Figure 39 illustrates the force balances and readout equipment and to the right of the picture is the multi-tube manometer. Mounted on the left hand side of this manometer is the oil-water manometer for measuring the differential pressure in the nozzle. Figure 40 shows the cavity pressure manometer to the bottom left together with the Baldwin bridge and differential pressure transducer for the probe. The force balance is also seen to the right of the photograph.

VIII. EXPERIMENTAL PROCEDURE

As was pointed out before in Part I, one of the problems to be faced in conducting tests of this nature is in obtaining a correct reading for the working section static pressure that is independent of model effects. The dimensions of the present nozzle made it

possible to measure this pressure at a point well upstream of the cascade. An orifice was located within the nozzle eight chord lengths from the center line of the balance spindle. It was used to record the static pressure in the tunnel as well as the differential pressure. To relate these readings to the working section a calibration was conducted in the clear tunnel prior to the main tests. The details of this calibration are given in Appendix V.

One of the fundamental points to be established in the cascade tests, if meaningful results were to be obtained, was the question of how best the cascade conditions could be simulated, i.e., what criterion must be used to determine the turning angle of the cascade under test conditions. In aerodynamic cascade work, the use of side wall boundary layer suction and boundary layer slots has been shown to improve the two-dimensionality of the flow through the cascade. The amount of suction to apply, however, is determined by matching the measured lift with the measuring turning angles according to simple two-dimensional theory. Here, therefore, the controlling influence is the boundary layer control. In the present tests, boundary layer control was not possible; however, the effects arising from these boundary layers were deemed to be much less than those occurring in aerodynamic cascades. The ability to guide the flow with the movable walls afforded a means of adjusting the turning angle to match that of the measured lift. This procedure, though, necessarily involves errors arising from neglecting the above real fluid effects. The method, however, provides a direct and simple

way of conducting the tests, and details are given in Appendix VI. Essentially the method is based on an iteration procedure dependent on matching successive measured lift coefficients with turning angles obtained from theory. In the final iteration the drag effect is accounted for as well. This method is essentially the same as that devised by Numachi (41) in conducting his cascade experiments.

Since the flow turning is purely a function of the circulation around each foil it was justifiable to extend this method of determining the wall angles to the partially cavitating region as well. For the fully cavitating region, however, this system could not be used, since it was observed experimentally that the lift force there was fairly independent of the wall setting. Furthermore, the lift in this region is not determined by circulation. It was therefore decided to adjust the wall angles until the cavities from all the foils were of equal length, thus ensuring an even pressure distribution across the downstream working section. It was felt that this criterion was fairly well founded. The walls were consequently maintained at one setting for the fully cavitating region. Complete justification of the above procedures could only be obtained by comparing the results of the experiment with those of a theory which would exactly and correctly model the real flow. This will be taken up in the following section.

The initial program of tests was intended to cover the fully wetted and cavitating performance of the cascade arranged as a compressor for both 1.25 and 0.625 solidity ratios. These tests

would cover the complete range of angles of attack attainable. The turbine configuration was likewise intended to be tested in the same detail. However, due to some difficulties experienced with one of the nozzle inserts, the program of testing was delayed and the scope of the experiments had to be reduced. Consequently, only the case of the compressor of solidity 1.25 was fully investigated. For the 0.625 solidity, two complete tests were conducted at 8^{o} and 9^{o} angles of attack. For the turbine configuration only fully wetted results were obtained at a solidity of 1.25.

The procedure adopted for carrying out the tests in the steady regime was as follows: The cascade was set in the particular configuration desired and fully wetted data was taken at a constant tunnel speed and pressure by changing the angle of attack of the hydrofoils. For each data point the wall angles were set according to the scheme already described. For the compressor of 1.25 solidity, the range of angles of attack varied from -2 degrees to 6 degrees. The angle of attack referred to here is the angle between the chord and the upstream flow direction. For this solidity larger angles of attack were not possible due to the limitation of the wall angles. The above tests were conducted at two tunnel speeds to gage the effects of Reynolds number.

For cavitating runs, the angle of attack was held fixed and the tunnel static pressure varied at constant tunnel speed to cover the range of cavitation from inception to the fully choked case. There, once again, the walls were adjusted to suit the measured lift and

drag for the partially cavitating region. In the fully cavitating region the procedure mentioned earlier was used. These tests were repeated for all the angles of attack.

Apart from the forces acting on the hydrofoil, the probe angle and the various relevant pressures were recorded for each data point. To account for any experimental errors arising in the readings an average of three independent readings was taken for each point.

The force coefficients measured on the hydrofoil were corrected for the viscous tare forces experienced by the supporting disk. These tare forces were obtained in an identical fashion to that used in the isolated hydrofoil study. The results of this investigation are given in Appendix VII. Corrections for the zero shifts of the force balance with tunnel pressure were also accounted for. The dynamic pressure obtained from the differential pressure reading, recorded by the oil manometer and the static pressure measured by a well-type mercury manometer were converted to the working section readings by the method explained in Appendix V. As the basic assumption in this system of measuring pressures was that the pressure orifice is unaffected by model effects, further corrections for the pressures were not necessary.

Unlike the isolated hydrofoil case, the points of detachment of the cavities in cascade were not predictable, even for angles of attack larger than 4 degrees. For the lower angles of attack from -2 degrees to approximately 6 degrees the cavities sprang from the leading edge of the foils on the under or flat surface. As these

cavities became long, however, some cavitation on the top of the hydrofoils occurred. The various ways in which cavitation occurred on the foils will be studied in the following section. However, it may be mentioned here that, as in the case of fully wetted cascades, the mean flow angle is the correct angle on which to base these effects, rather than the above mentioned angle of attack. Values of mean-flow angle of attack equal to and larger than 4 degrees were not possible for the 1.25 solidity due again to the limitations on turning angle. It should be mentioned in this connection that in all the cascade tests conducted the stagger angle of the cascade varies with change in angle of attack. Hence when evaluating the results this fact should be borne in mind.

Since, for the angles of attack investigated, the cavity detachment points were such that the cavity pressure could not be measured for most of the tests conducted, it was decided for consistency to base all cavitation numbers on vapor pressure.

The unsteady tests were conducted at the compressor solidity of 0.625 and at a single angle of attack of 9 degrees. The reasons for using the lower solidity was to enable a larger angle of attack to be used so that leading edge cavitation was obtained on the top surface of the foils. In these tests the tunnel speed was kept constant and the static pressure lowered through the region of unsteadiness in progressive steps. At each pressure the outputs of the pressure transducers were recorded by a direct print out recording oscillograph. From these outputs the basic frequency of the oscillations was

determined. From the pressure fluctuations an analysis was made of the flow behavior in the tunnel nozzle during this phase of cavitation. The details are given in Appendix VIII. Calibration of these transducers was carried out by varying the tunnel static pressure at zero tunnel speed and recording the output of each instrument at the various pressures. The cavity fluctuations were also recorded with the high speed movie camera enabling the behavior of the cavities on each of the foils to be observed in relation to one another. These sequences were formed into a short sound movie.

During the course of the experiment several limitations of the apparatus became evident. These limitations and their consequences will be reviewed in a later section. Possible remedies and improvements of the apparatus will also be discussed.

IX. EXPERIMENTAL RESULTS

The experimental results from the cascade tests will be reviewed in four parts. Firstly, the fully wetted data will be presented for both the compressor and turbine configurations. The fully choked case of the compressor will then be given followed by the cavitating performance of the compressor cascade, and finally the results from the unsteady region of cavitation will be presented.

Before doing this, however, it is in order to define a few of the parameters to be used. The definitions of various variables arising from these tests are illustrated in Figure 41. Appendix VIII gives the required formulae for reducing the data. The lift, drag and

moment coefficients based on upstream tunnel velocity are defined in exactly the same way as with the isolated hydrofoil study.

As is well known from cascade theory, the mean flow velocity is of special importance as it assumes the same role as that of the free stream velocity in wing theory. It is therefore usual in fully wetted cascade theory to present results in terms of the mean force coefficients, based on this velocity and on the forces perpendicular and parallel to it. Both presentations will be used in the present case. For the cavitating flow data, however, only the former representation will be used as it is deemed more useful in this case, insofar as the downstream flow conditions are not known a priori. The mean force coefficients may be expressed in terms of the measured coefficients from the experiment as shown in Appendix VIII.

Only one cavitation parameter is used in the presentation of the data; namely, that based on vapor pressure. The reason for this has been previously explained (see last section). The definition of this cavitation parameter is also given in Appendix VIII.

1. Fully Wetted Results

A. Compressor Cascade, Solidity $\sigma = 1.25$: Figure 42 illustrates the force coefficients as a function of the angle of attack α, for two values of the Reynolds number. It will be noticed from this graph that there is an apparently large Reynolds number effect on the drag. This effect may be somewhat exaggerated since the drag associated with the cavity pressure orifice will have some influence on these results. This orifice was not sealed with wax during the

fully wetted runs as it perhaps should have been, in order to obviate the necessity of shutting down the tunnel and removing the lucite window before conducting the cavitation runs. Apart from this effect the results exhibit very little scatter and small Reynolds number effects for the lift and moment. Figure 43 shows the same results in terms of the mean force coefficients and the mean flow angle of attack. In this figure a shift with Reynolds number occurs in the lift curve. This is partly the effect of the drag variation, which is now incorporated in this mean lift coefficient. It is seen from the graph that the zero lift angle of attack is approximately $-2^{o}45'$ and the lift at zero mean angle of attack 0.235, much smaller than the isolated hydrofoil values. The lift curves are curved and not straight lines as the stagger angle is not constant through the test and changes with angle of attack.

One of the aims of these cascade tests was to determine the feasibility of performing such tests in the water tunnel. To judge whether or not cascade conditions were being simulated, comparison of the experimental results was made with theory wherever possible, and the fully wetted experiment provides such an opportunity. Consequently, the data were compared with theoretical results obtained using Schlichting's three point method (24) and Mellor's more accurate theory (25). The outcome of this comparison for the compressor of solidity 1.25 is shown in Figure 44. From this graph it is seen that the experimental results fall below those of Mellor's theory by about 11 percent at zero mean angle of attack. When

account is taken of the varying stagger the curves are almost parallel; that is, the lift slopes are the same for both experiment and theory over the range tested. The discrepancy between theory and experiment is almost certainly due to real fluid effects. For example, it is known that the boundary layer growth on the foil will decrease the lift but not affect the lift slope which is borne out here. Furthermore, real fluid effects arise from boundary layer growth on the walls of the tunnel itself. These boundary layers cause the velocity through the cascade to accelerate, thus causing an effect on the performance characteristics of the cascade. Although some work has been done (50, 51) on this problem of flow acceleration, few conclusive results have yet been obtained as to the effects of this acceleration, and consequently its magnitude is not precisely known.

The comparison with the less exact theory of Schlichting indicates a slightly larger discrepancy but the general features are again similar. This result is plotted for a constant stagger of 45 degrees. A comparison of a few of the more important values of the characteristics of the cascade from the two theories and from experiment are given in Table I below.

TABLE I

$\sigma = 1.25$, $\gamma = 45^\circ$	Schlichting	Mellor		Experiment
		Constant β	Varying β	
C_{Lm} at $\alpha_m = 0$	0.2704	0.2660	0.2652	0.233
Zero Lift Angle	$-3^\circ 44'$	$-3^\circ 36'$	$-3^\circ 28'$	$-2^\circ 45'$

In the light of the many real fluid effects unaccounted for by the theory, the above agreement is considered to be quite satisfactory.

Figure 45 illustrates the lift-drag ratio based on upstream conditions, the turning angle as measured from the wall angles, and the leaving angle as functions of the angle of attack α. Here again a large Reynolds number effect is apparent in the lift-drag ratio being due once more to the effect previously mentioned. Over the range tested the turning angle is almost a linear function of the angle of attack. The leaving angle is very nearly a constant except for the negative angles of attack. Since the pattern of flow over the hydrofoils changes somewhat when passing through the zero angle of attack this result is not too surprising. Application of a modified Constant's rule devised by Carter (52) for circular arc mean lines expresses the deviation angle as

$$\frac{\delta}{\theta/2} = \frac{m}{\sqrt{\sigma}}$$

where δ = the deviation angle measured between the velocity leaving the blade and the tangent to the mean camber line at the trailing edge

θ = angle subtended by the tangents to the mean camber line at the leading and trailing edges

σ = solidity ratio

m = a function of β, the stagger angle.

From Reference 52 the value of m for $\beta = 45^{\circ}$ is given to be 0.31. The deviation angle for this case thus becomes $4^{\circ}46'$. Since

$\theta = 17^{\circ}10'$ for the hydrofoil in question, the mean deviation angle is given by

$$\delta = \frac{\theta}{2} - \alpha_2 = 8^{\circ}35' - 3^{\circ}24' = 5^{\circ}11' .$$

Hence there is good agreement between the two values.

The final graph in this section, Figure 46, illustrates how well the iteration method used for setting the walls, accomplished its purpose. Here we have plotted the mean lift coefficient as a function of the turning angle. The theoretical value obtained from two-dimensional momentum considerations is also shown plotted. Very good agreement is obtained. Also in the figure are the turning angles as measured by the probe downstream of the cascade. This data is shown plotted as the flagged points on the graph. It is generally seen that the probe measures a larger turning than is obtained from the lift force. This effect can probably be attributed to the acceleration caused by the side wall boundary layers on the flow through the cascade, which can give rise to this effect.

B. Compressor Cascade, Solidity $\sigma = 0.625$: Only two angles of attack were studied at this solidity, hence very limited results were obtained. However, comparison with Mellor's theory for this case shows the same type of agreement as for the larger solidity. Comparison of these results is given in Table II below:

TABLE II

$\sigma = 0.625$, $\gamma = 45^{\circ}$	Mellor, Varying β	Experiment
C_{Lm} at $\alpha_m = 3^{\circ}51'$	0.7399	0.655
$\alpha = 8^{\circ}00'$		
C_{Lm} at $\alpha_m = 4^{\circ}35'$	0.8074	0.690
$\alpha = 9^{\circ}00'$		

Application of the modified Constant's rule referred to above yields a deviation angle of $6^{\circ}44'$ in this case. Experimentally, an average deviation angle of $7^{\circ}53'$ is obtained. Hence, once more reasonably good correlation is obtained between experiment and theory.

C. Turbine Cascade, Solidity $\sigma = 1.25$: The performance of the cascade in the turbine configuration is illustrated in Figures 47 to 50. Figure 47 shows the behavior of the force coefficients as a function of the angle of attack. For this configuration only one Reynolds number was investigated. Figure 48 shows these values in terms of the mean quantities. Here again the stagger angle varies with angle of attack. The experimental zero lift angle is $-6^{\circ}30'$. Shown on the graph is the theoretical curve obtained from Schlichting's three point method. In this case the theoretical zero lift angle of attack is $-6^{\circ}36'$ which is very close to the experimental value. It will be seen that much better agreement exists between the theoretical and experimental curves for the turbine. This result is to be

expected as the boundary layer effects in this case are not as severe as in the case of the compressor due to the favorable pressure gradient across a turbine.

In Figure 49 the lift-to-drag ratio, turning angle θ, and leaving angle α_2 are illustrated as functions of the angle of attack α. Applying the modified Constant's rule for the deviation angle in this case will again give $4^{\circ}46'$. From the experimental results the value $5^{\circ}05'$ is obtained.

The final Figure 50 shows the accuracy with which the wall settings were obtained. Here again the probe readings have been plotted as flagged points. Although there is some tendency for these values to be larger than the wall angles, this effect is somewhat reduced, indicating the fact that boundary layer effects are not as prevalent in this case. The theoretical curve is again obtained from simple two-dimensional momentum considerations.

2. Fully Choked Results - The data from the fully choked flow conditions provide a further means of checking the validity of the experimental results obtained. This fully choked condition corresponds essentially to the case of having infinitely long cavities trailing from the hydrofoils. This problem has been treated theoretically by Betz and Petersohn (36) using a hodograph method of solution. Their results were used to calculate the normal force coefficient C_N and turning angle θ for the two cases of the compressor configurations. The normal force coefficient referred to is the normal force acting on the hydrofoils referred to the upstream dynamic head.

Figure 51 illustrates the comparison of these two quantities obtained from theory and from the experiment for the solidity of 1.25. The values of 0.625 solidity are shown in the insert.

Firstly, let us consider the values of C_N. At the lower angles of attack there is a large discrepancy between the two results, but as the angle of attack increases a fairly good agreement is reached for both solidities. This behavior, however, is entirely justified since at angles of attack below 6 degrees cavitation on the hydrofoils commences at the leading edge but on the flat side of the hydrofoil. Under choked conditions, as will be discussed in the following section, the cavities originate from the under side leading edge on the one hand and from a point three quarters of the chord downstream from the leading edge on the upper surface. The net effect of this type of cavitation would be to decrease the lift force as is indeed the fact. At angles of attack larger than 6 degrees, normal cavitation occurs in that the cavities spring from the leading edge on the top surface of the hydrofoils and from the trailing edge.

Due to the excessive blockage occurring in the tunnel working section under these choked conditions at the higher angles of attack, one would expect the lift coefficients to be larger than those predicted by the theory. It seems that this is the tendency for the high solidity case and is definitely true for the lower solidity.

As has been previously explained the wall angles in the fully cavitating region were set to have uniform cavitation. It is therefore not too surprising that some scatter should occur in these values.

Surprisingly enough, though, the experimental values tend to distribute themselves about the theoretical value. At the higher angles there seems to be a definite tendency for the experimental values to be much less than the theory even for the 0.625 solidity case, the maximum difference being about two and one-half degrees. The reason for this behavior is not entirely clear.

Although it cannot be said that very good agreement exists, it seems reassuring that the values were of the right orders of magnitude and that the trend in these results would lead one to suspect that in the valid region of comparison where the cavity separation points are fixed and the cavity occurs from the top surface of the foils, a good correlation would be obtained. Due to the limitations of the apparatus, however, it was not possible to investigate this region further.

3. Cavitating Performance

A. Compressor Configuration, Solidity $\sigma = 1.25$: The cavitating performance of the cascade is given in Figures 52 to 59. Each of these figures shows the behavior of the force coefficient with the cavitation parameter K_v for a given angle of attack α. The photographs illustrate the type of cavitation occurring on the hydrofoils at various cavitation numbers.

The general behavior of all the graphs is seen to be similar. During the region of partial cavitation very little happens to the force coefficients and they virtually remain constant. On decreasing the cavitation parameter further, however, there is a gradual drop in the lift coefficient, with a corresponding rise in drag and a change in

moment. As the angle of attack is increased, these changes in the force coefficients become more sudden. The experimental fully wetted values are shown on these graphs as is the point of cavitation inception and the point where the cavity becomes equal to the chord length.

Comparing this behavior with the isolated hydrofoil study it is seen that the initial increase in lift coefficient with corresponding decrease in drag obtained in this latter case no longer holds. An explanation for this may be found in the fact that at this rather high solidity the pressure field of the neighboring blade effectively removes any advantage gained from the initial cavitation. If this is the case it would be anticipated that at lower solidities some lift increase will be apparent; this in fact occurs as will be seen later.

Shown plotted in the graphs for $\alpha = 5^{o}$ and 6^{o} are theoretical curves obtained from a linearized theory by the author of a cavitating cascade of flat plate hydrofoils given in Reference 53 and reproduced in Appendix IX. Only these two angles have been presented since at lower angles of attack cavitation occurs on the bottom side of the foil making a formal comparison with the theory invalid. At 5^{o} in fact this type of cavitation takes place; however, the comparison is extended to include this borderline case. It will be seen that the experimental values are above the theoretical ones by about thirty percent. Apart from the linearization, this discrepancy is also due to the effects of camber and thickness not accounted for in the theory. Note further that in the theory the stagger is 45^{o} whereas the experimental values

are 40^{o} and 39^{o} respectively.

In Figure 60 a graph illustrating the types of cavitation occurring on the hydrofoils is shown. The different regions are clearly illustrated in this figure. It will be seen that lower than 6^{o} angle of attack the cavitation passes through two distinct phases, whereas above this angle the normal leading edge type cavitation is obtained. The line of minimum K_v obtainable in the present tunnel arrangement is also shown on the graph. The shaded area indicated in the figure represents the unsteady regime of cavitation bridging the partially and fully cavitating flow regions.

From 35 mm. data photographs similar to those shown in Figures 55(b) and 58(b), cavity length measurements were obtained. Figure 61 illustrates the behavior of the cavitation parameter K_v with cavity length to chord ratio for a few angles of attack. The region spanning the chord length has been dotted to represent the unsteady region. From these graphs one of the basic experimental difficulties in carrying out these cavitating cascade tests is brought out. It will be noticed that for angles of attack larger than 2^{o} the cavitation parameter reaches an asymptotic value fairly rapidly, usually before $\ell/c = 0.5$. From then on the smallest change in tunnel pressure will cause the cavity lengths to grow enormously. As can be imagined it is extremely difficult to obtain repeatable data in this region as the cavity lengths are quite hard to control. To obtain good results many readings have to be taken.

No comparison is made with theory for the cavity lengths for

two specific reasons. Firstly, the values of cavity length in the partially cavitating region are obtained by judgment based on observation of the cavities and are therefore not extremely accurate. Secondly, as already mentioned the cavities occur on the bottom side of the hydrofoils for all the angles of attack excepting 6°. A valid comparison is therefore not justifiable in this instance.

B. Compressor Configuration, Solidity $\sigma = 0.625$:

Figures 62 and 63 represent the behavior of the cascade force coefficients with cavitation. With reference to a previous remark, it is seen that some initial increase in lift occurs with cavitation. As the cavity approaches the chord length there is a corresponding increase in the drag. This behavior closely resembles that of the isolated hydrofoil case. The photographs again illustrate the type of cavitation that occurs.

In Figure 62 the theoretical curve obtained from Appendix IX of C_L as a function of cavitation number is included for a cascade of 0.5 solidity and 45° stagger. The values are obtained at an angle of attack of 6°. These cascade parameters were the closest to the experimental ones available from Reference 53.

Figure 64 illustrates some values of cavity length measurements obtained from the photographs. The values obtained from the linearized theory presented in Appendix IX are also shown plotted for the case of 0.5 solidity and angle of attack of 6°. Although the cascade parameters are not the same and therefore a comparison is really not justified, it is interesting to note that these values are of

the same order of magnitude. Values of the theory for the exact cascade values tested were not available from the computed data obtained from Reference 53.

4. Unsteady Flow Results - From the traces on the printouts from the oscillograph the frequency of the pressure pulsations in the tunnel caused by the fluctuating cavity could be determined. It was found that in general although there was a phase shift in the pressure responses, the basic frequencies at all the pressure points were the same and corresponded to that of the cavity fluctuation as observed by a high speed movie camera. For the region of maximum oscillations the frequency of vibration was again found to be a function of velocity as previously obtained in the isolated hydrofoil case. These runs were taken at an angle of attack of 9^{o} with the 0.625 solidity compressor. The results are shown in Table III

TABLE III

Velocity ft/sec	Frequency c.p.s.	Reduced Frequency cf/V
31.55	12.62	0.13
27.90	11.79	0.14

A sample of one of these traces is shown in Figure 65.

Following the procedure outlined in Appendix VIII, the fluctuation in velocity was determined at the plane of the nozzle orifice, 30 inches upstream from the balance center line. It was found that during the period of maximum oscillation at a nominal

tunnel speed of 31.58 ft/sec and a cavitation parameter of 0.63 the velocity at this plane could be represented as

$$V_N = 21.73 + 1.12 \cos(\omega t + \psi) \text{ ft/sec}$$

where $\psi = 73^{o}22'$, the phase of the velocity with respect to the pressure fluctuations. From this result it is seen that the amplitude of the fluctuating velocity component is about 5 percent of the mean flow velocity. This somewhat surprising result would indicate that the fluctuation in velocity is not only due to the cavity volume change, which would only account for about three percent of the above value (estimated from approximate cavity size measurements taken from the high speed movie), but must arise as a consequence of the dynamic response of parts of the tunnel itself.

It is entirely likely that the nozzle inserts, which, it may be recalled, are manufactured from polyurethane, are susceptible to dynamic response. In point of fact, some delays were caused in the initial phases of the experiment due to these inserts "breathing". Since the nozzle orifice was located in a plane containing both these inserts, they may have contributed to this fluctuation. However, it would seem worthwhile to investigate this point further since if the effects are inherent in the tunnel, the running of unsteady flow experiments would be subject to these effects.

The behavior of the cavity during this period of oscillation is very similar to that occurring in the single hydrofoil case. Furthermore, a close examination from the movie strips of the relative

behaviors of such cavity lengths on each hydrofoil indicates that no propagation of the cavity occurs along the cascade. However, these results were obtained from the low solidity compressor having only three blades. It had been thought that perhaps the unsteady cavitation would propagate along the cascade axis in a similar fashion to the phenomenon of propagating stall experienced in many turbo-machines. This observation would necessarily have to be taken as a preliminary one until the apparatus is modified so as to accommodate more blades at a lower solidity than is at present possible. These modifications of the apparatus for extending its versatility will be discussed in the following section.

X. CONCLUSIONS

PART I - Isolated Hydrofoil Study

The characteristics of a plano-convex hydrofoil have been described for non-cavitating and cavitating flows. It was found that the cavitation behavior can be divided into three regimes: a partially cavitating region, a fully cavitating region, and a region separating these two in which the flow is always unsteady.

In the partial and fully-cavitating regions the forces are steady and well defined in terms of the cavitation number and angle of attack. In the unsteady zone, however, the forces fluctuate and the cavity oscillates violently. The fluctuating normal force on the hydrofoil measured in the present experiments has an amplitude variation of $\pm$ 10 percent of its mean value. The reduced frequency of the force oscillations appears principally to be a function of the angle of attack. Reduced frequencies based on chord length and tunnel velocity are in the range of 0.10 to 0.20 for angles of attack of 10° or less and for the tunnel velocities used. For the present tests the cavity fluctuations are in phase with the force oscillations and the variation in cavity length is of the order of 60 percent of the chord.

The present investigations of the unsteady region of cavitation on an isolated hydrofoil were carried out with the aim of acquiring some information on the processes involved and to obtain a general qualitative and quantitative picture of the unsteady phenomenon. Clearly much work has still to be carried out before a complete

understanding of this region of cavitation is fully realized. Experimental and theoretical studies to determine the effects of tunnel boundaries and possible free surfaces are also necessary.

PART II - Cascade Study

During the course of this investigation several limitations of the experimental configuration used became apparent. Although the design requirements of the modifications to the existing working section were entirely satisfied, it was found that for the basic solidity used larger turning angles than could be accommodated were required in order to obtain a comprehensive survey of the performance of the cascade. Furthermore in the turbine configuration the blockage effects of the cascade and the movable walls were too large to enable supercavitating performance of the cascade to be realized. For the 0.625 solidity these effects were greatly reduced and the scope of the experiment in this case was increased, in that larger angles of attack can be considered while still being able to cope with the flow turning.

A remedy for this situation is to decrease the chord size of the models used in the test. This, however, would necessitate manufacturing models from high grade stainless steels. With this modification lower solidities could be achieved. The shortening of the movable walls would further help in extending the range of turning angles obtainable.

It was previously pointed out that in the region of full cavitation a constant bubble length is extremely hard to maintain. It is thought

that this effect is partly due to the unsteadiness in the flow through the working section due to the sudden discharge of water into the diffuser section. The installation of some form of exit flow guidance at this point would help in alleviating this effect. It is contemplated at present to install a honeycomb at this section in order to achieve this purpose. This addition has not, as yet, been undertaken as it requires some changes in the basic tunnel design.

The results obtained in the present tests include the performance characteristics of two compressor cascades of solidity 1.25 and 0.625 under varying conditions of cavitation from non-cavitating to fully cavitating flow. Also presented is the fully wetted performance of a turbine cascade of 1.25 solidity. It is found that as in the case of the isolated hydrofoil the cavitation can be divided into the three regions, those of partial cavitation, full cavitation and an unsteady region separating these two. Comparison of the experimental results with those of existing theories shows fair agreement. The questions of real fluid effects such as side wall boundary layer growth and secondary flow losses occurring in the cascade were not investigated. These losses contribute greatly to the discrepancies existing between experimental and theoretical results. However, it is found from the results of the present investigations that these discrepancies are not as large as those found in aerodynamic cascade tests when no account is made for the above viscous effects.

The data obtained from the cascades investigated are sufficiently encouraging to state definitely that the basic design and procedures

used in conducting the present tests have proved the feasibility of using the water tunnel as a cascade tunnel. Certain modifications, as those previously mentioned, are necessary to ensure greater adaptability of the apparatus, but meaningful results have been obtained with the present configuration.

XI. REFERENCES

1. Helmholtz, H. — Phil. Mag., Vol. 36, 1868.
2. Kirchoff, G. — J. reine agnew. Math., Vol. 70, 1869.
3. Riabouchinsky, D. — Proc. Math. Soc., London, Series 2, Vol. 19, 1920.
4. Efros, D. A. — Comptes Rendues (Doklady)Acad.Sci., URSS Vol. 41, 1946.
5. Kreisel, G. — "Cavitation with Finite Cavitation Numbers", Admiralty Research Laboratory Report No. R1/H/36, 1946.
6. Roshko, A. — "A New Hodograph for Free-Streamline Flow Theory", NACA TN 3168, 1954.
7. Wu, T. Y. — "A Wake Model for Free-Streamline Flow Theory, Part I: Fully and Partially Developed Wake Flows and Cavity Flows Past an Oblique Flat Plate, California Institute of Technology Engineering Division Report No. 97-2, 1961.
8. Tulin, M. P. — "Steady Two-dimensional Cavity Flows about Slender Bodies", David Taylor Model Basin Report No. 834, 1953.
9. Parkin, B. R. — "Linearized Theory of Cavity Flow in Two Dimensions", Rand Corporation Report P-1745, 1959.
10. Walchner, O. — "Profilmessungen bei Kavitation", Hydro-mechanishe Probleme des Schiffsantriebes, edited by Kempf, G. and Foerster, E., 1932.
11. Reichart, H. — "The Laws of Cavitation Bubbles at Axially Symmetrical Bodies in a Flow", Report and Translations No. 766, Ministry of Aircraft Production, 1946.
12. Balhan, J. — "Metingen aan Enige Bij Scheepsschroenen Gebruikelijke Profielen in Vlokke Stroming Mit en Zonder Cavitie", Ned. Scheepsbouwkundig Proefstation te Wageningen, 1951.

13. Acosta, A. J. "A Note on Partial Cavitation of Flat Plate Hydrofoils", California Institute of Technology Hydrodynamics Laboratory Report No. E-19.9, 1955.

14. Kermeen, R.W. "Water Tunnel Tests of NACA 4412 and Walchner Profile 7 Hydrofoils in Noncavitating and Cavitating Flows", California Institute of Technology Hydrodynamics Laboratory Report No. 47-5, 1956.

15. Parkin, B.R. "Experiments on Circular Arc and Flat Plate Hydrofoils in Noncavitating and Full Cavity Flows", California Institute of Technology Hydrodynamics Laboratory Report No. 47-6, 1956.

16. Wu, T. Y. "A Free Streamline Theory for Two-dimensional Fully Cavitated Hydrofoils", Journal of Mathematics and Physics, Vol. 35, No. 3, 1956.

17. Meijer, M.C. "Some Experiments on Partly Cavitating Hydrofoils", Int. Shipbuilding Progress, Vol. 6, No. 60, 1959.

18. Geurst, J.A. "Linearized Theory for Partially Cavitated Hydrofoils", Int. Shipbuilding Progress, Vol. 6 No. 60, 1959.

19. Knapp, R.T. "Recent Investigations of the Mechanics of Cavitation and Cavitation Damage", Trans. of the A.S.M.E., Vol. 77, 1955.

20. Wu, T. Y. "A Note on the Linear and Non-linear Theories for Fully Cavitated Hydrofoils", California Institute of Technology Hydrodynamics Laboratory Report No. 21-22, 1956.

21. Pistolesi, E. "On the Calculation of Flow Past an Infinite Screen of Thin Airfoils", NACA TM 968, 1941.

22. Garrick, I.E. "On the Plane Potential Flow Past a Lattice of Arbitrary Airfoils", NACA TR 788, 1944.

23. Katzoff, S.
Finn, R.S.
Lawrence, J.C. "Interference Method for Obtaining the Potential Flow Past an Arbitrary Cascade of Airfoils", NACA TN 1252, 1947.

24. Schlichting, H. "Berechung der reibungslesen inkompressiblen Stromung fur ein vergegebenes ebenes Schaufelgitter", V.D.I. Forschungsheft 447, 1955.

25. Mellor, G. L. "An Analysis of Axial Compressor Cascade Aerodynamics", Part I, Journal of Basic Engineering, Trans. of the A.S.M.E., Vol. 81, 1959.

26. Katzoff, S. Bogdonoff, H.E. Boyet, H. "Comparisons of Theoretical and Experimental Lift and Pressure Distributions on Airfoils in Cascade", NACA TN 1376, 1947.

27. Erwin, J. R. Emery, J. C. "Effect of Tunnel Configuration and Testing Technique on Cascade Performance", NACA TN 2028, 1950.

28. Katzoff, S. Hannah, M.E. "Further Comparisons of Theoretical and Experimental Lift and Pressure Distributions on Airfoils in Cascade at Low-Subsonic Speed", NACA TN 2391, 1951.

29. Herrig, L. J. Emery, J. C. Erwin, J. R. "Systematic Two-dimensional Cascade Tests of NACA 65-Series Compressor Blades at Low Speeds", NACA RM L51G31, 1951.

30. Schlichting, H. Scholz, N. "Uber die Theoretische Berechnung der Stromungsverluste eines ebenen Schaufelgitters", Ing. Archiv, Vol. 19, 1951.

31. Lieblein, S. Rondebush, W. H. "Theoretical Loss Relations for Low-Speed-Two-Dimensional-Cascade Flow", NACA TN 3662, 1956.

32. Lieblein, S. Rondebush, W. H. "Low-Speed Wake Characteristics of Two-Dimensional Cascade and Isolated Airfoil Sections", NACA TN 3771, 1956.

33. Lieblein, S. "Analysis of Experimental Low-Speed Loss and Stall Characteristics of Two-Dimensional Compressor Blade Cascades", NACA TM E57A28, 1957.

34. Lieblein, S. "Loss and Stall Analysis of Compressor Cascades", Journal of Basic Engineering, Trans. of the A.S.M.E., Vol. 81, 1959.

35. Lakshminarayana, B. Horlock, J. H. — "Review: Secondary Flows and Losses in Cascades and Axial-Flow Turbomachines", Int. J. Mech. Sci., Vol. 5, 1963.

36. Betz, A. Petersohn, E. — "Application of the Theory of Free Jets", NACA TM 667, 1941.

37. Cohen, H. Sutherland, C.D. — "Finite Cavity Cascade Flow", Rensselaer Polytechnic Institute, Mathematics Report No. 14, 1958.

38. Acosta, A.J. Hollander, A. — "Remarks on Cavitation in Turbomachines", Engineering Division, California Institute of Technology Report No. E-79.3, 1959.

39. Stripling, L. B. Acosta, A. J. — "Cavitation in Turbo-Pumps: Part I", Journal of Basic Engineering, Trans. of the A.S.M.E., Vol. 84, 1962.

40. Acosta, A. J. — "Cavitating Flow Past a Cascade of Circular Arc Hydrofoils", California Institute of Technology Engineering Division Report No. E-79.2, 1950.

41. Numachi, F. — "Cavitation Tests on Hydrofoils in Cascade", Trans. of the A.S.M.E., Vol. 75, 1953.

42. Knapp, R. T. Levy, J. O'Neill, J. P. Brown, F. B. — "The Hydrodynamics Laboratory of the California Institute of Technology", Trans. of the A.S.M.E., Vol. 70, 1948.

43. Hotz, G. M. McGraw, J. T. — "The High Speed Water Tunnel Three-Component Force Balance", California Institute of Technology Hydrodynamics Laboratory Report No. E-47.1, 1955.

44. Gadd, G. E. — "An Air-Blowing Technique for Measuring Pressures in Water", National Physical Laboratory SH R 24/61, 1961.

45. Williams, D. H. Brown, A. F. Miles, C.J.W. — "Tests on Four Circular-Back Aerofoils in the Compressed Air Tunnel", A.R.C. Technical Report, R&M No. 2301, 1948.

46. McCullough, G. B. Gault, D.E. — "Boundary Layer and Stalling Characteristics of the NACA 64A006 Airfoil Section", NACA TN 1923, 1949.

47. Carrow, D.D. "A Note on the Boundary Layer and Stalling Characteristics of Aerofoils", A.R.C., C.P. No. 174, 1950.

48. Kiceniuk, T. "A Two-Dimensional Working Section for the High-Speed Water Tunnel at the California Institute of Technology", Cavitation Research Facilities and Techniques, A.S.M.E., 1964.

49. Muskhelishvili, N. I. "Singular Integral Equations", P. Noordhoff Ltd., Groningen, Holland, 1946.

50. Kubota, S. "Cascade Performance with Accelerated or Decelerated Axial Velocity", Bulletin of the J.S.M.E., Vol. 5, No. 19, 1962.

51. Pollard, D.
Horlock, J. H. "A Theoretical Investigation of the Effect of Change in Axial Velocity on the Potential Flow through a Cascade of Aerofoils", A.R.C., CP No. 619, 1963.

52. Carter, A.D.S.
Hughes, H. P. "A Theoretical Investigation into the Effect of Profile Shape on the Performance of Aerofoils in Cascade", A.R.C. R&M No. 2384, 1946.

53. Wade, R. B. "Flow Past a Partially Cavitating Cascade of Flat Plate Hydrofoils", California Institute of Technology Engineering Report No. E-79.4, 1963.

PART I

Figures 1 - 27

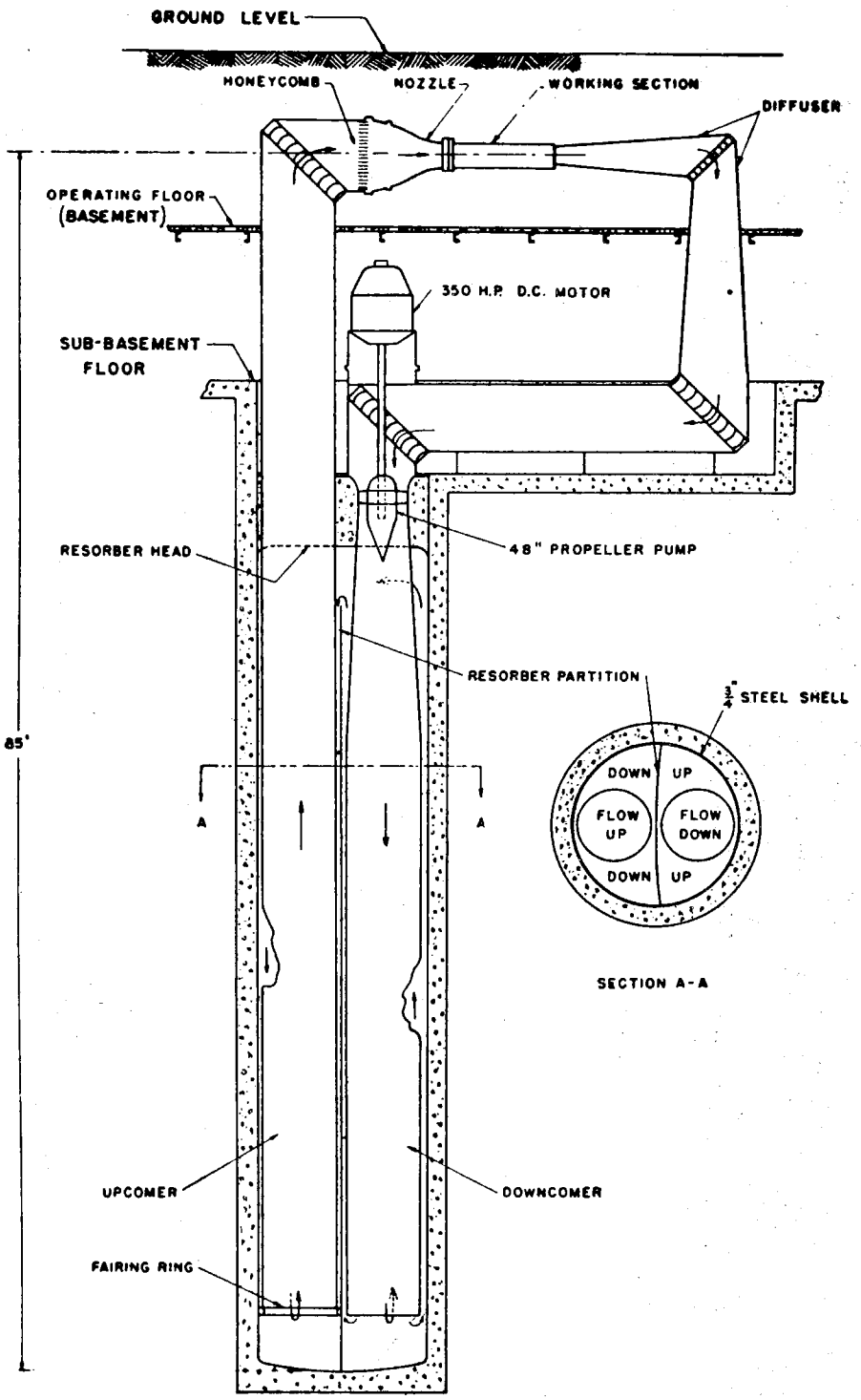

Fig. 1 - Water tunnel circuit

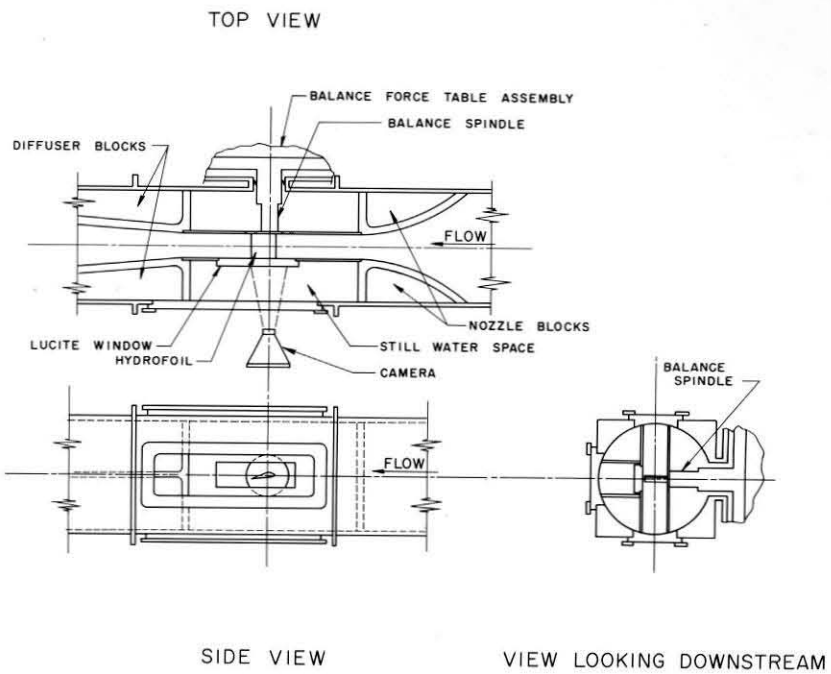

Fig. 2 - Schematic diagram of water tunnel working section

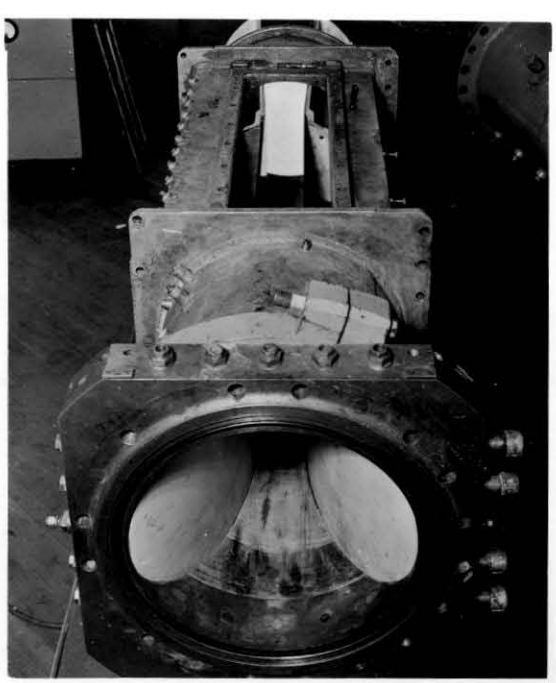

Fig. 3 - View of inserts installed in tunnel

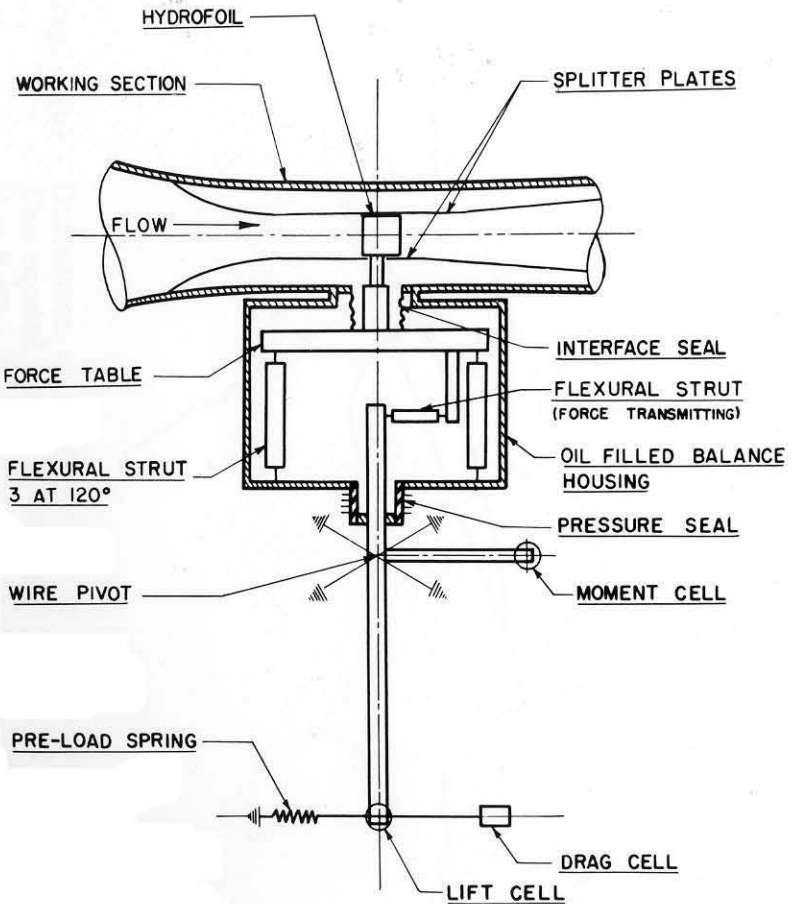

Fig. 4 - Schematic drawing of force balance

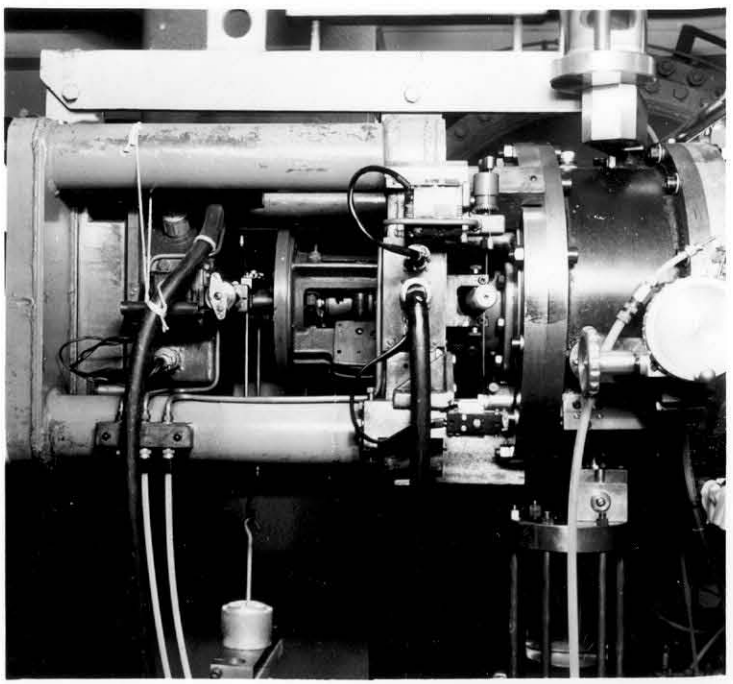

Fig. 5 - Close-up of force balance mounted on tunnel (to the right)

Fig. 6(a) - Isolated hydrofoil model

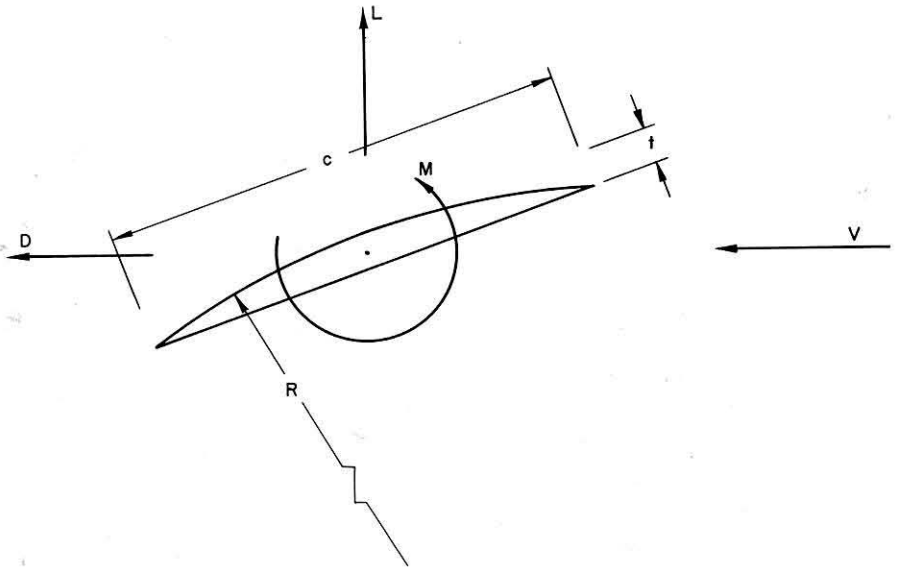

Fig. 6(b) - Definition of positive sense of forces and moments. The model dimensions are: c = 2.77 in., t = 0.19 in., R = 5 in., S = 2.85 in.

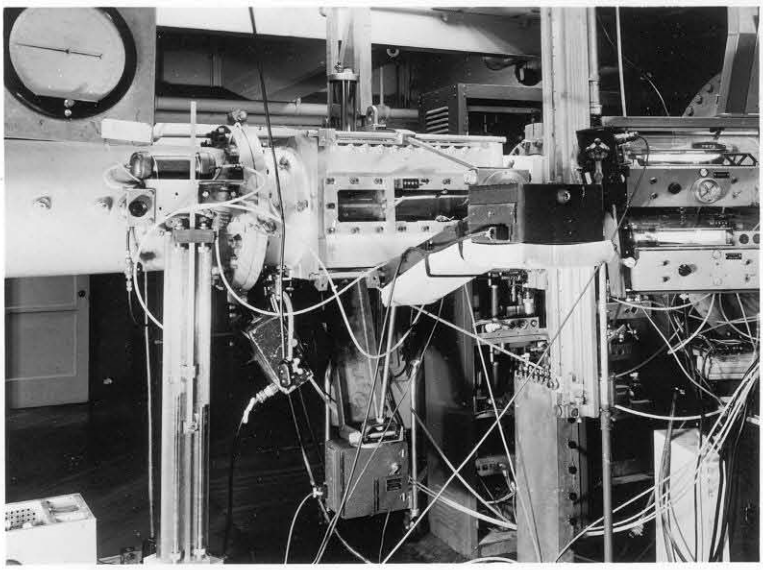

Fig. 7 - General test set up for steady force runs showing manometers, force balances and recording cameras

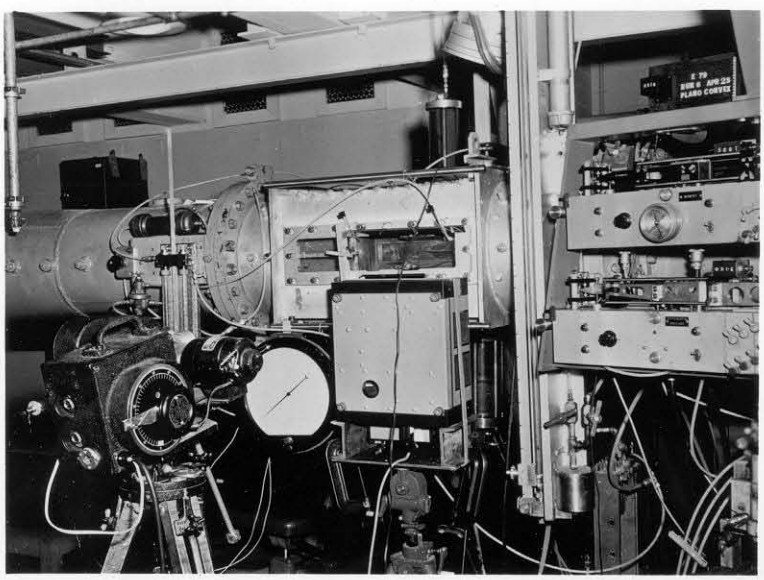

Fig. 8 - Test set up for oscillating runs showing high speed movie camera and recording oscillograph in vertical position

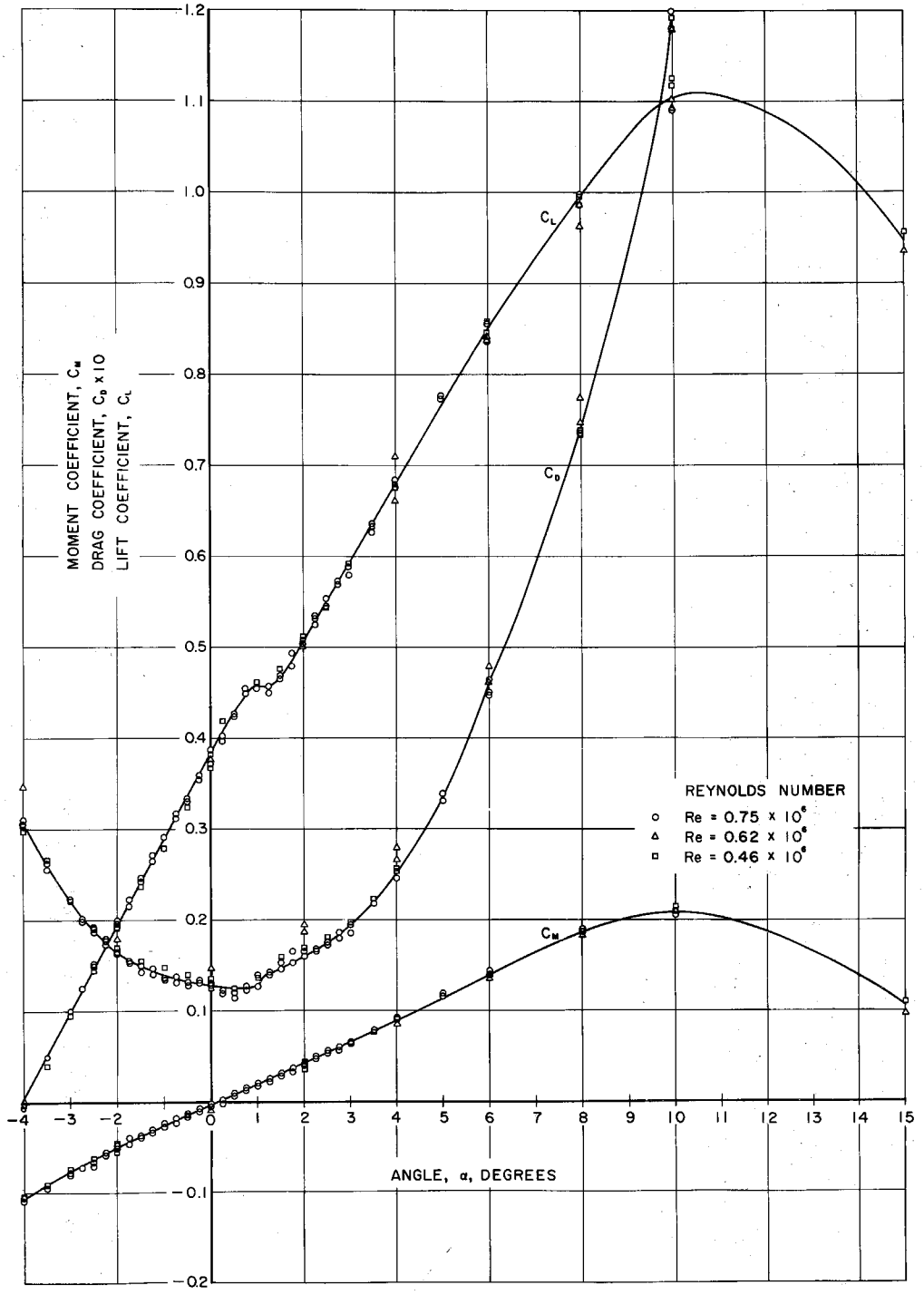

Fig. 9 - Force coefficients as functions of angle of attack for non-cavitating flow at several Reynolds numbers for the plano-convex hydrofoil

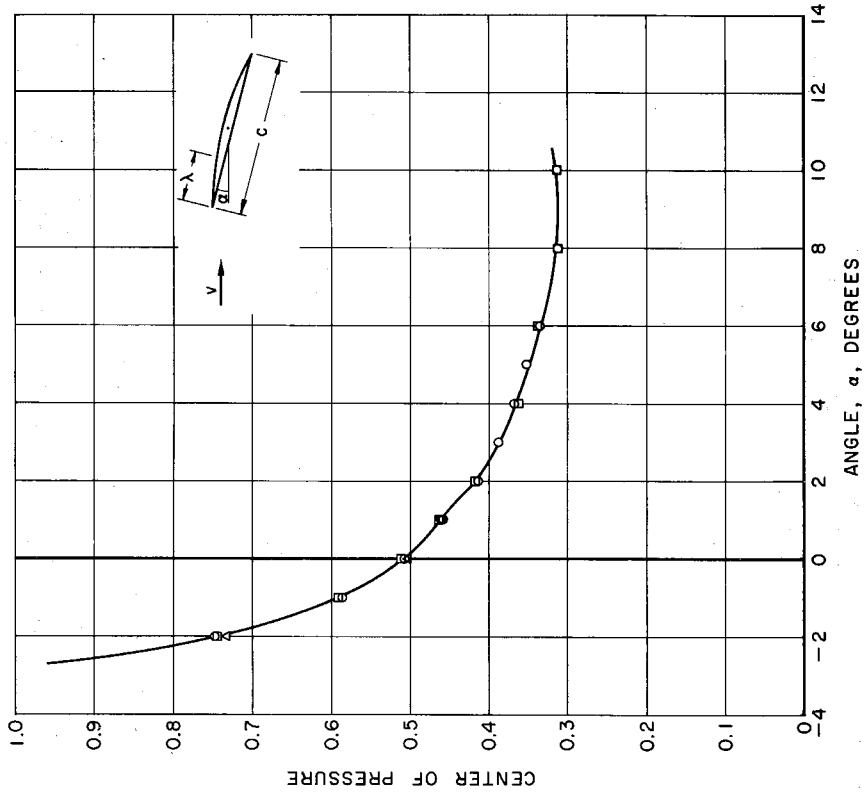

Fig. 11 - Variation of center of pressure location λ/c with angle of attack for non-cavitating flow at the same Reynolds numbers indicated in Fig. 9

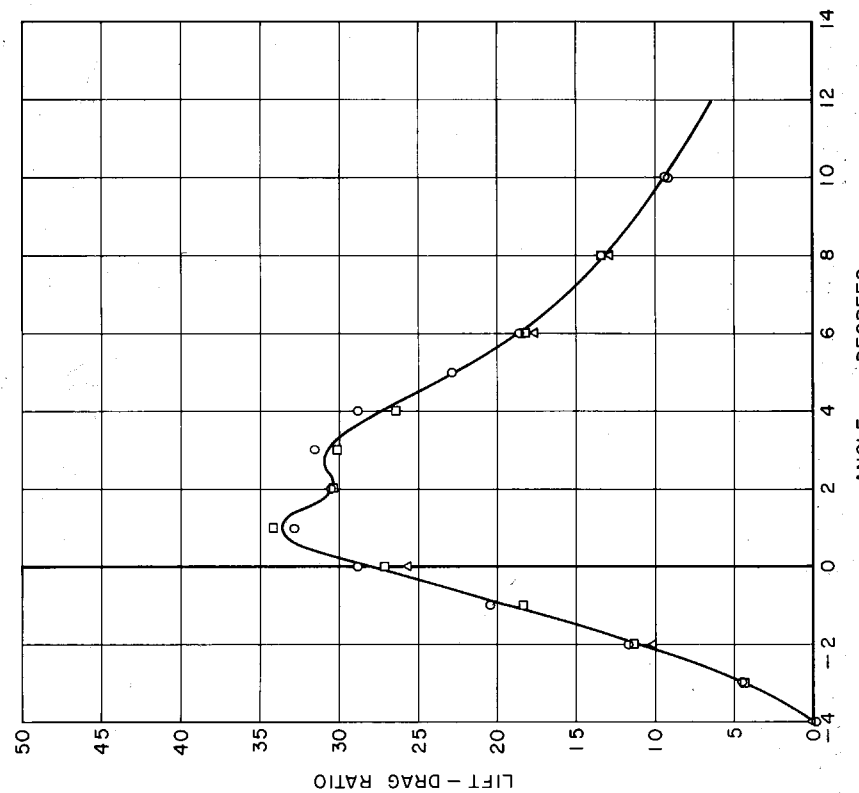

Fig. 10 - Lift-to-drag ratio as a function of angle of attack for non-cavitating flow, at the same Reynolds numbers indicated in Fig. 9

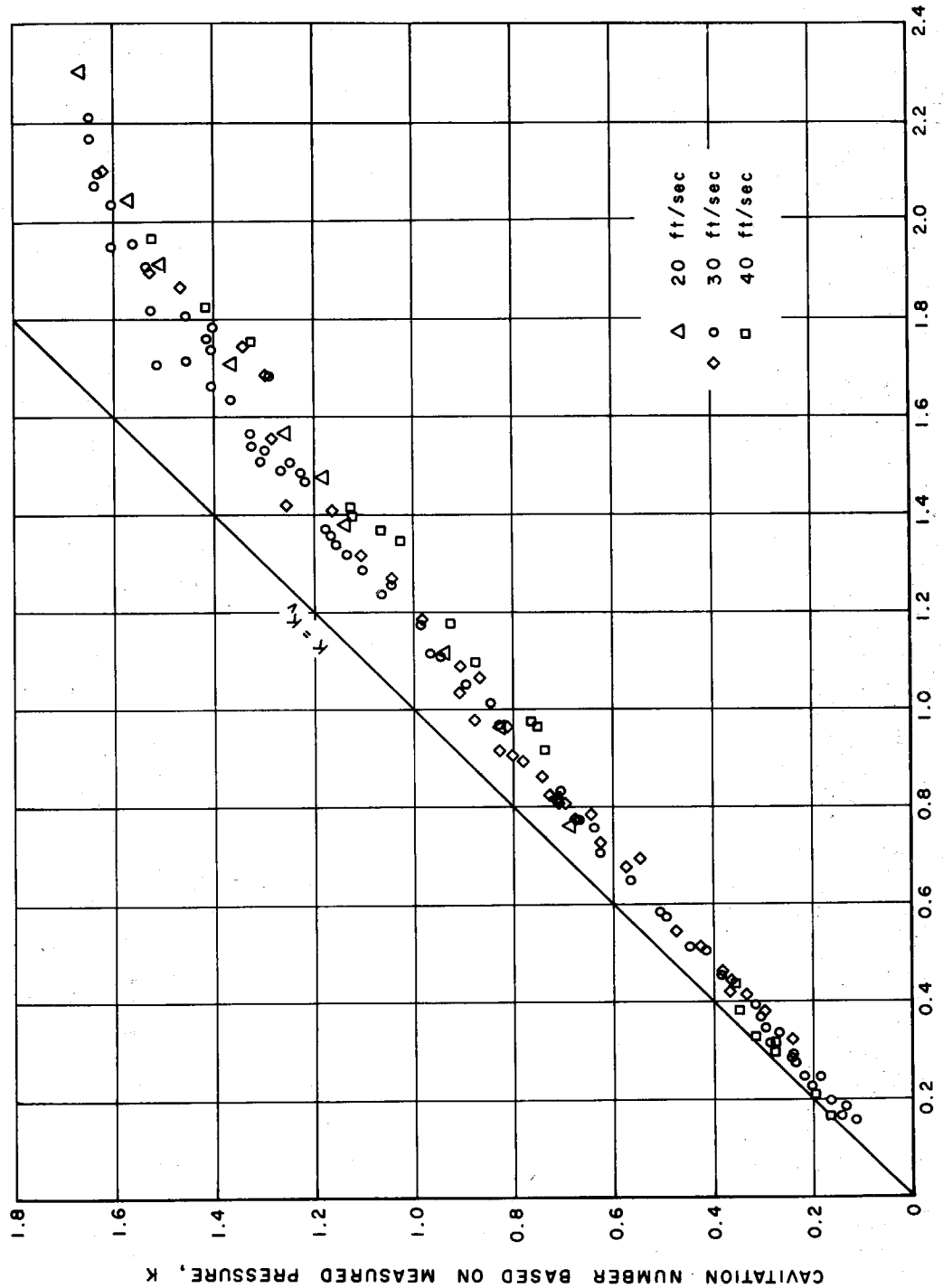

Fig. 12 - Comparison of measured cavitation number to that based on vapor pressure

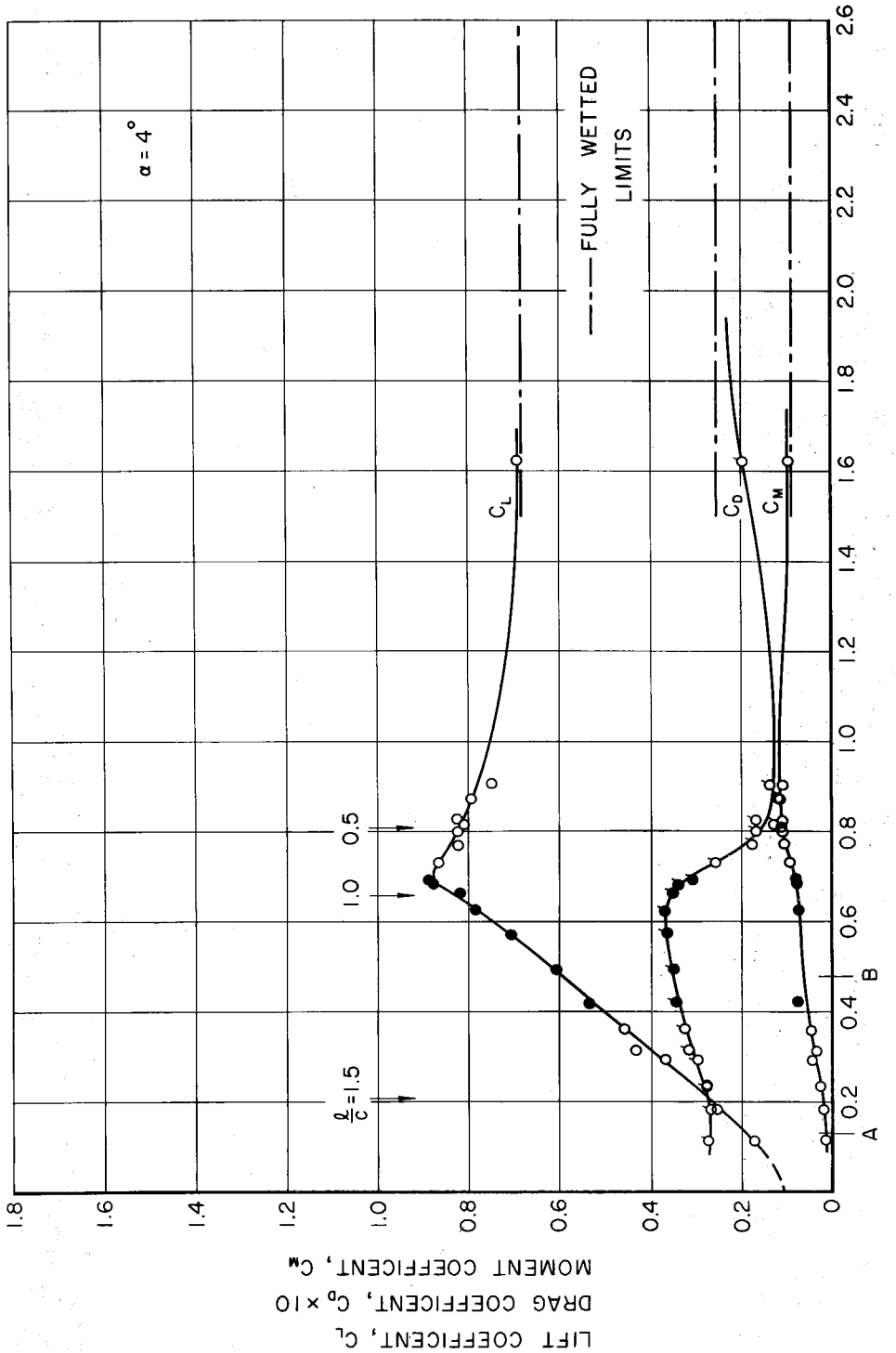

Fig. 13(a) - Force coefficients as functions of cavitation number at an angle of attack of 4° for a plano-convex hydrofoil of 7 percent thickness. Note all drag points are flagged.

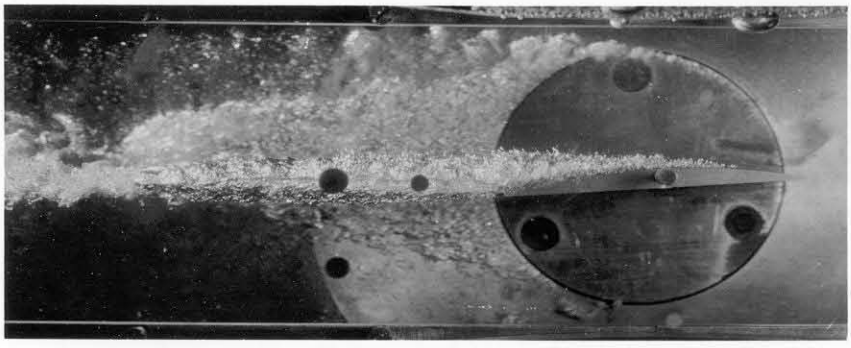

A. K = 0.131

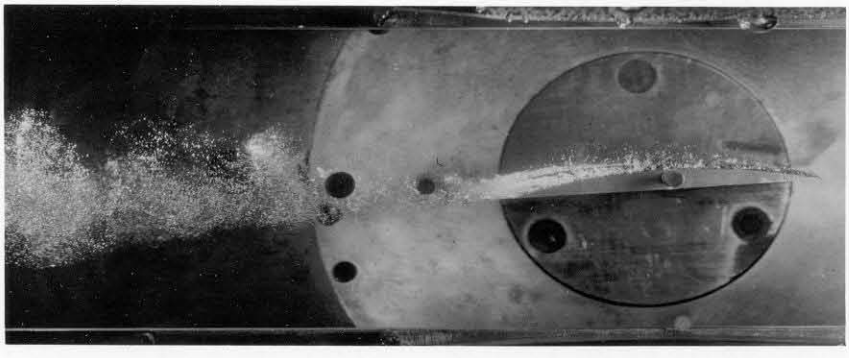

B. K = 0.480

Fig. 13(b) - Cavitation occurring on a plano-convex hydrofoil at an angle of attack of 4° at various cavitation numbers, K. The letters are those referred to in Fig. 13(a).

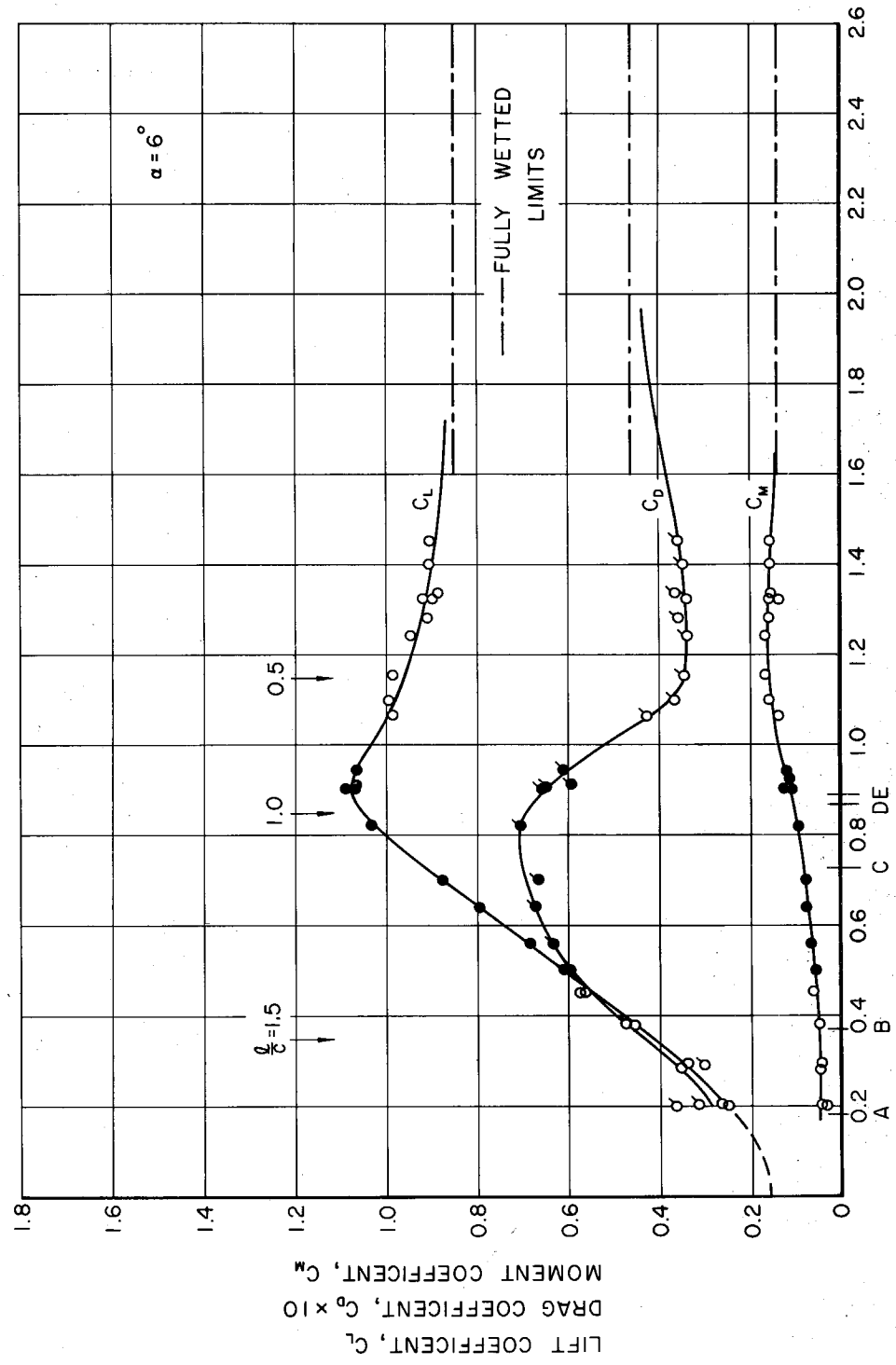

Fig. 14(a) - Force coefficients as functions of cavitation number at an angle of attack of 6° for a plano-convex hydrofoil of 7 percent thickness. Note all drag points are flagged.

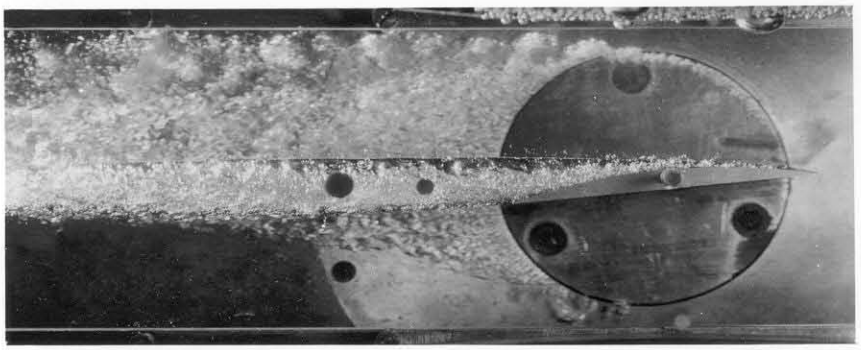

A. K = 0.183

B. K = 0.386

Fig. 14(b) - Cavitation occurring on a plano-convex hydrofoil at an angle of attack of 6° at various cavitation numbers, K. The letters are those referred to in Fig. 14(a).

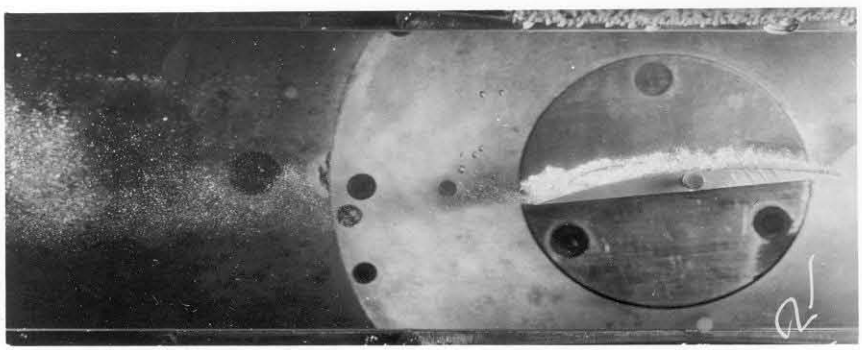

C. K = 0.730

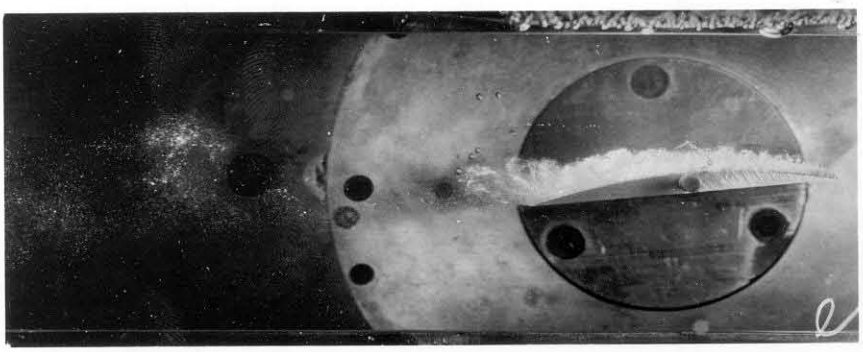

D. K = 0.870

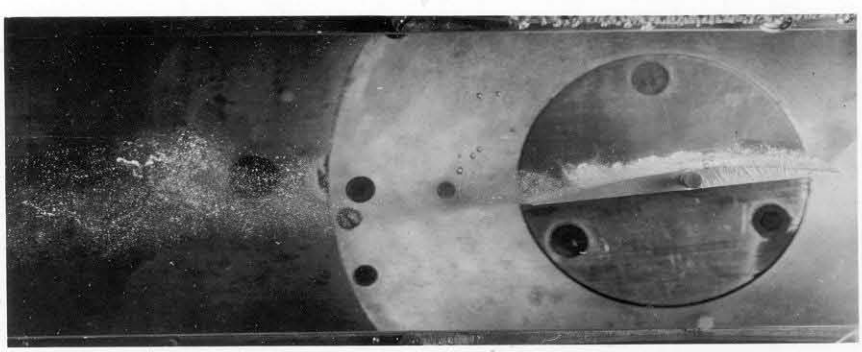

E. K = 0.890

Fig. 14(b) - Cavitation occurring on a plano-convex hydrofoil at an angle of attack of 6° at various cavitation numbers, K. The letters are those referred to in Fig. 14(a).

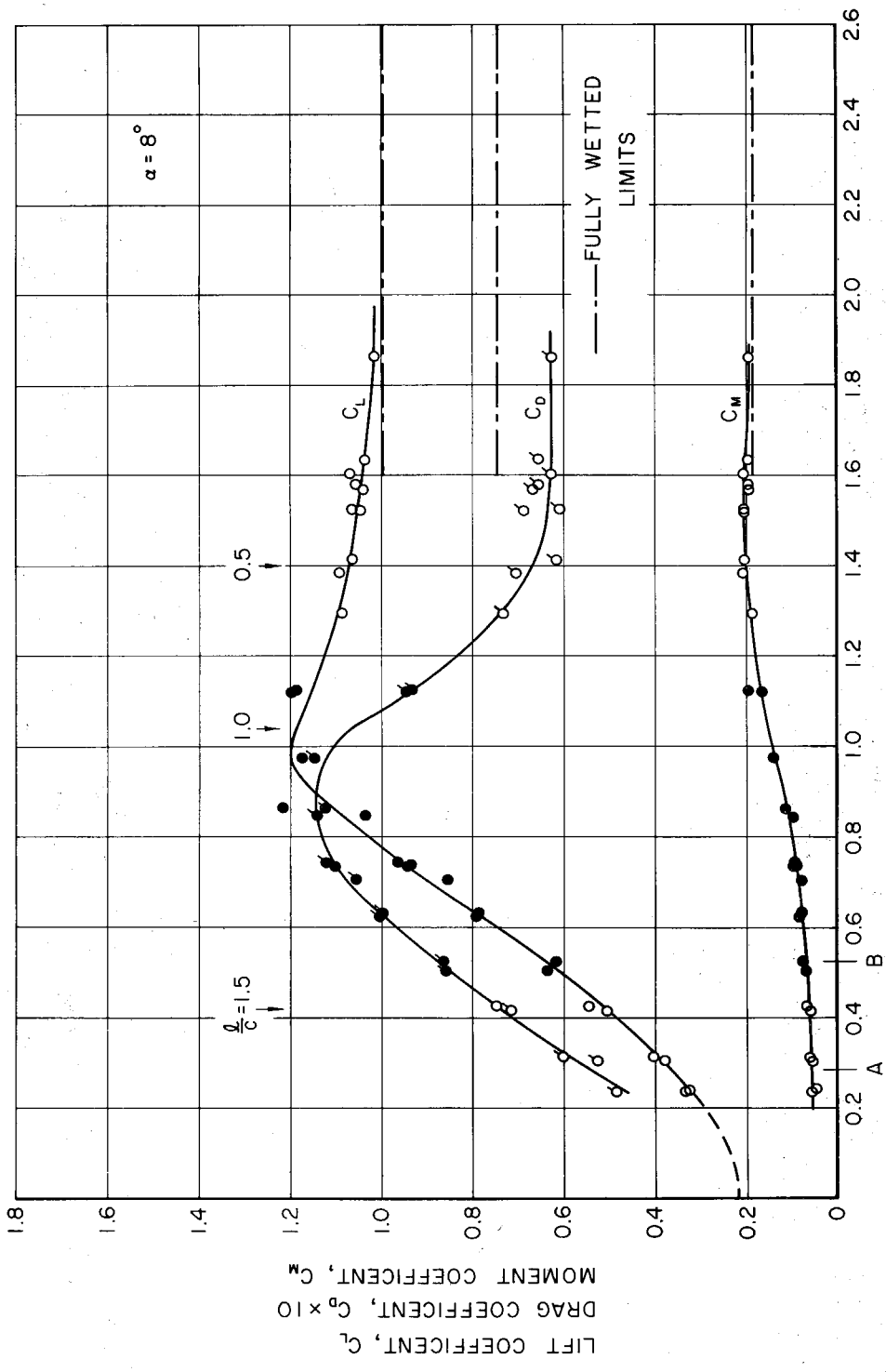

Fig. 15(a) - Force coefficients as functions of cavitation number at an angle of attack of 8^{o} for a plano-convex hydrofoil of 7 percent thickness. Note all drag points are flagged.

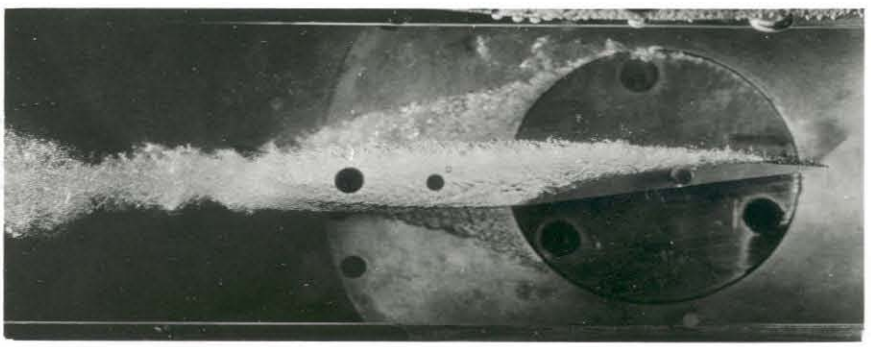

A. K = 0.285

B. K = 0.522

Fig. 15(b) - Cavitation occurring on a plano-convex hydrofoil at an angle of attack of 8° at various cavitation numbers, K. The letters are those referred to in Fig. 15(a).

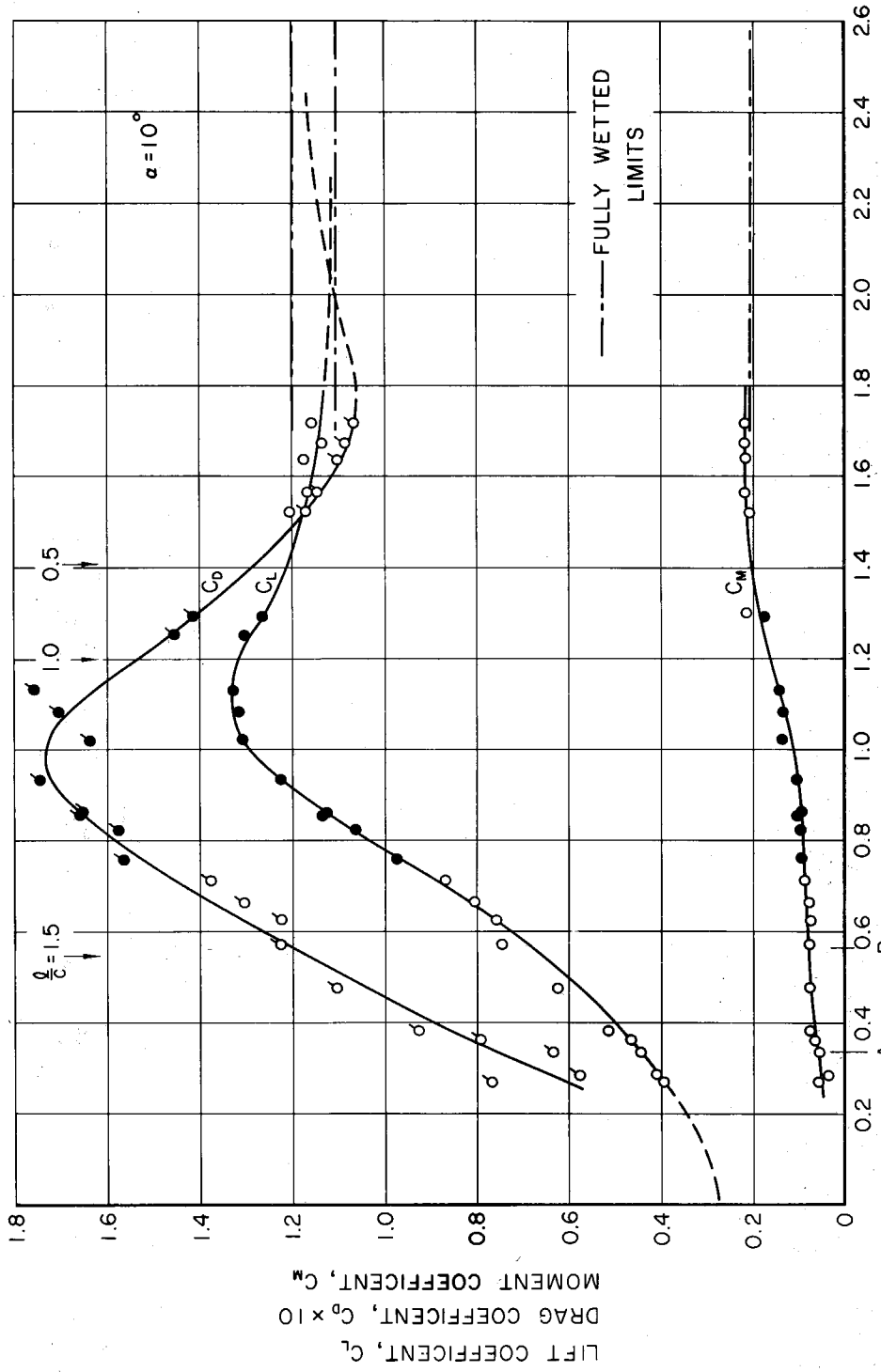

Fig. 16(a) - Force coefficients as functions of cavitation number at an angle of attack of 10° for a plano-convex hydrofoil of 7 percent thickness. Note all drag points are flagged.

A. K = 0.331

B. K = 0.561

Fig. 16(b) - Cavitation occurring on a plano-convex hydrofoil at an angle of attack of 10^{o} at various cavitation numbers, K. The letters are those referred to in Fig. 16(a).

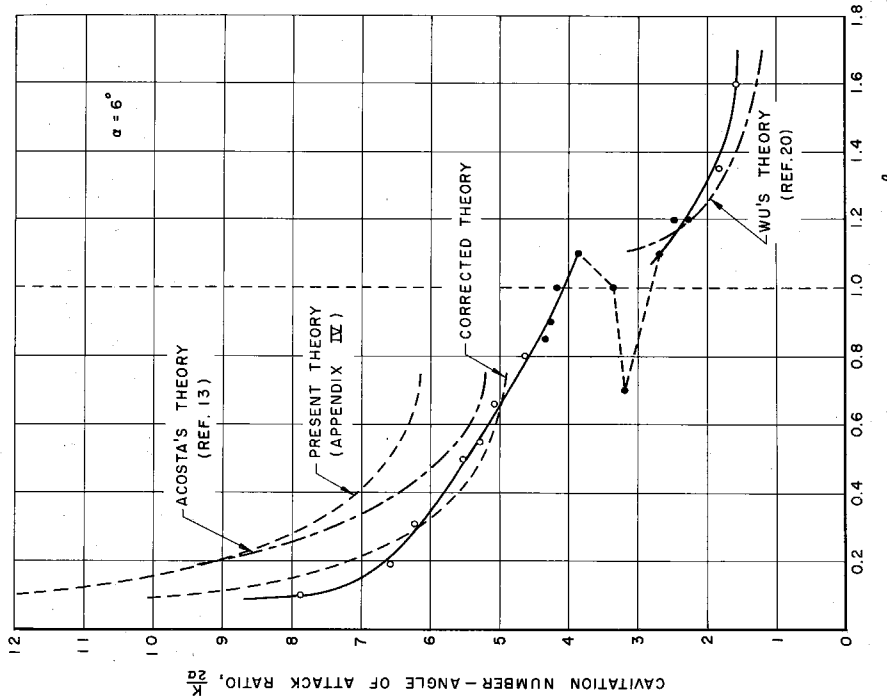

Fig. 18 - Cavitation number divided by angle of attack as a function of the cavity length to chord ratio for a plano-convex hydrofoil at an angle of attack of 6°

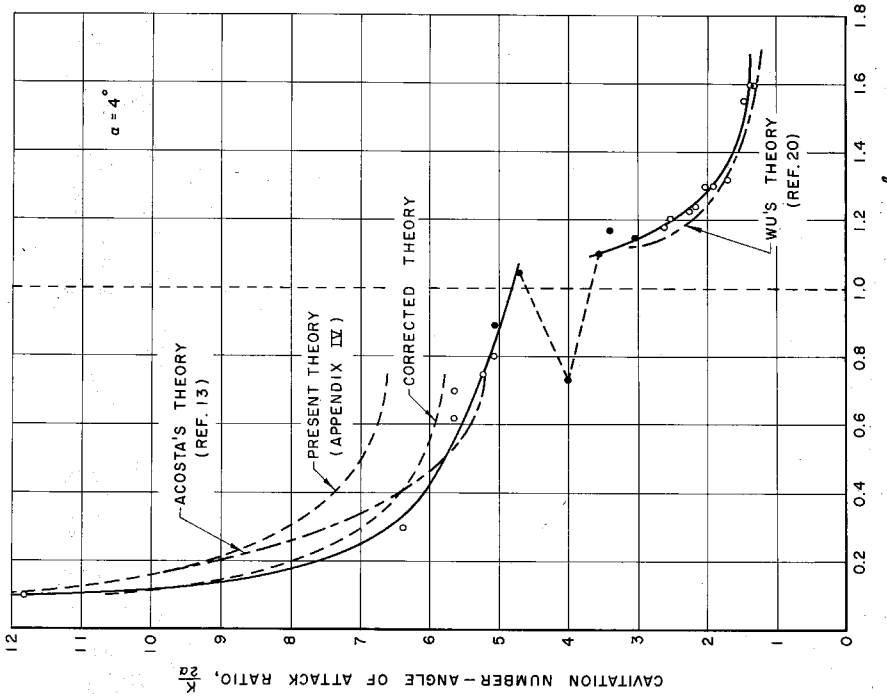

Fig. 17 - Cavitation number divided by angle of attack as a function of the cavity length to chord ratio for a plano-convex hydrofoil at an angle of attack of 4°

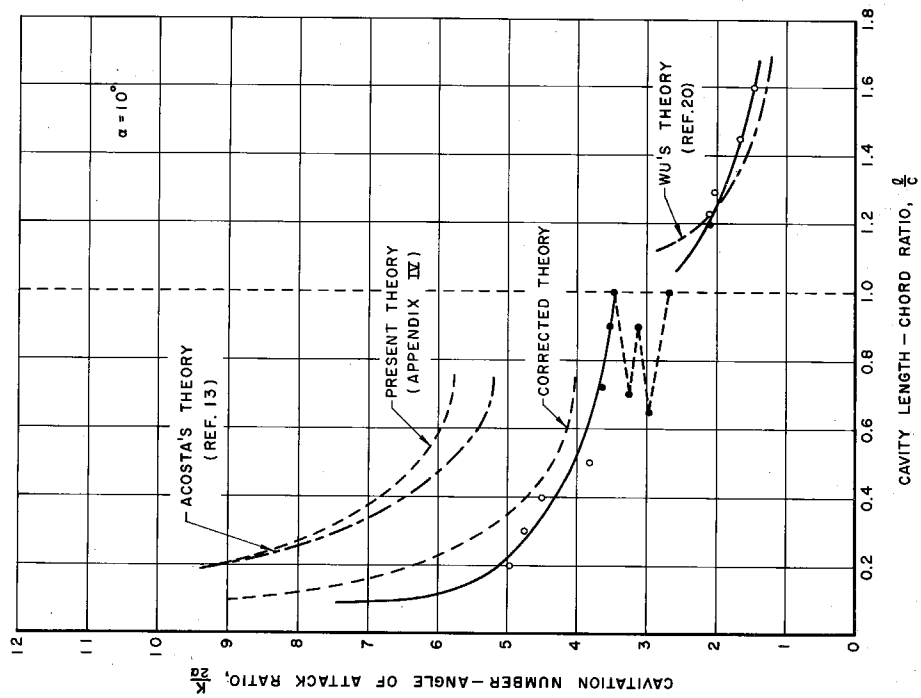

Fig. 20 - Cavitation number divided by angle of attack as a function of the cavity length to chord ratio for a plano-convex hydrofoil at an angle of attack of 10°

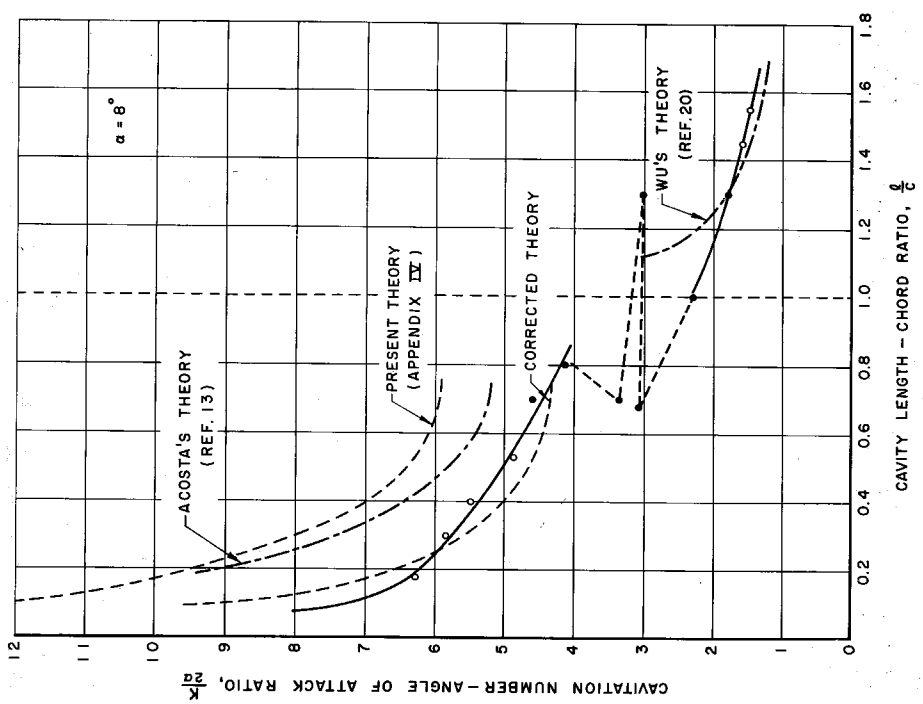

Fig. 19 - Cavitation number divided by angle of attack as a function of the cavity length to chord ratio for a plano-convex hydrofoil at an angle of attack of 8°

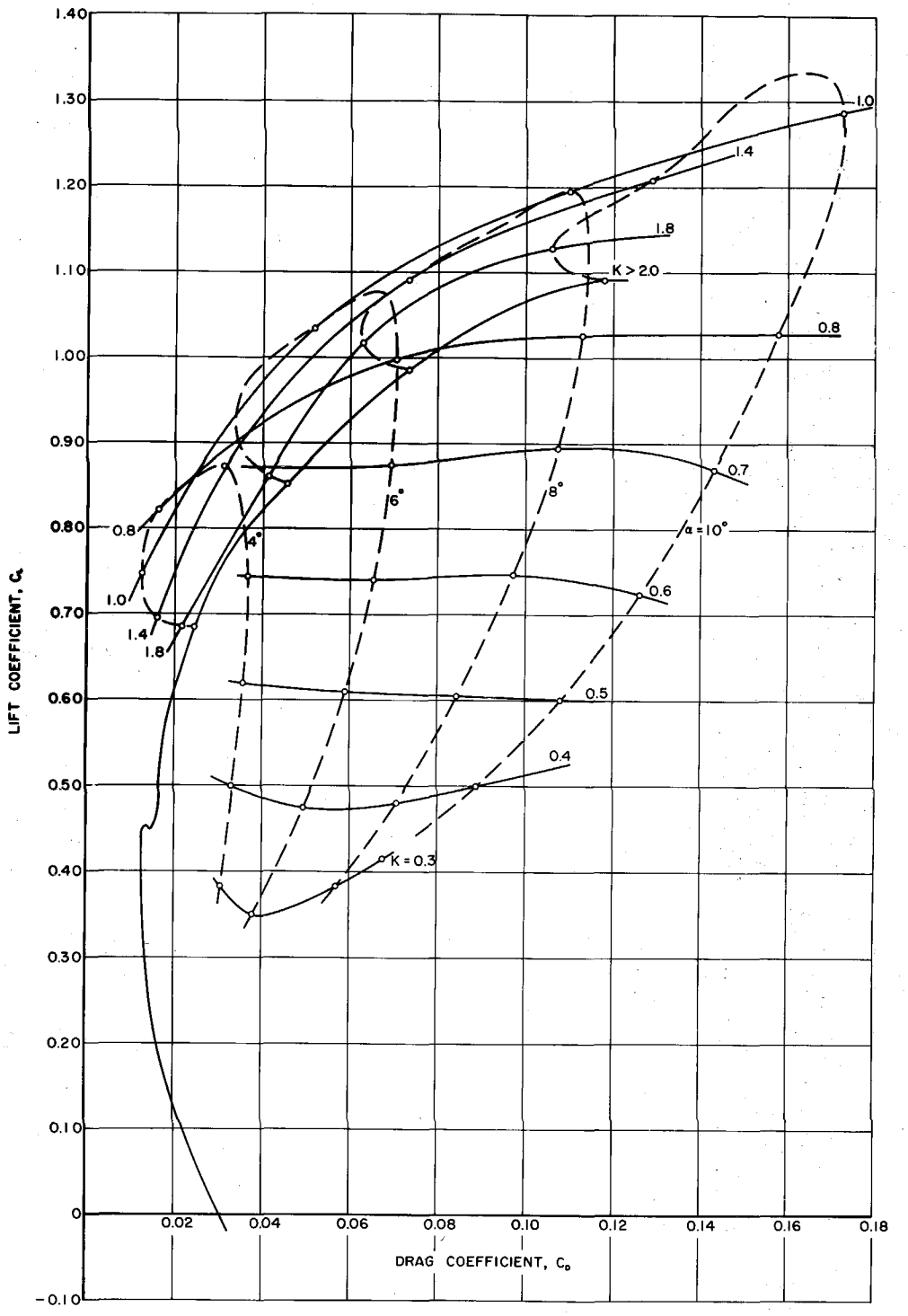

Fig. 21 - Polar diagram of the plano-convex hydrofoil section for the range tested

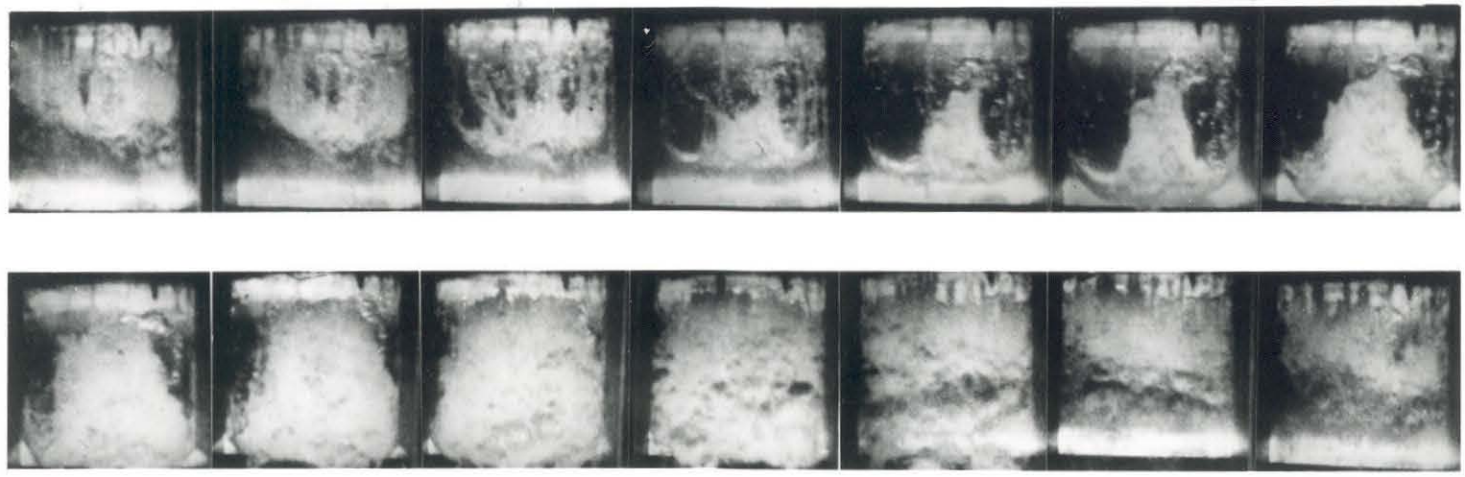

Fig. 22 - This sequence of photographs shows a plan view of the cavity during one cycle of oscillation beginning with the top left hand picture and proceeding along each row. The flow is from top to bottom, at a tunnel speed of 27 ft/sec, with the leading edge of the plano-convex hydrofoil at the top in each case. The angle of attack is 6^{o} and the cavitation number is 0.90. The time lapse between each photograph is 0.0042 seconds.

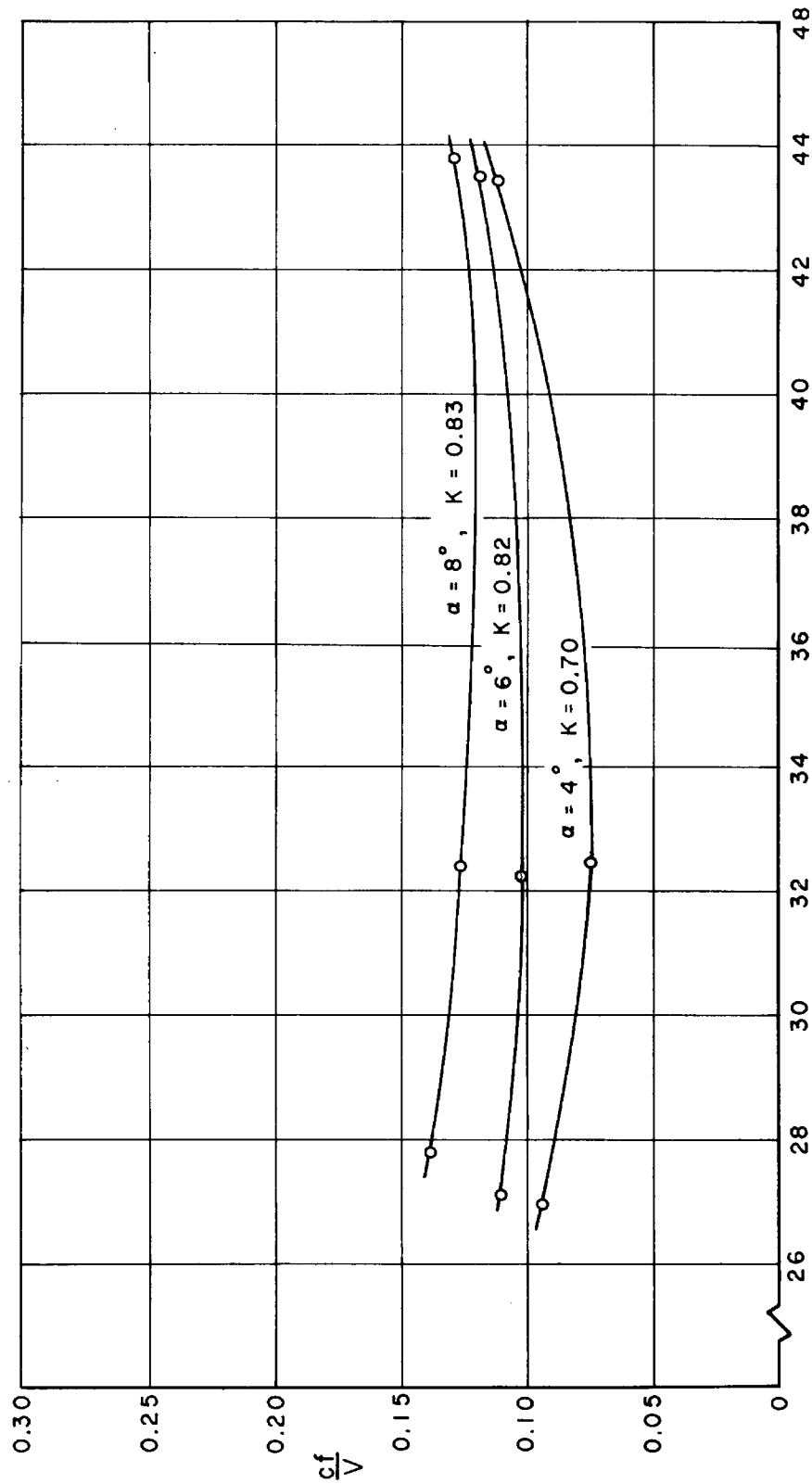

Fig. 23 - Reduced frequency during the phase of maximum oscillations as a function of tunnel speed for varying angles of attack. The Reynolds number range is from 0.62×10^6 to 1.05×10^6.

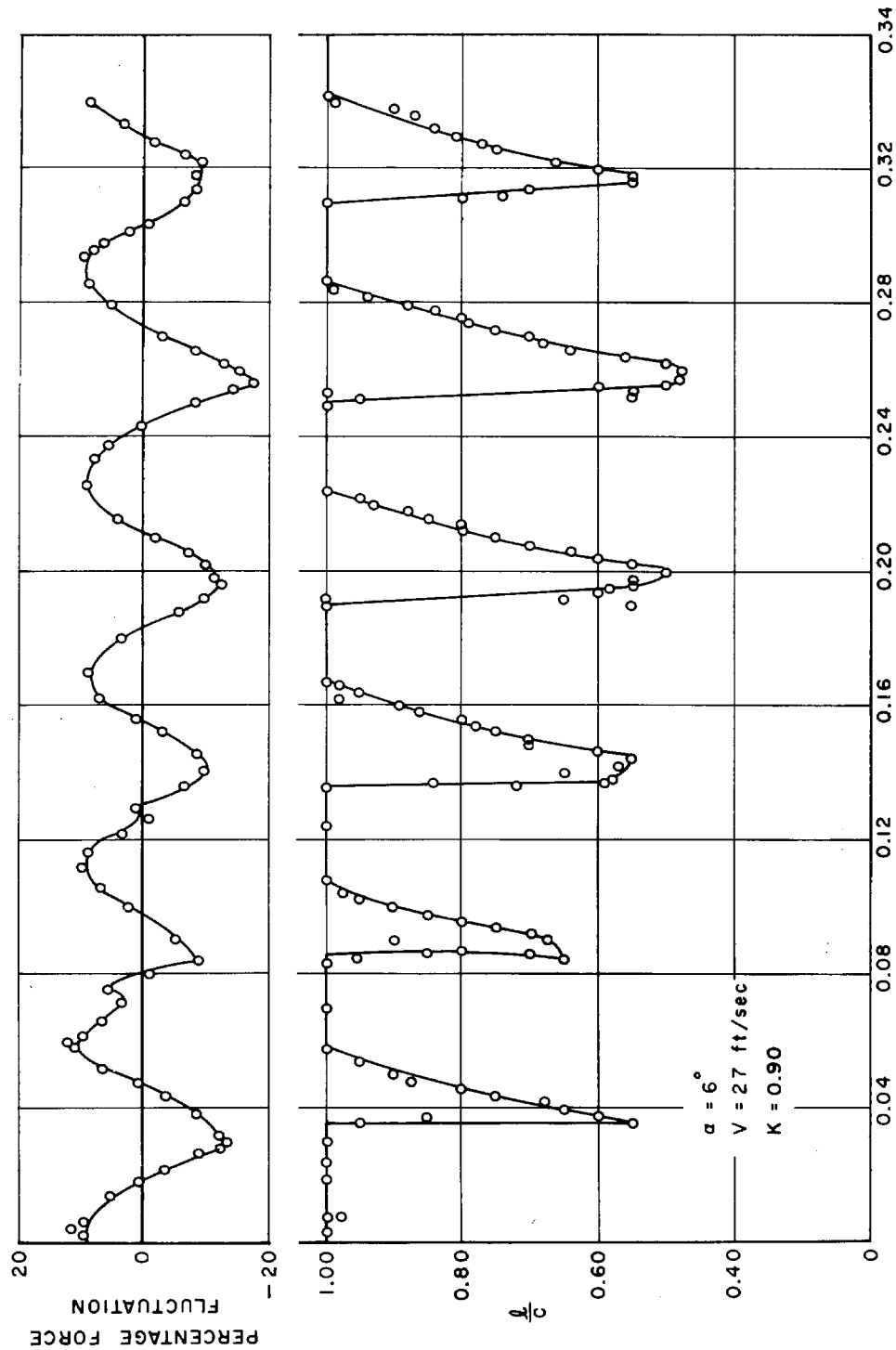

Fig. 24 - Percentage force fluctuations and cavity length oscillation as a function of time in the region of maximum oscillations for an angle of attack of 6°, tunnel speed of 27 ft/sec and cavitation number of 0.90.

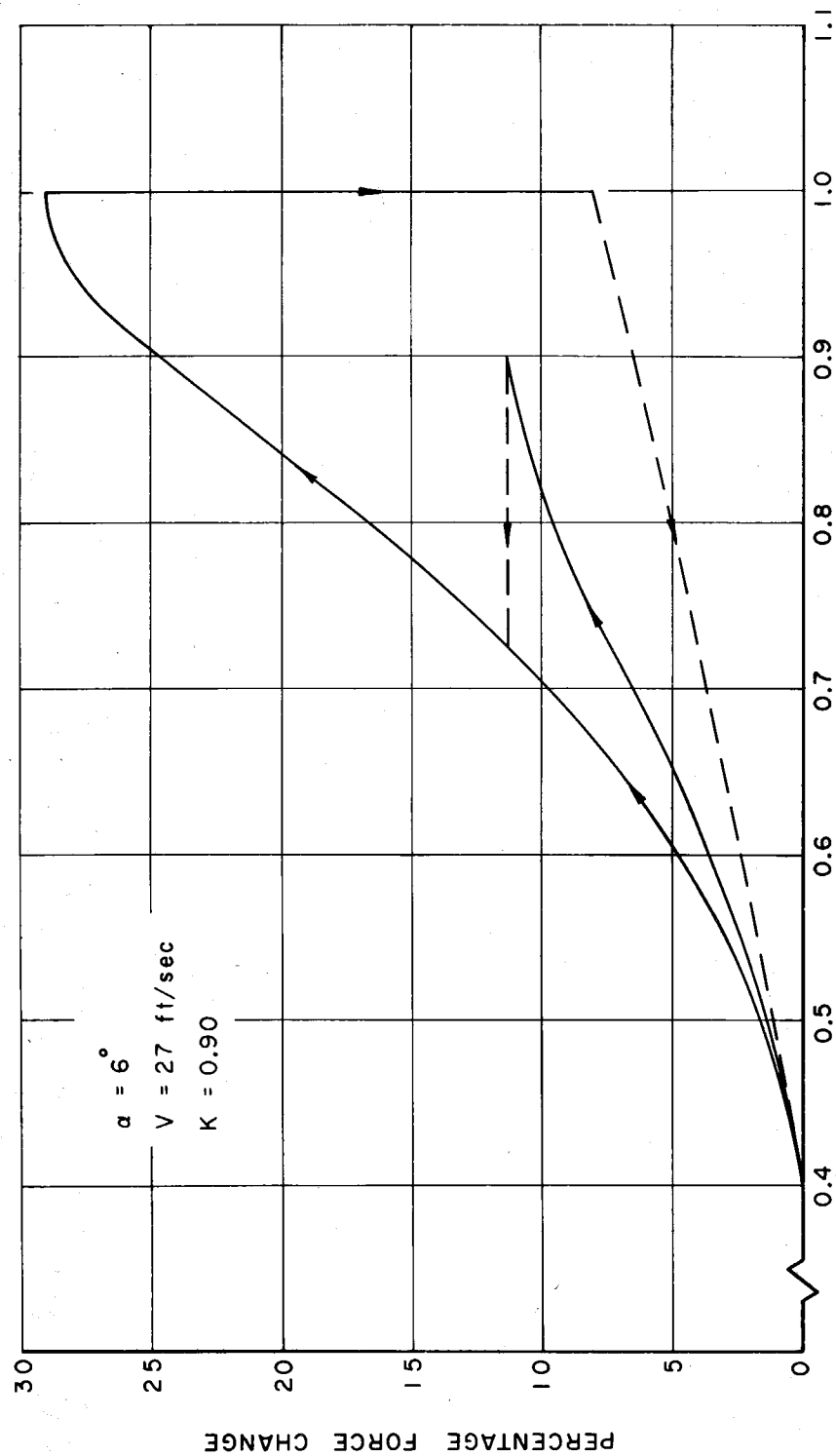

Fig. 25 - Percentage force change as a function of cavity length to chord ratio during maximum oscillations for angle of attack of 6°, tunnel speed of 27 ft/sec and cavitation number of 0.90.

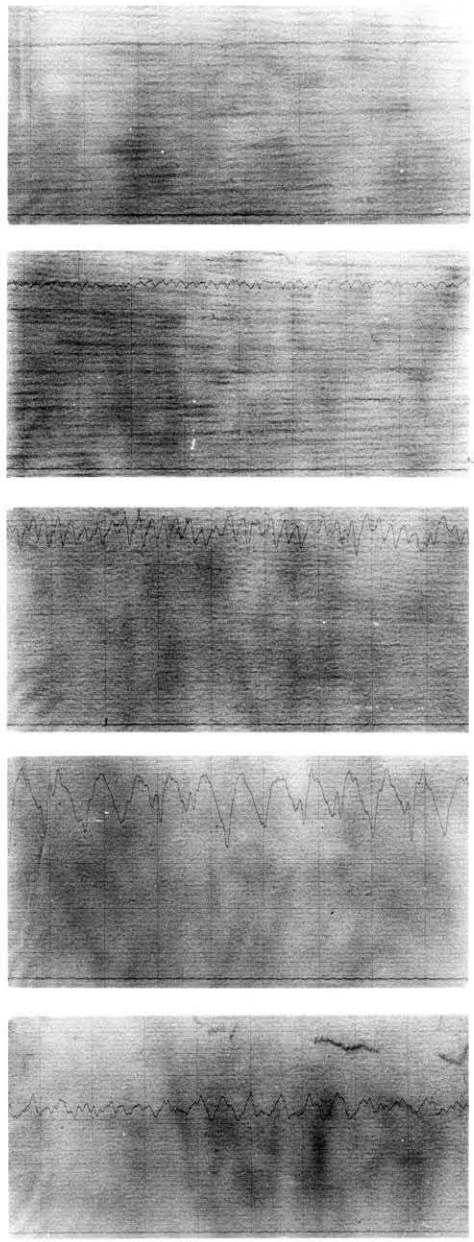

Fig. 26 - Traces of the oscillating force as recorded from the strain gage output as a function of time. Each time division represents 0.1 seconds. The zero force datum is also illustrated at the bottom of each picture. The tunnel speed is 31.4 ft/sec at an angle of attack of 6°. The sequence begins with the top trace taken at a cavitation number of 1.69 and proceeds downward with corresponding cavitation numbers of 0.18, 1.03, 0.93 and 0.48. The point of maximum oscillation is given by the fourth trace.

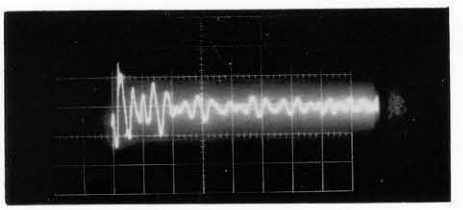

lift

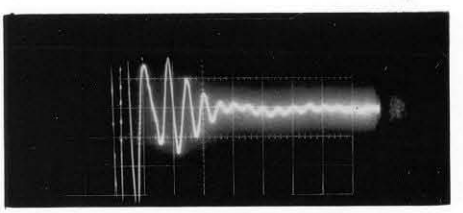

drag

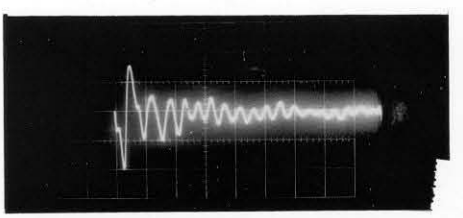

moment

Fig. 27 - Response of balance system to shock excitation in the lift, drag and moment directions respectively. The time base is 10 msec/div.

PART II

Figures 28 - 65

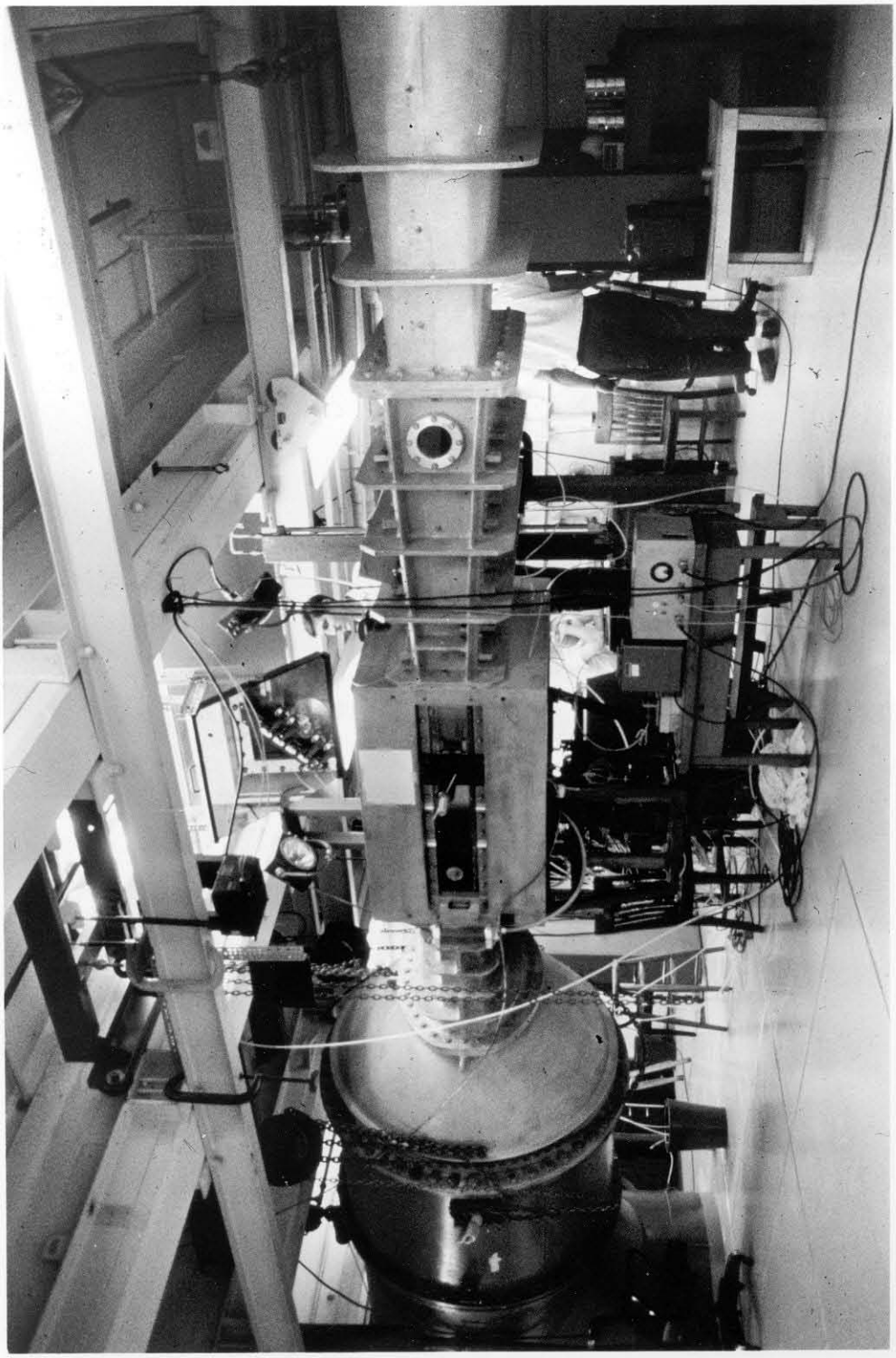

Fig. 28 - View of water tunnel working section for cascade studies.

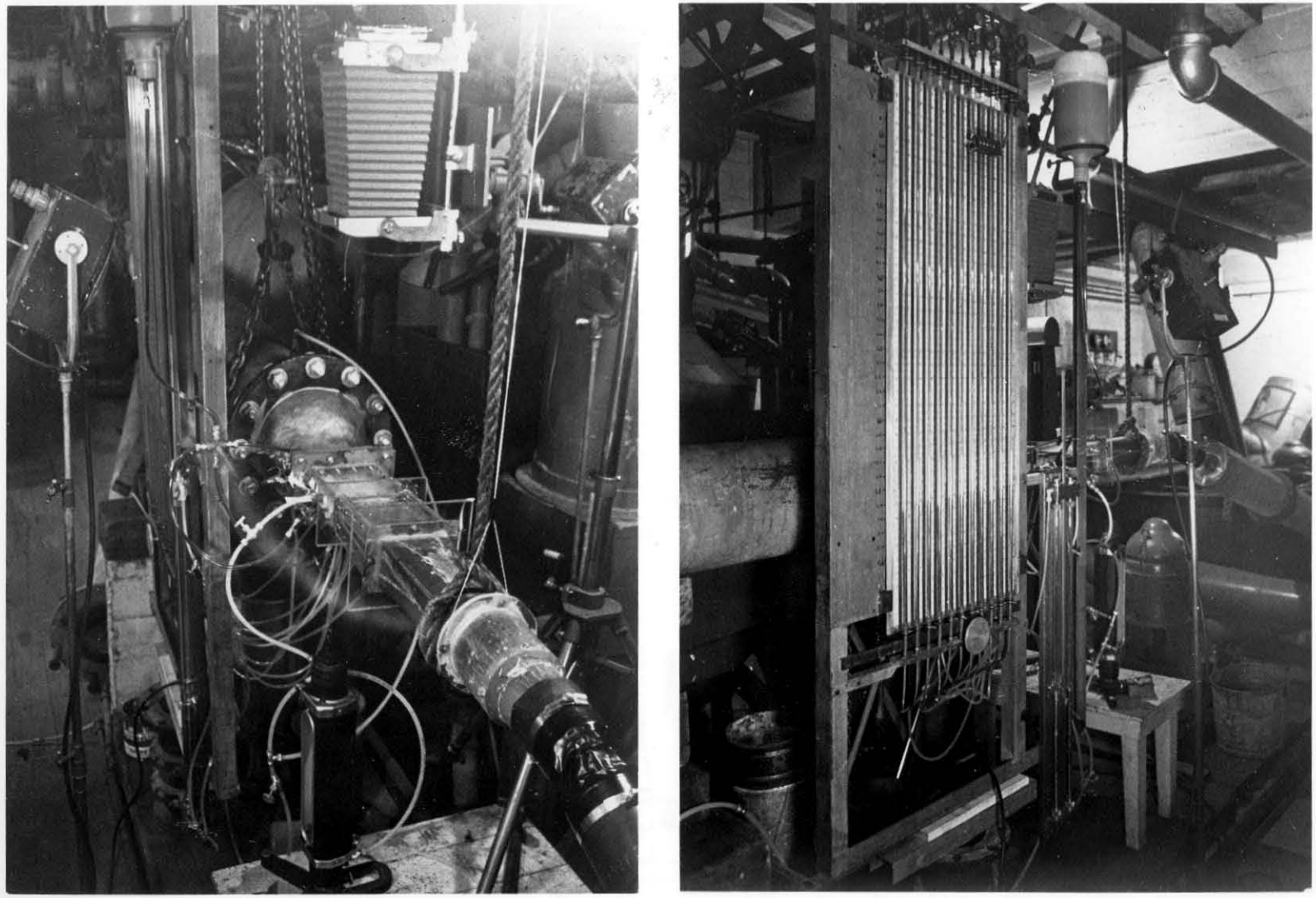

Fig. 29 - Experimental set-up for 1/6th model tests.

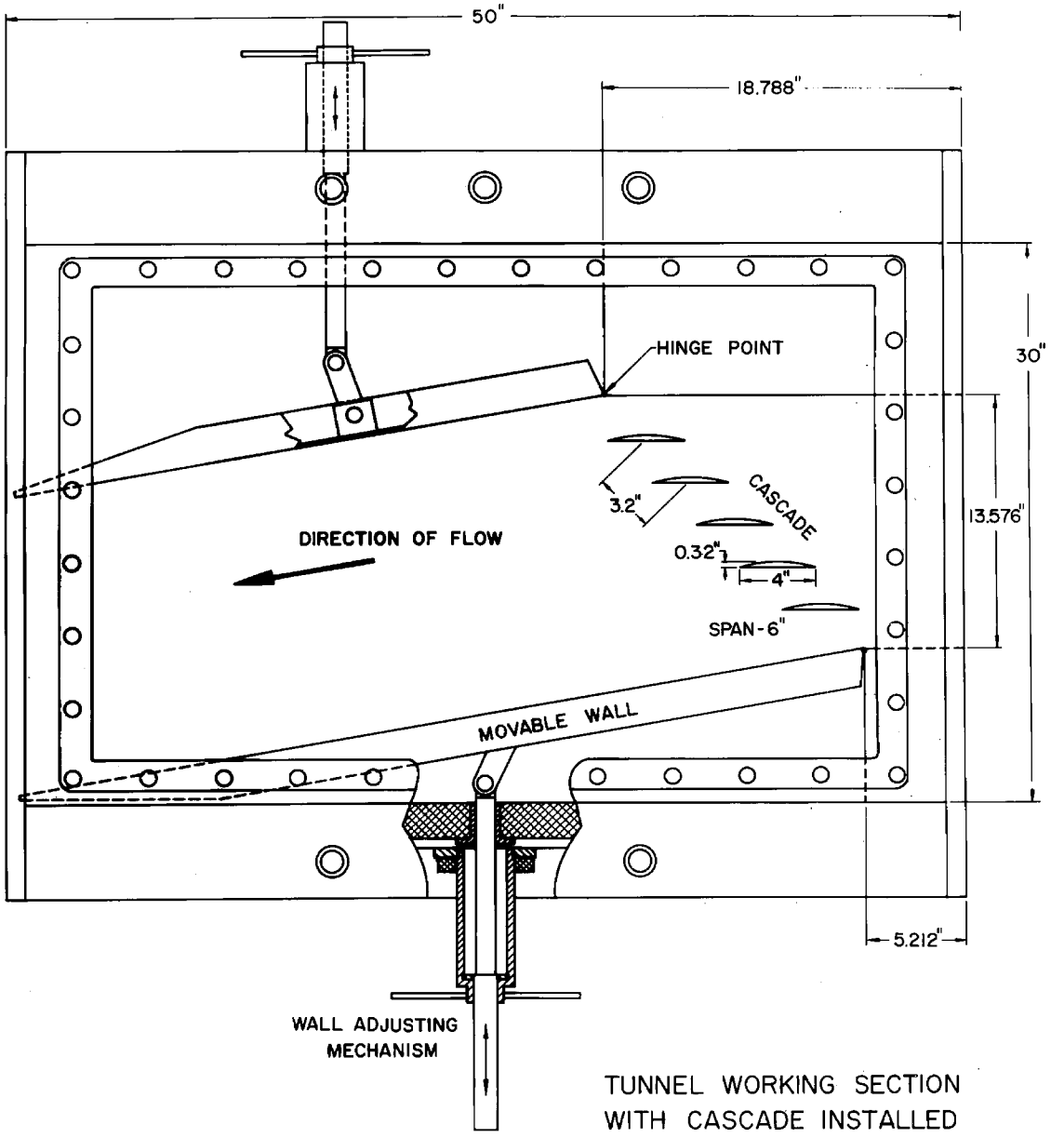

Fig. 30 - Schematic layout of cascade in the tunnel working section.

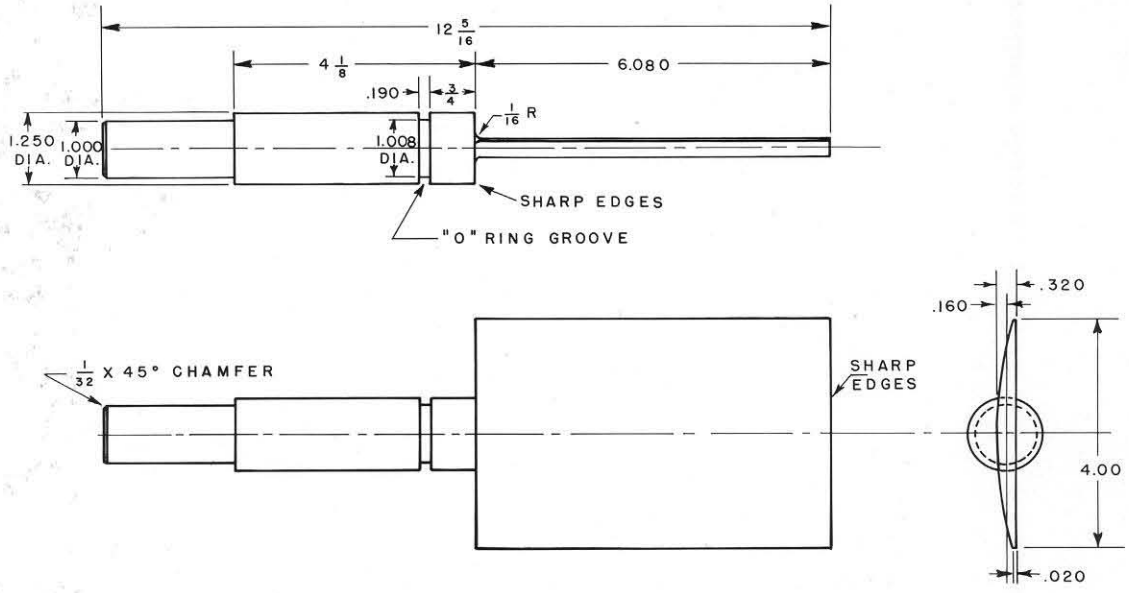

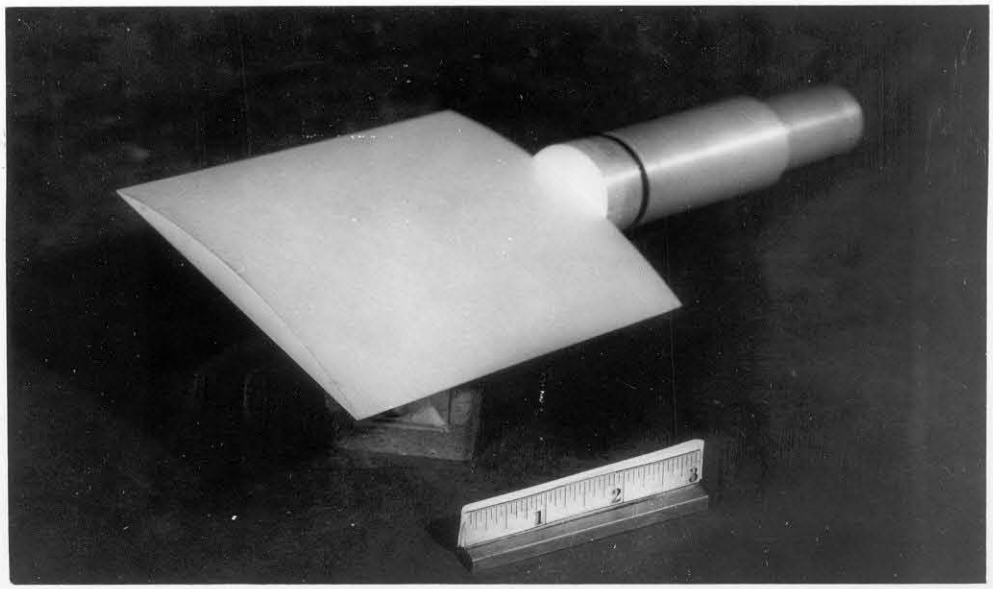

Fig. 31 - Drawing and photograph of one of the cascade hydrofoils.

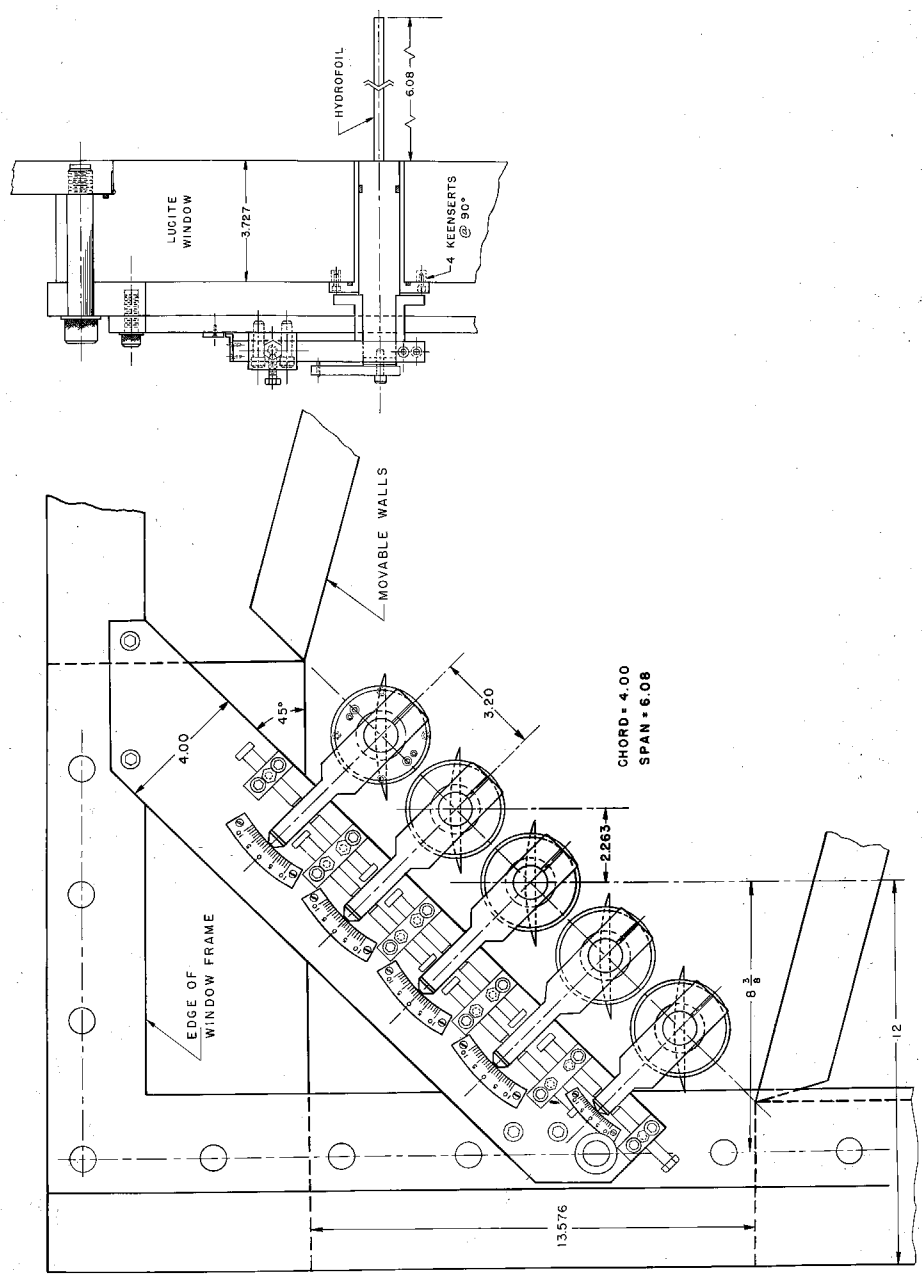

Fig. 32 - Drawing illustrating the angle changing mechanism devised for cascade studies.

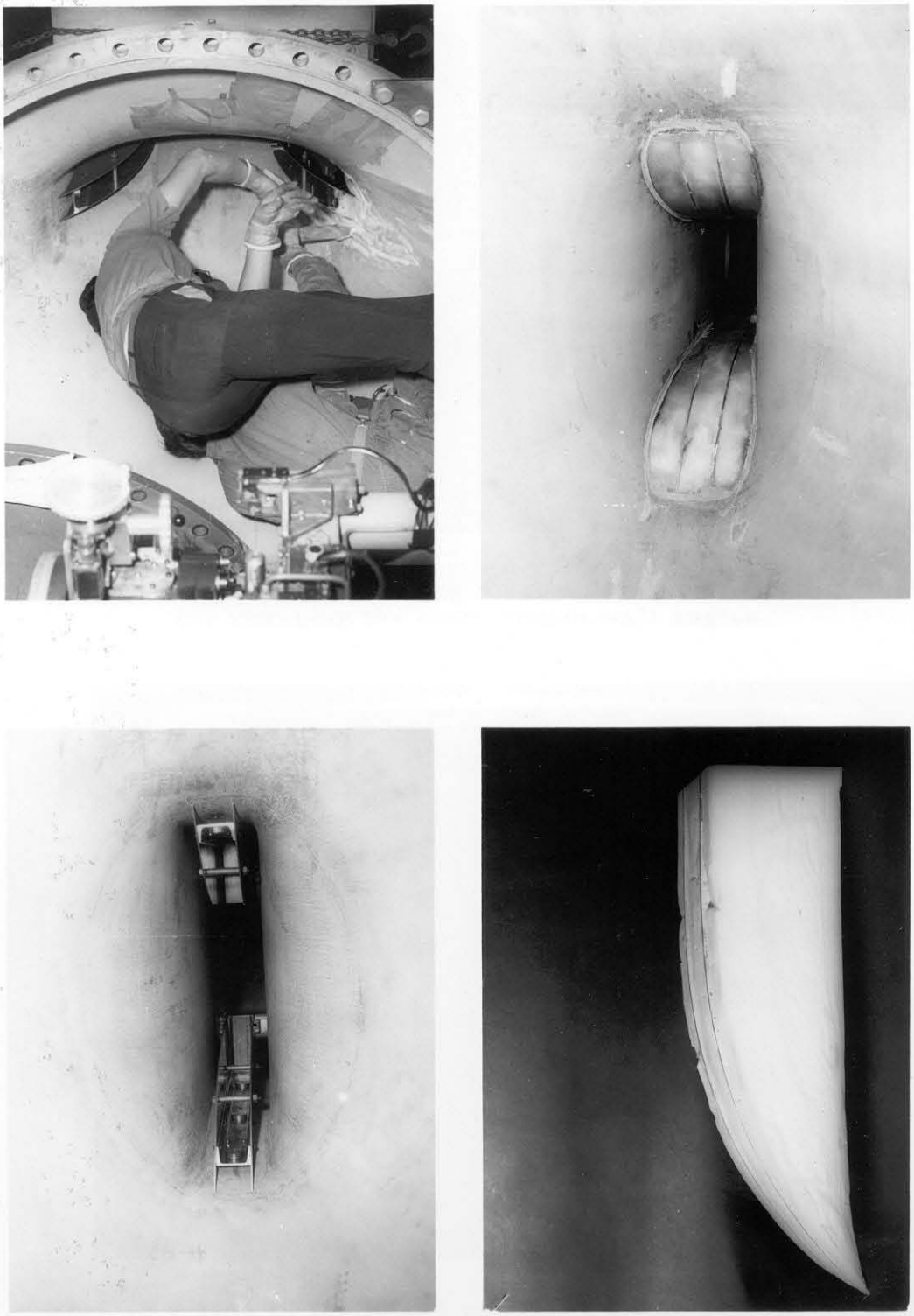

Fig. 33 - The various stages in the manufacture of the nozzle inserts for the cascade studies.

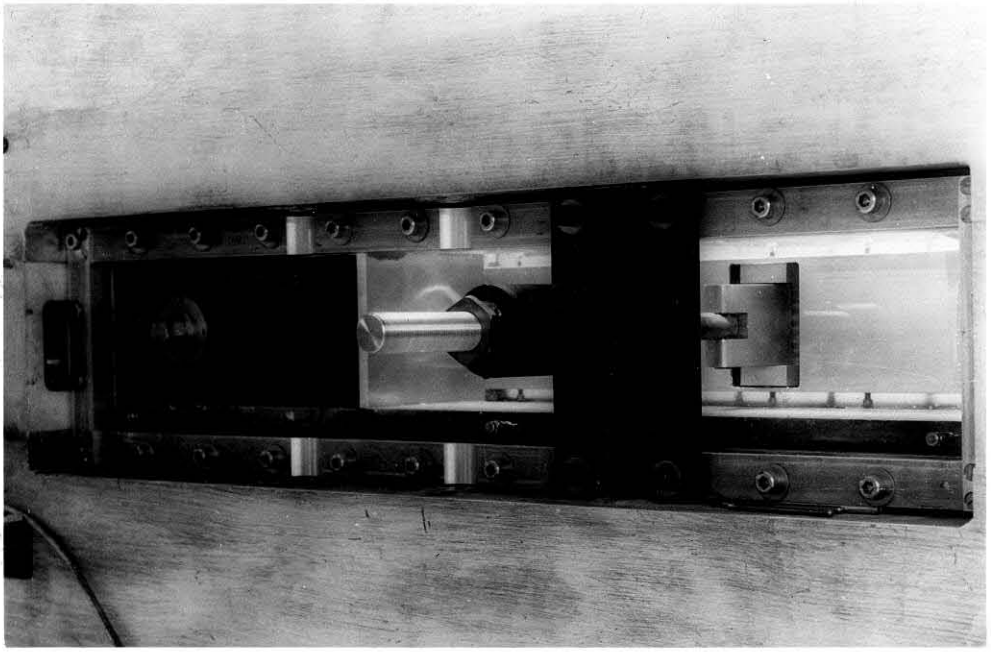

Fig. 34 - View of the actuating mechanism mounted in the tunnel for for changing the downstream wall angles.

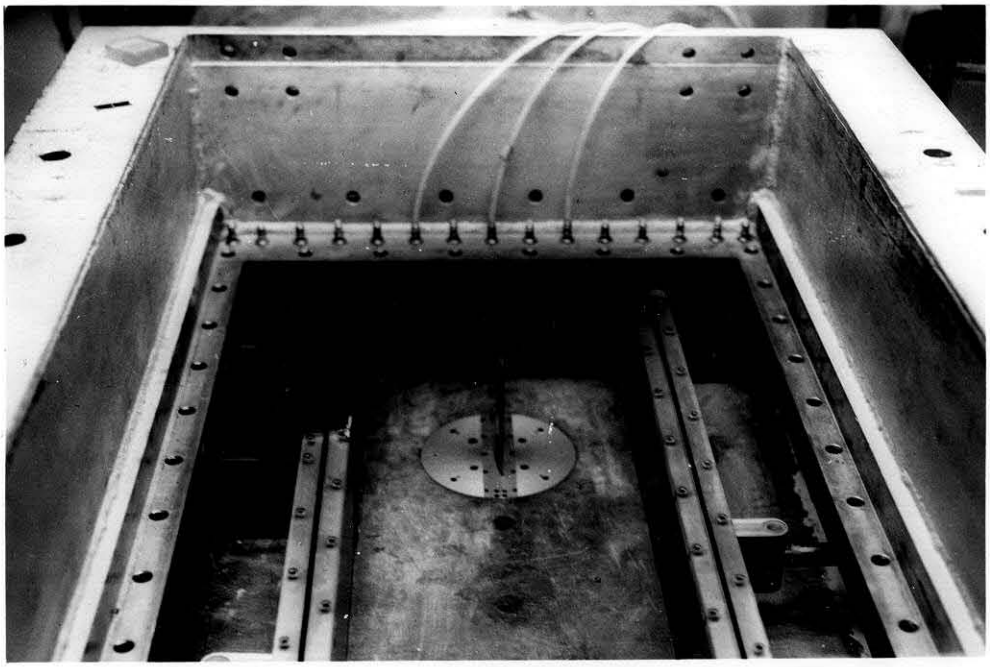

Fig. 35 - View of the tunnel working section with the center foil mounted to the balance spindle.

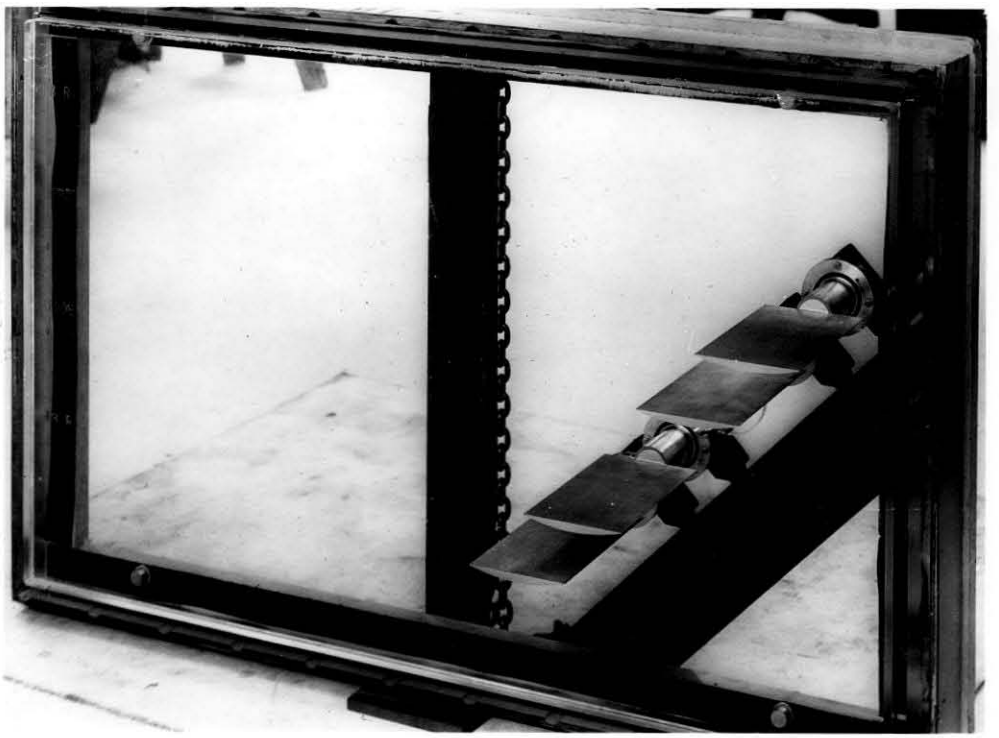

Fig. 36 - The lucite window with four hydrofoils mounted ready for assembly in water tunnel.

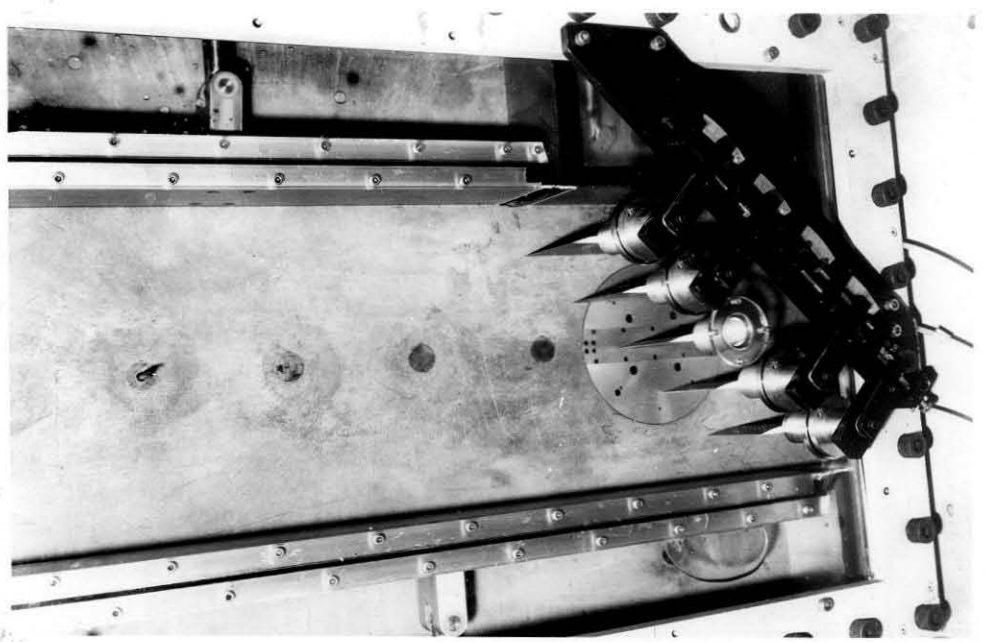

Fig. 37 - The final arrangement of the cascade in the water tunnel.

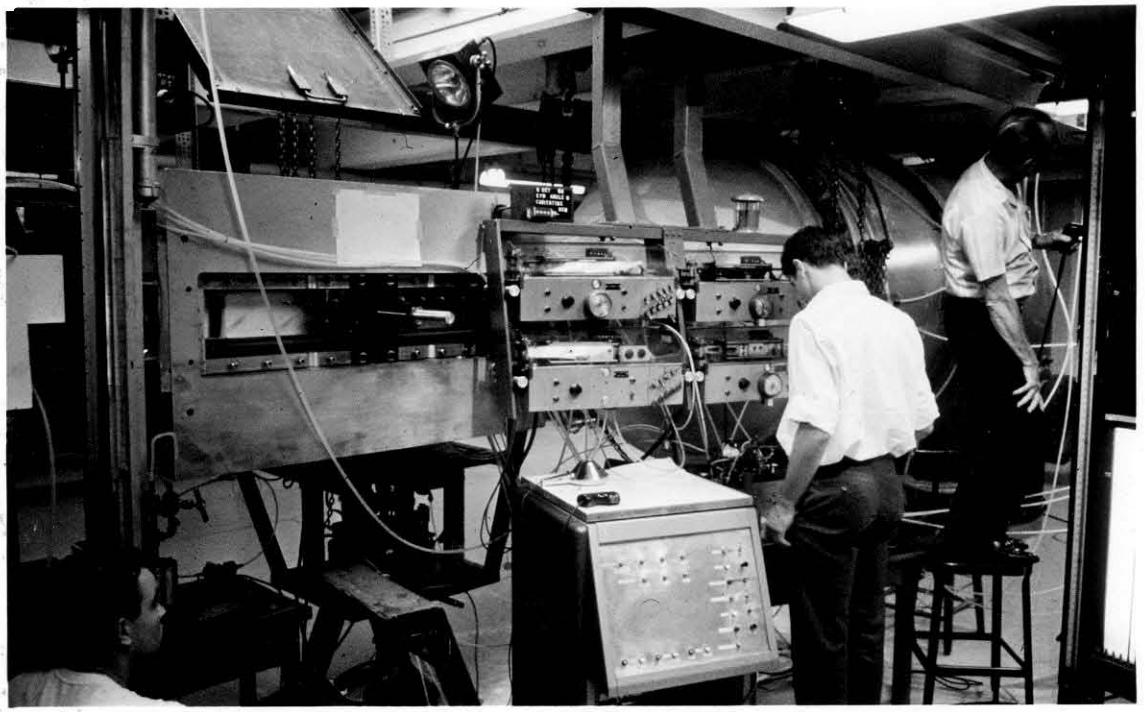

Fig. 38 - Views of general working area.

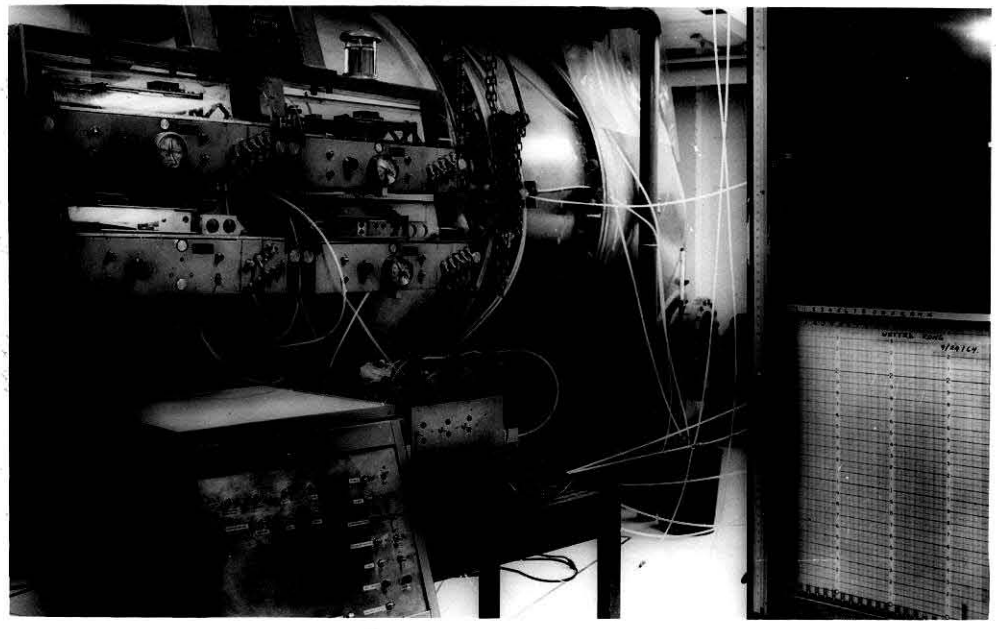

Fig. 39 - View of the force console and multi-tube manometer.

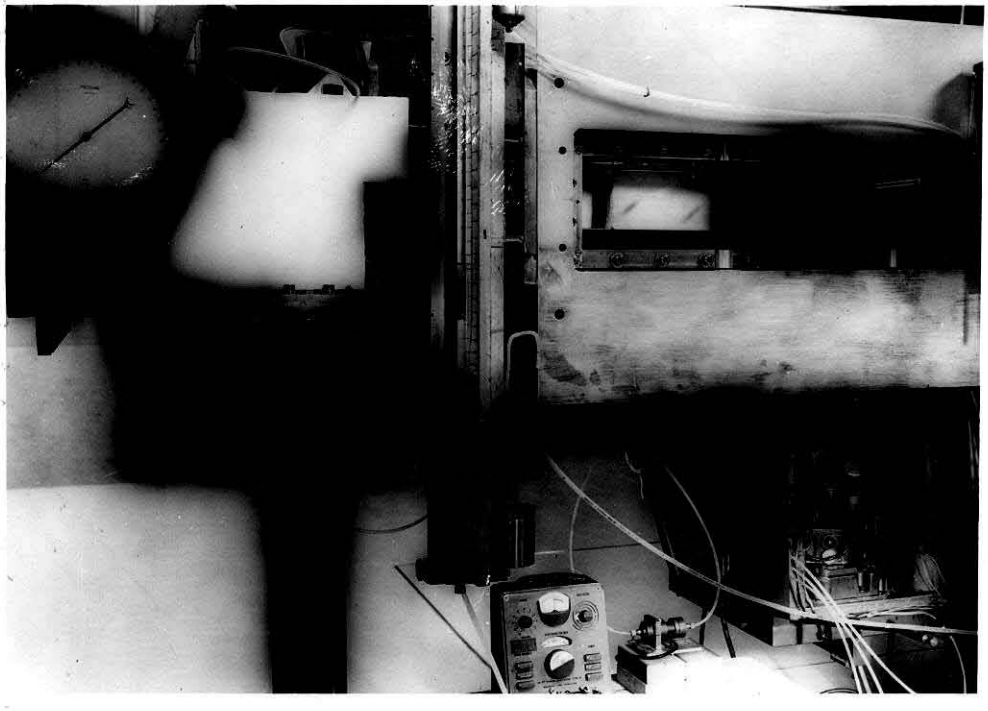

Fig. 40 - View of manometer for measuring cavity pressure and balancing bridge network for directional probe and the force balance.

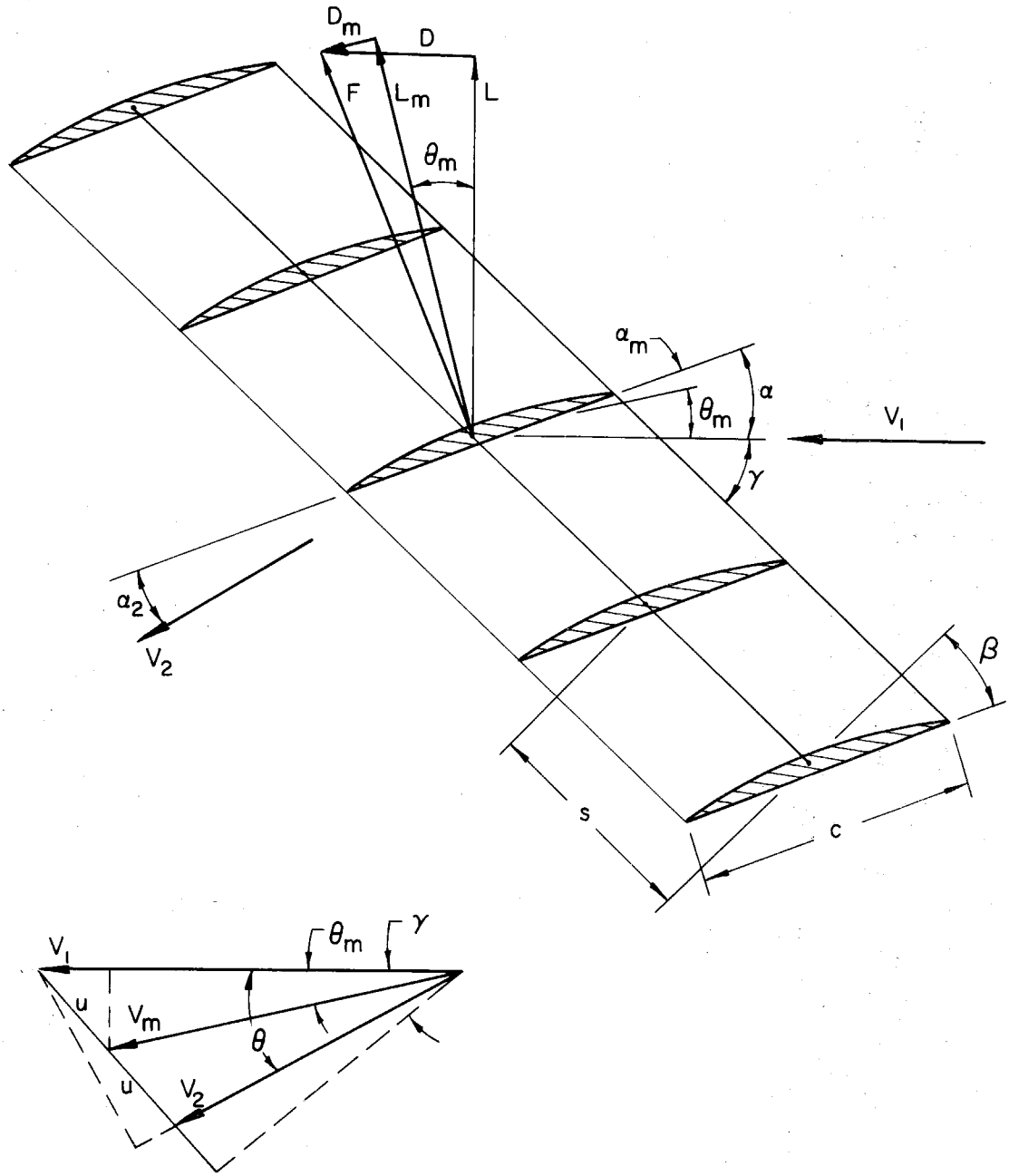

Fig. 41 - Definition of cascade parameters and other notation used.

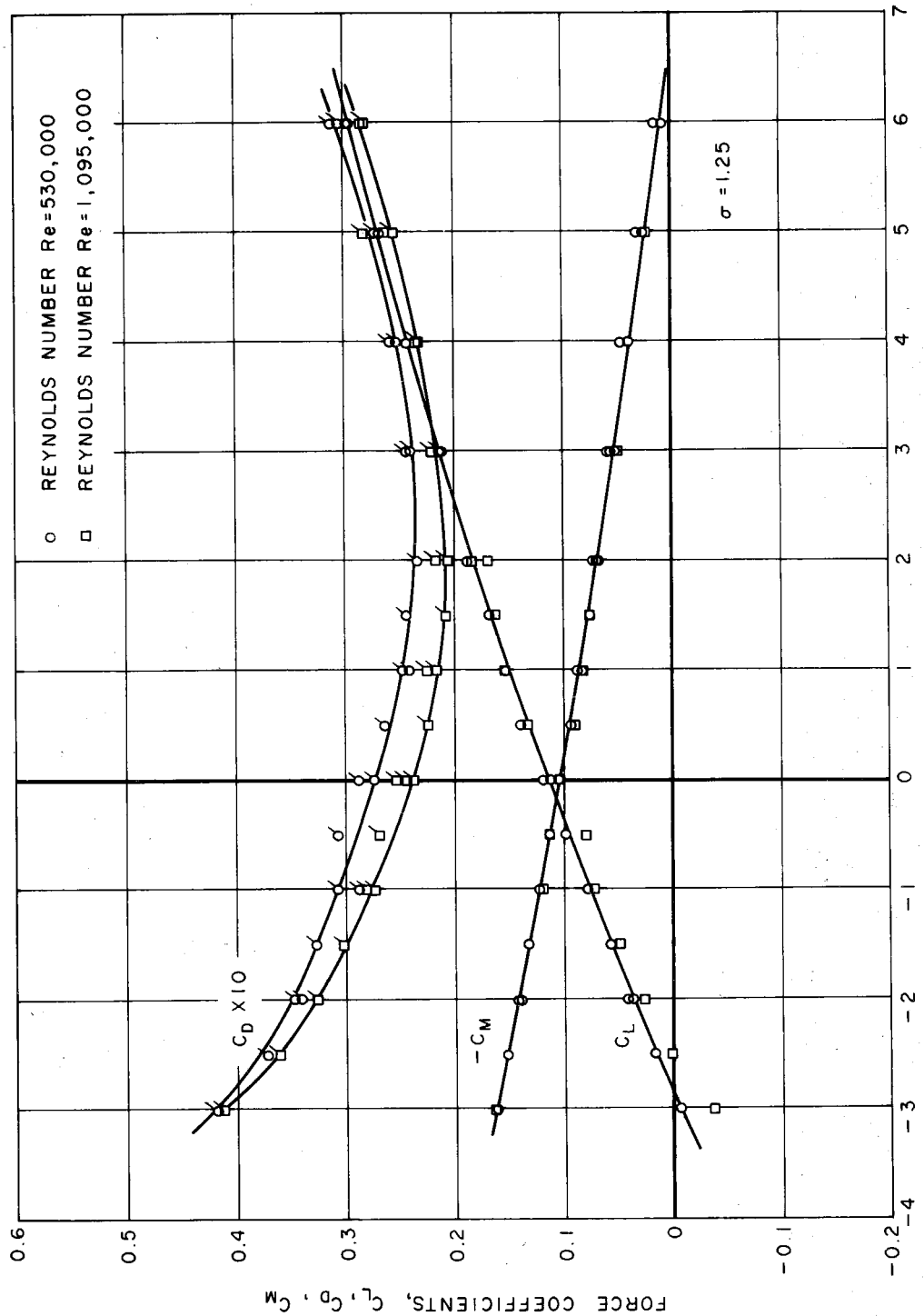

Fig. 42 - Force coefficients based on upstream velocity as a function of angle of attack for fully wetted compressor cascade of solidity $\sigma = 1.25$, for two Reynolds numbers.

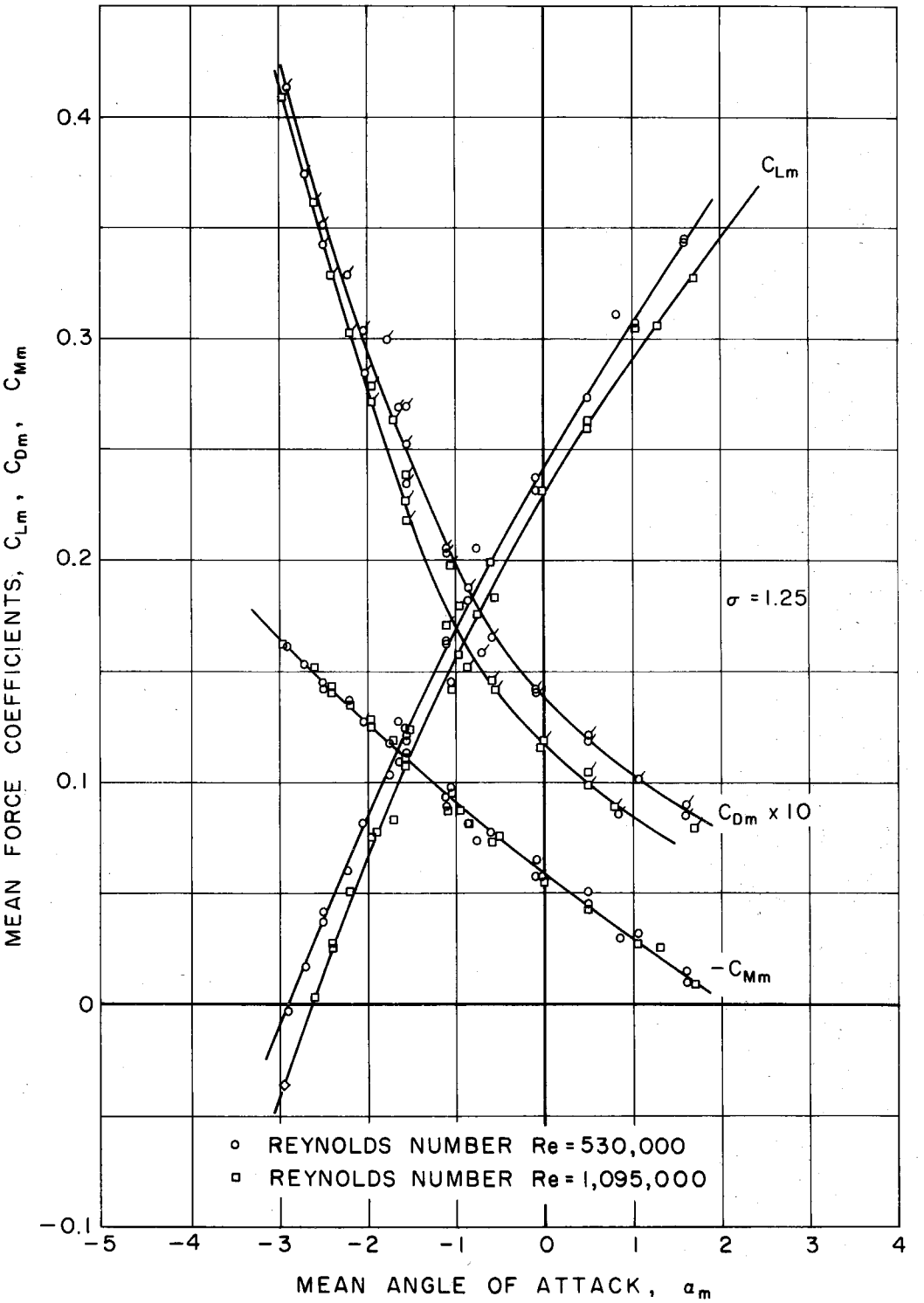

Fig. 43 - Force coefficients based on mean flow velocity as a function of the vector mean angle of attack for compressor cascade of solidity σ = 1.25 for two Reynolds numbers.

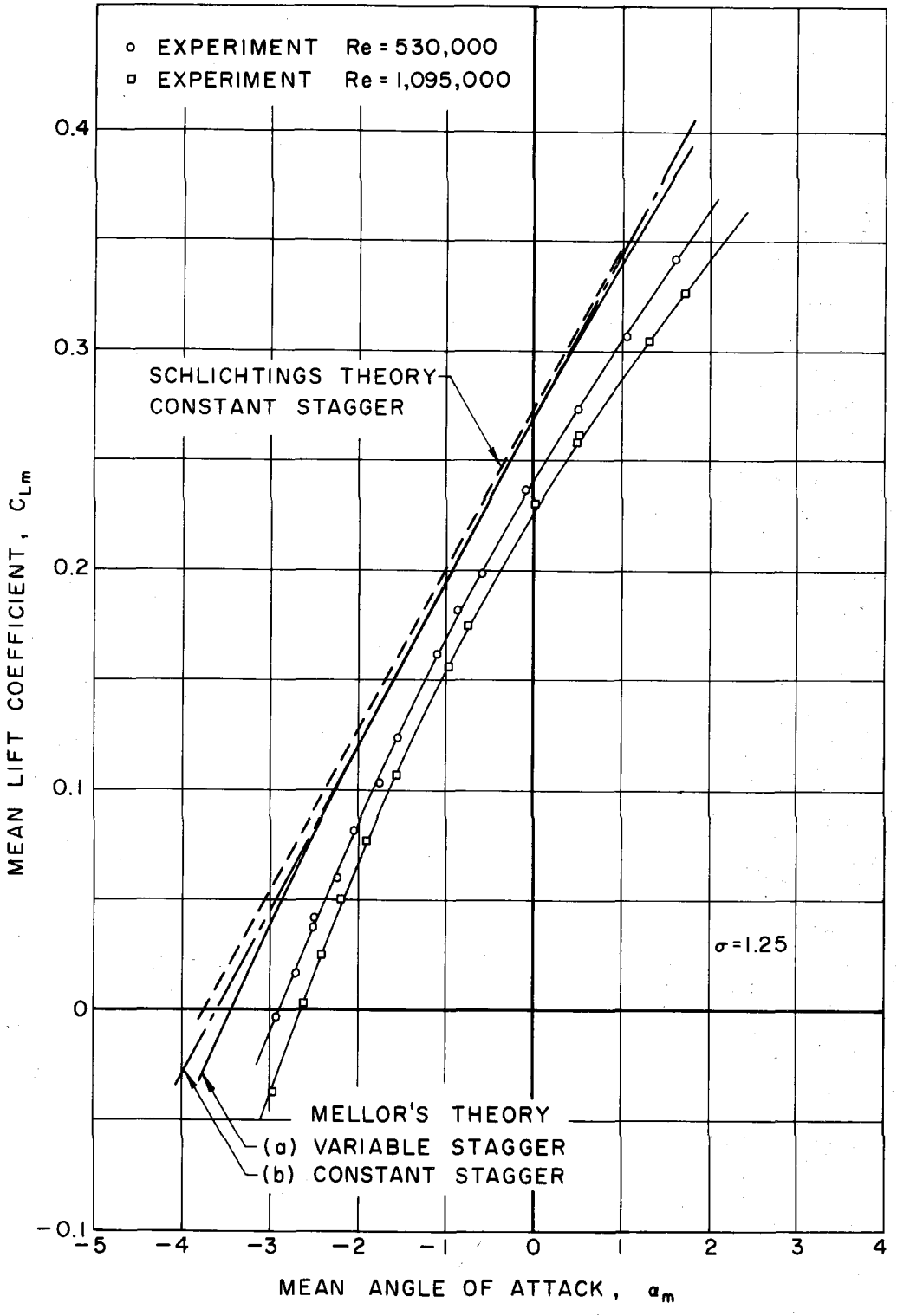

Fig. 44 - Comparison of the experimental lift coefficient with theory for compressor cascade of solidity $\sigma = 1.25$.

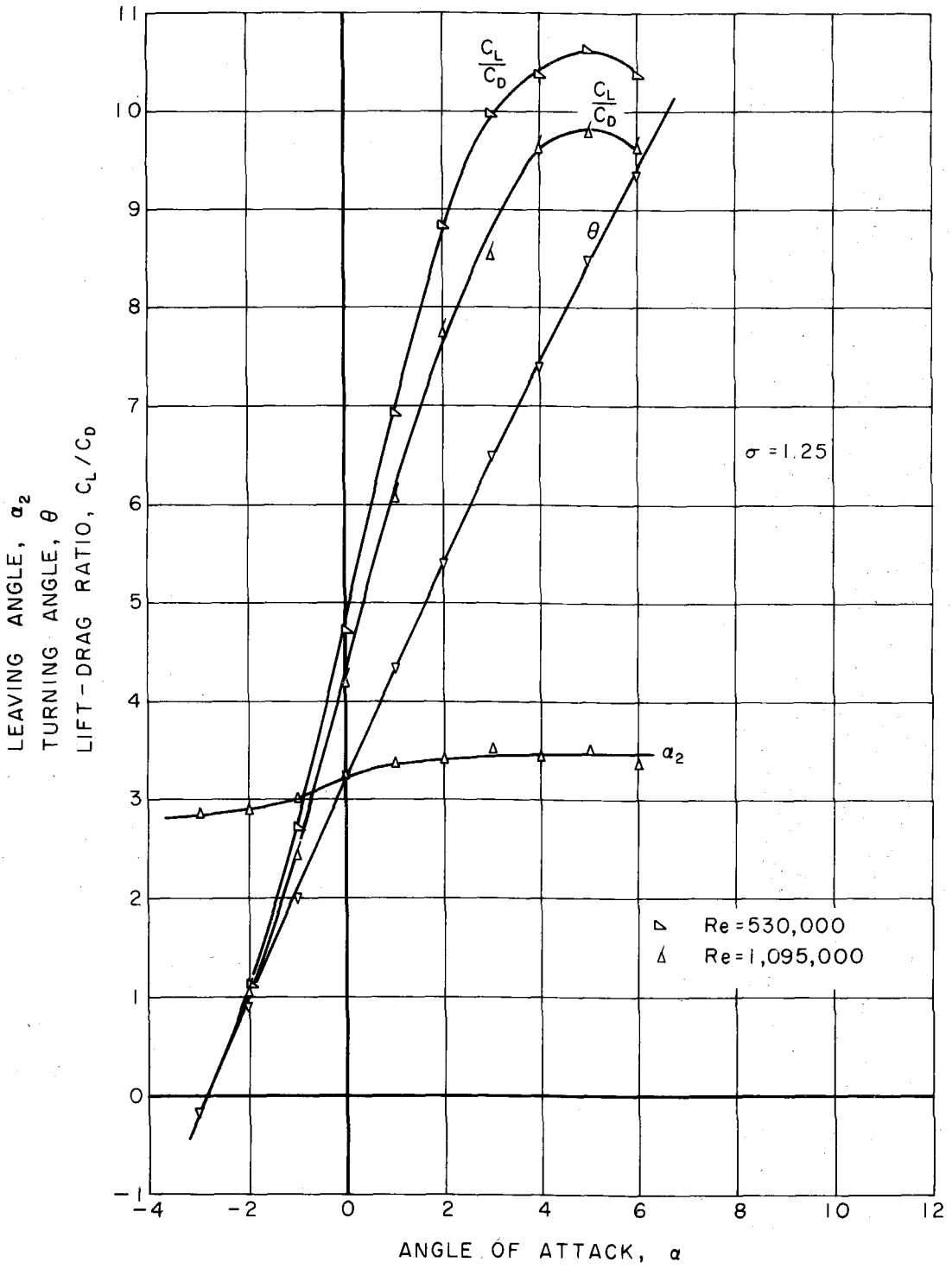

Fig. 45 - Lift-to-drag ratio, turning angle and leaving angle as a function of the angle of attack α for compressor cascade of solidity $\sigma = 1.25$ for two Reynolds numbers.

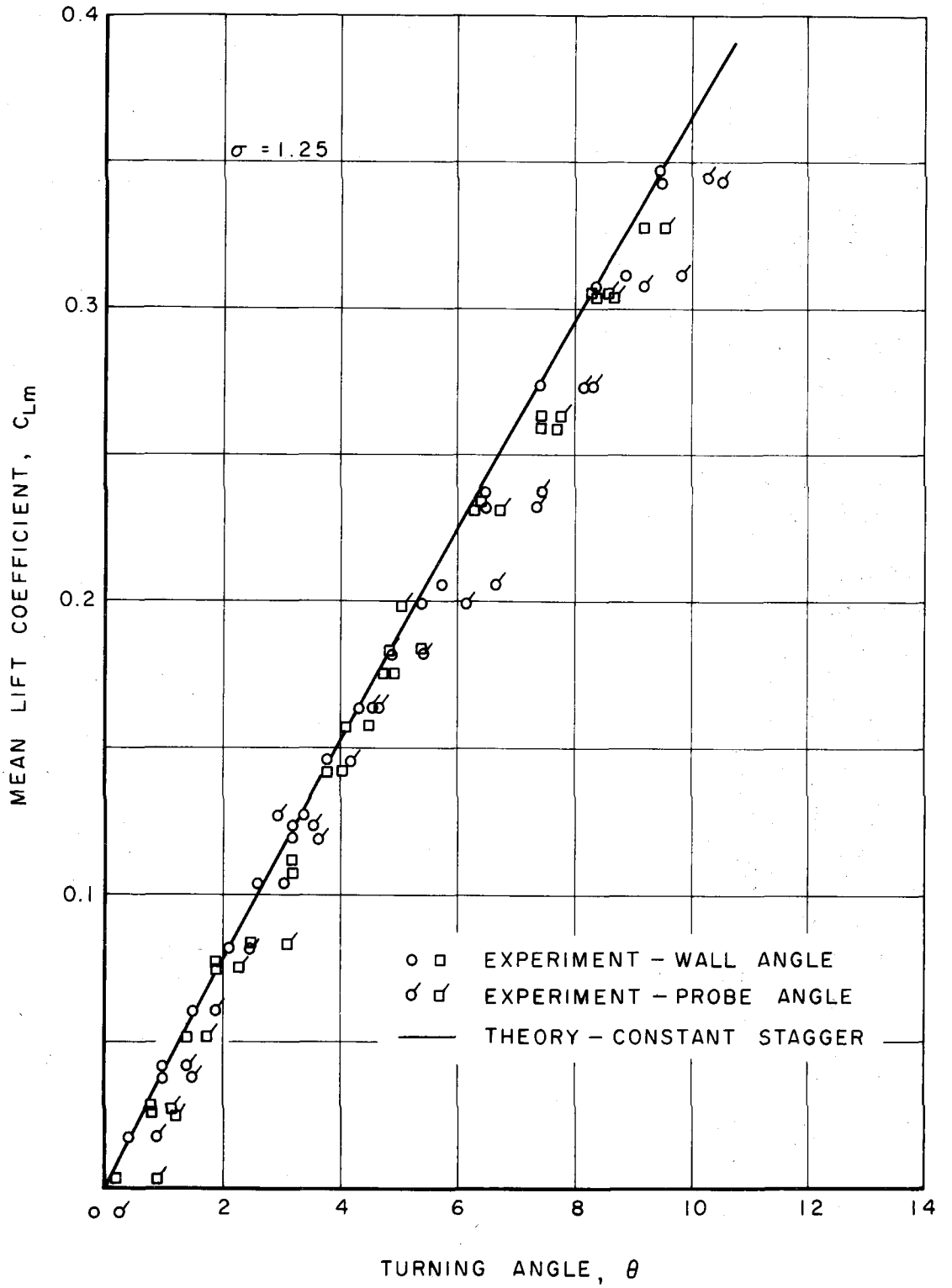

Fig. 46 - Comparison of the measured mean lift coefficient with turning angle as obtained from the wall angle and from probe measurements with theoretical values for a compressor cascade of solidity $\sigma = 1.25$.

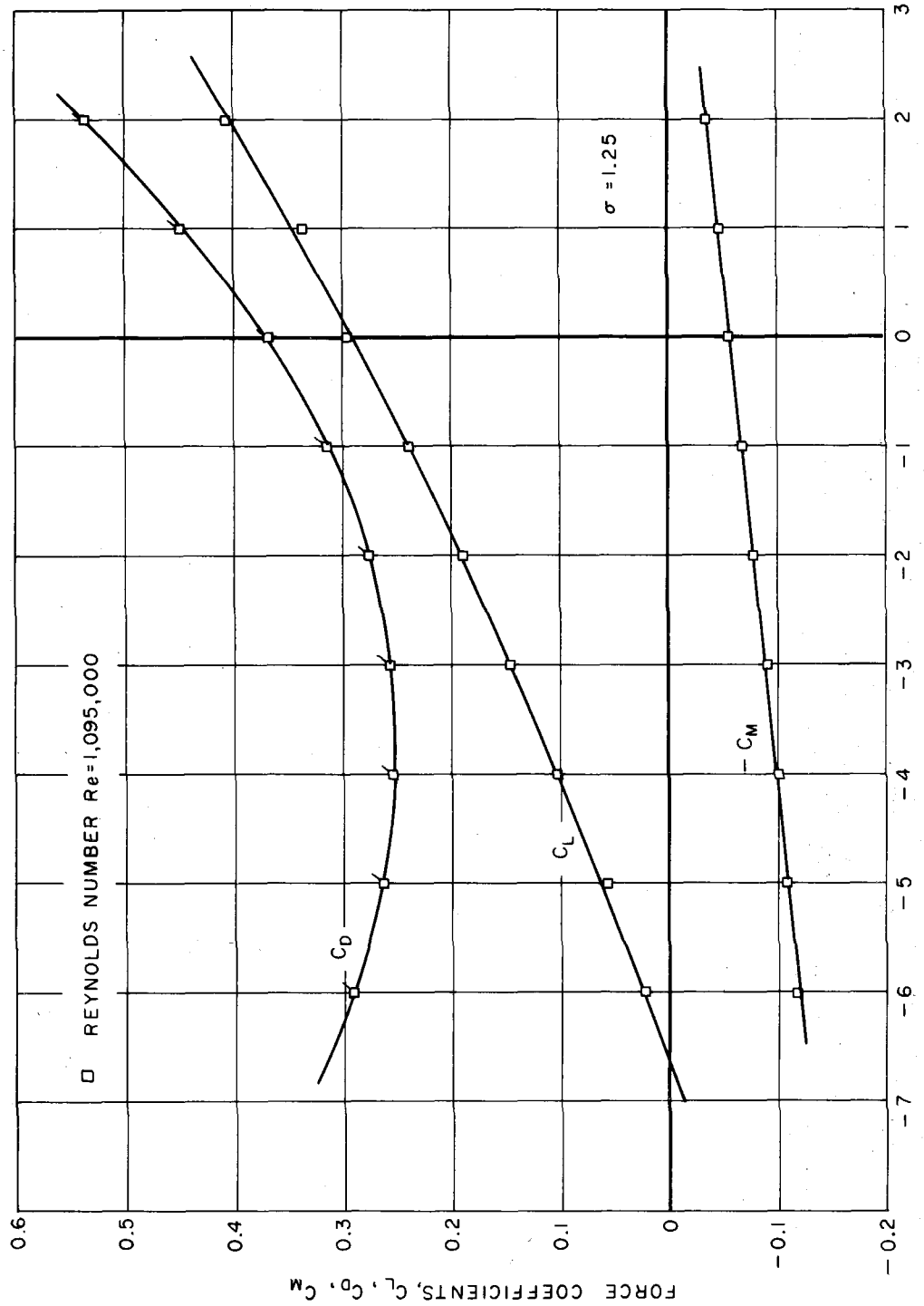

Fig. 47 - Force coefficients based on upstream velocity as a function of angle of attack for fully wetted turbine cascade of solidity σ = 1.25.

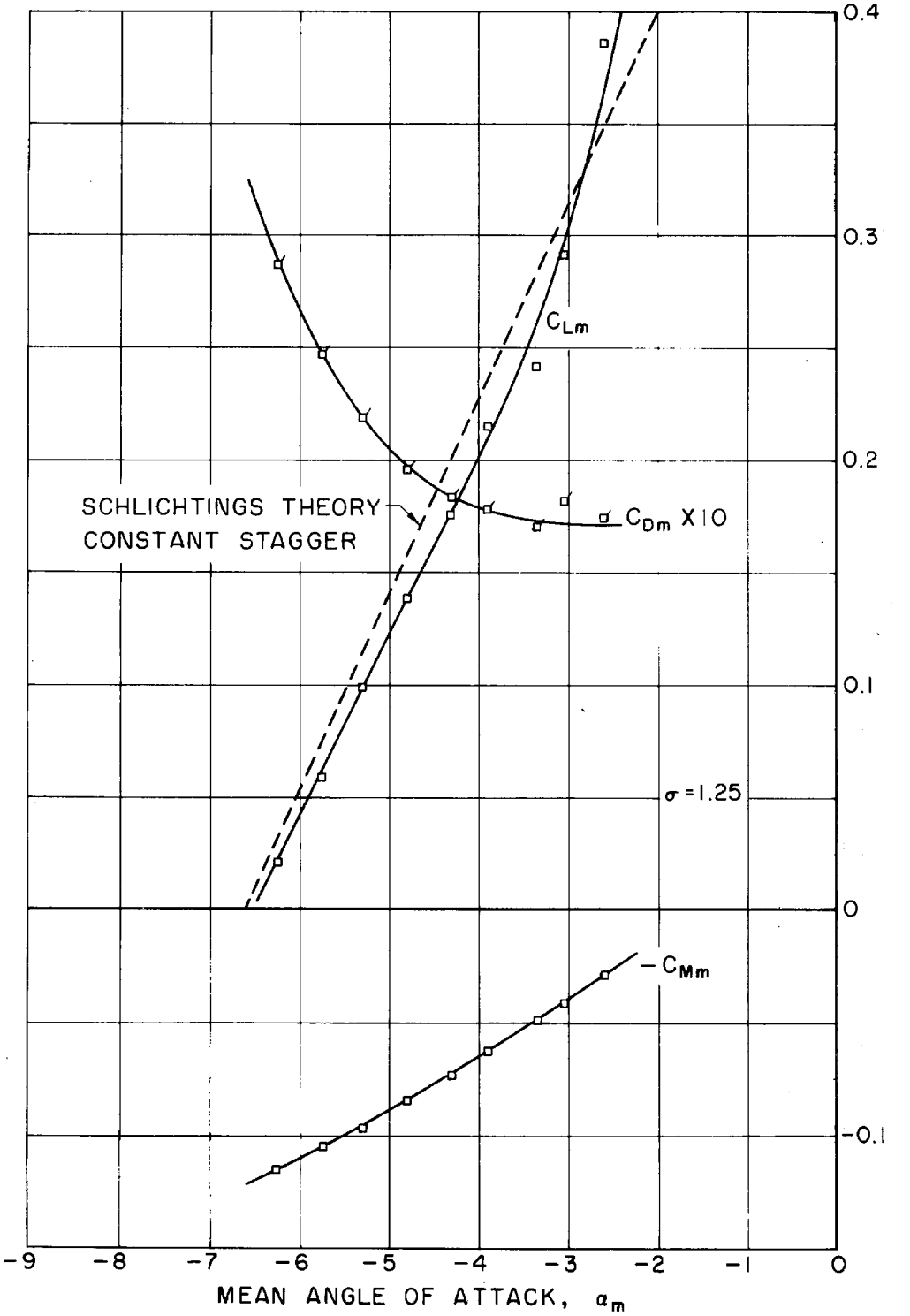

Fig. 48 - Force coefficients based on mean flow velocity as a function of the vector mean angle of attack for turbine cascade of solidity σ = 1.25.

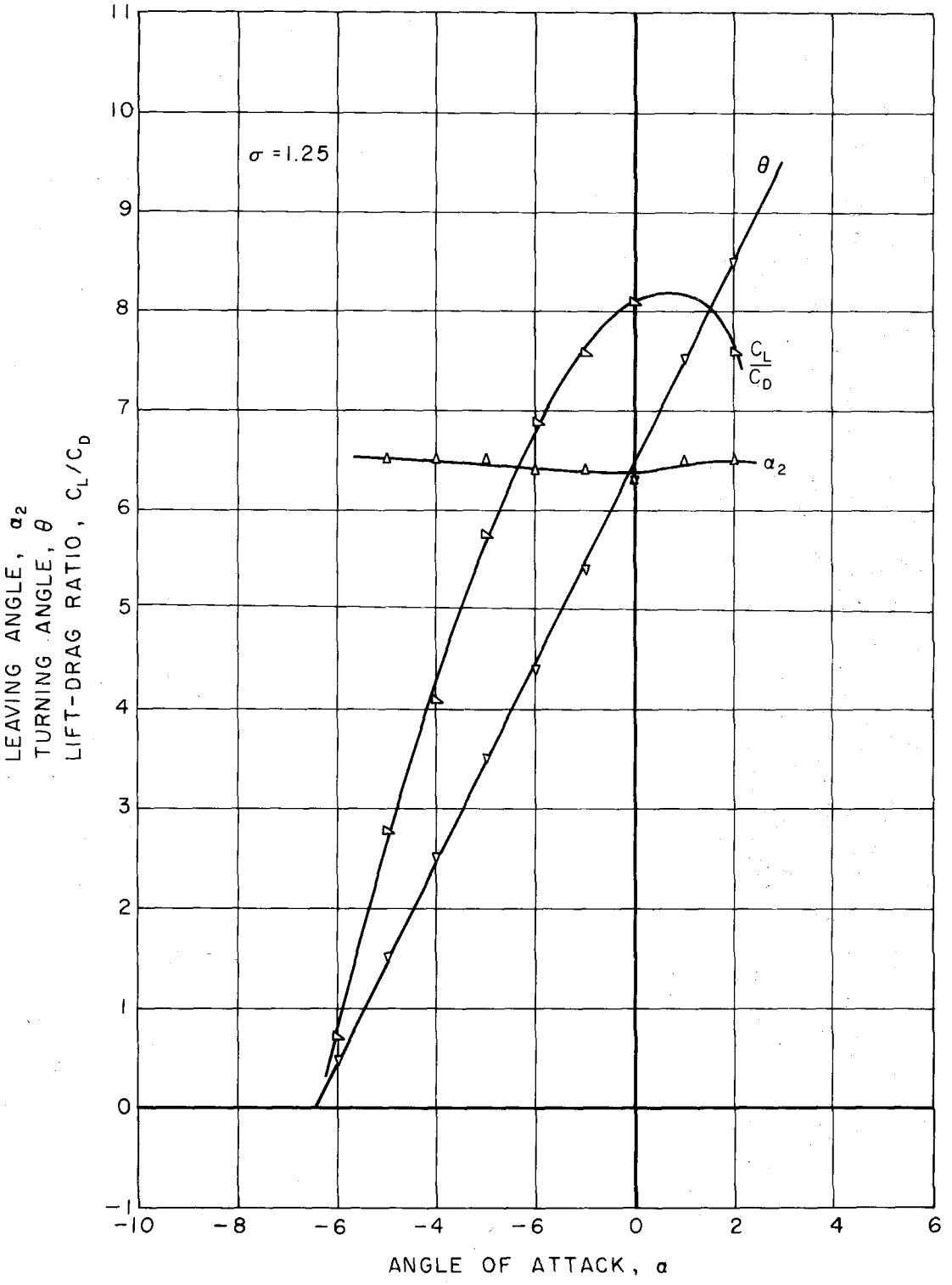

Fig. 49 - Lift-to-drag ratio, turning angle and leaving angle as a function of the angle of attack α for turbine cascade of solidity $\sigma = 1.25$.

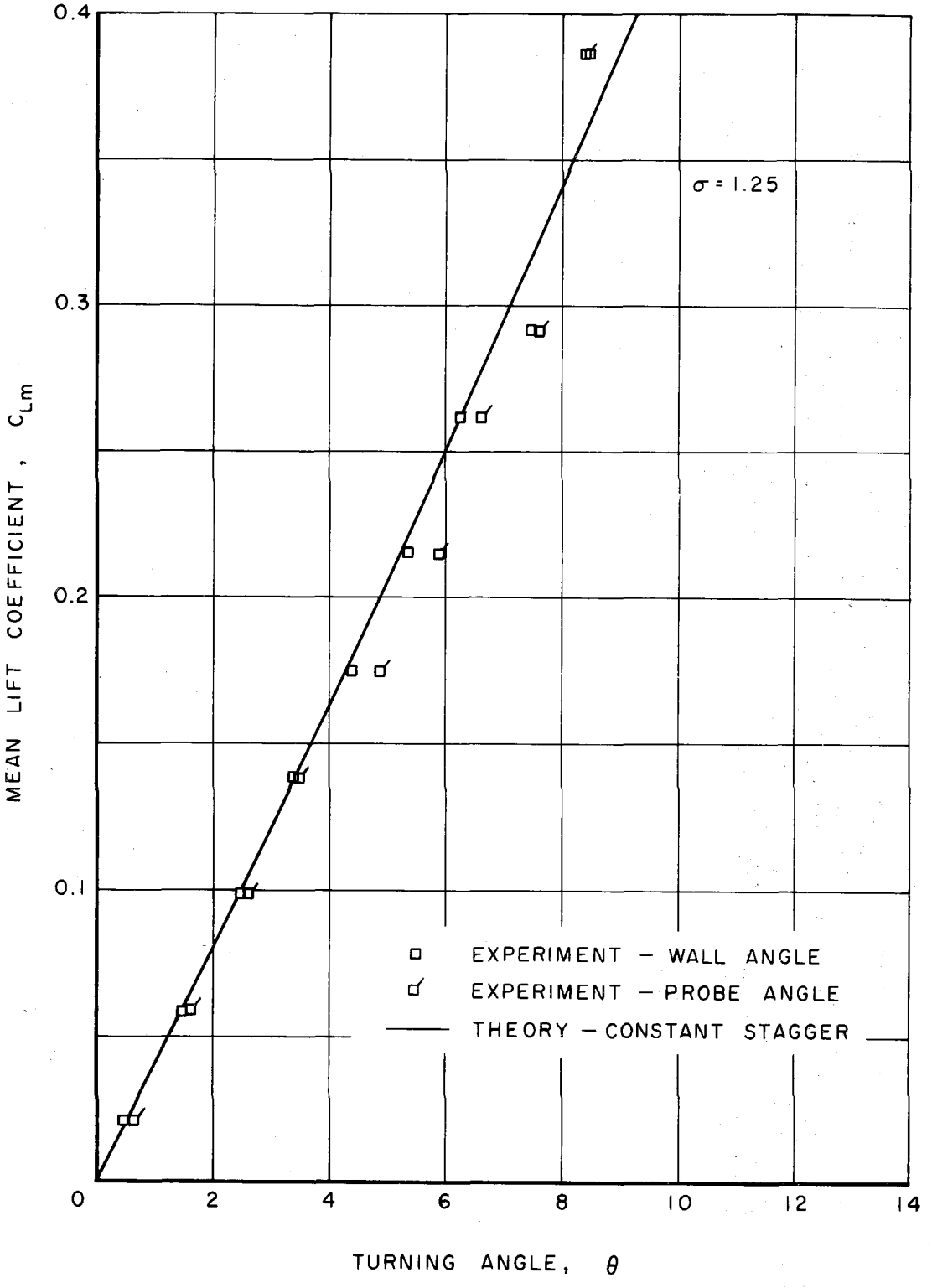

Fig. 50 - Comparison of the measured mean lift coefficient with turning angle as obtained from the wall angle and from probe measurements with theoretical values for a turbine cascade of solidity $\sigma = 1.25$.

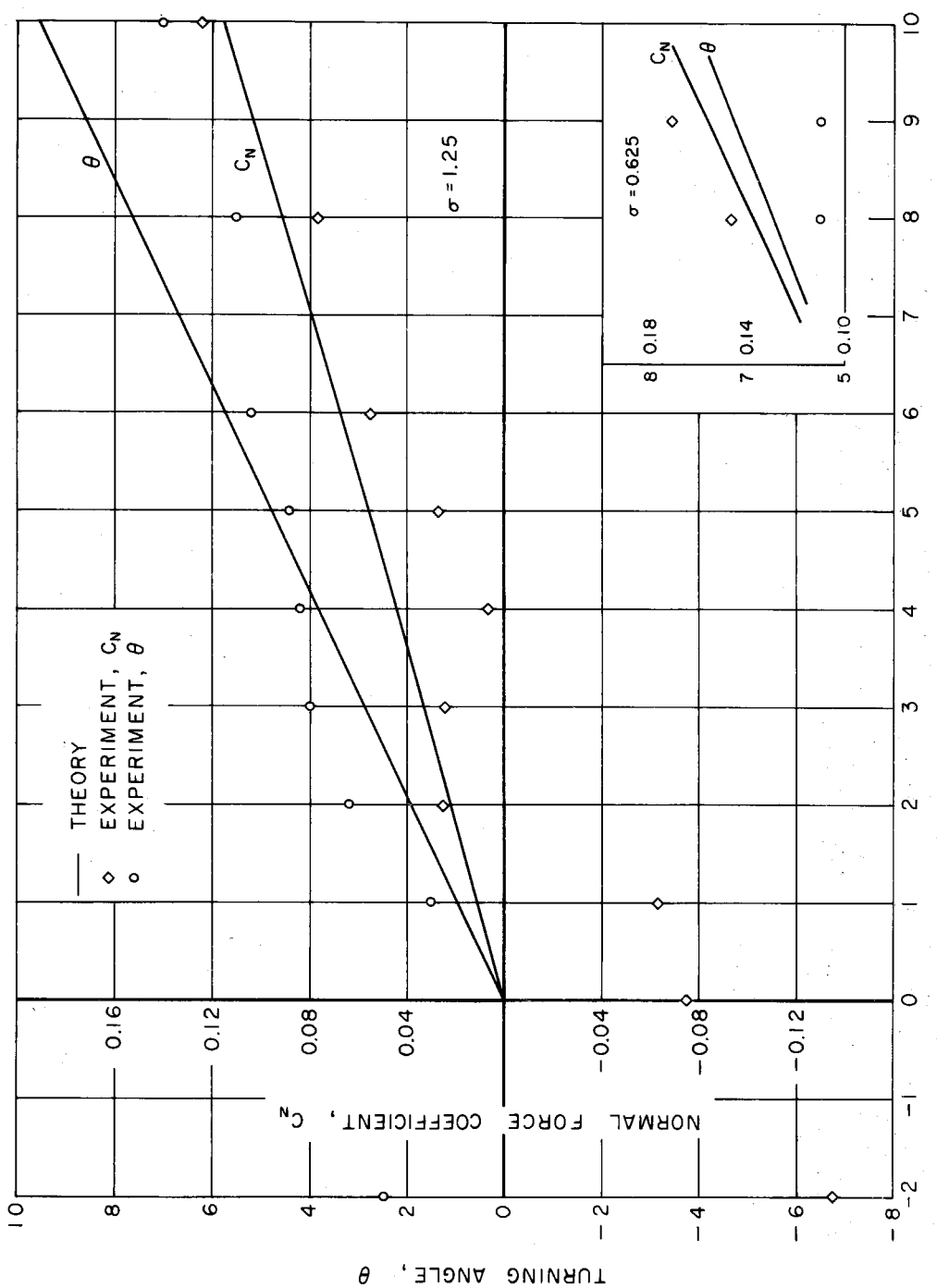

Fig. 51 - Comparison of normal force coefficient based on upstream velocity and the turning angle as a function of angle of attack α with theory for fully choked flow in a compressor cascade of solidity $\sigma = 1.25$. The insert shows this comparison for a solidity $\sigma = 0.625$.

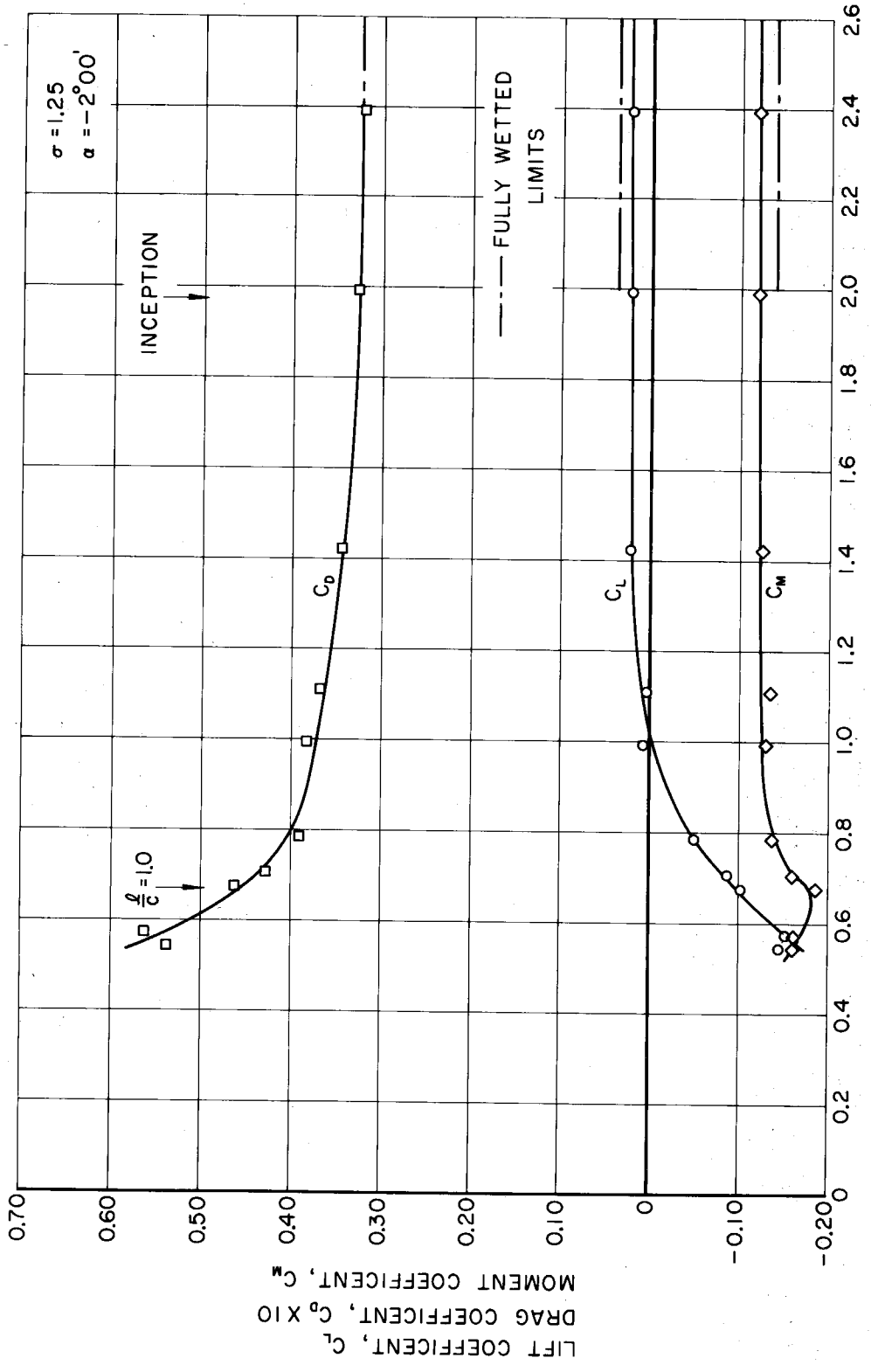

Fig. 52 - Variation of the force coefficients based on upstream velocity with the cavitation parameter K_v for an angle of attack of -2° in a compressor cascade of solidity $\sigma = 1.25$.

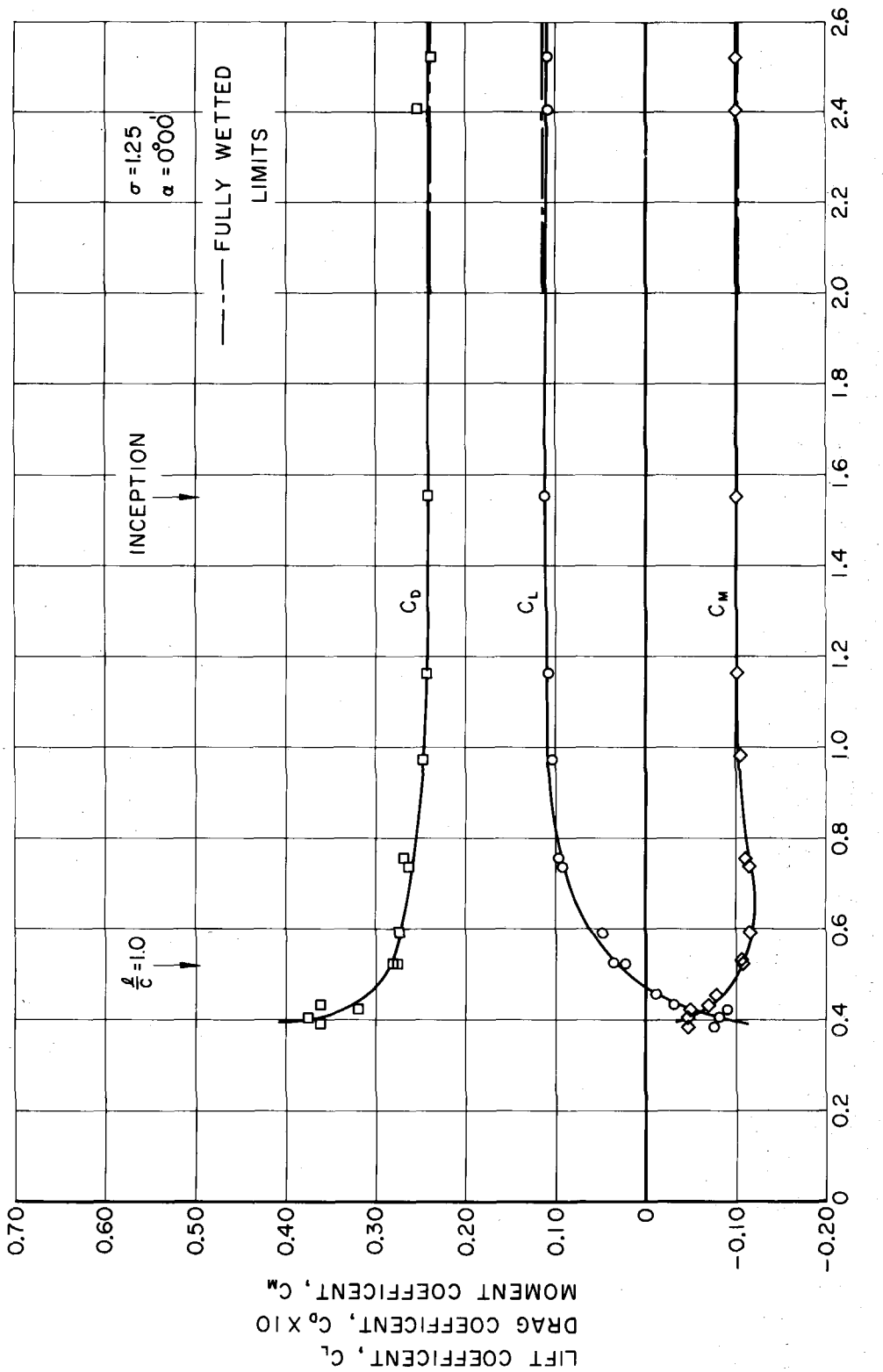

Fig. 53 - Variation of the force coefficients based on upstream velocity with the cavitation parameter K_v for an angle of attack of 0° in a compressor cascade of solidity $\sigma = 1.25$.

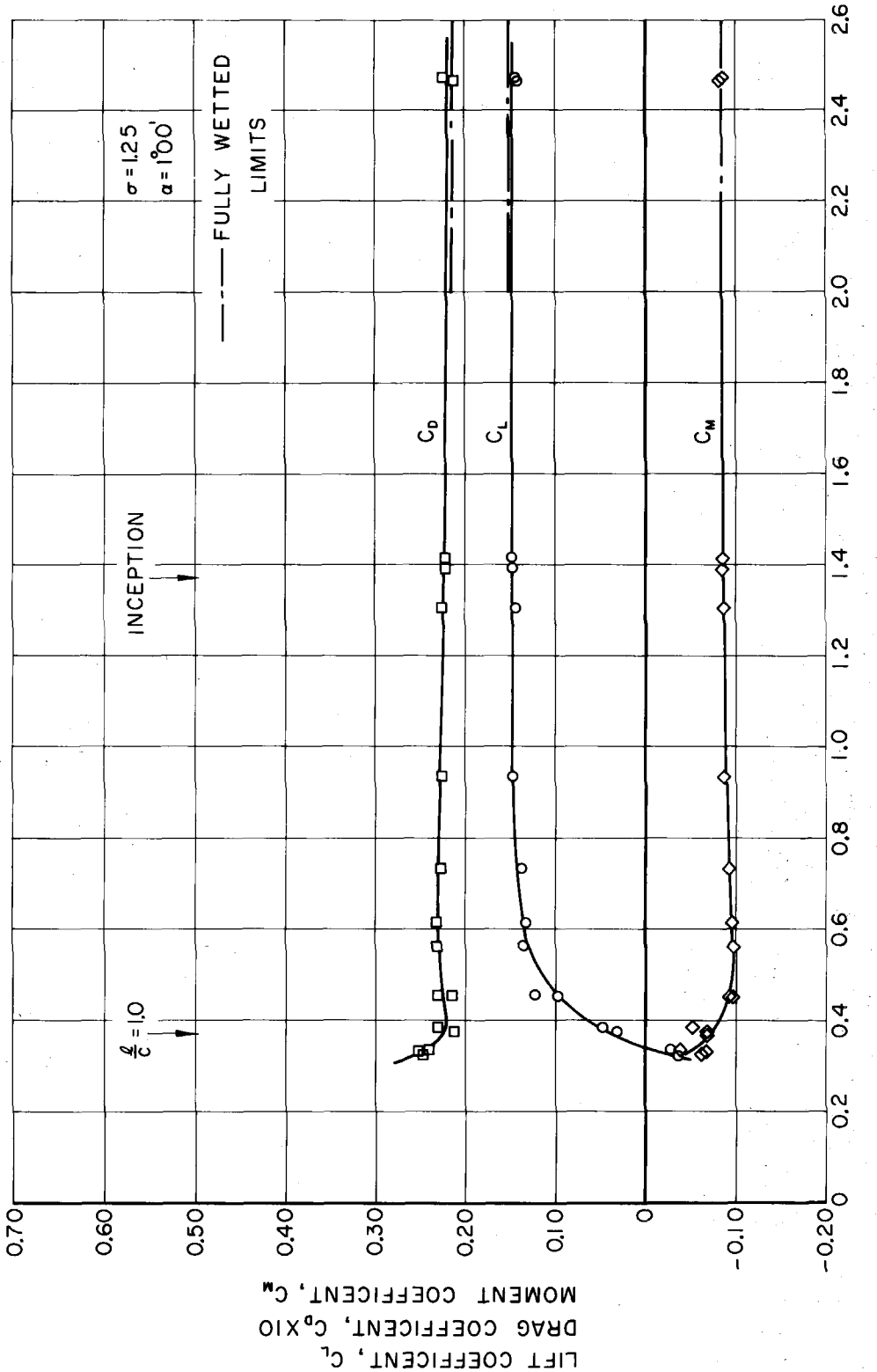

Fig. 54 - Variation of the force coefficients based on upstream velocity with the cavitation parameter K_v for an angle of attack of 1° in a compressor cascade of solidity σ = 1.25.

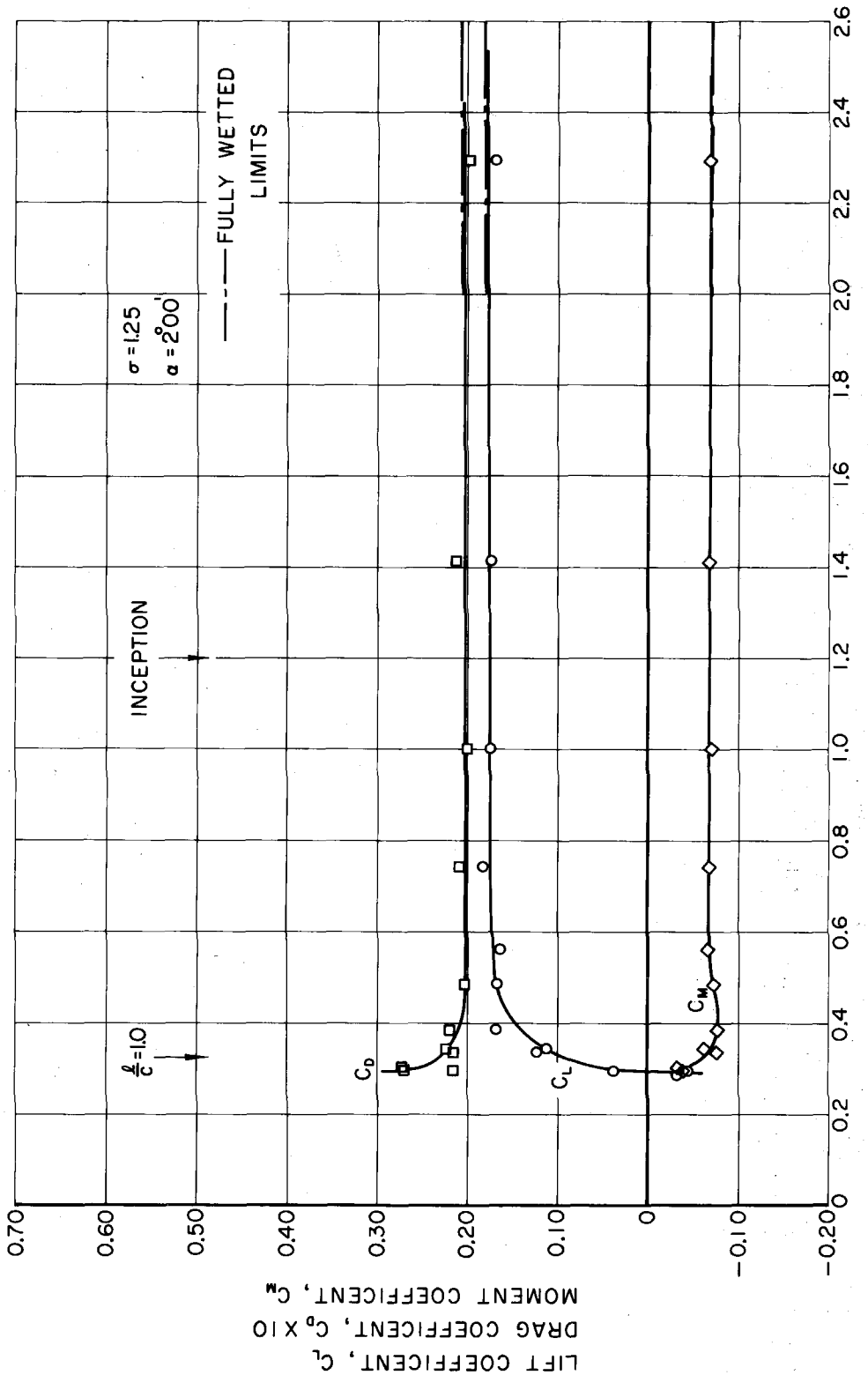

Fig. 55(a) - Variation of the force coefficients based on upstream velocity with the cavitation parameter K_v for an angle of attack of 2° in a compressor cascade of solidity σ = 1.25.

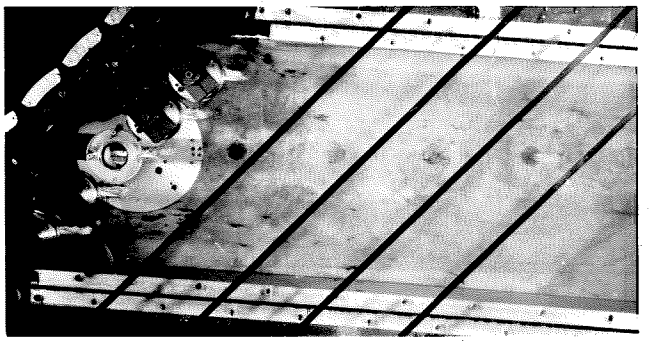

$K_v = 0.35$ $\theta = 3^o12'$

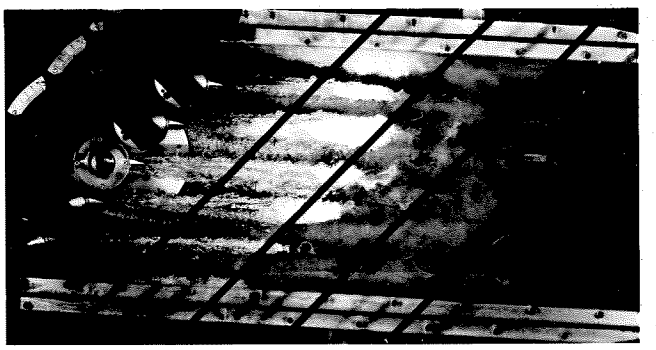

$K_v = 0.29$ $\theta = 3^o12'$

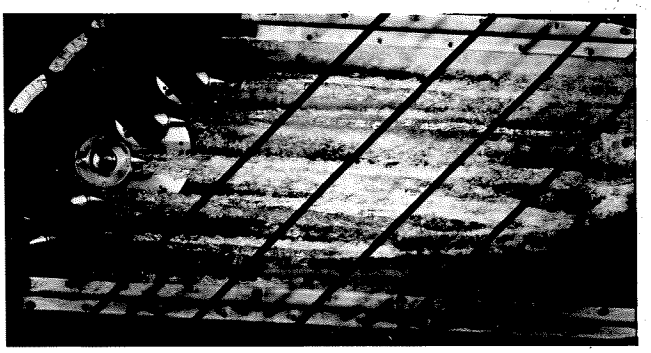

$K_v = 0.28$ $\theta = 3^o12'$

Fig. 55(b) - Cavitation occurring in a compressor cascade of solidity $\sigma = 1.25$ for various cavitation parameters K_v at an angle of attack of 2^o.

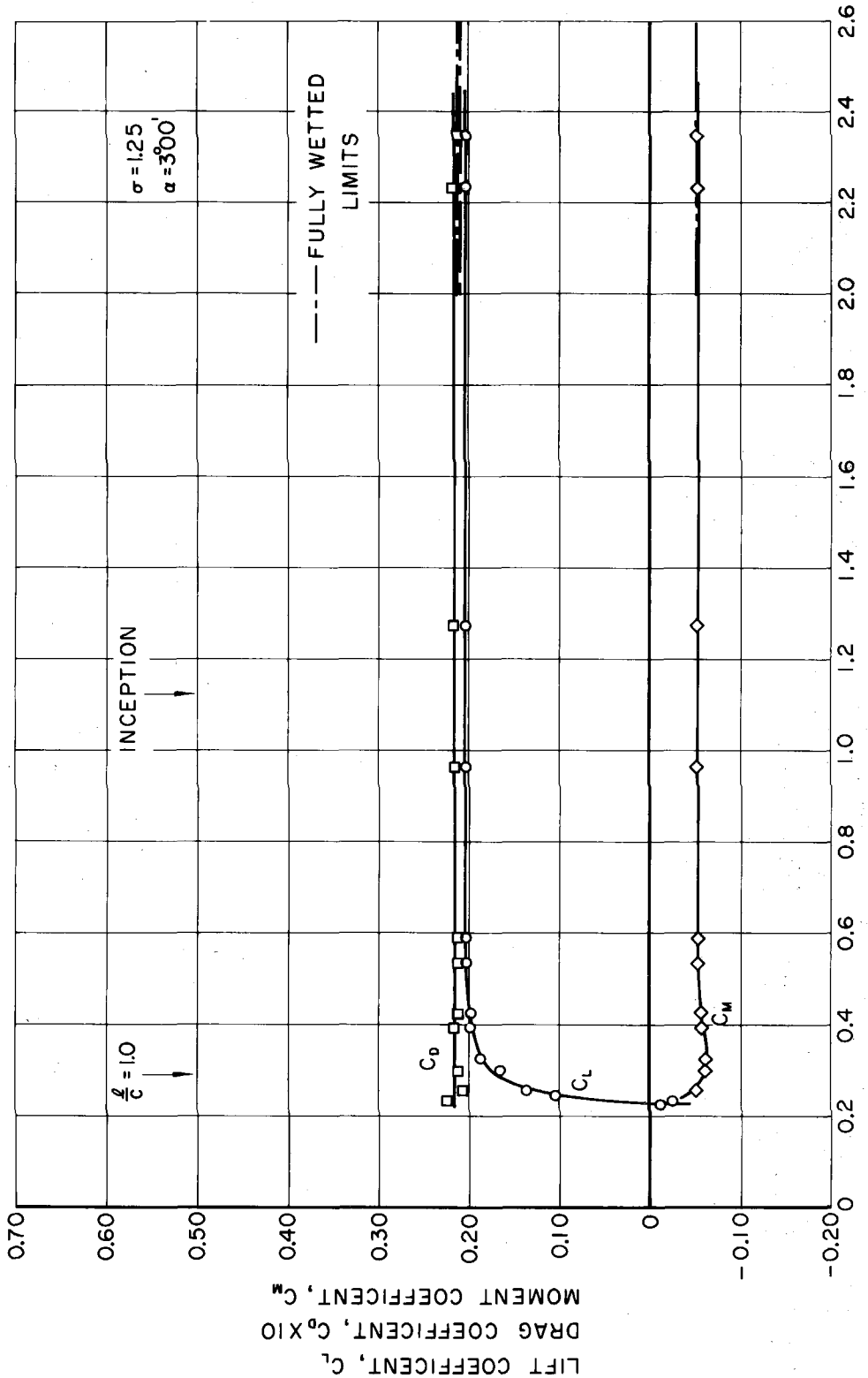

Fig. 56 - Variation of the force coefficients based on upstream velocity with the cavitation parameter K_v for an angle of attack of 3° in a compressor cascade of solidity $\sigma = 1.25$.

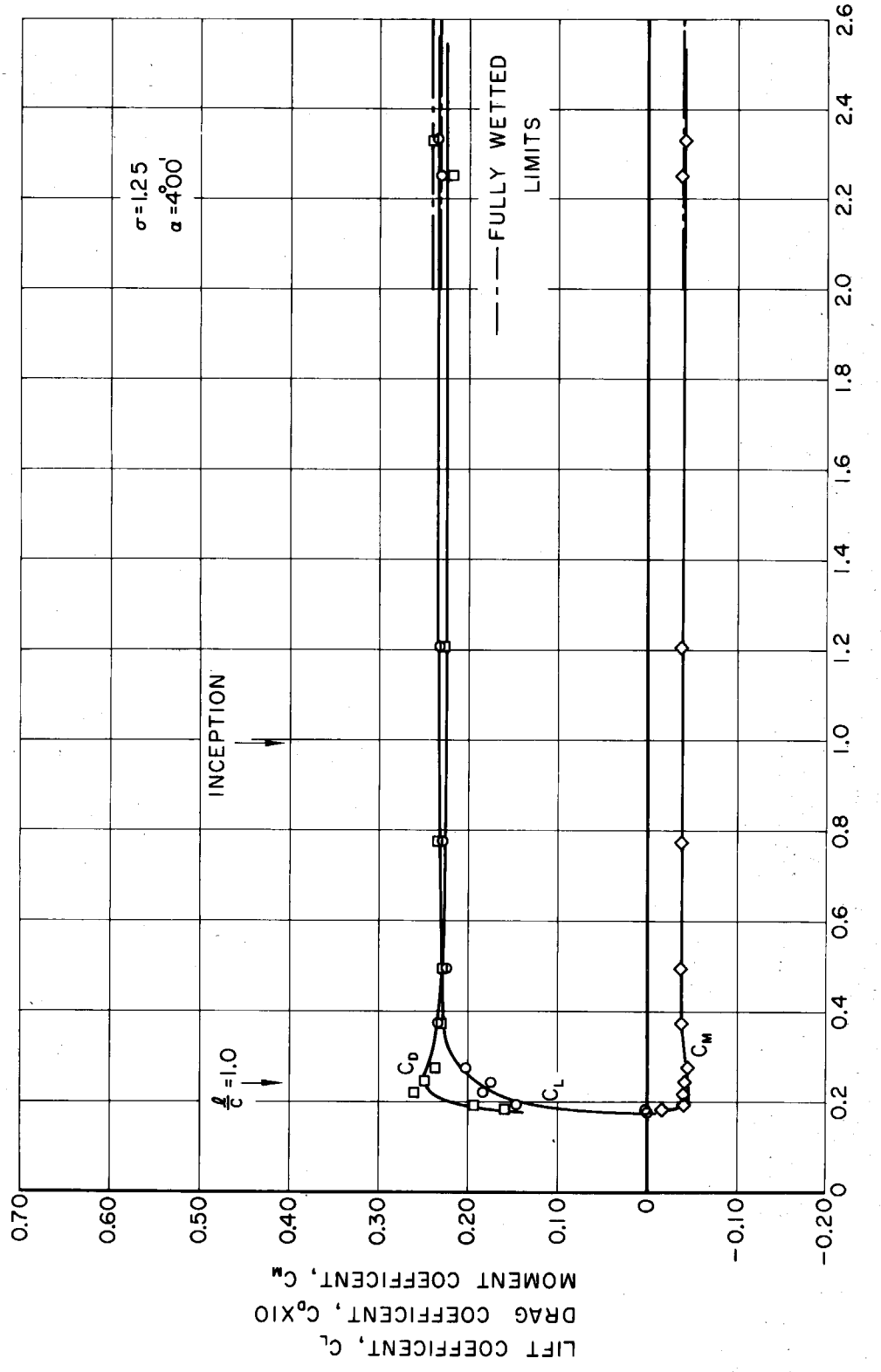

Fig. 57 - Variation of the force coefficients based on upstream velocity with the cavitation parameter K_v for an angle of attack of 4° in a compressor cascade of solidity σ = 1.25.

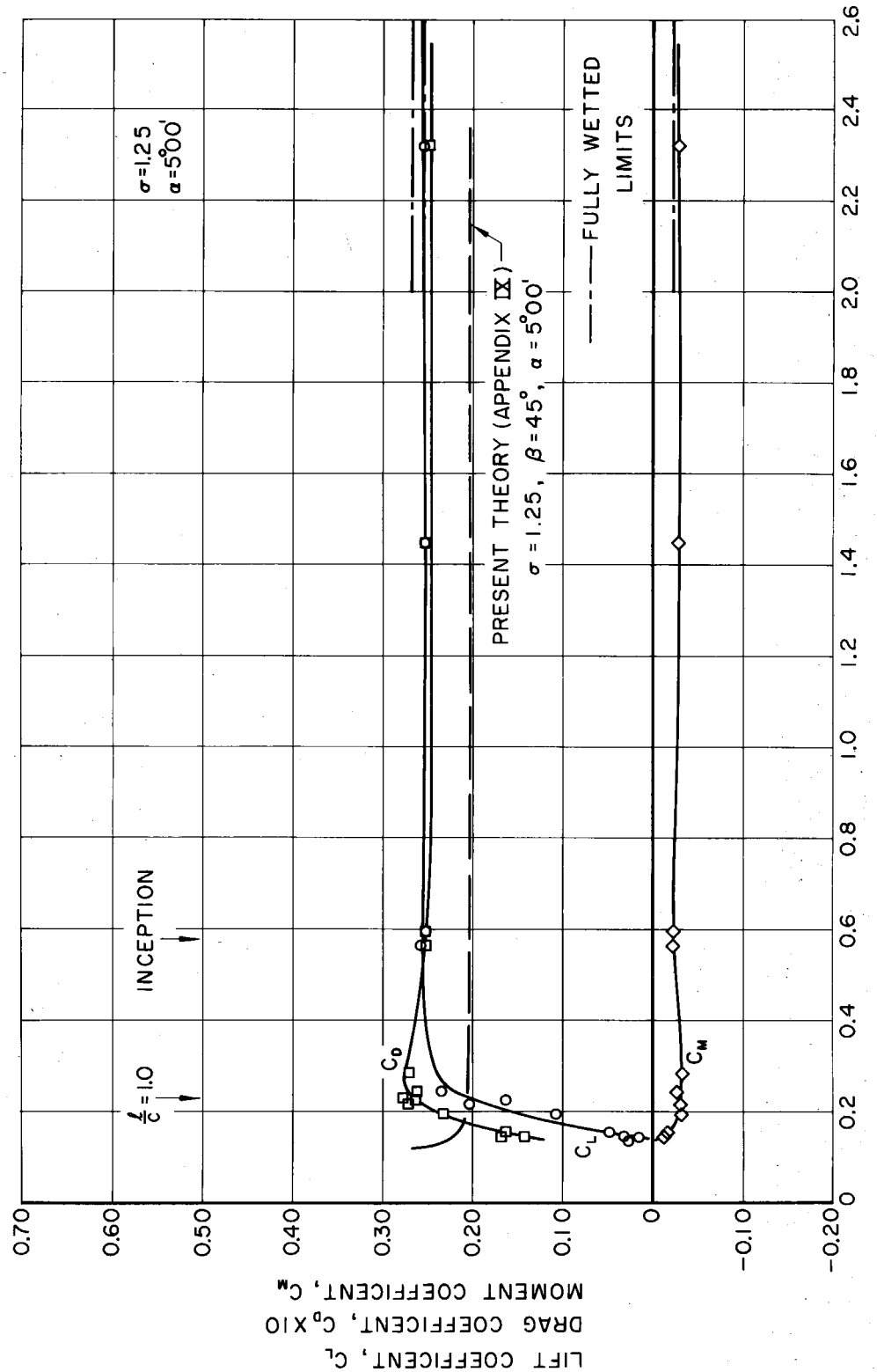

Fig. 58(a) - Variation of the force coefficients based on upstream velocity with the cavitation parameter K_v for an angle of attack of 5° in a compressor cascade of solidity σ = 1.25.

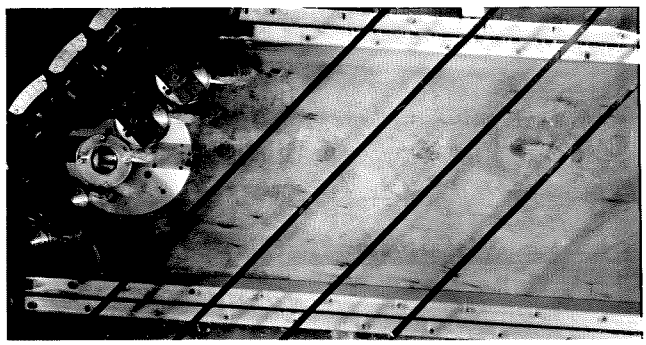

$K_v = 0.26$ $\theta = 4^o24'$

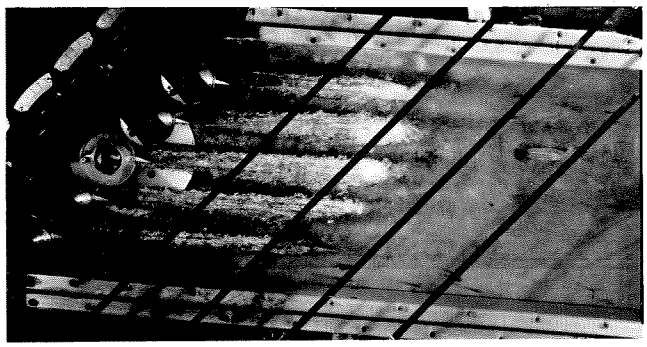

$K_v = 0.15$ $\theta = 4^o24'$

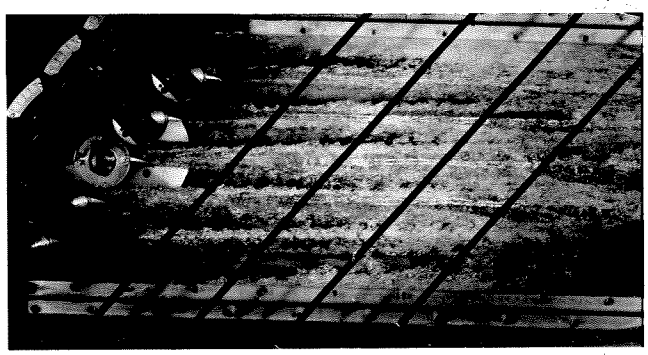

$K_v = 0.13$ $\theta = 4^o24'$

Fig. 58(b) - Cavitation occurring in a compressor cascade of solidity $\sigma = 1.25$ for various cavitation parameters K_v at an angle of attack of 5^o.

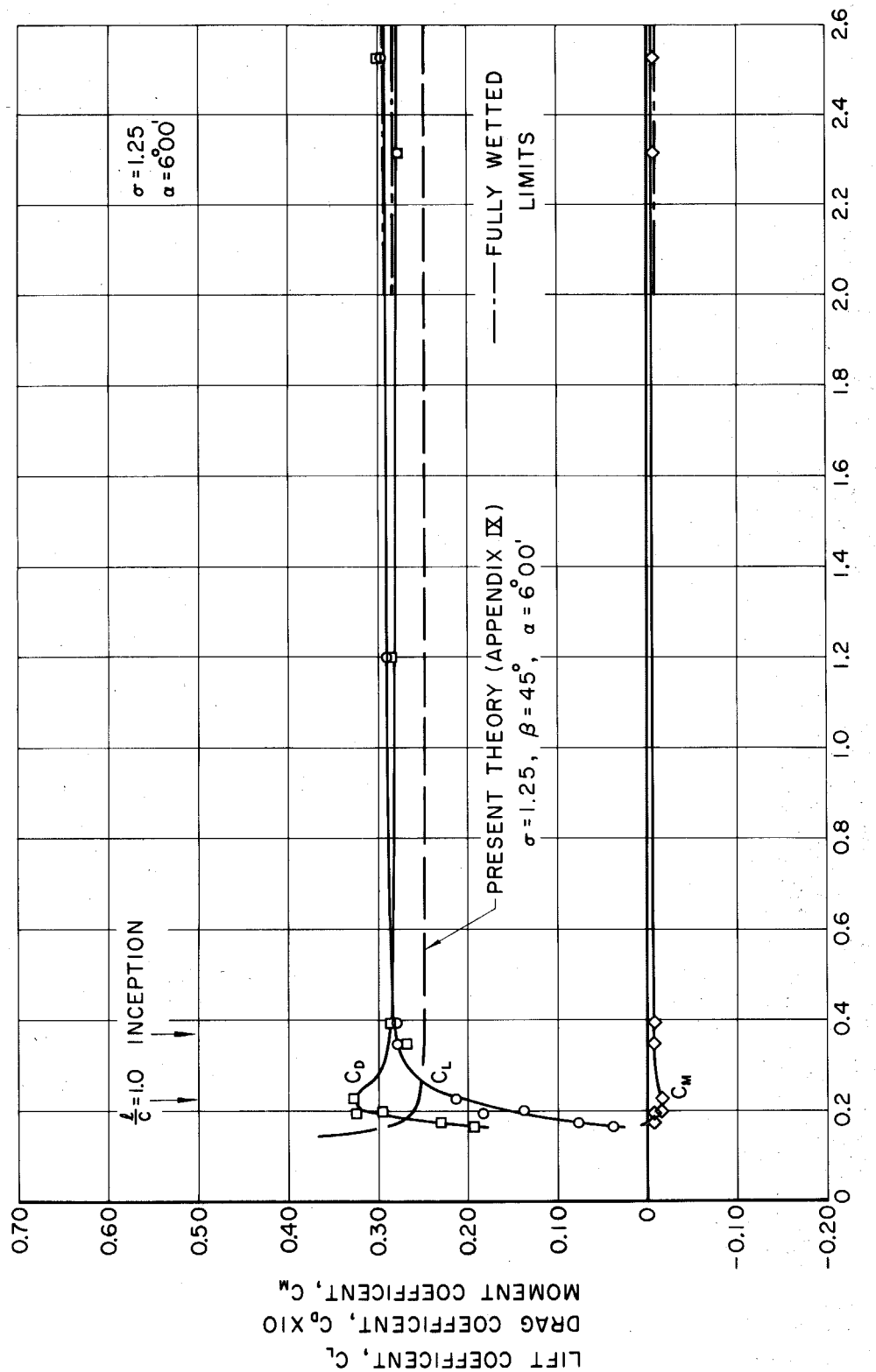

Fig. 59 - Variation of the force coefficients based on upstream velocity with the cavitation parameter K_v for an angle of attack of 6° in a compressor cascade of solidity $\sigma = 1.25$.

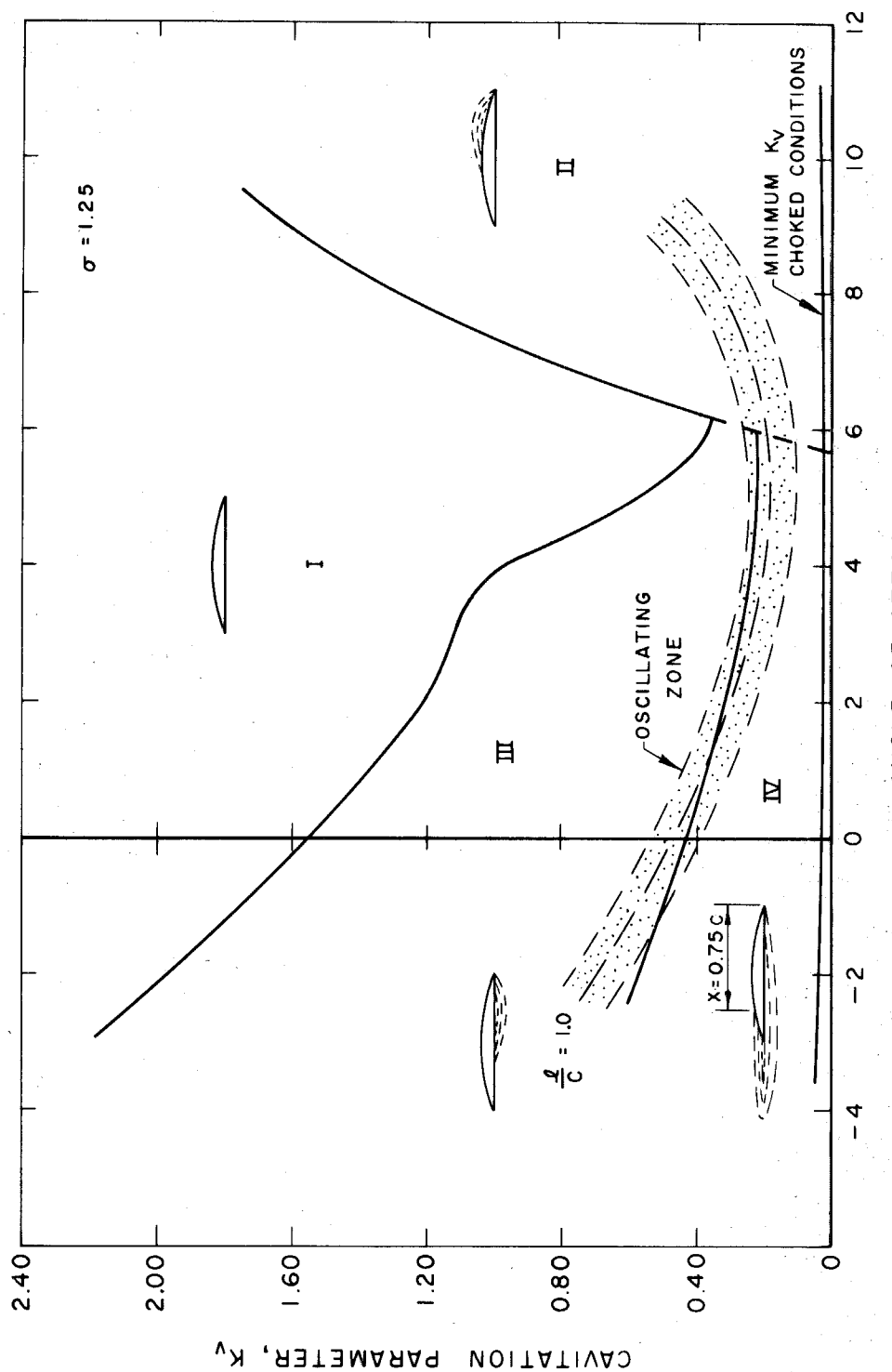

Fig. 60 - Cavitation diagram for a plano-convex hydrofoil in a compressor cascade of solidity $\sigma = 1.25$. Region I - Fully wetted region. Region II - Cavitation on upper surface only. Region III - Cavitation on lower surface only. Region IV - Cavitation occurs on both surfaces.

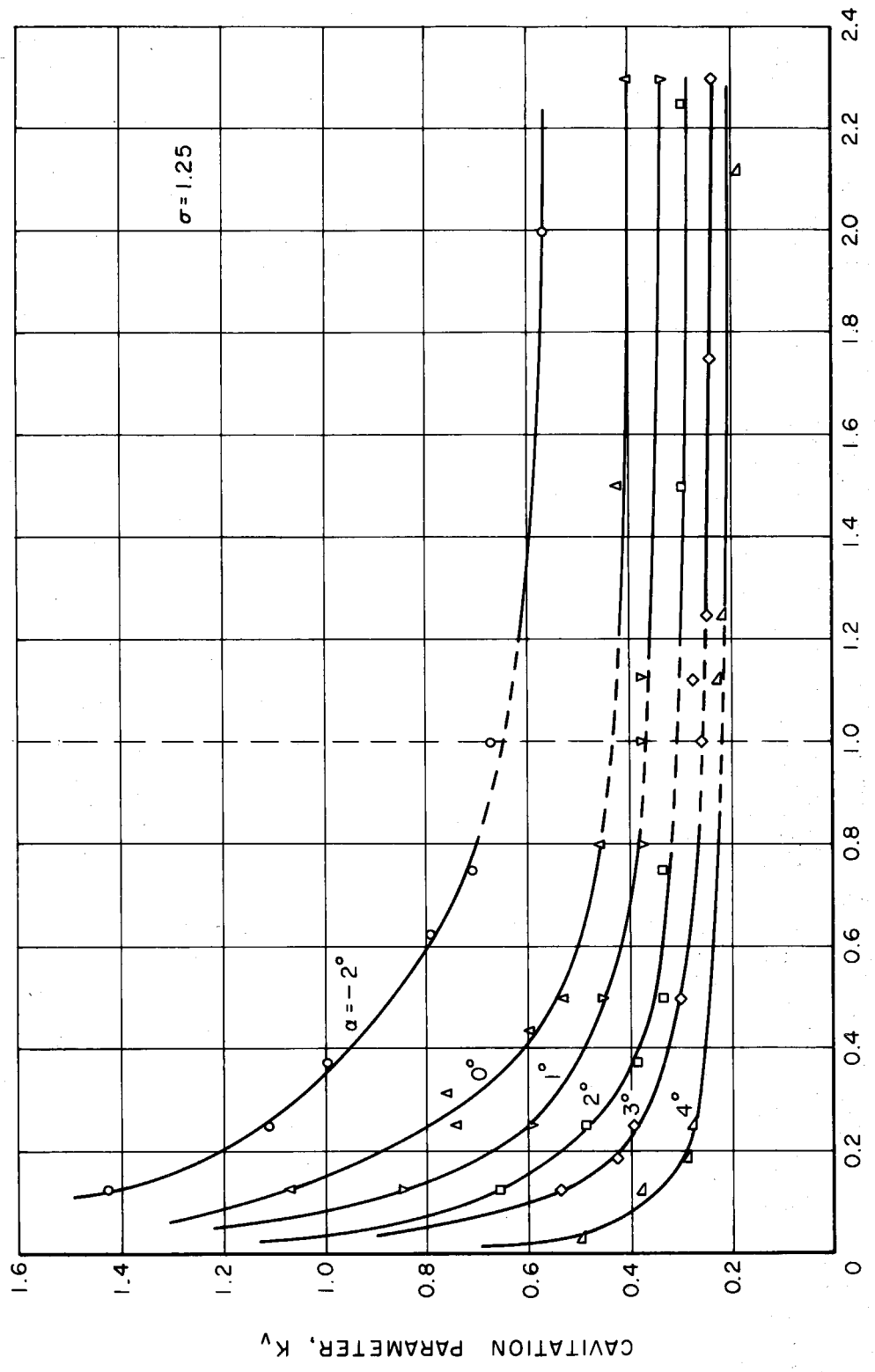

Fig. 61 - Cavitation parameter K_v as a function of the length of cavity to chord ratio for various angles of attack in a compressor cascade of solidity $\sigma = 1.25$.

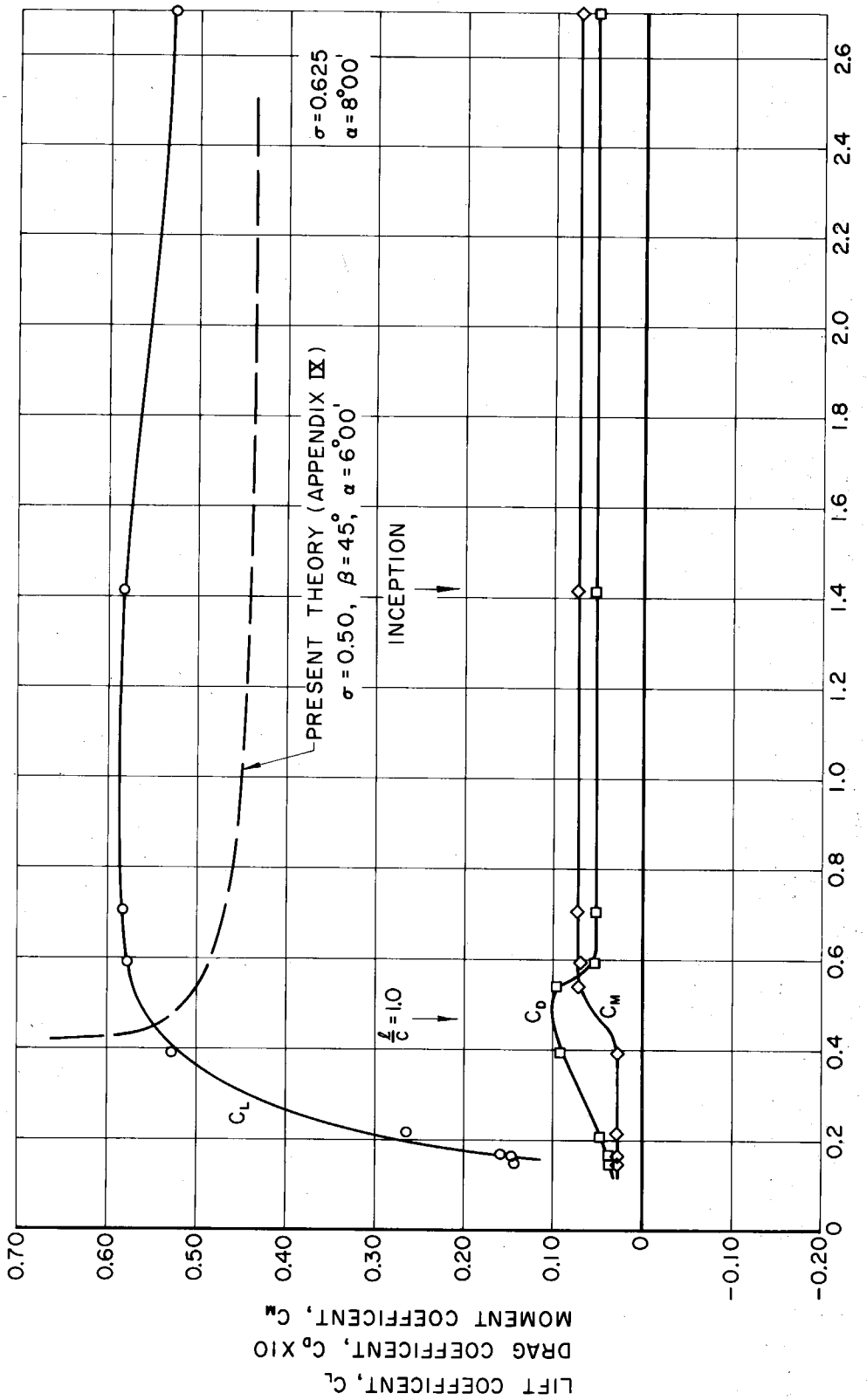

Fig. 62(a) - Variation of the force coefficients based on upstream velocity with the cavitation parameter K_v for an angle of attack of 8^o in a compressor cascade of solidity $\sigma = 0.625$.

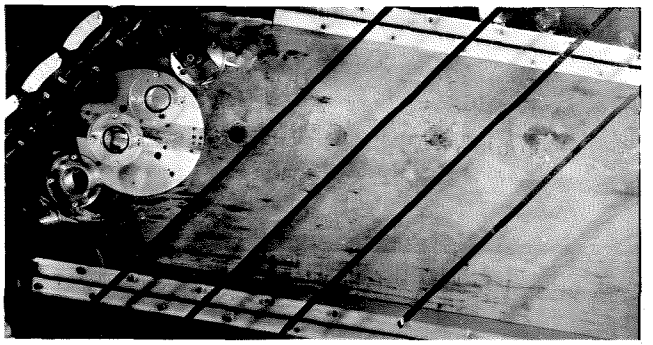

$K_v = 0.39$ $\theta = 9^{\circ}06'$

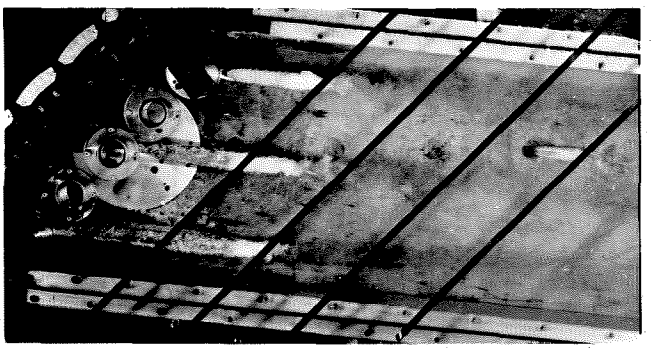

$K_v = 0.17$ $\theta = 5^{\circ}30'$

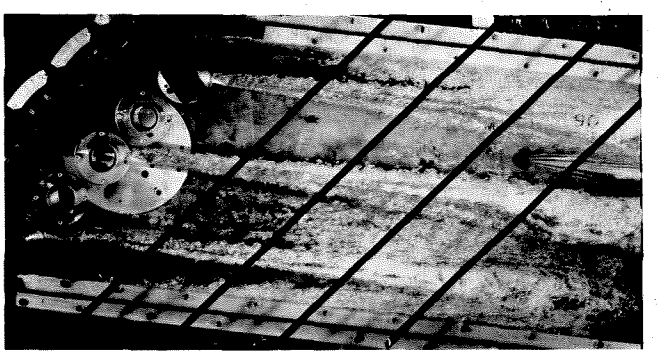

$K_v = 0.15$ $\theta = 5^{\circ}30'$

Fig. 62(b) - Cavitation occurring in a compressor cascade of solidity $\sigma = 0.625$ for various cavitation parameters K_v at an angle of attack of 8°.

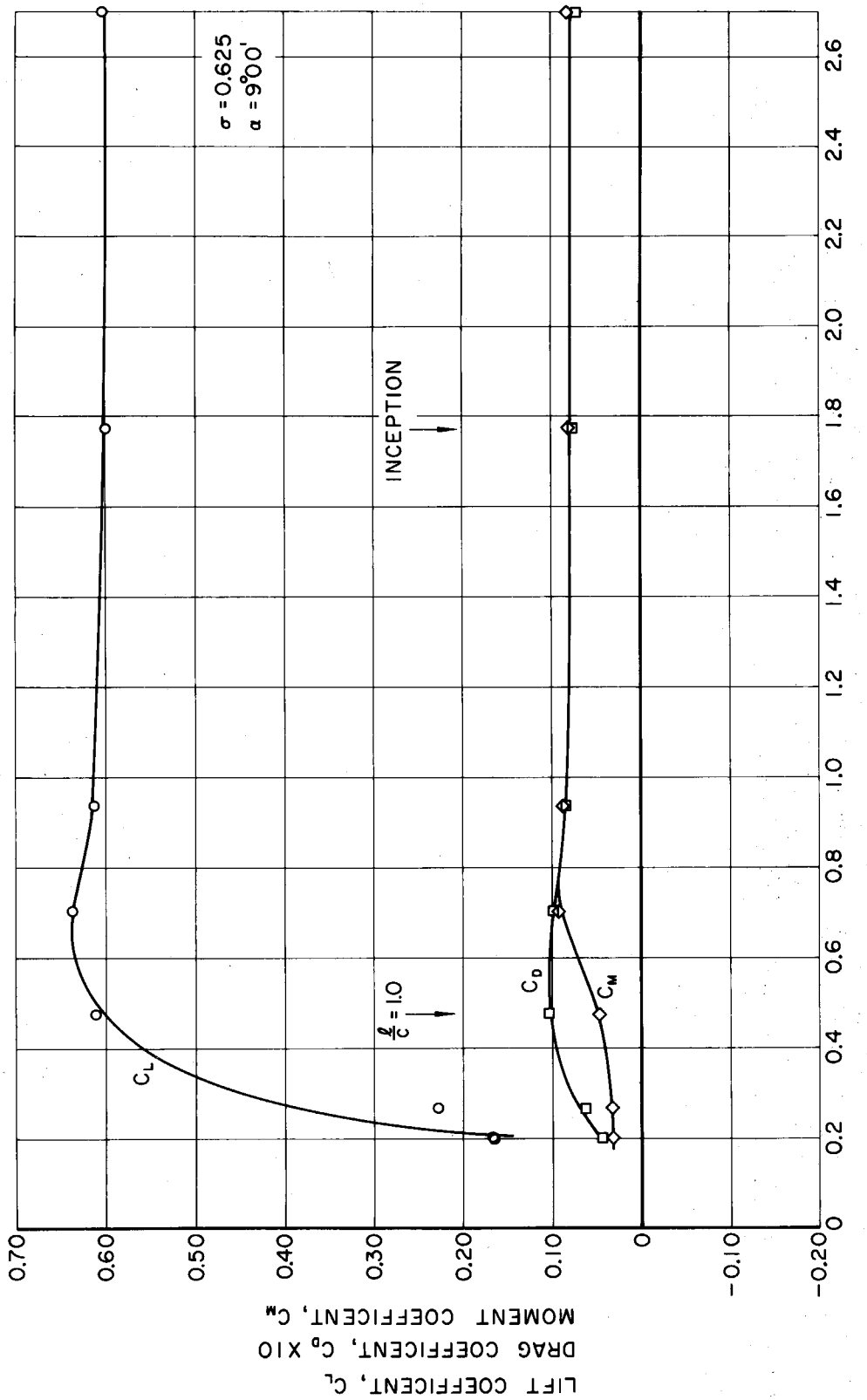

Fig. 63(a) - Variation of the force coefficients based on upstream velocity with the cavitation parameter K_v for an angle of attack of 9° in a compressor cascade of solidity σ = 0.625.

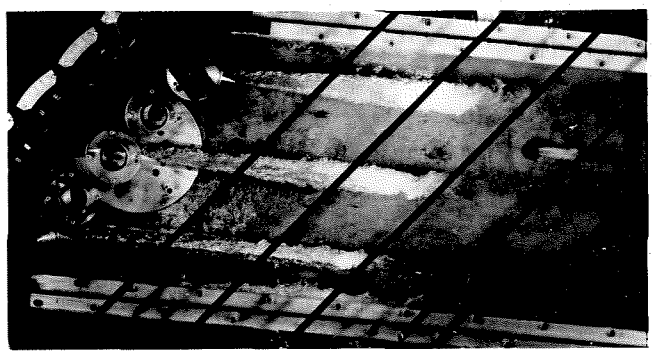

$K_v = 0.20$ $\theta = 5^{o}30'$

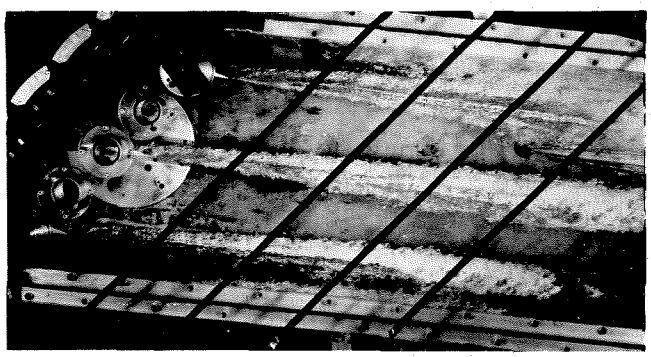

$K_v = 0.19$ $\theta = 5^{o}30'$

Fig. 63(b) - Cavitation occurring in a compressor cascade of solidity $\sigma = 0.625$ for various cavitation parameters K_v at an angle of attack of 9^{o}.

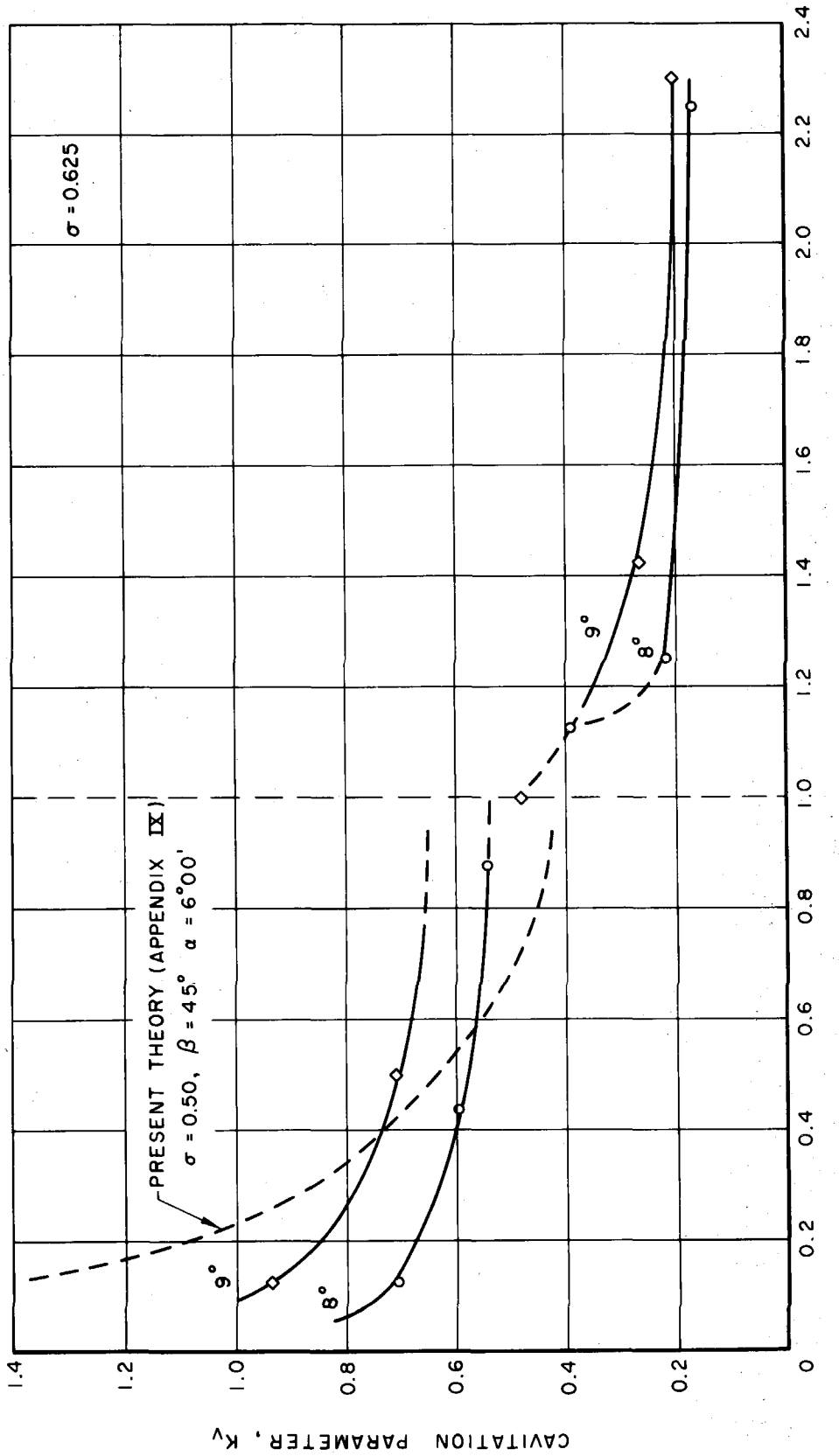

Fig. 64 - Cavitation parameter K_v as a function of the length of cavity to chord ratio for two angles of attack in a compressor cascade of solidity $\sigma = 0.625$.

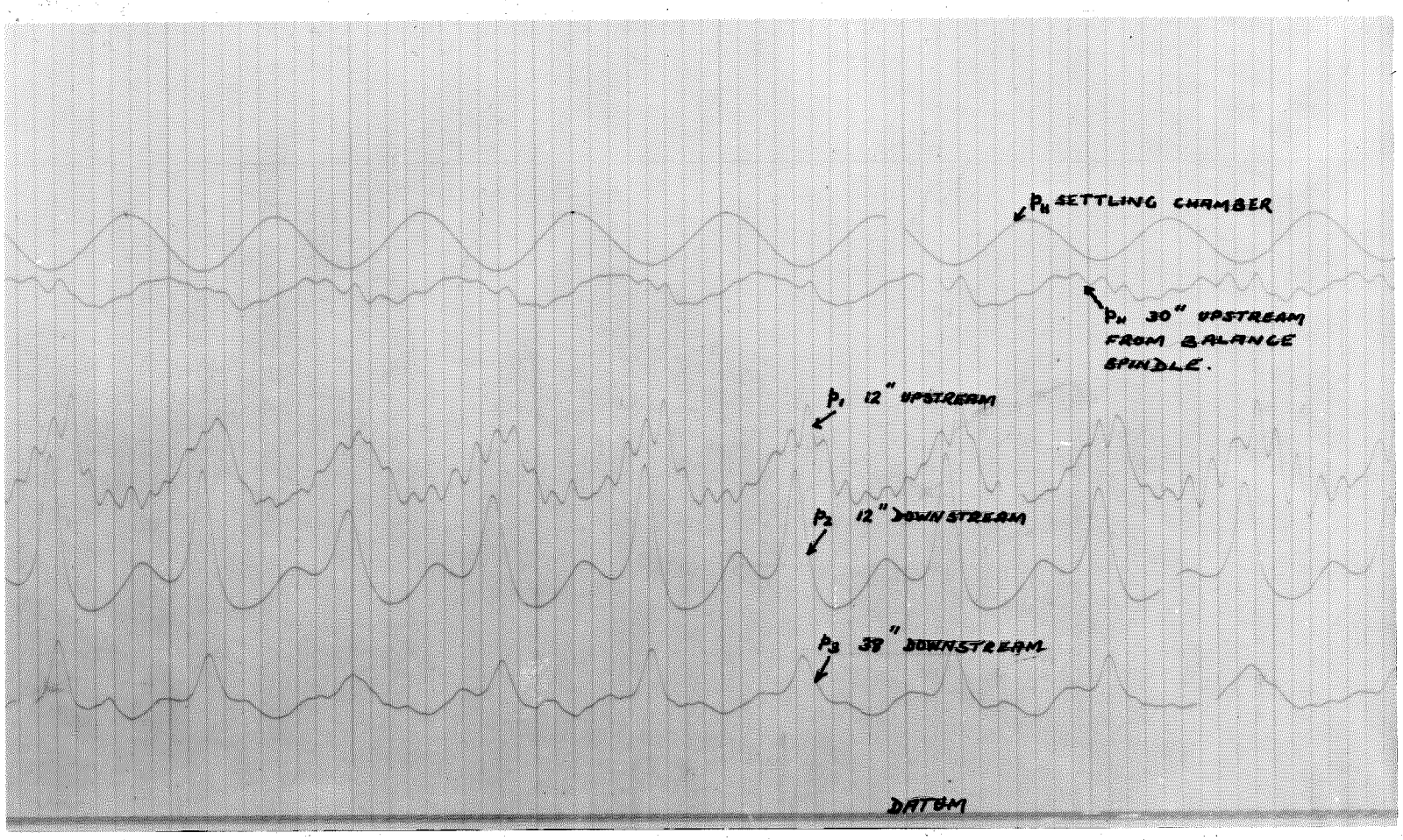

Fig. 65 - Traces of the fluctuating pressures measured at various points in the tunnel under conditions of maximum oscillations for a compressor cascade of solidity $\sigma = 0.625$. The tunnel speed is 31.58 ft/sec with a cavitation parameter $K_v = 0.63$. The model is at an angle of attack of 9^o. The fundamental frequency is 12.5 cycles/sec.

APPENDIX I

NOTATION AND SYMBOLS

A, B, C	constants
A	plan form area = (s x c)
c	chord length
C_D	drag coefficient = $\frac{D}{A\rho V^2/2}$
C_L	lift coefficient = $\frac{L}{A\rho V^2/2}$
C_M	moment coefficient = $\frac{M}{Ac\rho V^2/2}$
C_P	pressure coefficient = $\frac{\Delta p}{\rho V^2/2}$
D	drag force on model
f	frequency of oscillations
i	$\sqrt{-1}$
K	corrected cavitation number $\frac{p - p_k}{\rho V^2/2}$
K_v	cavitation number based on vapor pressure $\frac{p - p_v}{\rho V^2/2}$
ℓ	cavity length
L	lift force on model
M	moment on model about center of section
p	tunnel static pressure
p_k	measured cavity pressure

p_v	vapor pressure of water
R	radius of circular surface of model
R_e	Reynolds number = $\frac{Vc}{\nu}$
S	span
t	thickness of hydrofoil
V	tunnel velocity
u, v	velocity components in x, y directions
w	u - iv, complex velocity function
z	x + iy, complex physical plane
α	angle of attack measured from chord line
β	stagger angle, angle between normal to chord line and cascade axis
γ	cascade angle, angle between axis of cascade and normal to upstream velocity
δ	deviation angle, angle between exit flow direction and tangent to circular surface at the trailing edge
λ	distance of center of pressure from leading edge
ν	kinematic viscosity of water
θ	turning angle measured between upstream flow and downstream flow directions
φ, a	transformation parameters, defined in text
ψ, n	auxiliary functions, defined in text

ρ	density of water
σ	solidity, ratio of chord to spacing
ζ	$\xi + i\eta$, auxiliary complex plane
$( )_1$	denotes upstream conditions
$( )_2$	downstream conditions
$( )_m$	mean conditions
$( )_h$	homogeneous solution
$( )'$	perturbation components
$\overline{( )}$	complex conjugate quantity

APPENDIX II

TARE FORCE CORRECTIONS FOR ISOLATED HYDROFOIL TESTS

Presented here are the results of the tests carried out to determine the tare forces acting on the hydrofoil mounting disk. The results have been reduced to coefficient form to facilitate their application to the test data.

Fig. A2.1 shows the lift force acting on the disk as a function of the cavitation number for different angles of attack. Fig. A2.2 indicates the behavior of the drag force and Fig. A2.3 illustrates the tare force corrections for lift, drag and moment in fully wetted flow, as a function of angle of attack.

The detailed method for obtaining these results, as previously mentioned, is reported in Reference 14.

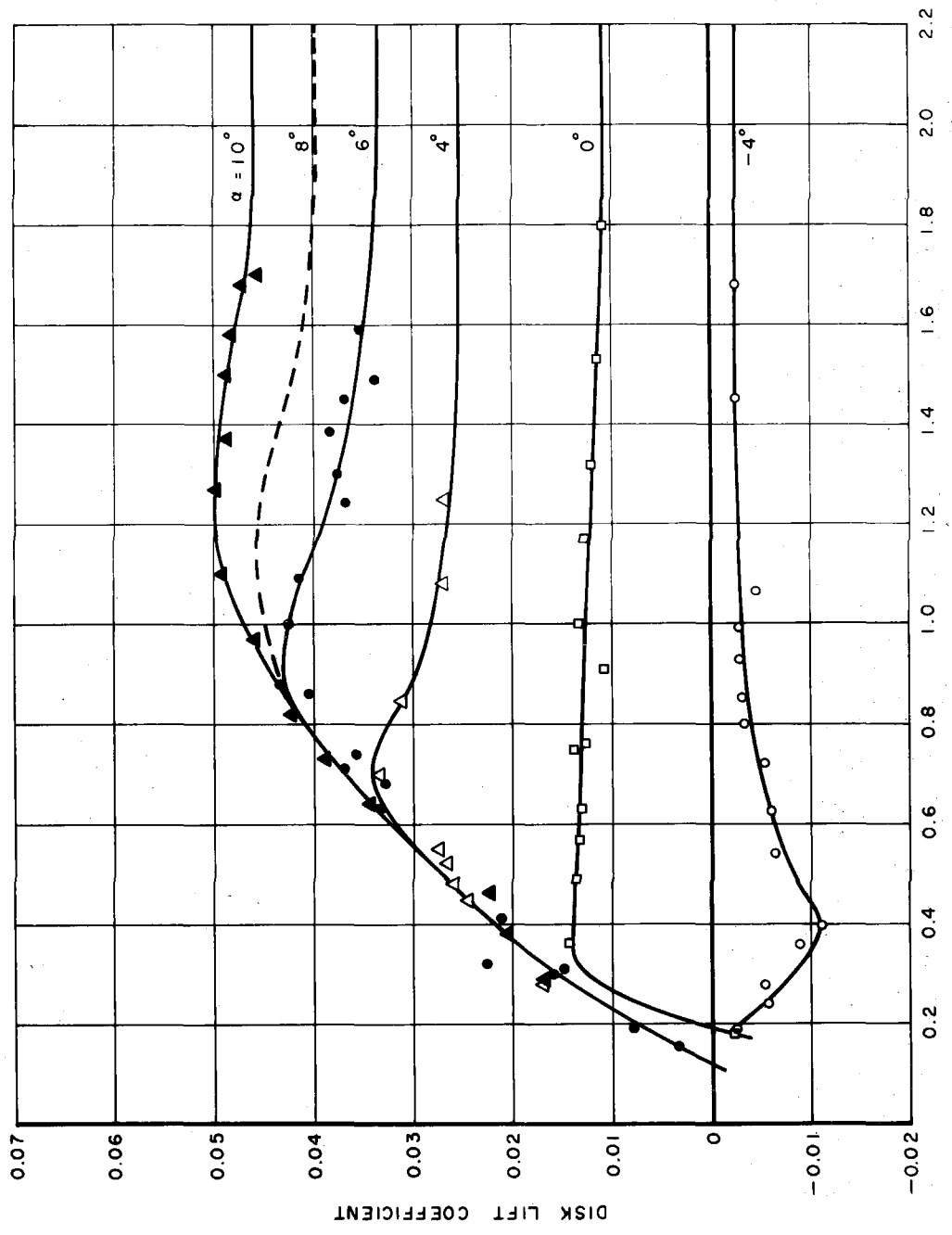

Fig. A2.1 - Tare lift force coefficient on disk as a function of cavitation number.

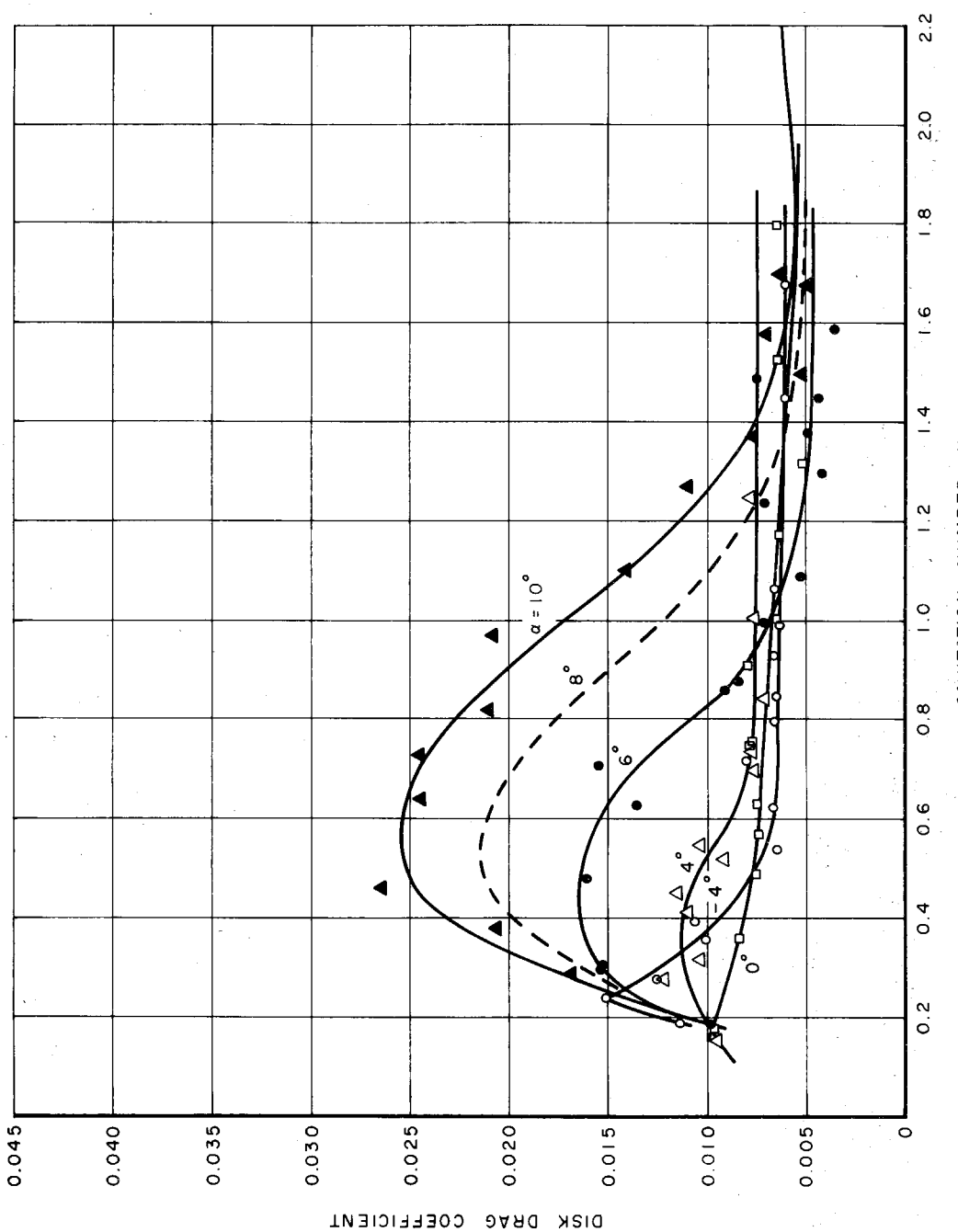

Fig. A2.2 - Tare drag force coefficient on disk as a function of cavitation number.

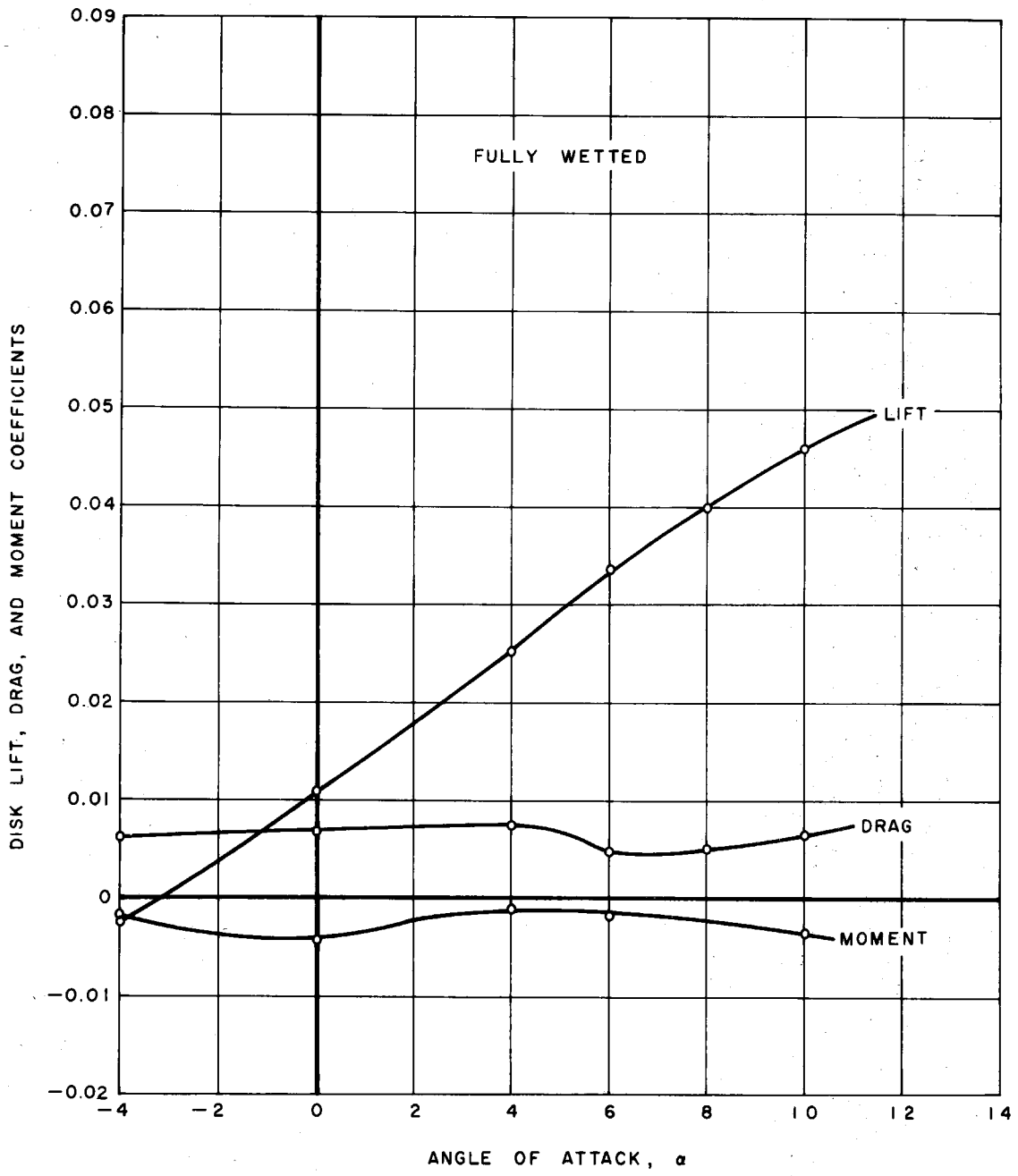

Fig. A2.3 - Tare force coefficients as a function of angle of attack for non-cavitating flow.

APPENDIX III

CORRECTIONS FOR MODEL INTERFERENCE EFFECTS FOR ISOLATED EXPERIMENTS

The method of correcting for the model interference effects is presented in this appendix. Before proceeding with the method used it must be stated that this correction endeavors only to account for the induced circulation by the model and does not deal with other tunnel effects such as the wall effects and static pressure gradient effects. The notation to be used is illustrated in the following Figure.

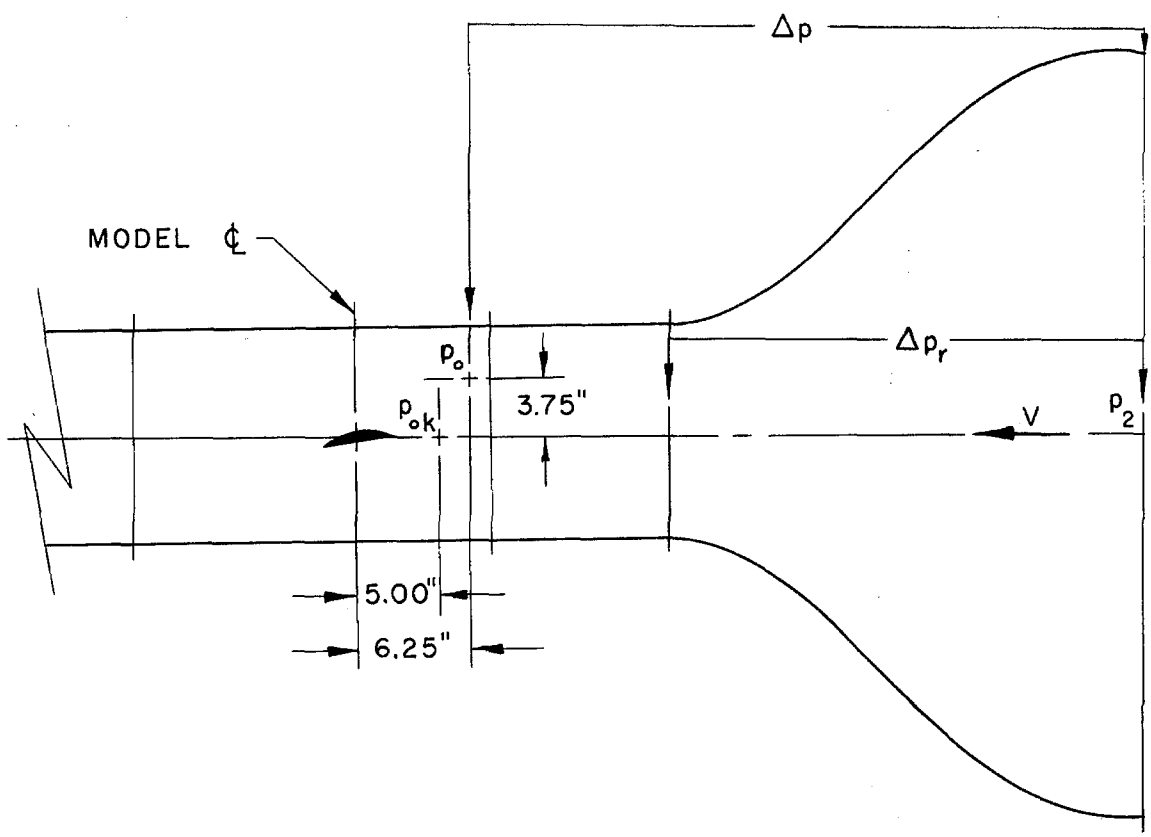

Fig. A3.1 Diagrammatic sketch illustrating notation used in applying model interference corrections.

The method is designed so as to apply the corrections to the results in coefficient form. The procedure used is as follows: The static pressure was measured at all the pressure taps in the working section (p_o , p_{ok}), as was the differential pressure used in calculating the dynamic head Δp, for the entire range of velocities used in the experiment.

All conditions of cavitation on the model at various angles of attack were considered. The differential pressure across the main nozzle Δp_r was recorded and this reading used as a reference, it being relatively insensitive to the circulation effect. The lift force on the model was also recorded, this being a measure of the induced circulation around the hydrofoil.

The ratio

$$\frac{p_2 - p_o}{\Delta p_r} = \frac{\Delta p}{\Delta p_r}$$

is then plotted as a function of C_L^* , the lift coefficient based on the uncorrected dynamic head Δp. This ratio is a function of C_L, say $h(C_L)$. The value of this function at zero lift is defined as

$$h(0) = \frac{p_2 - p}{\Delta p_r} \qquad \text{(A3.1)}$$

where we now define p as the true working section static pressure. From these results the following correction procedure can be evolved. From equation (A3.1) we find

$$\frac{p - p_o}{\Delta p} = \frac{p_2 - h(0)\Delta p_r - p_o}{\Delta p}$$

$$= \frac{h(C_L) - h(0)}{h(C_L)} = f(C_L) \quad , \quad \text{say}$$

hence

$$p = f(C_L)\Delta p + p_o \quad .$$

The force coefficients obtained directly from the experiment are defined as (in suitable units)

$$C_f^* = \frac{F}{(p_2 - p_o)} = \frac{F}{\Delta p}$$

The corrected force coefficient, however, is

$$C_f = \frac{F}{(p_2 - p)}$$

hence we obtain

$$C_f = \frac{F}{p_2 - f(C_L)\Delta p - p_o} \quad ,$$

$$= \frac{F}{\Delta p \{ 1 - f(C_L) \}} \quad ,$$

i.e.
$$C_f = \frac{C_f^*}{1 - f(C_L)} \qquad \text{(A3.2)}$$

Thus the corrected force coefficient may be calculated from the force coefficient obtained from direct measurement, once the function $f(C_L)$ has been determined.

In a similar way, the cavitation number can be corrected.

Since the measured cavitation number is given by

$$K^* = \frac{p_{ok} - p_k}{\Delta p} \quad ,$$

the corrected cavitation number can be expressed as

$$K = \frac{(p - p_k)}{(p_2 - p)} \quad ,$$

$$= \frac{f(C_L)\Delta p + p_o - p_k}{p_2 - f(C_L)\Delta p - p_o} \quad ,$$

$$= \frac{f(C_L)\Delta p + p_{ok} - p_k - p_{ok} + p_o}{\Delta p \left\{ 1 - f(C_L) \right\}} \quad ,$$

$$= \frac{f(C_L)}{1 - f(C_L)} + \frac{K^*}{1 - f(C_L)} - \frac{\delta p_k}{\Delta p \left\{ 1 - f(C_L) \right\}} \, ,$$

$$K = \frac{1}{1 - f(C_L)} \left[K^* + \left\{ f(C_L) - \frac{\delta p_k}{\Delta p} \right\} \right] \quad . \quad \text{(A3.3)}$$

All the functions in equations (A3.2) and (A3.3) can be determined from the calibration tests, hence the corrected force coefficients and cavitation numbers can be found.

The functions

$$\frac{1}{1 - f(C_L)} \qquad \text{and} \qquad \left\{ f(C_L) - \frac{\delta p_k}{\Delta p} \right\}$$

are shown plotted in Fig. A3.2.

The results show quite a large scatter particularly in the latter function. This is due to the fact that the pressure differences

δp_k being measured are quite small and due to the normal surging in the pressure lines to the manometers this difference is extremely difficult to obtain with accuracy, thus giving rise to the large scatter. This effect is also apparent in the graph for the function $1/\left\{1 - f(C_L)\right\}$ although here the effect is relatively much smaller and a definite trend in the correction with lift coefficient is evident. At a lift coefficient of 1.0 this correction is approximately 3 percent.

The corrections have been presented as functions of lift only. This is not to say that there is no drag effect on the measurements. A drag effect was looked for in the results but this, it is felt, was lost in the scatter as the drag effect at the angles of attack investigated are of the same order of magnitude as the scatter obtained.

It seems, therefore, that short of improving the accuracy of the normal measuring techniques the drag effect is unobtainable at these low angles of attack. However, at larger angles of attack, of the order of 25^o, this effect should be apparent.

The points shown plotted, as mentioned, cover all the experimental conditions investigated. However, no endeavor is made to distinguish these points as no definite dependence was observed on velocity, static pressure, etc.

It would seem, at first glance, that no correction would be necessary to the data at zero lift. This is indeed the case for the factor $1/\left\{1 - f(C_L)\right\}$ which is unity at zero lift. The factor $\left\{f(C_L) - \frac{\delta p_k}{\Delta p}\right\}$, however, incorporates in it a correction which accounts for the use of two different pressure taps p_{ok} and p_o

in the working section for the determination of the cavitation number. At zero lift we see that, since f(0) is zero, $-\delta p_k/\Delta p$ has the value 0.02, approximat ely,

$$\text{i.e.} \qquad \frac{p_o - p_{ok}}{\Delta p} \simeq 0.02 \quad .$$

This pressure difference arises from the boundary layer effect and its value, in fact, checks with calibration results of the two-dimensional working section obtained in Reference 14.

The corrections were applied to the results in the following manner. The force coefficients and cavitation number are calculated from the experimental readings. For each data point the corrections $1/\{1 - f(C_L)\}$ and $\left\{f(C_L) - \frac{\delta p_k}{\Delta p}\right\}$ for the given lift is read off Fig. A3.2, and applied to the results. The tare force correction is then applied and these final results are the ones shown plotted.

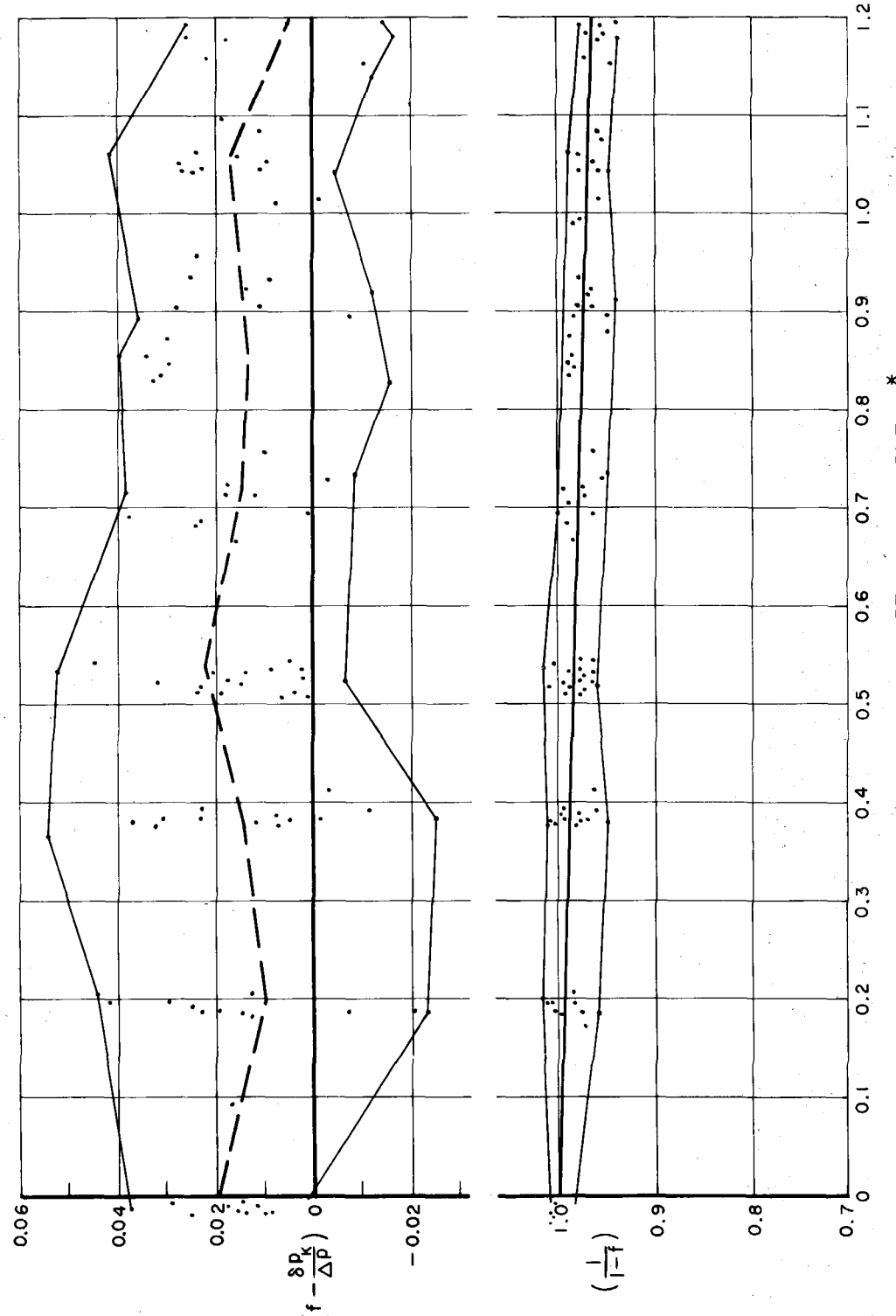

Fig. A3.2 - Model interference corrections for the force coefficients and the cavitation number.

APPENDIX IV

LINEARIZED THEORY OF PARTIALLY CAVITATING PLANO-CONVEX HYDROFOIL INCLUDING THE EFFECTS OF CAMBER AND THICKNESS

The present appendix deals with the linearized treatment of the flow over a single hydrofoil having a flat pressure surface and a circular arc suction side. The flow is treated as a two-dimensional, steady, inviscid flow. Further assumptions made are those of incompressibility and irrotationality.

Formulation of Problem - The hydrofoil is held at an angle of attack, α to the free stream velocity, V as illustrated in Fig. A4.1. For the present problem it is assumed that a cavity forms on the top side of the hydrofoil starting at the leading edge. The cavity then terminates on the upper surface. The angle subtended by the tangents to the circular surface at the leading and trailing edges, Ω, is assumed to be small as is the angle of attack, α. These assumptions are in keeping with the linearized theory (9).

With these assumptions it is possible to consider the velocity field as a perturbation on the free stream velocity V, allowing one to write the velocity at any point in the fluid as

$$\bar{q} = V(1 + u', v') = V(u, v)$$

where u', v' are the perturbation components. Furthermore the equation for the circular arc suction surface can be written in the form

$$\frac{d\eta}{dx} = \frac{\Omega}{2}(1 - 2x) \quad .$$

The boundary conditions on the velocity function, within the framework of the linearized theory, are therefore, with the help of Bernoulli's equation,

$$v = -V\alpha + \frac{V\Omega}{2}(1 - 2x), \quad \text{for the top wetted surface}$$

$$v = -V\alpha \quad , \quad \text{for the bottom wetted surface}$$

$$u = V(1 + \frac{K}{2}) \quad , \quad \text{on the cavity surface.}$$

K is the cavitation number defined as

$$K = \frac{p - p_c}{\rho V^2/2} \quad ,$$

where

p = pressure at infinity

p_c = cavity pressure .

These boundary conditions are applied along a slit representing the body in the physical plane, as illustrated in Fig. A4.2.

From the initial assumptions that the velocity is incompressible and irrotational, the function

$$W(z) = u - iv$$

is therefore an analytic function of the complex variable z.

The transformation

$$\zeta = ia\sqrt{\frac{z}{z - 1}}$$

where

$$a = \sqrt{\frac{1 - \ell}{\ell}} \quad ,$$

transforms the slit in the z-plane into the upper half ζ-plane, such that the entire real axis of the ζ-plane becomes the surface of the foil. Furthermore the region $0 < \xi < 1$ becomes the cavity surface. With this transformation the point of infinity in the z-plane is transformed into the point ia in the ζ - plane as seen in Fig. A4.3. The relevant boundary conditions are also shown in this figure.

Further conditions to be satisfied are that the velocity at infinity be equal to the free stream velocity V, i.e.,

$$\lim_{z \longrightarrow \infty} w(z) = V$$

and that the cavity-hydrofoil system form a closed body. This requirement may be expressed as

$$\int_{\text{body}} dh = 0$$

where h represents the ordinates of points on the body-cavity system.

Furthermore, at the trailing edge, due to the finite trailing edge angle of the hydrofoil, the velocity must behave logarithmically there. This replaces the usual Kutta condition at the trailing edge.

Considering the function

$$w(z) = W(z) - V\left(1 + \frac{K}{2}\right) - iV\alpha ,$$

in the ζ-plane, we have:

$$\text{Imaginary part } w = 0 \qquad -\infty < \xi < 0$$

$$\text{Real part } w = 0 \qquad 0 < \xi < 1$$

$$\text{Imaginary part } w = -\frac{V\Omega}{2}\left[1 - 2x(\xi)\right] \qquad 1 < \xi < \infty$$

If we continue $w(z)$ analytically through the interval $0 < \xi < 1$ into

the lower half plane, such that

$$w(\bar{\zeta}) = \overline{w(\zeta)} \quad ,$$

then the real part of w is an uneven function of η and the imaginary part of w is an even function of η. We can thus formulate the following boundary value problem in the ζ-plane.

$$w^+ + w^- = 0 \qquad -\infty < \xi < 0$$

$$w^+ - w^- = 0 \qquad 0 < \xi < 1$$

$$w^+ + w^- = -2i \frac{V\Omega}{2} \left[1 - 2x(\xi)\right] \qquad 1 < \xi < \infty$$

where the superscripts refer to the value of $w(\zeta)$ as $\eta \longrightarrow \pm 0$. The problem thus reduces to a Hilbert problem the solution of which can be found by applying the procedures given in Reference 49.

Solution of Problem

Let us first consider the homogeneous problem

$$H^+ + H^- = 0 \qquad -\infty < \xi < 0$$

$$H^+ - H^- = 0 \qquad 0 < \xi < 1$$

$$H^+ + H^- = 0 \qquad 1 < \xi < \infty$$

It can be seen that $H(\zeta)$ is continuous for $0 < \xi < 1$ but has a jump for ξ outside of this range. A function satisfying these conditions is

$$H = \sqrt{\zeta\,(\zeta - 1)}$$

where we take the branch cuts of H to be along the real axis outside the interval $0 < \xi < 1$, and we further require that

$$H \sim \zeta \qquad \text{as} \qquad \zeta \longrightarrow \infty$$

We now consider the function, $G(\zeta) = \frac{w(\zeta)}{H(\zeta)}$. The boundary conditions for this function are

$$G^+ - G^- = \frac{w^+}{H^+} - \frac{w^-}{H^-} = (w^+ + w^-)/H^+ = 0 \qquad -\infty < \xi < 0$$

$$G^+ - G^- = \frac{w^+}{H^+} - \frac{w^-}{H^-} = (w^+ - w^-)/H^+ = 0 \qquad 0 < \xi < 1$$

$$G^+ - G^- = \frac{w^+}{H^+} - \frac{w^-}{H^-} = (w^+ + w^-)/H^+ = \frac{-iV\Omega}{\sqrt{\xi(\xi-1)}}\left[1 - 2x(\xi)\right] \qquad 1 < \xi < \infty$$

Now, by means of Plemelj's formula, we can express an analytic function in the upper half plane by its values along the entire real axis according to the formula

$$F(z) = \frac{1}{2\pi i} \int_{-\infty}^{\infty} \frac{f(x)}{x - z}\, dx$$

where $f(x) = f^+(x) - f^-(x)$.

Accordingly, we obtain

$$G(\zeta) = -\frac{V\Omega}{2\pi} \int_{1}^{\infty} \frac{1 - 2x(\xi)}{\sqrt{\xi(\xi - 1)}\,(\xi - \zeta)}\, d\xi$$

This solution represents a particular solution of the problem; the general solution is given by

$$w(\zeta) = -\frac{V\Omega}{2\pi}\sqrt{\zeta(\zeta - 1)} \int_{1}^{\infty} \frac{1 - 2x(\xi)}{\sqrt{\xi(\xi - 1)}\,(\xi - \zeta)}\, d\xi + P(\zeta)\sqrt{\zeta(\zeta - 1)}$$

where $P(\zeta)$ is a rational function of ζ which can have poles only at the points $\xi = 0, 1$. Since the trailing edge is at infinity in the ζ-plane, $w(\zeta)$ can at most behave logarithmically there. This behavior is a consequence of the linearized thickness effect. Hence $P(\zeta)$ can only be of the form

$$\frac{A\zeta + B}{\zeta(\zeta + 1)}$$

where A, B are real constants. We finally get for our solution

$$w(\zeta) = -\frac{V\Omega}{2\pi}\sqrt{\zeta(\zeta - 1)}\int_1^\infty \frac{1 - 2x(\xi)}{\sqrt{\xi(\xi - 1)}\,(\xi - \zeta)}\,d\xi + \frac{A\zeta + B}{\sqrt{\zeta(\zeta - 1)}}\,,$$

where $x(\xi)$ can be obtained from the transformation equation as

$$x(\xi) = \frac{\xi^2}{\xi^2 + a^2}\,.$$

The constants A and B can be evaluated from the condition that $w(\zeta) = V$ at $\zeta = ia$.

As we will only be concerned with evaluating the above integral at $\zeta = ia$, we can write the above integral as

$$I = \int_1^\infty \frac{\xi(a^2 - \xi^2)}{\sqrt{\xi(\xi - 1)}\,(\xi^2 + a^2)^2}\,d\xi + ia\int_1^\infty \frac{(a^2 - \xi^2)}{\sqrt{\xi(\xi - 1)}\,(\xi^2 + a^2)^2}\,d\xi$$

For purposes of computation it is more convenient to change the limits of integration to a finite interval. By successively substituting $\xi = 1/t$ and $t = 1 - x^2$, the above integrals reduce to

$$I = 2\int_0^1 \frac{(a^2t^2 - 1)}{(1 + a^2t^2)^2}\,dx + i\,2a\int_0^1 \frac{(a^2t^2 - 1)}{(1 + a^2t^2)^2}\,dx$$

or, $I = I_1 + i\,I_2$,

where I_1 and I_2 are functions of a only. The integrals are represented in this fashion as it simplifies the numerical integration

process. It is possible to evaluate these integrals in closed form but this leads to a very complicated and messy expression which is not very useful.

As mentioned these integrals will give a logarithmic behavior at infinity in the ζ-plane - corresponding to the trailing edge in the physical plane - due to the finite angle subtended there. The constants A and B can now be evaluated. After some manipulation we obtain

$$A = -V \frac{(1 + a^2)^{\frac{1}{4}}}{a^{\frac{1}{2}}} \left[\frac{K}{2} \sin \frac{\psi}{2} + a \cos \frac{\psi}{2} \right] + \frac{V\Omega}{2\pi} (1 + a^2)^{\frac{1}{2}} \left[I_1 \sin \psi + I_2 \cos \psi \right]$$

and

$$B = -Va^{\frac{1}{2}} (1 + a^2)^{\frac{1}{4}} \left[\frac{K}{2} \cos \frac{\psi}{2} - a \sin \frac{\psi}{2} \right] + \frac{V\Omega}{2\pi} a (1 + a^2)^{\frac{1}{2}} \left[I_1 \cos \psi - I_2 \sin \psi \right]$$

where $\psi = \pi + \tan^{-1} 1/a$. These expressions express the constants A and B in terms of the parameter a only. The first terms in the above expressions correspond to the flat plate solution and the camber and thickness effects are incorporated in the second terms.

The relationship between the cavitation number K and the cavity length ℓ is obtained by applying the closure condition. This condition may be written in the following form

$$\int_{\text{body}} dh = \int_{\text{body}} v \, dx = 0$$

or

$$\mathrm{Im} \int_{\text{body}} W(\zeta) \frac{dz}{d\zeta} \, d\zeta = 0$$

where Im denotes the imaginary part of the integral. Furthermore, we are interested in the lift on the body. Within the limitations of thin airfoil theory this is given by

$$C_L = -\frac{2}{U} \int_{\text{body}} u \, dx$$

or

$$C_L = -\frac{2}{U} \, \mathrm{Re} \int_{\text{body}} W(\zeta) \frac{dz}{d\zeta} \, d\zeta$$

where Re denotes the real part of the integral. Since the body is now the entire real axis in the ζ-plane, we have to evaluate the integral

$$K = \int_{+\infty}^{-\infty} W(\zeta) \frac{dz}{d\zeta} \, d\zeta$$

where $\frac{dz}{d\zeta} = \frac{2a^2\zeta}{(\zeta - ia)^2(\zeta + ia)^2}$.

Since $\frac{dz}{d\zeta} \sim \frac{1}{\zeta^3}$ as $\zeta \longrightarrow \infty$ there is no contribution to the integral by completing the contour by a large circle R and letting $R \longrightarrow \infty$. The value of the integral is then given by the residue of the integrand at the double pole $\zeta = ia$. Since the integral traverses the body in a counter-clockwise fashion in the z-plane which corresponds to a clockwise sense in the ζ-plane, we have

$$K = -2\pi i \left[\text{ Residue at } \zeta = ia \right]$$

which reduces to

$$K = -\pi a\left[\frac{dW}{d\zeta}\right] ia \quad .$$

Carrying out the indicated procedure and separating the result into real and imaginary parts we obtain, after considerable algebra, the following expressions for the closure condition and for the lift coefficient

$$\frac{\pi A}{2Va^{\frac{1}{2}}(1+a^2)^{\frac{1}{4}}}\cos\frac{3\psi}{2} + \frac{\pi B}{2Va^{\frac{3}{2}}(1+a^2)^{\frac{3}{4}}}\left[\sin\frac{3\psi}{2} + 2a\sin\frac{3\psi}{2}\right]$$

$$+ \frac{\Omega}{2}a^{\frac{1}{2}}(1+a^2)^{\frac{1}{4}}\left[\left(\frac{1}{a}I_2 - I_4\right)\sin\frac{\psi}{2} + I_3\cos\frac{\psi}{2}\right]$$

$$+ \frac{\Omega}{4}\frac{1}{a^{\frac{1}{2}}(1+a^2)^{\frac{1}{4}}}\left[I_1\left(\sin\frac{\psi}{2} + 2a\cos\frac{\psi}{2}\right)\right.$$

$$\left. - I_2\left(\cos\frac{\psi}{2} - 2a\sin\frac{\psi}{2}\right)\right] = 0$$

and

$$C_L = -\frac{\pi A a^{\frac{1}{2}}}{V(1+a^2)^{\frac{3}{4}}}\sin\frac{3\psi}{2} + \frac{\pi B}{Va^{\frac{1}{2}}(1+a^2)^{\frac{3}{4}}}\left[\cos\frac{3\psi}{2} - 2a\sin\frac{3\psi}{2}\right]$$

$$- \Omega a^{\frac{3}{2}}(1+a^2)^{\frac{1}{4}}\left[\left(\frac{1}{a}I_2 - I_4\right)\cos\frac{\psi}{2} - I_3\sin\frac{\psi}{2}\right]$$

$$+ \frac{\Omega}{2}\frac{a^{\frac{1}{2}}}{(1+a^2)^{\frac{1}{4}}}\left[I_1\left(\cos\frac{\psi}{2} - 2a\sin\frac{\psi}{2}\right)\right.$$

$$\left. + I_2\left(\sin\frac{\psi}{2} + 2a\cos\frac{\psi}{2}\right)\right]$$

where

$$I_3 = 4a \int_0^1 \frac{t^2(a^2t^2 - 1)}{(1 + a^2t^2)^3} \, dx$$

$$I_4 = 4a^2 \int_0^1 \frac{t^3(a^2t^2 - 1)}{(1 + a^2t^2)^3} \, dx$$

From these results the graphs shown in Figs. A4.4 -A4.17 were obtained. The computations were carried out on the 7094 IBM computer. The range of values investigated was for angles of attack from 2^o to 10^o and values of Ω, or alternatively thickness ratios from 2 percent to 10 percent.

Limiting Cases:

If we consider the case where $\Omega = 0$ then we are dealing with a flat plate. The solution of this problem has already been given by Acosta (13) and Geurst (18). On carrying out the above procedures with $\Omega = 0$ we obtain

$$\frac{K}{2a} = \frac{1}{(1/\ell - 1)^{\frac{1}{2}}} \left[\frac{2}{\ell} - 1 + \frac{2}{\ell^{\frac{1}{2}}} (1/\ell - 1)^{\frac{1}{2}} \right]$$

and

$$C_L = \pi a \left[1 + \frac{1}{(1 - \ell)^{\frac{1}{2}}} \right]$$

which are the results previously obtained by the above authors. Note that as $\ell \longrightarrow 0$ in the above we obtain

$$C_L \longrightarrow 2\pi\alpha \ .$$

which is the fully wetted result for the flat plate.

Discussion:

The effect of angle of attack on lift coefficient for a given thickness ratio is shown in Figs. A4.4 to A4.10 as a function of cavitation number. As would be expected the lift coefficient increases with increase in the angle of attack. In the linearized theory the validity of the results is usually restricted to a certain range of cavitation numbers due to the type of cavity closure used. For the present case this range of validity holds for values of cavity length-to-chord ratio less than about 0.75. This is apparent from Figs. A4.11 to A4.17 where it is seen that the cavitation number reaches a minimum value at this point. Values outside this range would give rise to the possibility of two cavity lengths for any given cavitation number.

It will be noticed from the curves in Figs. A4.11 to A4.17 that as the angle of attack increases the cavity behavior approaches that of the flat plate case, t/c = 0. This trend can be interpreted as the fact that at the higher angles of attack the profile section has little effect on the cavity shape, a conclusion that may easily be reached from geometrical considerations of the cavity-body system.

Figs. A4.18 to A4.21 are cross plots of the above results illustrating the effect of profile contour on the performance of the hydrofoil under cavitating conditions. Only curves for two angles of attack $\alpha = 6^\circ$ and 10° are shown. It is seen that the effects of

camber and thickness are to increase lift at any given cavitation number with a corresponding increase in cavity length.

It should be noted that the above calculations are based on the assumption that the cavity arises from the leading edge at all times. Under certain configurations of angle of attack and thickness ratio this assumption may not be physically possible, as brought out by the findings of the present experimental investigation where at lower angles of attack a cavity starts downstream of the leading edge at the point of maximum thickness. This should therefore be kept in mind when applying the above results.

It may be noted that the fully wetted results obtained from this linearized theory for a hydrofoil of 7 percent thickness ratio give a zero lift angle of attack of $-4^{\circ}18'$ with a corresponding lift coefficient of 0.442 at zero angle of attack. This compares with values of $-4^{\circ}10'$ and 0.479 obtained by conformal mapping techniques.

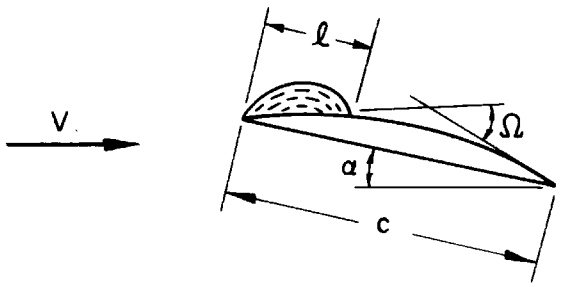

Fig. A4.1 - Partially cavitating plano-convex hydrofoil.

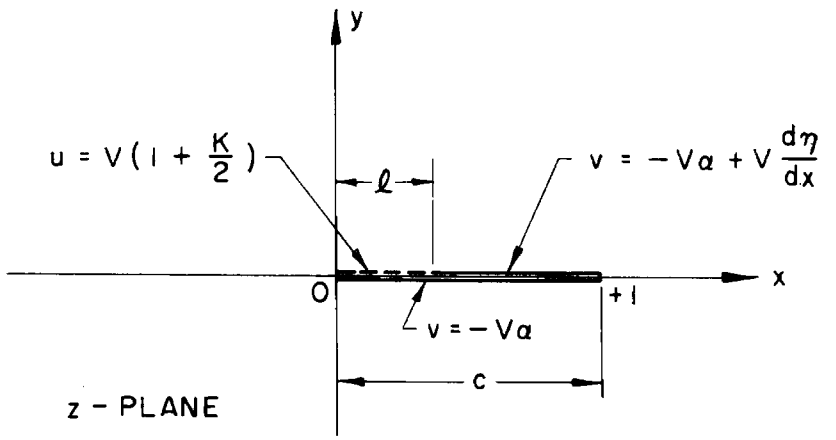

Fig. A4.2 - Linearized problem in physical z-plane

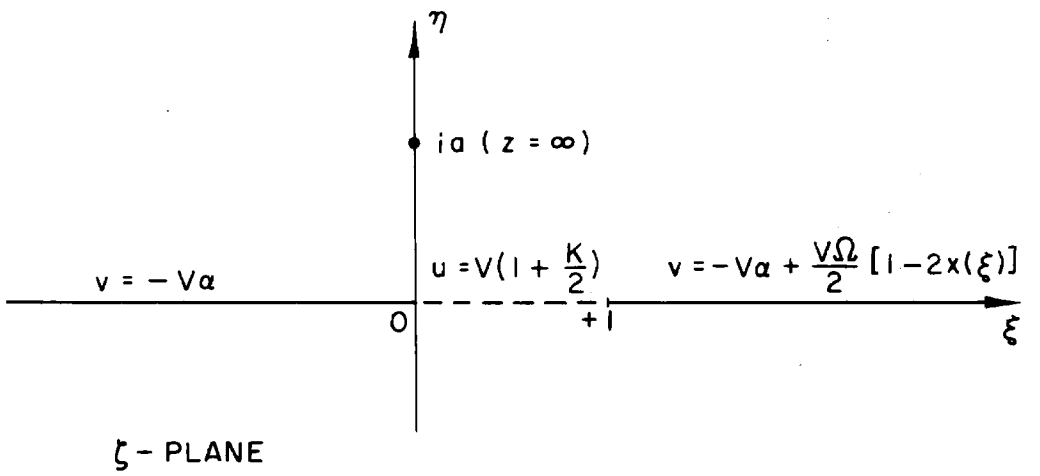

Fig. A4.3 - Transform ζ-plane.

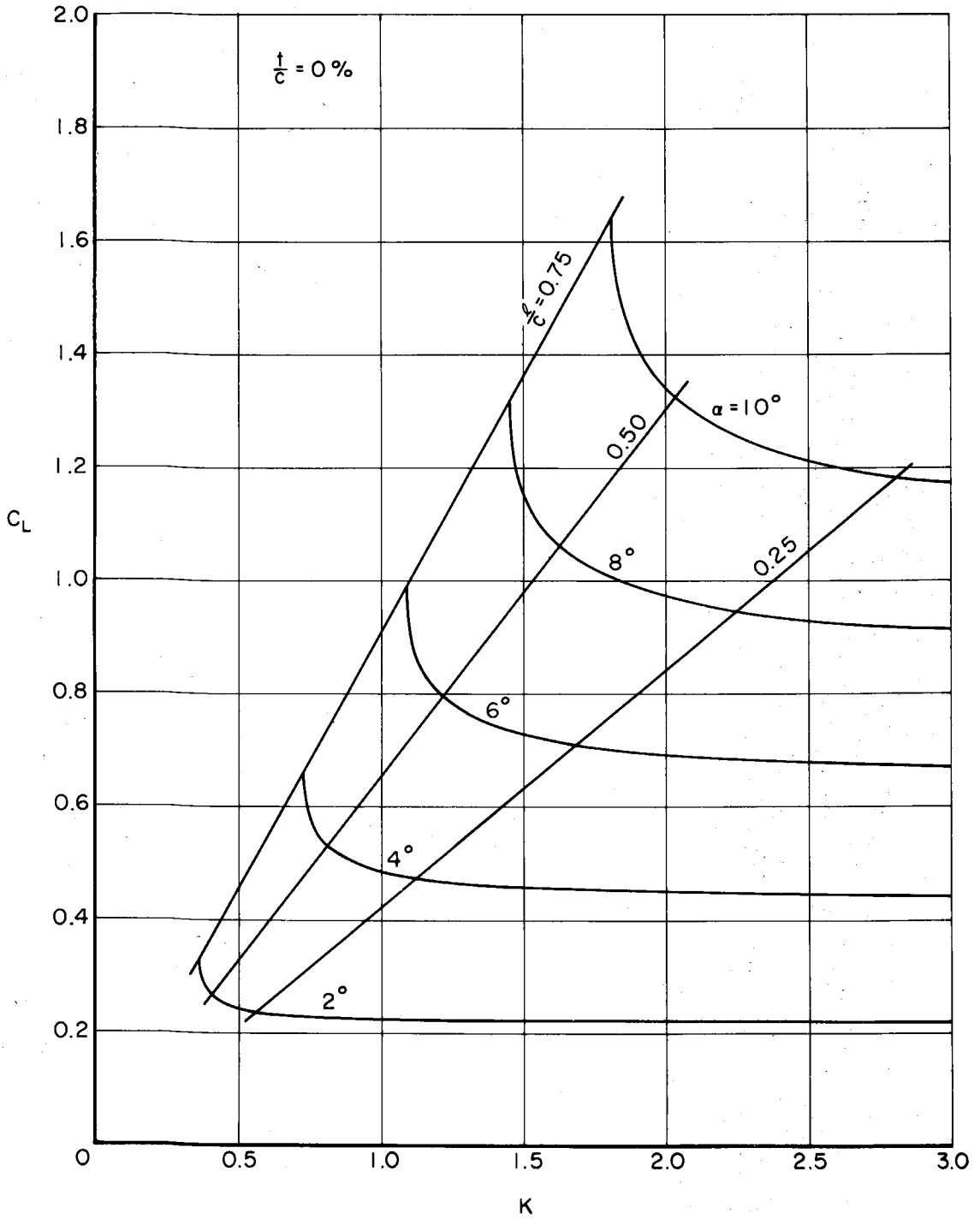

Fig. A4.4 - Lift coefficient versus cavitation number K at various angles of attack α for a thickness ratio of 0%.

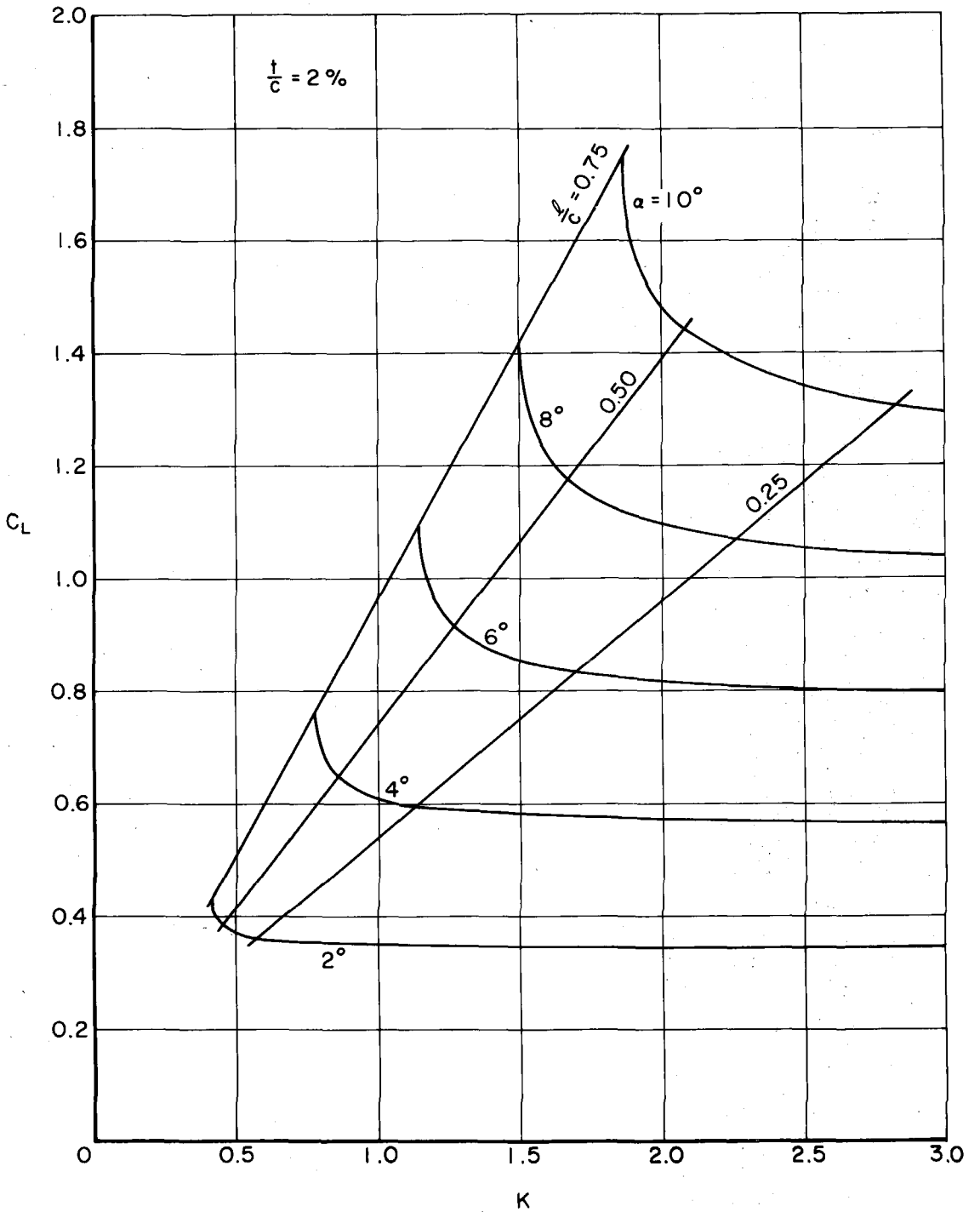

Fig. A4.5 - Lift coefficient versus cavitation number K at various angles of attack α for a thickness ratio of 2%.

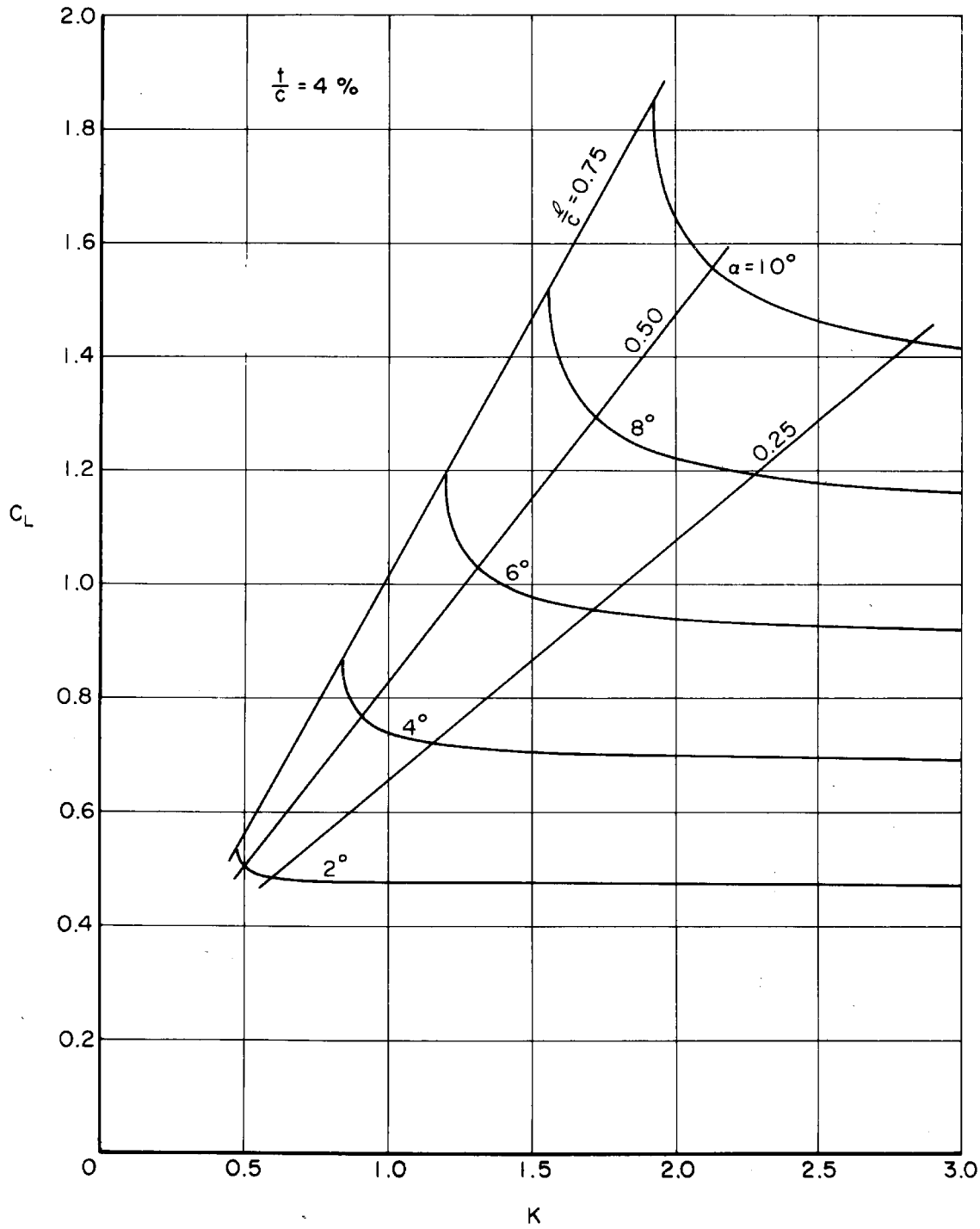

Fig. A4.6 - Lift coefficient versus cavitation number K at various angles of attack α for a thickness ratio of 4%.

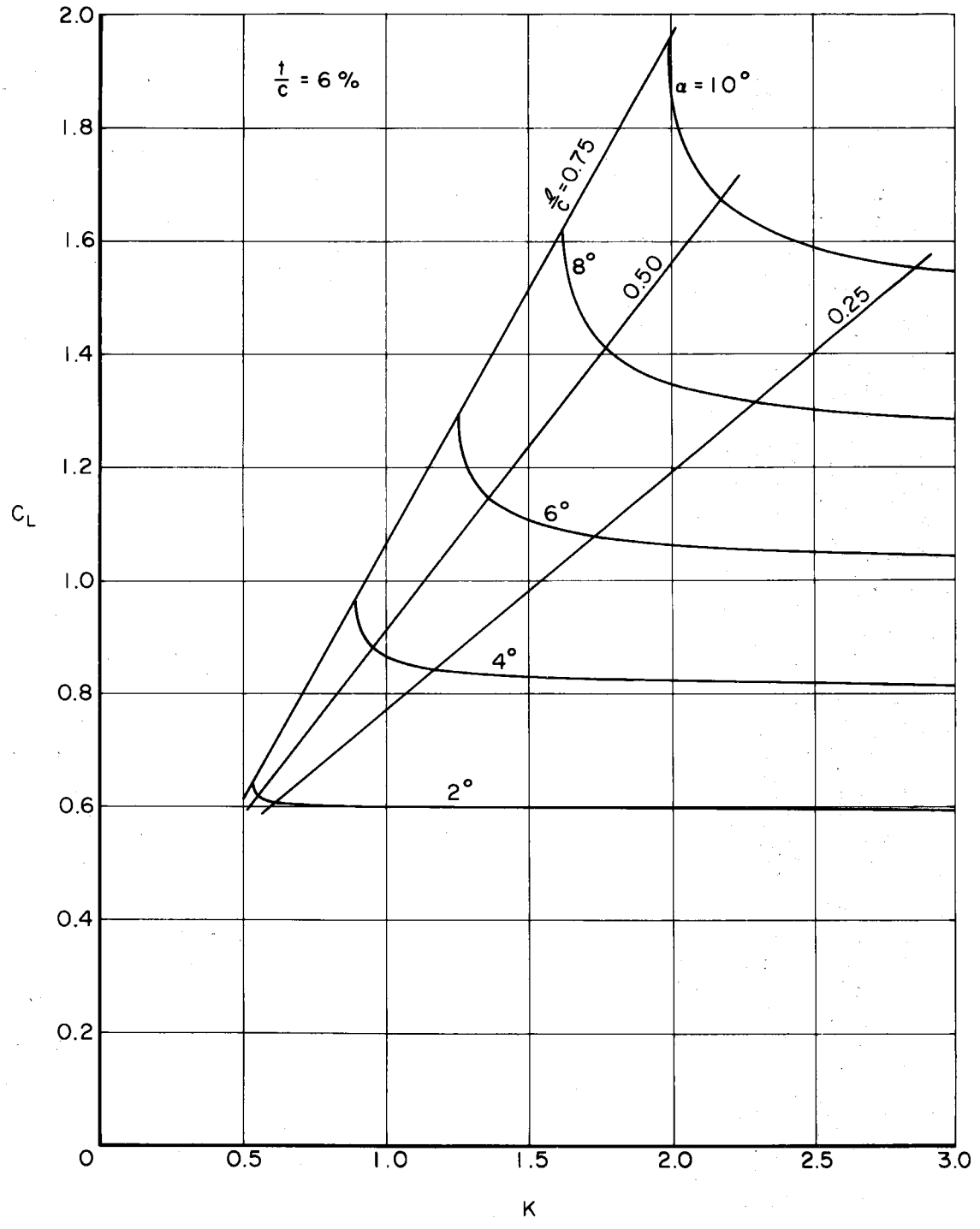

Fig. A4.7 - Lift coefficient versus cavitation number K at various angles of attack α for a thickness ratio of 6%.

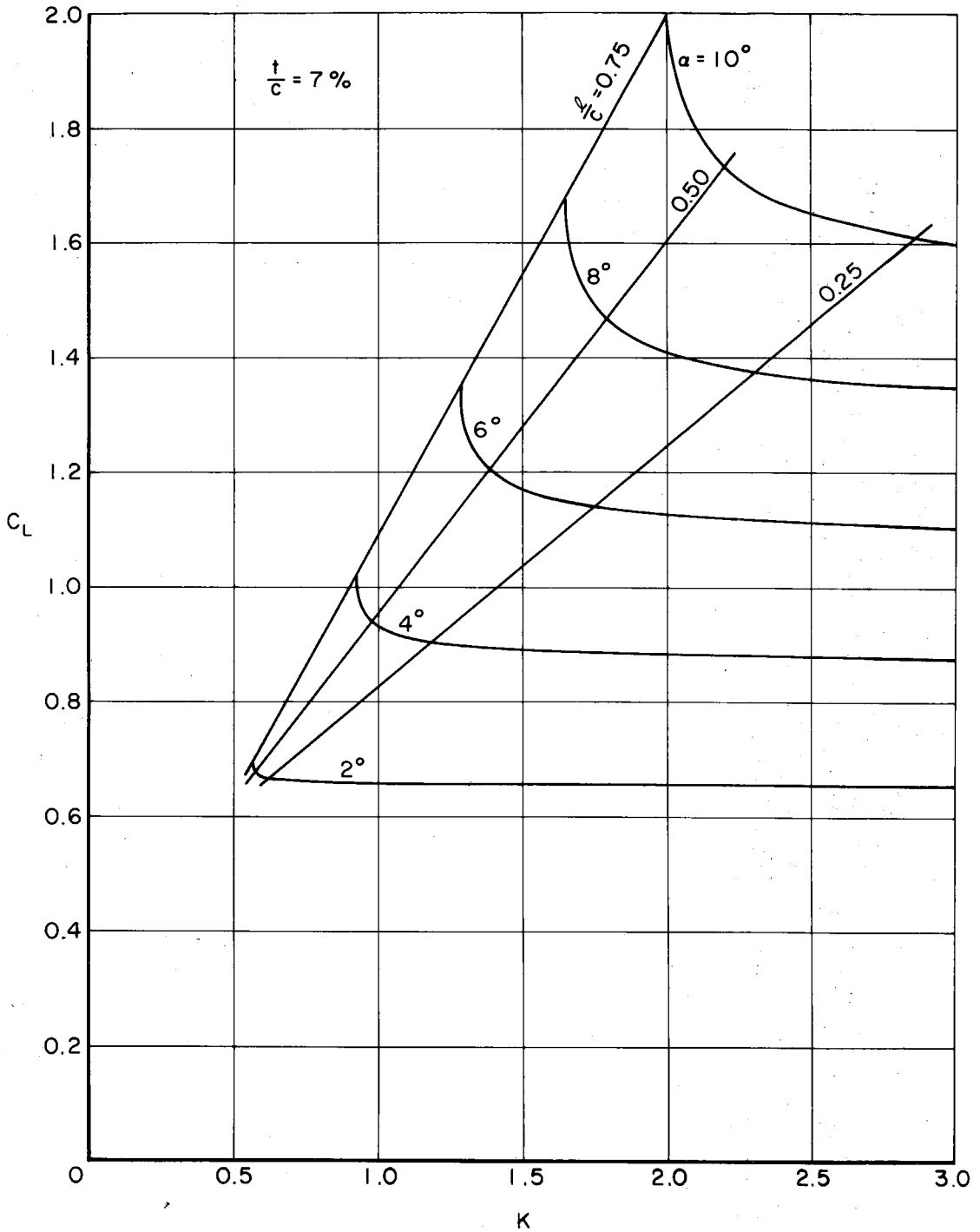

Fig. A4.8 - Lift coefficient versus cavitation number K at various angles of attack α for a thickness ratio of 7%.

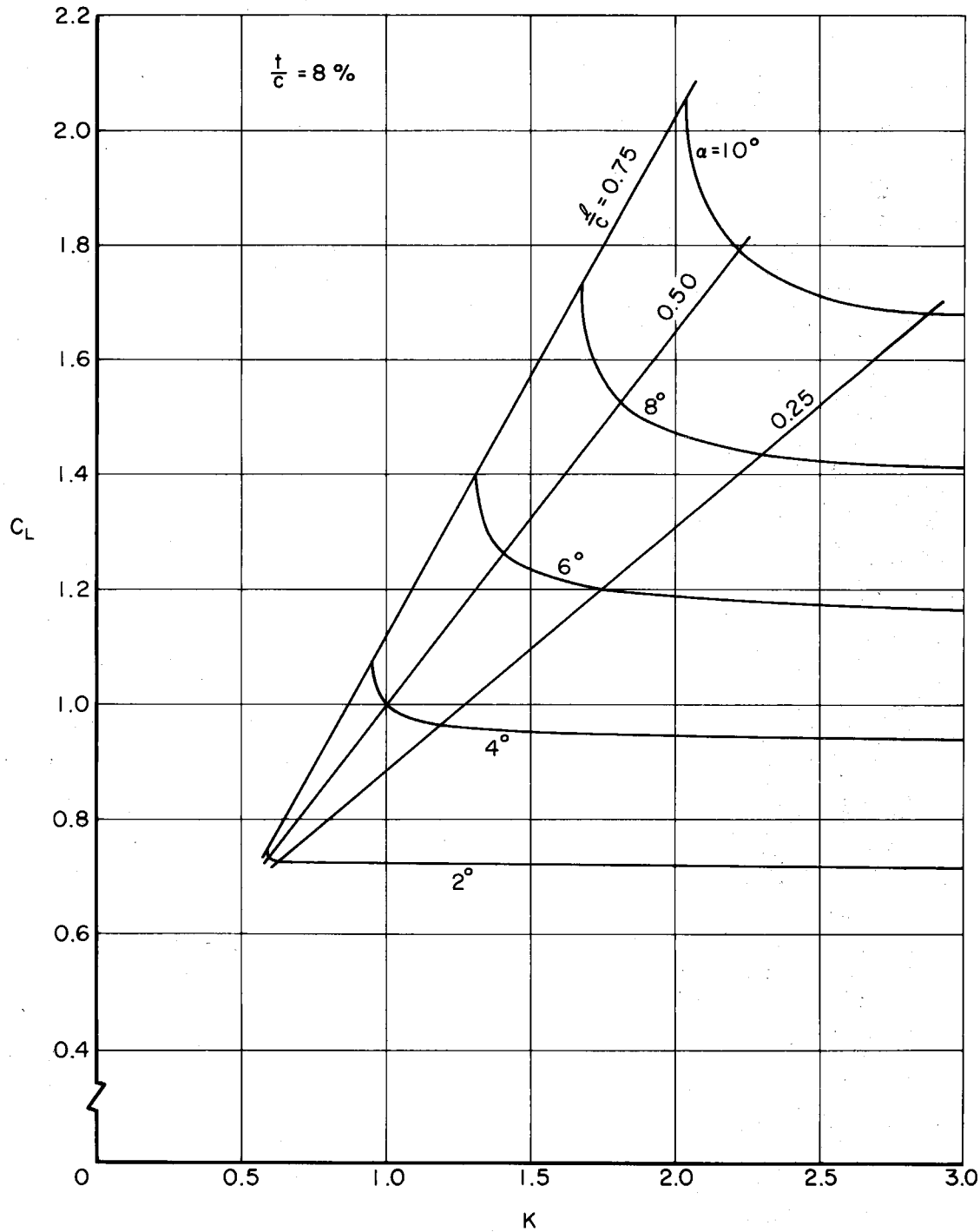

Fig. A4.9 - Lift coefficient versus cavitation number K at various angles of attack α for a thickness ratio of 8%.

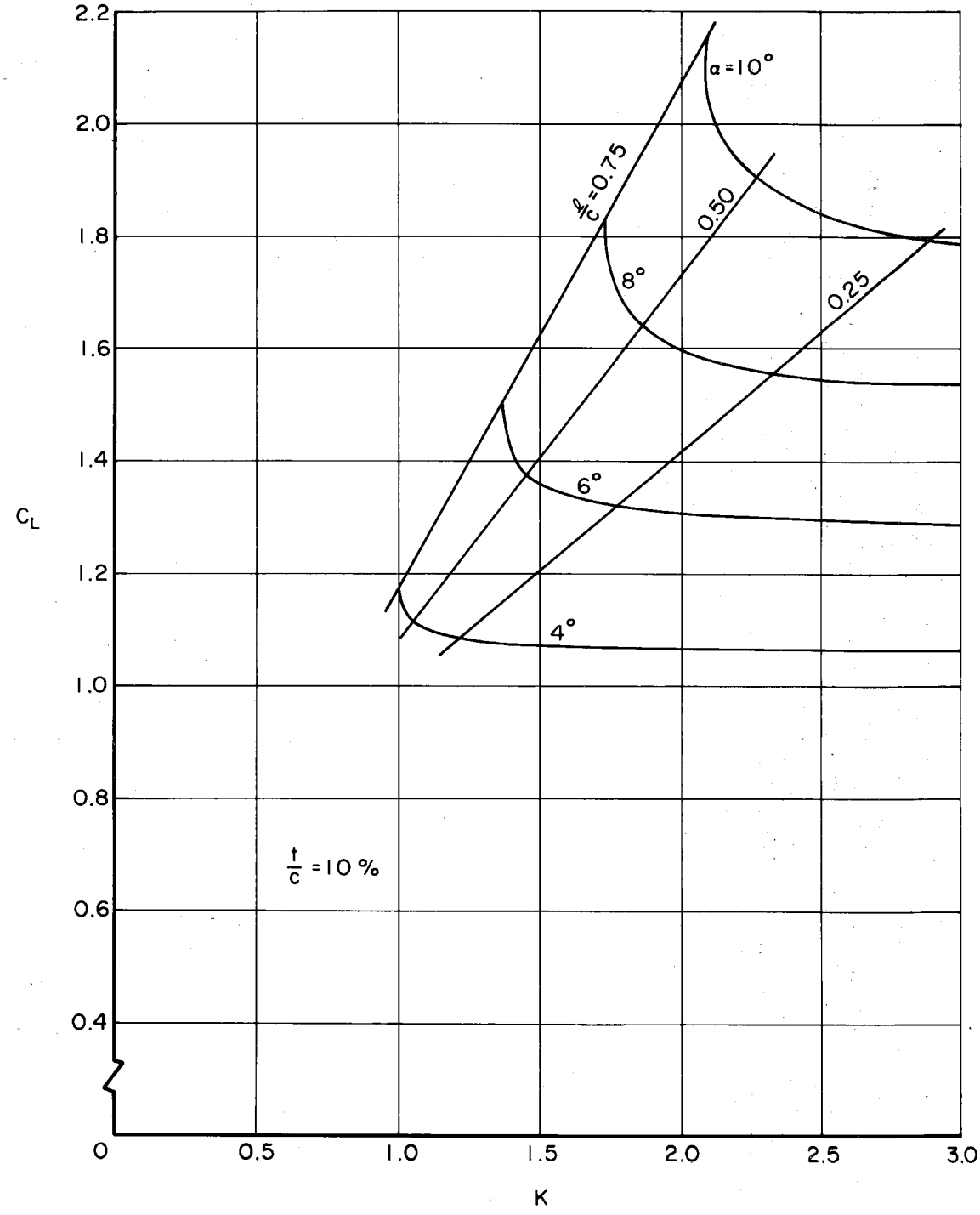

Fig. A4.10 - Lift coefficient versus cavitation number K at various angles of attack α for a thickness ratio of 10%.

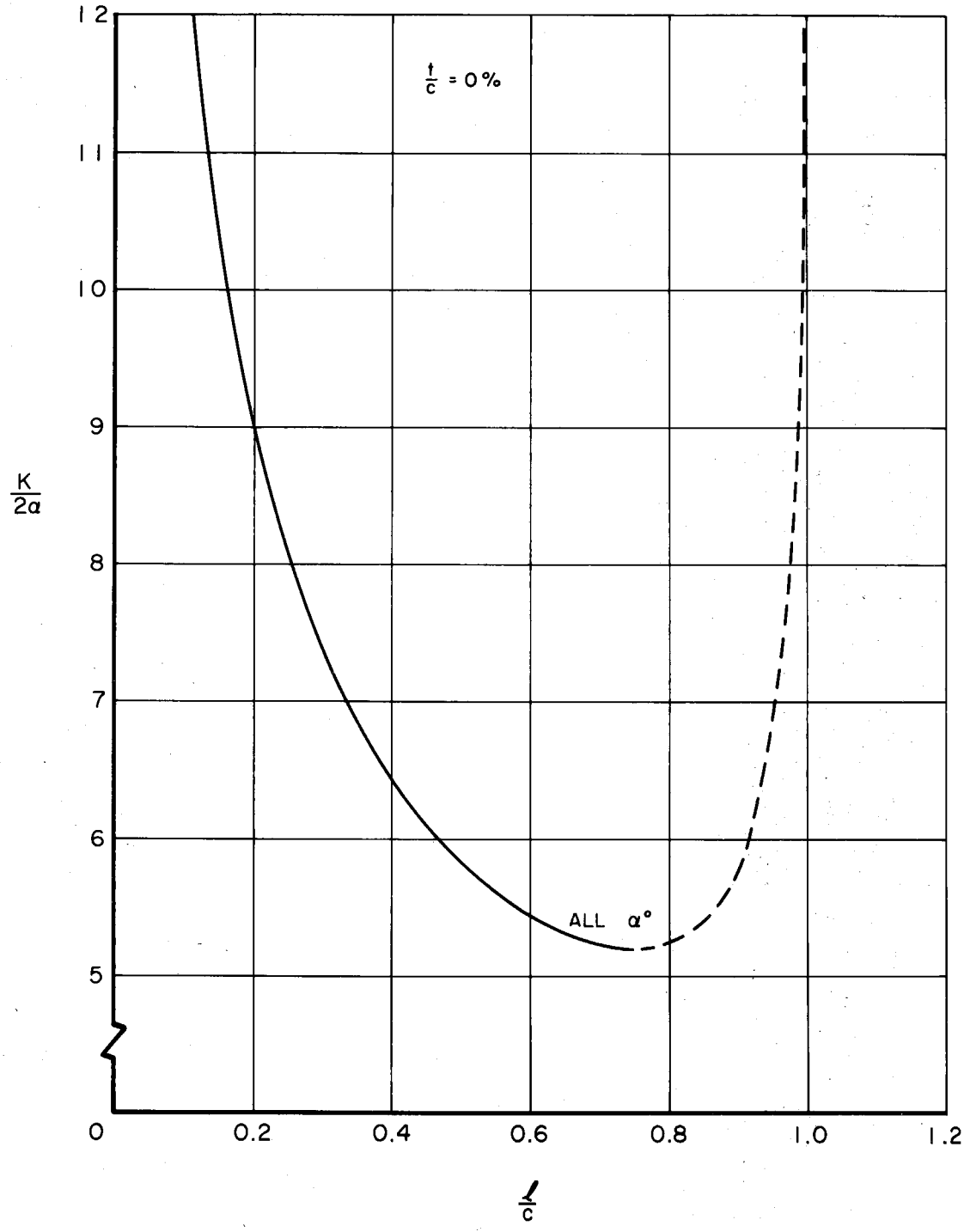

Fig. A4.11 - Ratio of cavitation number to twice the angle of attack α as a function of cavity length-to-chord ratio at various angles of attack α for a thickness ratio of 0%.

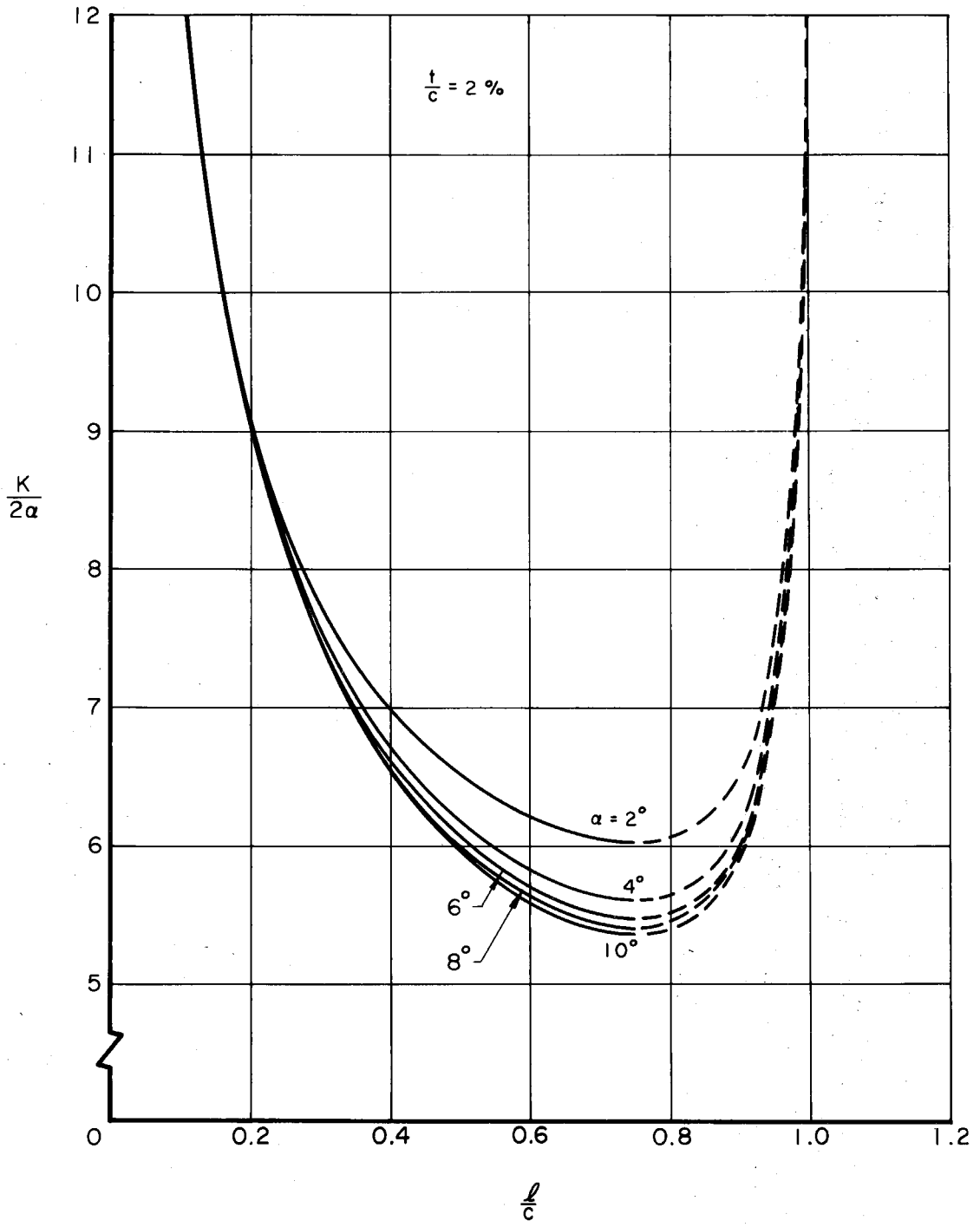

Fig. A4.12 - Ratio of cavitation number to twice the angle of attack α as a function of cavity length-to-chord ratio at various angles of attack α for a thickness ratio of 2%.

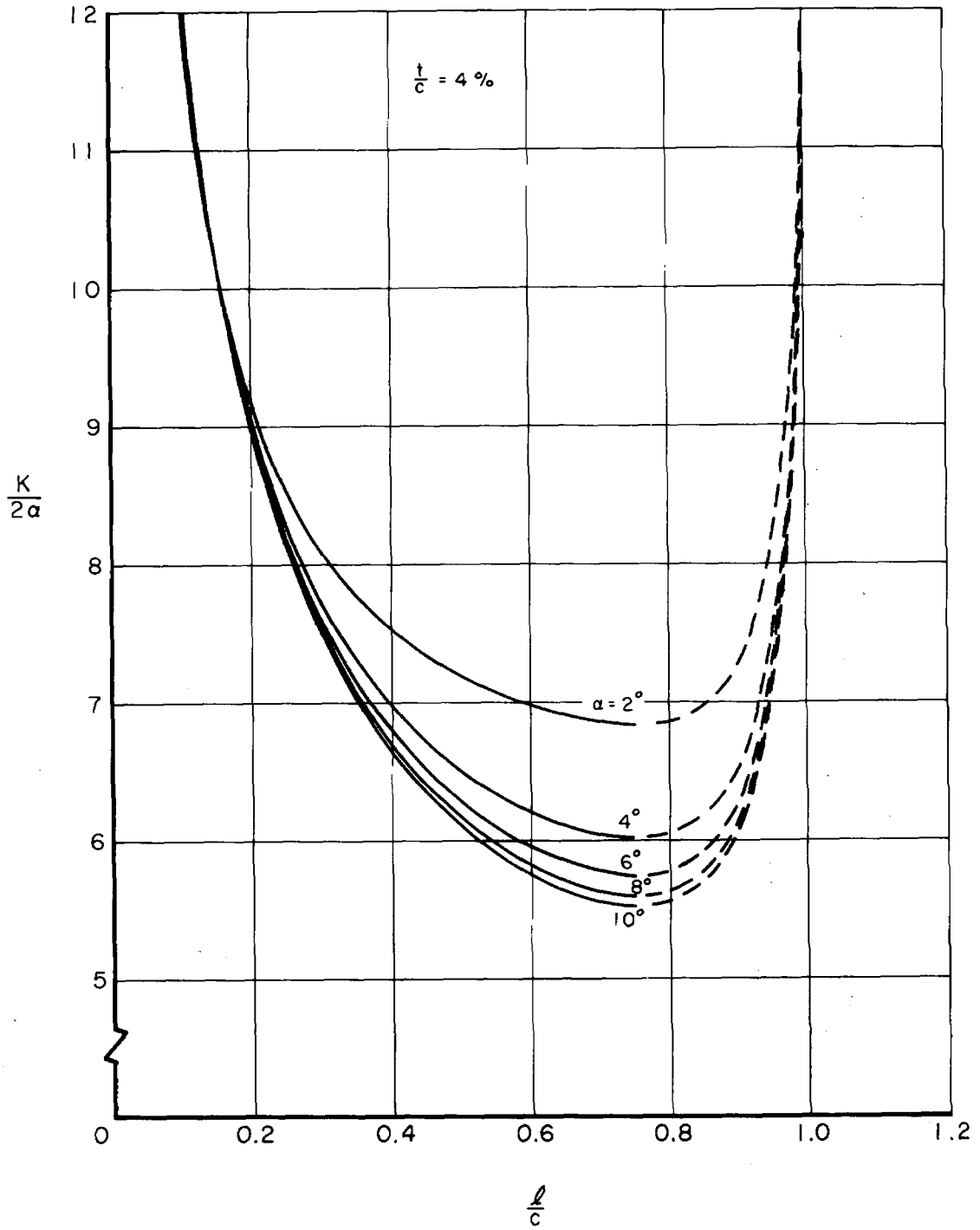

Fig. A4.13 - Ratio of cavitation number to twice the angle of attack α as a function of cavity length-to-chord ratio at various angles of attack α for a thickness ratio of 4%.

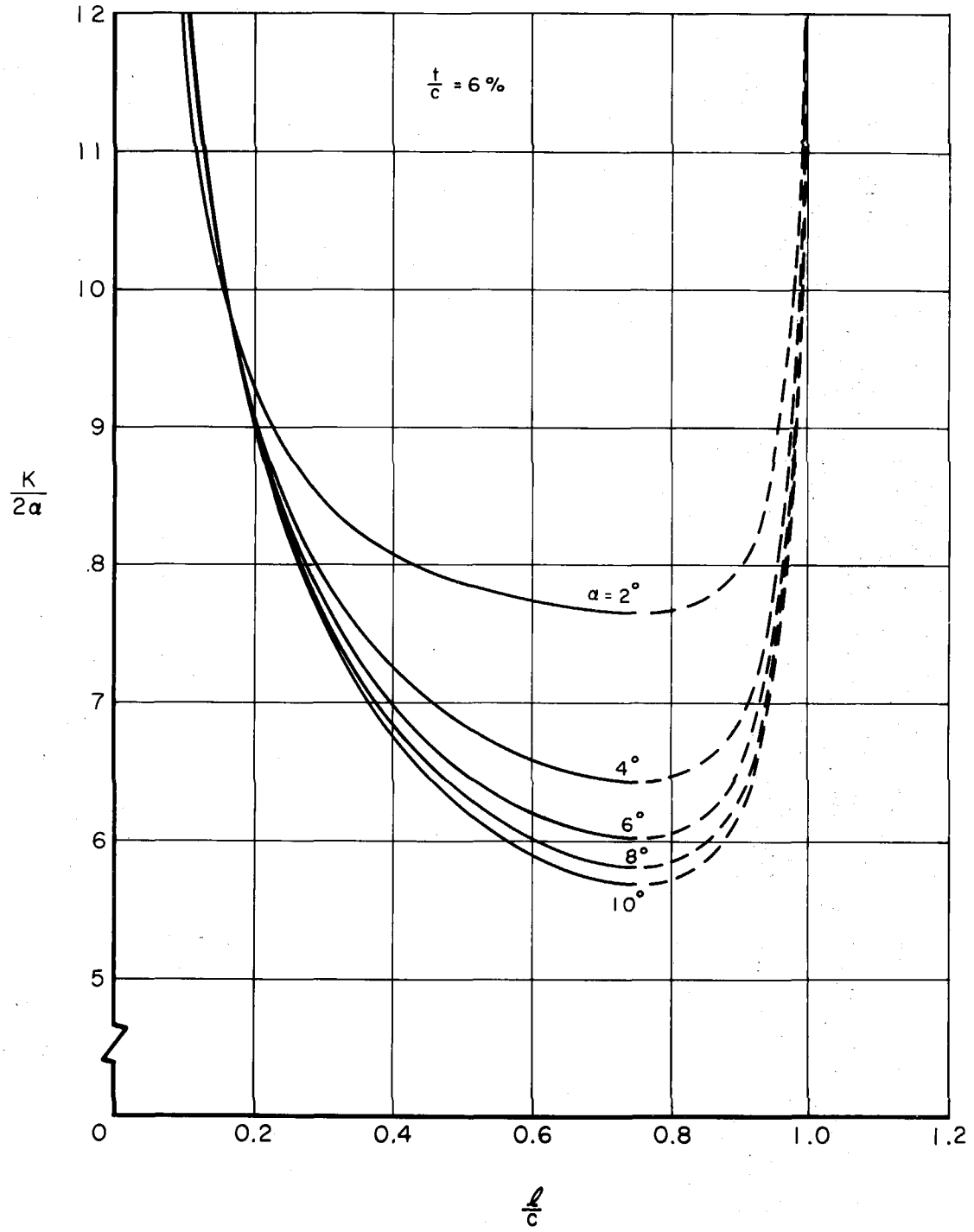

Fig. A4.14 - Ratio of cavitation number to twice the angle of attack α as a function of cavity length-to-chord ratio at various angles of attack α for a thickness ratio of 6%.

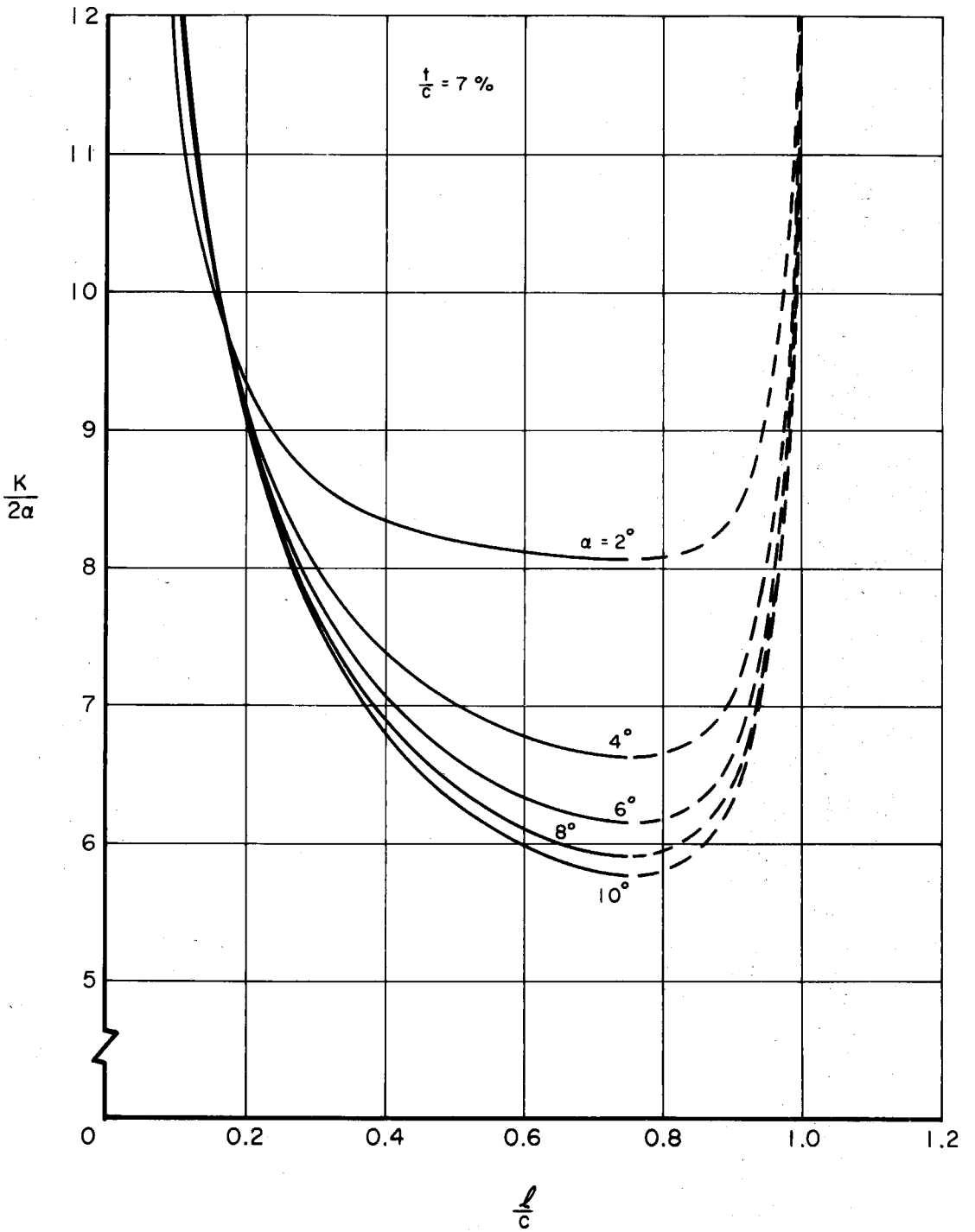

Fig. A4.15 - Ratio of cavitation number to twice the angle of attack α as a function of cavity length-to-chord ratio at various angles of attack α for a thickness ratio of 7%.

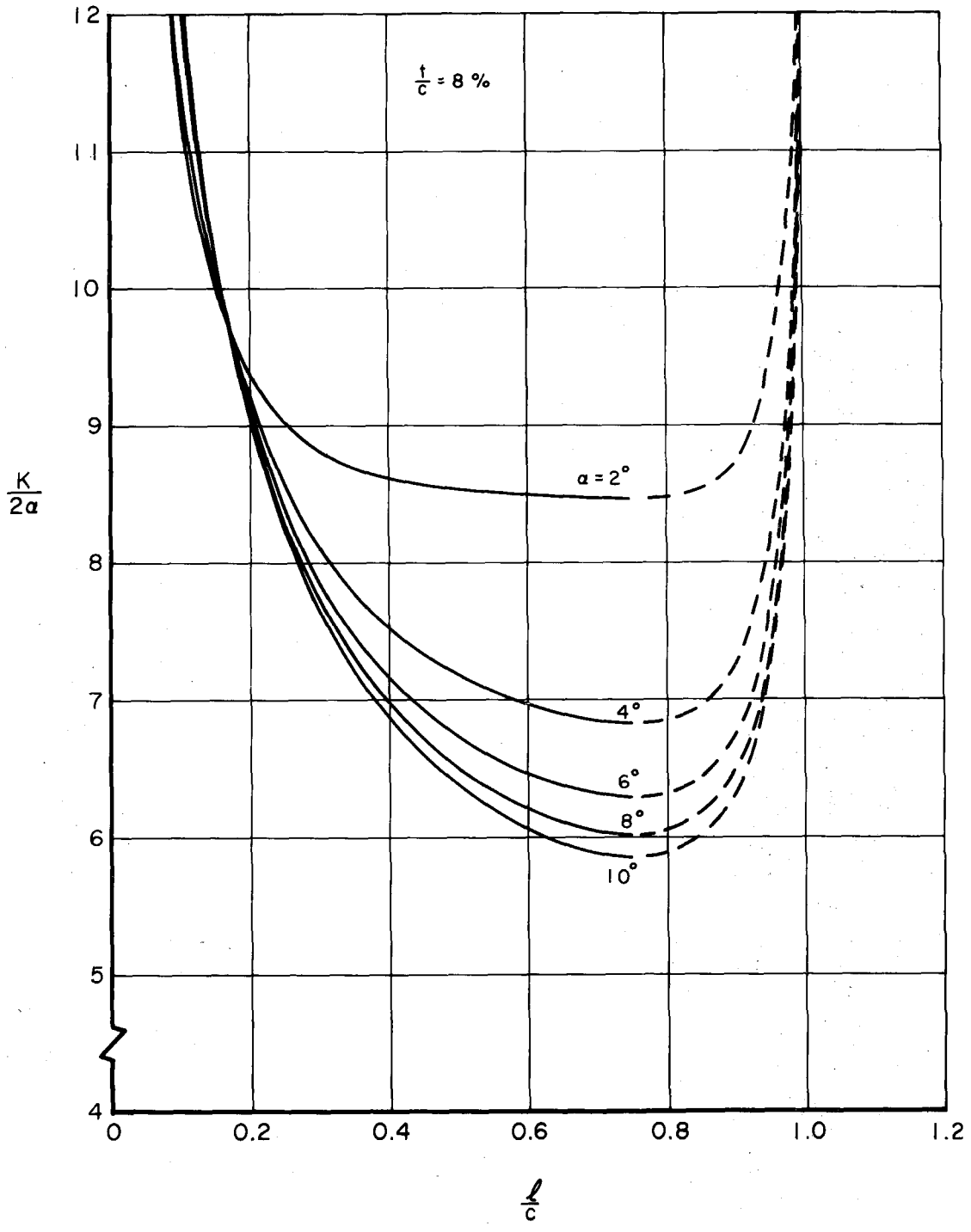

Fig. A4.16 - Ratio of cavitation number to twice the angle of attack α as a function of cavity length-to-chord ratio at various angles of attack α for a thickness ratio of 8%.

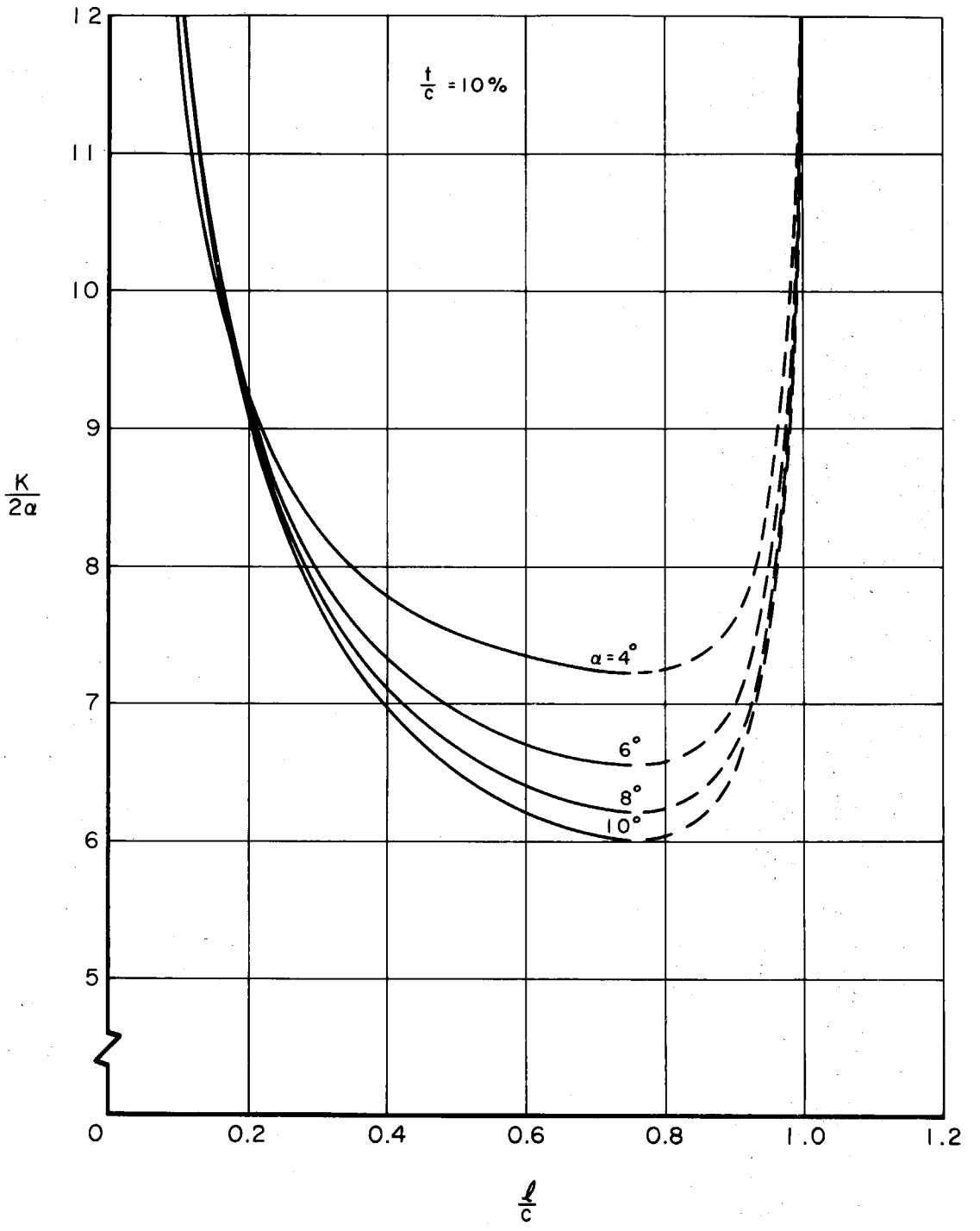

Fig. A4.17 - Ratio of cavitation number to twice the angle of attack α as a function of cavity length-to-chord ratio at various angles of attack α for a thickness ratio of 10%.

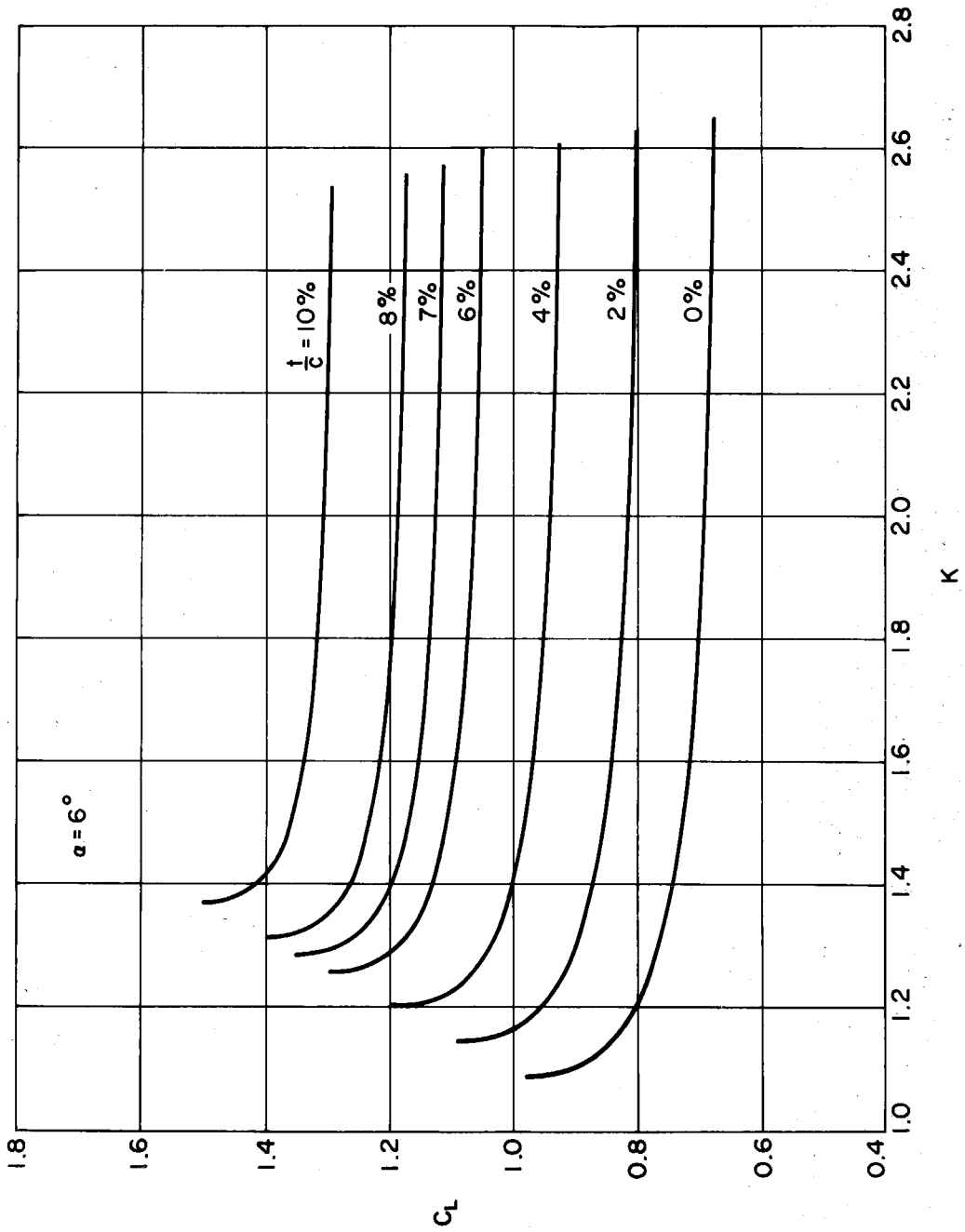

Fig. A4.18 - Lift coefficient versus cavitation number K for various thickness ratios at a fixed angle of attack of 6°.

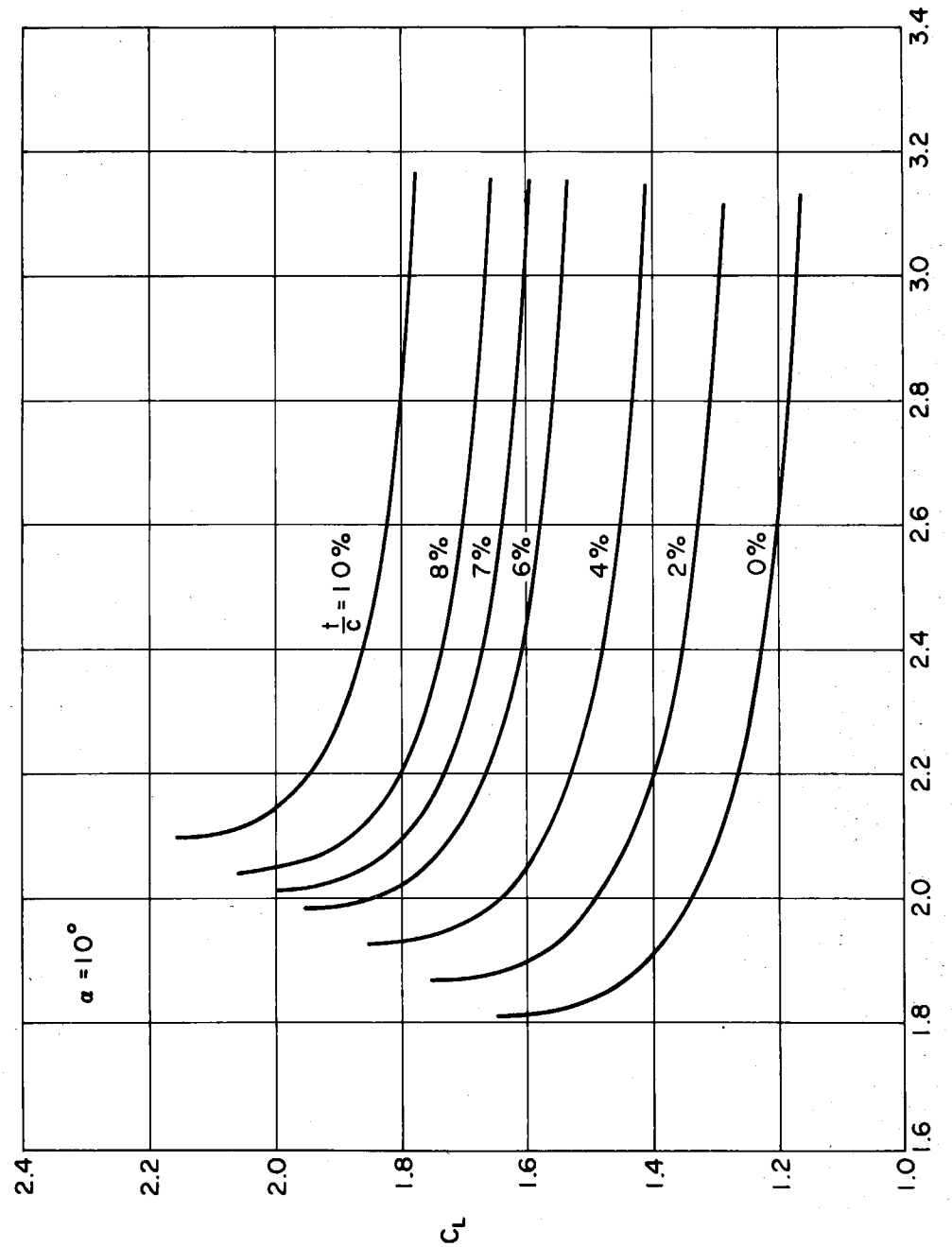

Fig. A4.19 - Lift coefficient versus cavitation number K for various thickness ratios at a fixed angle of attack of 10^{o}.

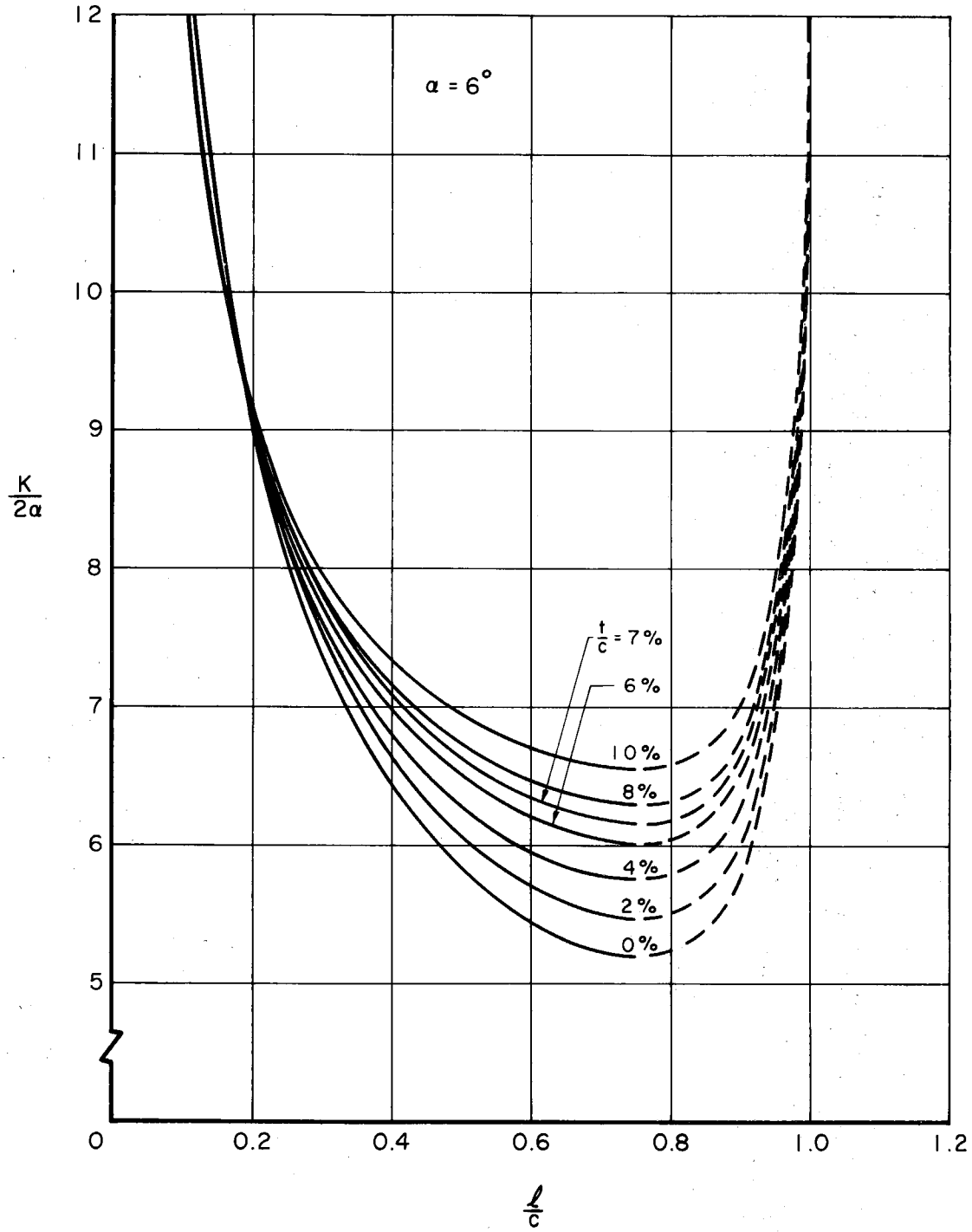

Fig. A4.20 - Ratio of cavitation number to twice the angle of attack as a function of cavity length-to-chord ratio for various thickness ratios at a fixed angle of attack of 6^{o}.

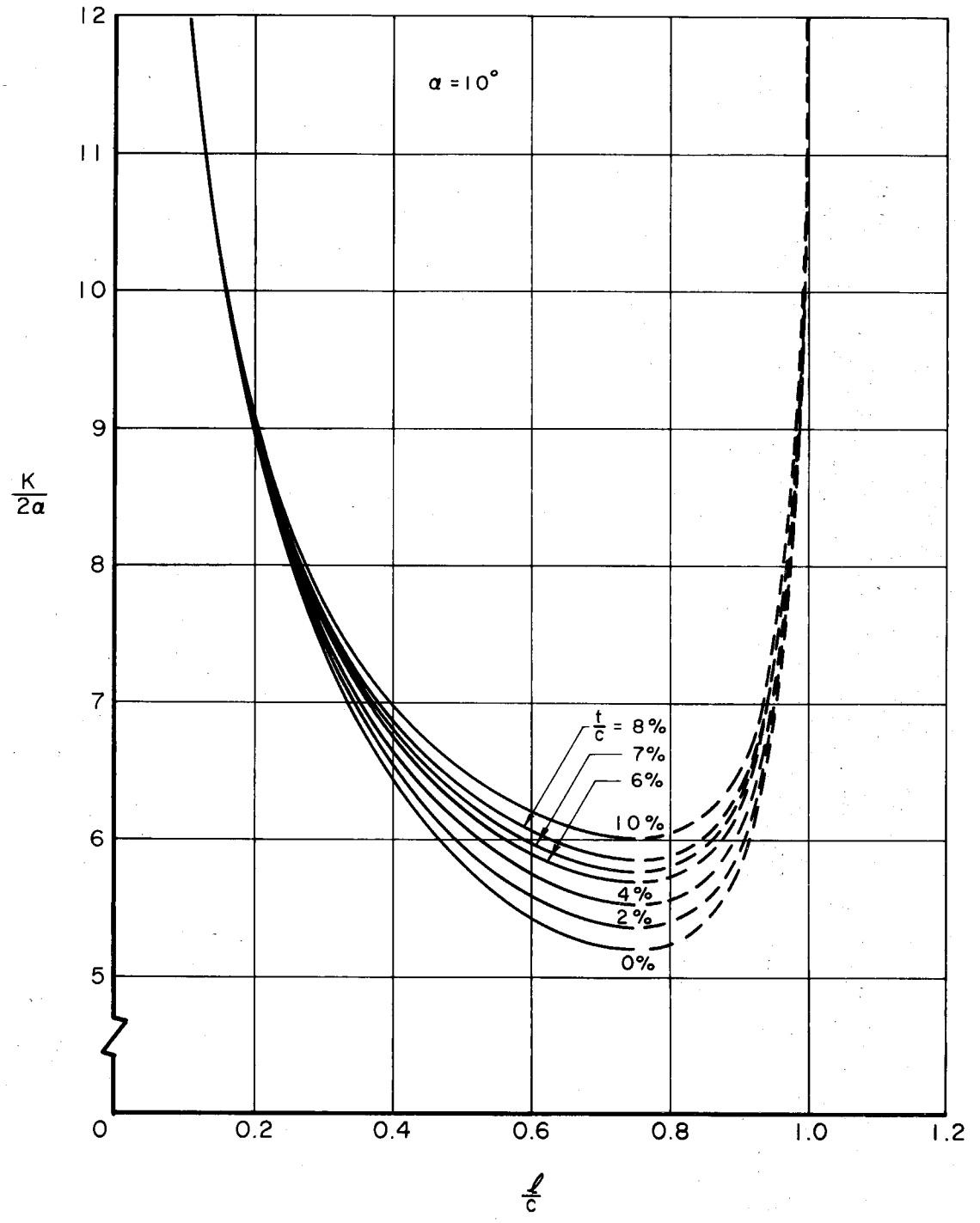

Fig. A4.21 - Ratio of cavitation number to twice the angle of attack as a function of cavity length-to-chord ratio for various thickness ratios at a fixed angle of attack of 10^{o}.

APPENDIX V

CALIBRATION OF MODIFIED TWO-DIMENSIONAL WORKING SECTION

The calibration of the modified working section was undertaken with several aims in view. Since this particular arrangement had never been run before it was of interest to determine whether the design was performing as anticipated and to obtain some idea of the flow characteristics and boundary layer effects. The influence of the movable walls on the pressure distribution in the tunnel was also investigated. The main purpose of the calibration, however, was to correlate the readings of static pressure and differential pressure obtained at the measuring orifice in the nozzle with those measured at a pressure tap located 6 inches upstream of the balance center line. This correlation would enable all static pressures and differential pressures during the tests to be taken at the nozzle orifice, thus obviating any model influences on these readings. The nozzle orifice was deemed to be sufficiently far upstream from the cascade that effects due to circulation and drag would be of negligible importance.

The tests were conducted in the following manner: For constant tunnel speed, static pressure readings were taken at 6 inch intervals along the center line of the tunnel over the entire length of the working section. These readings were recorded with respect to the pressure in the settling chamber with the multi-tube mercury manometer. The

static pressure at the nozzle orifice was recorded on a well-type mercury manometer and the differential pressure across the nozzle to this point was recorded on the oil manometer. From these readings the static pressure distribution along the tunnel center line was found. These readings were repeated for several tunnel speeds.

At each tunnel speed the tunnel ambient pressure was changed and the tests repeated for various pressures to determine if any effect was discernable on the correlation function between the nozzle orifice and the working section orifice. These runs were all carried out with the walls parallel. The effects of changing the wall angles on the pressure distribution in the tunnel were also investigated.

Fig. A5.1 illustrates the pressure distributions in tunnel working section together with the effects of varying wall angle for the three tunnel speeds investigated, viz., 15 ft/sec, 25 ft/sec and 35 ft/sec. The pressure coefficients are referred to the static pressure at the orifice 6 inches upstream from the balance center line. The nozzle orifice reading is shown at -24 inches. It will be noticed that the pressure coefficient at this pressure point is little affected by change in wall angle. Furthermore, it is seen that there is very little pressure undershoot at the nozzle throat which confirms the expectations of the design. Thus little chance exists for cavitation to occur here. This was further confirmed by running the clear tunnel at very low pressures. The general behavior of the curves is fully as expected. The boundary layer effects in the parallel walls are quite reasonable, being 4 percent of the dynamic head 30 inches downstream

from the reference point.

Fig. A5.2 gives the correlation function, f, essentially as a function of tunnel speed represented here by the differential pressure H_1, across the nozzle to the nozzle orifice. The results shown represent the averages of many readings. However, extremely little scatter occurred in these readings. The function f is defined as the ratio of the differential pressure, H_2, across the tunnel nozzle to the working section to the differential pressure, H_1. It will be seen that this ratio is very nearly constant over the range of velocities examined, indicating that there are virtually no Reynolds number effects on this reading.

The evaluation of this function enables the true dynamic head and the tunnel static pressure in the working section to be determined from readings of these quantities at the nozzle orifice. These are obtained simply as follows. Since

$$H_1 = p_H - p_N \quad \text{and} \quad H_2 = p_H - p_T$$

and since

$$f = \frac{H_2}{H_1}$$

we thus have

$$H_2 = H_1 f(H_1) \tag{A5.1}$$

and

$$p_T = p_N - \left[f(H_1) - 1\right] H_1 \tag{A5.2}$$

Therefore, knowing f, H_1, and p_N, one can determine H_2 and p_T.

Under test conditions therefore we obtain from equations A5.1 and A5.2 the dynamic head and tunnel static pressure that would exist in the clear working section.

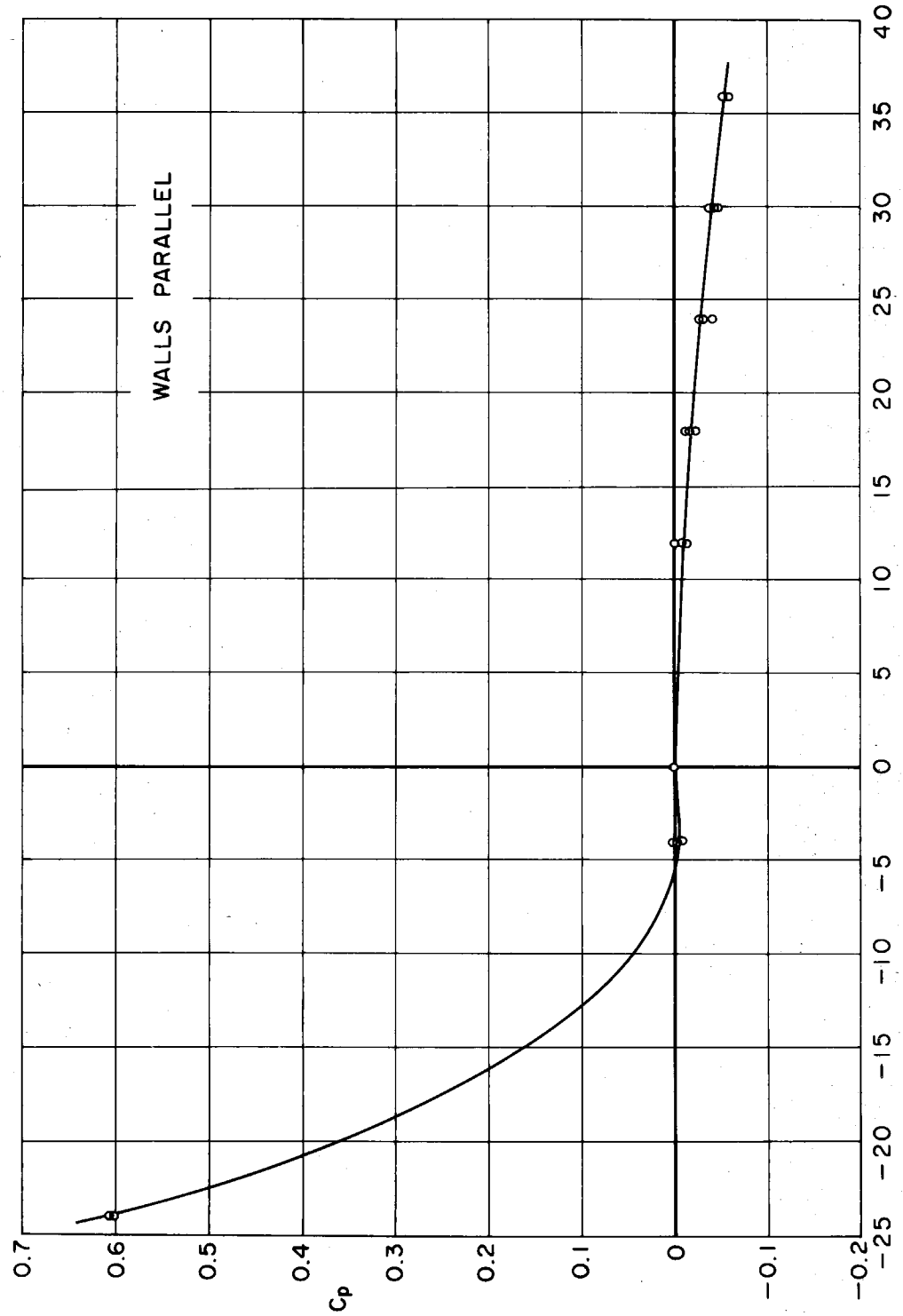

Fig. A5.1(a) - Pressure distributions along the working section center line for several Reynolds numbers as a function of distance from the pressure orifice 6" upstream of the balance center line - walls parallel.

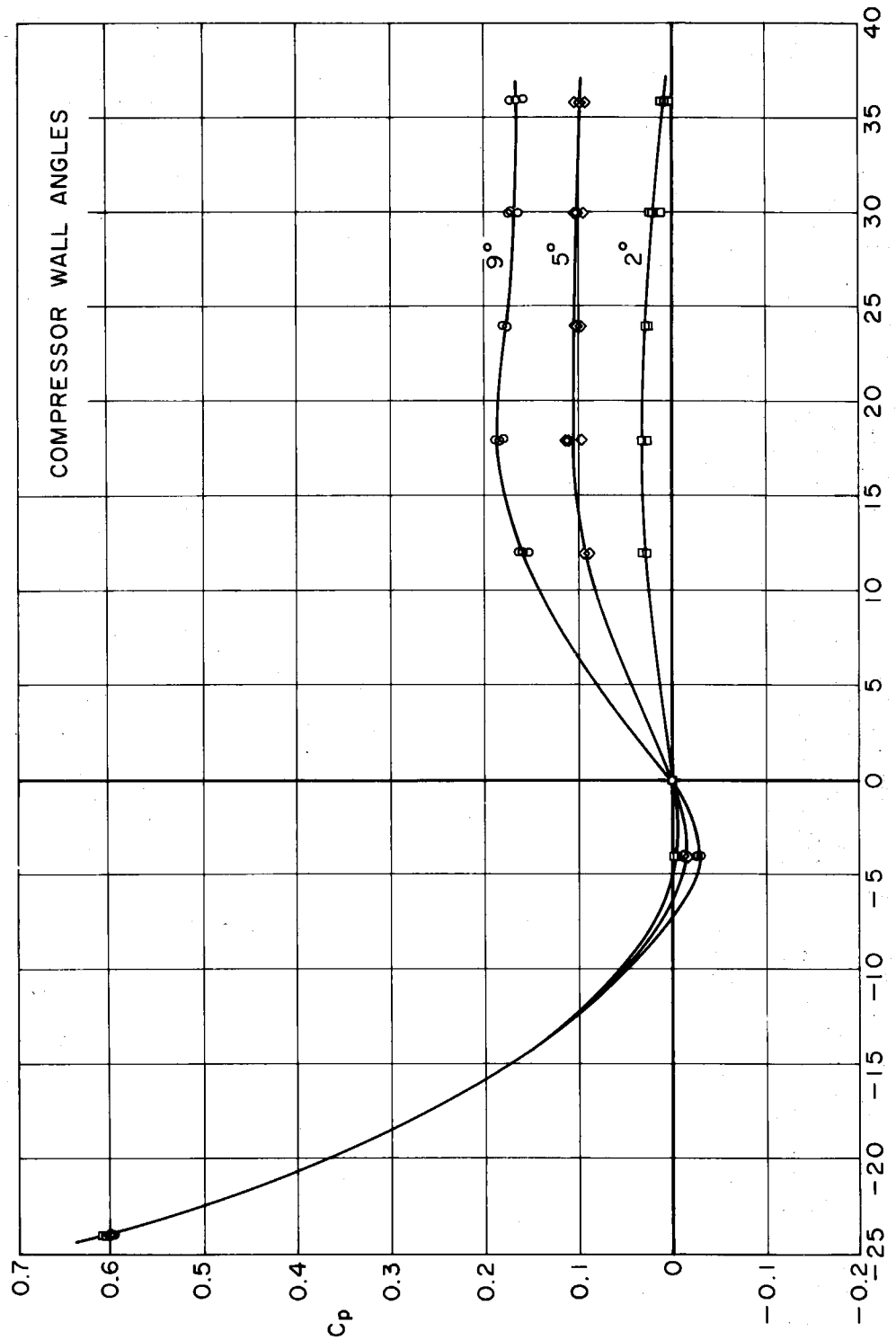

Fig. A5.1(b) - Pressure distributions along the working section center line for several Reynolds numbers as a function of distance from the pressure orifice 6" upstream of the balance center line - compressor wall angles.

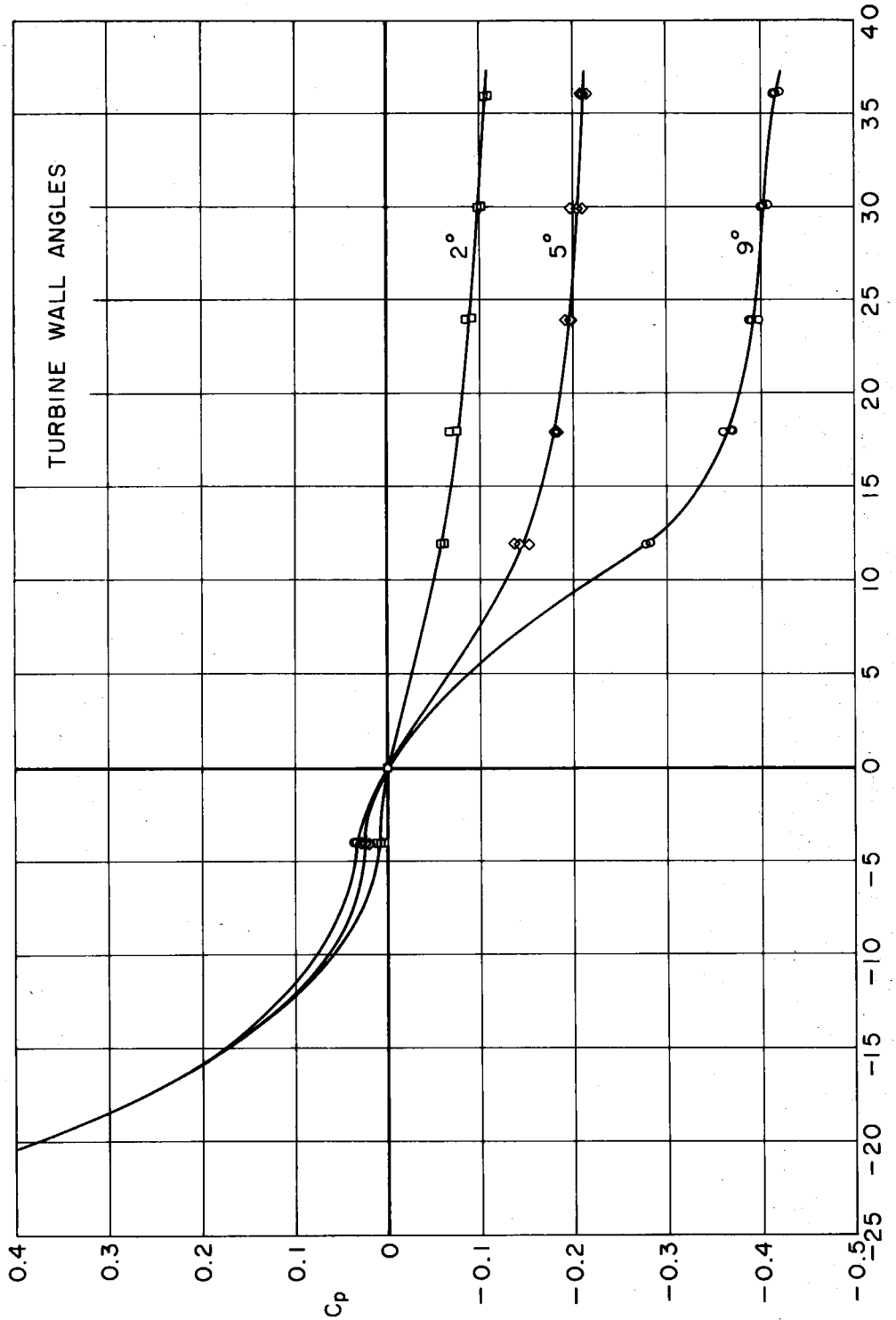

Fig. A5.1(c) - Pressure distributions along the working section center line for several Reynolds numbers as a function of distance from the pressure orifice 6" upstream of the balance center line - turbine wall angles.

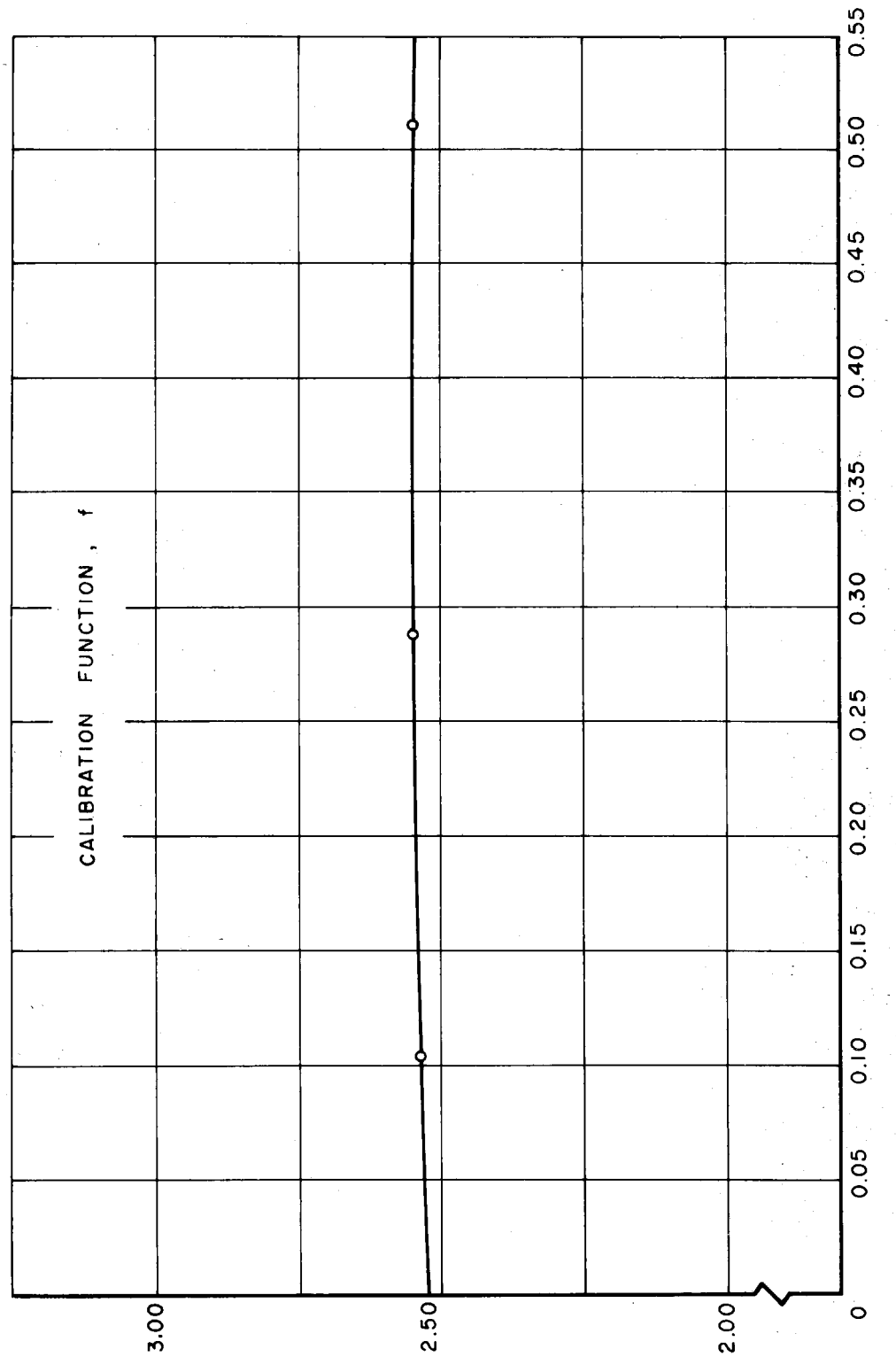

Fig. A5.2 - Calibration function, f as a function of the pressure difference, H_1 for the working section used in the cascade tests.

APPENDIX VI

METHOD OF SETTING THE DOWNSTREAM WALL ANGLES

The iteration procedure used for setting the wall angles in the fully wetted and partially cavitating regions is presented here. Before describing the method the relevant formulae used will be derived for both the compressor and turbine configurations.

Compressor Configuration - With reference to Fig. 41, we have

$$L_m = L \cos \theta_m + D \sin \theta_m$$

where L and D are the measured lift and drag on the force balance. Defining the force coefficients in the following way

$$C_{Lm} = \frac{L_m}{\rho V_m^2 c/2}; \quad C_L = \frac{L}{\rho V_1^2 c/2}; \quad C_D = \frac{D}{\rho V_1^2 c/2}$$

we obtain

$$C_{Lm} = (C_L \cos \theta_m + C_D \sin \theta_m) V_1^2/V_m^2 \quad .$$

However, from the velocity triangles in Fig. 41 we have the following relationship

$$V_m^2 = V_1^2 + u^2 - 2V_1 u \cos (\tfrac{\pi}{2} - \gamma)$$

i.e.,
$$\frac{V_m^2}{V_1^2} = 1 + \frac{u^2}{V_1^2} - 2\frac{u}{V_1} \cos (\tfrac{\pi}{2} - \gamma)$$

but
$$V_1 \sin \theta = 2 u \sin (\tfrac{\pi}{2} - \gamma + \theta)$$

or $$\frac{u}{V_1} = \frac{\sin \theta}{2 \cos (\gamma - \theta)} = \chi \text{ , say}$$

From this equation we have $\chi = \chi \quad (\gamma, \theta)$, hence this quantity is only a function of the turning angle θ once the cascade geometry is known. We therefore have that

$$\frac{V_m^2}{V_1^2} = 1 + \chi^2 - 2 \chi \sin \gamma$$

which in turn is only a function of θ.

As an initial approximation we neglect the drag term in the expression for the lift coefficient above. This is certainly justifiable since under most circumstances $C_D \sin \theta_m << C_L \cos \theta_m$. Doing this we obtain

$$C_{Lm} = C_L \cos \theta_m \; V_1^2 / V_m^2$$

or

$$C_L = \frac{C_{Lm}}{\cos \theta_m} \frac{V_m^2}{V_1^2} \quad .$$

Now, from the Kutta-Joukowski law for the cascade, we have that

$$L_m = \rho V_m \Gamma = \rho V_m (2us)$$

hence

$$C_{Lm} = \frac{4u}{\sigma V_m}$$

where $\sigma = \frac{c}{s}$, the solidity ratio.

Therefore

$$C_{Lm} = \frac{4}{\sigma \cos \theta_m} \cdot \frac{u}{V_m} \cdot \frac{V_m}{V_1}$$

Again, from the velocity triangles, we find that

$$V_1 - u \cos\left(\frac{\pi}{2} - \gamma\right) = V_m \cos \theta_m$$

or

$$\cos \theta_m = \frac{V_1}{V_m}\left[1 - \frac{u}{V_1} \sin \gamma\right]$$

$$\cos \theta_m = \frac{1}{(1 + \chi^2 - 2\chi \sin\gamma)^{\frac{1}{2}}}\left[1 - \chi \sin \gamma\right].$$

We can therefore finally write

$$C_L = \frac{4}{\sigma} \chi \cdot \frac{(1 + \chi^2 - 2\chi \sin\gamma)}{(1 - \chi \sin \gamma)}$$

This expression is purely a function of the turning angle, θ for any given cascade geometry.

In the above formulation the approximation made was in neglecting the drag term. If this term is considered as a correction term to the above expression, we have as error the term $-C_D \tan \theta_m$ which can be written as

$$- C_D \cdot \frac{\chi \cos \gamma}{(1 - \chi \sin \gamma)}$$

This error term is known as a function of θ provided the drag coefficient is known for the particular lift conditions.

Based on the above formulae the following iteration for setting the walls is adopted.

Step 1 - For any given angle of attack α the walls are adjusted while monitoring the lift balance until a rough setting is obtained.

Step 2 - The lift coefficient is then obtained from the balance and

differential pressure reading and the corresponding turning is read off the C_L versus θ curve in Fig. A6.1, obtained from the above equations. The walls are then readjusted to this value.

Step 3 - The new lift is calculated and the procedure repeated, if necessary. When the values are in close agreement the drag is also determined and from the tan θ_m versus θ curve a value of tan θ_m is read off and the correction term is thus obtainable. This gives a new value for C_L from which a more accurate value of θ can be found.

Step 4 - This last process may be repeated until no further change occurs.

Usually the method converges very rapidly. After two iterations, in fact, a fairly accurate angle is obtained. One correction for drag is all that is necessary to achieve final convergence to within experimental values.

Turbine Configuration: The procedure used here is identical with the preceding one. The relevant formulae are

$$C_L = \frac{4}{\sigma} \chi \cdot \frac{(1 + \chi^2 + 2\chi \sin\gamma)}{(1 + \chi \sin\gamma)}$$

and for the correction term we obtain

$$- C_D \tan \theta_m = - C_D \frac{\chi \cos \gamma}{(1 + \chi \sin\gamma)}$$

These formulae are simply obtained by replacing γ by $-\gamma$ in the previous formulae. These functions are plotted in Fig. A6.2.

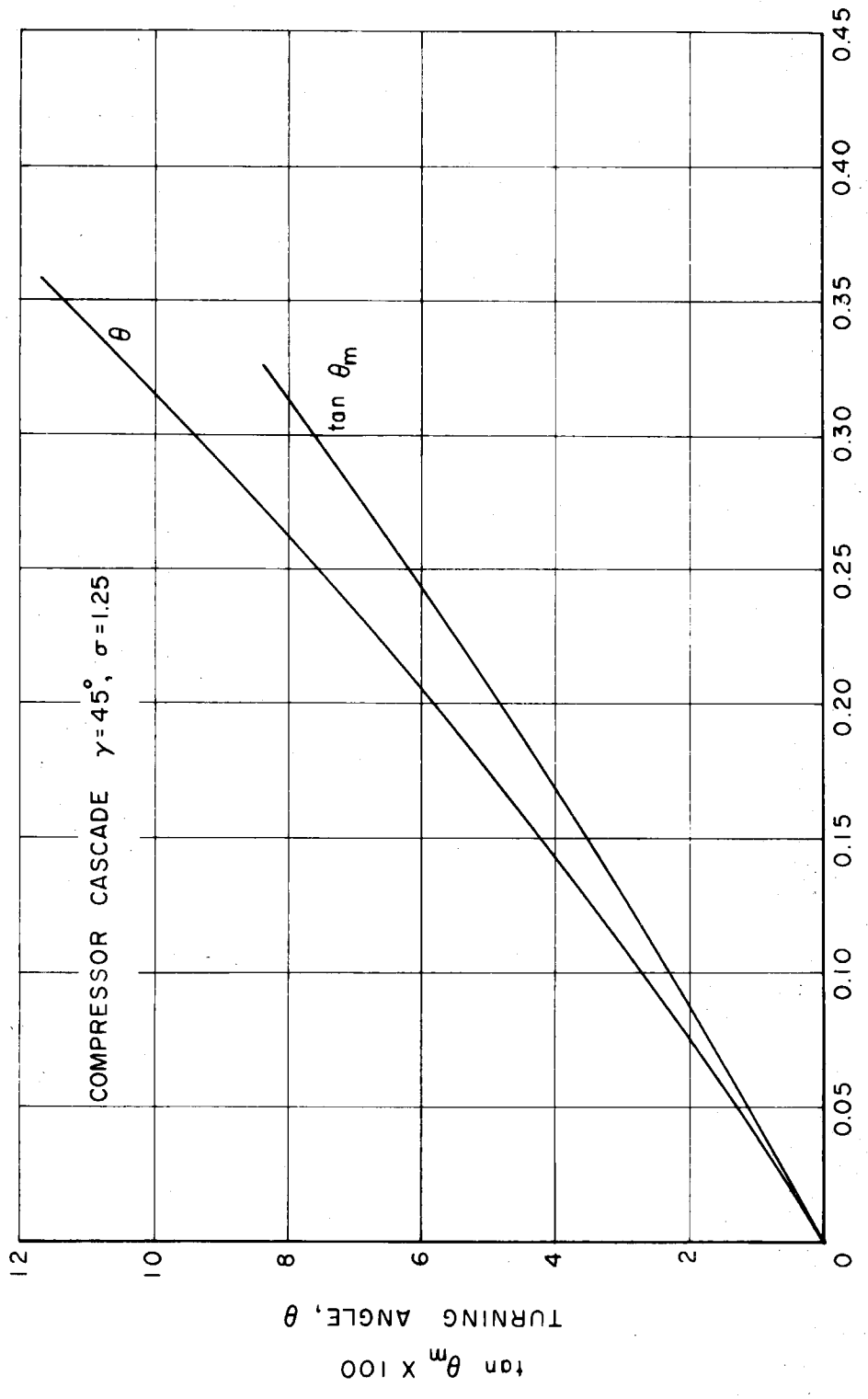

Fig. A6.1 - Lift coefficient based on upstream flow and the tangent of the mean turning angle θ_m as a function of turning angle for compressor cascade.

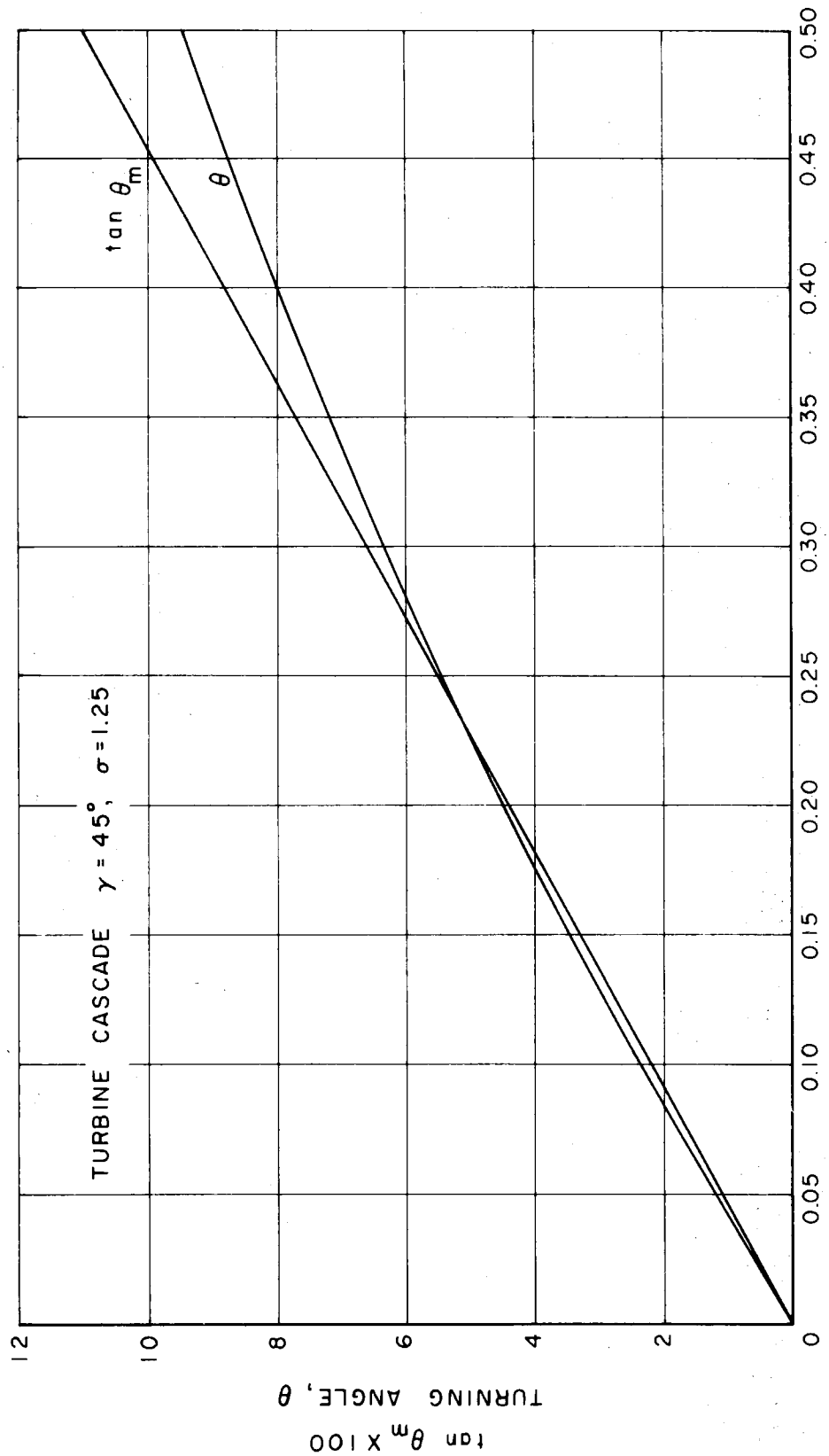

Fig. A6.2 - Lift coefficient based on upstream flow and the tangent of the mean turning angle θ_m as a function of turning angle for turbine cascade.

APPENDIX VII

TARE FORCE CORRECTIONS FOR CASCADE EXPERIMENTS

The tare forces acting on the fairing plate were obtained by remounting the center foil of the cascade from the lucite window and inserting a blank disk on the balance spindle. An extra model had been manufactured for this purpose. The procedure used was then identical with that for the isolated hydrofoil. Further details may also be obtained from Reference 14.

The results of this test are presented in graphical form in Figs. A7.1 - A7.3 for the compressor of 1.25 solidity.

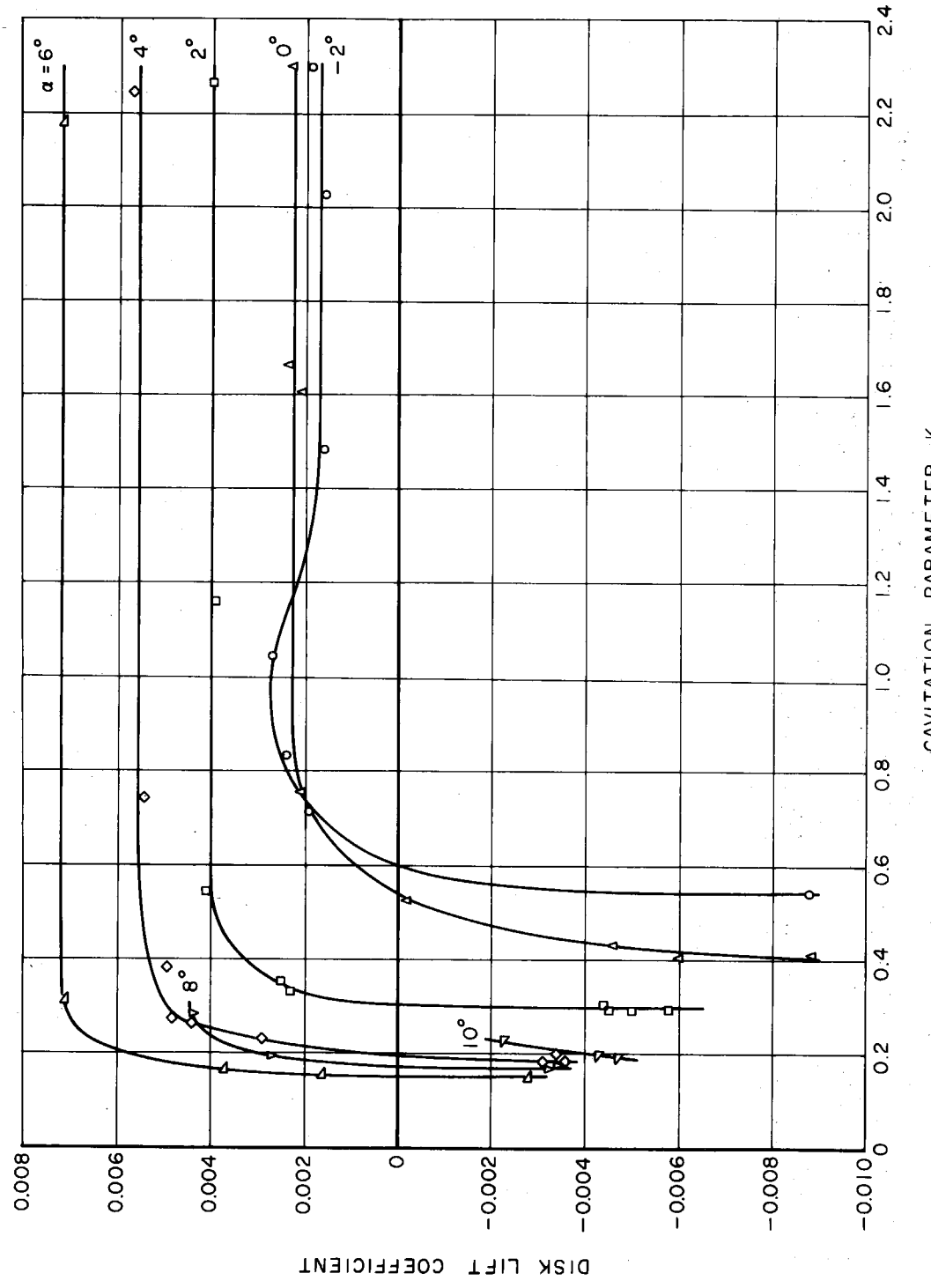

Fig. A7.1 - Tare lift force coefficient on disk as a function of cavitation parameter for compressor cascade of solidity $\sigma = 1.25$.

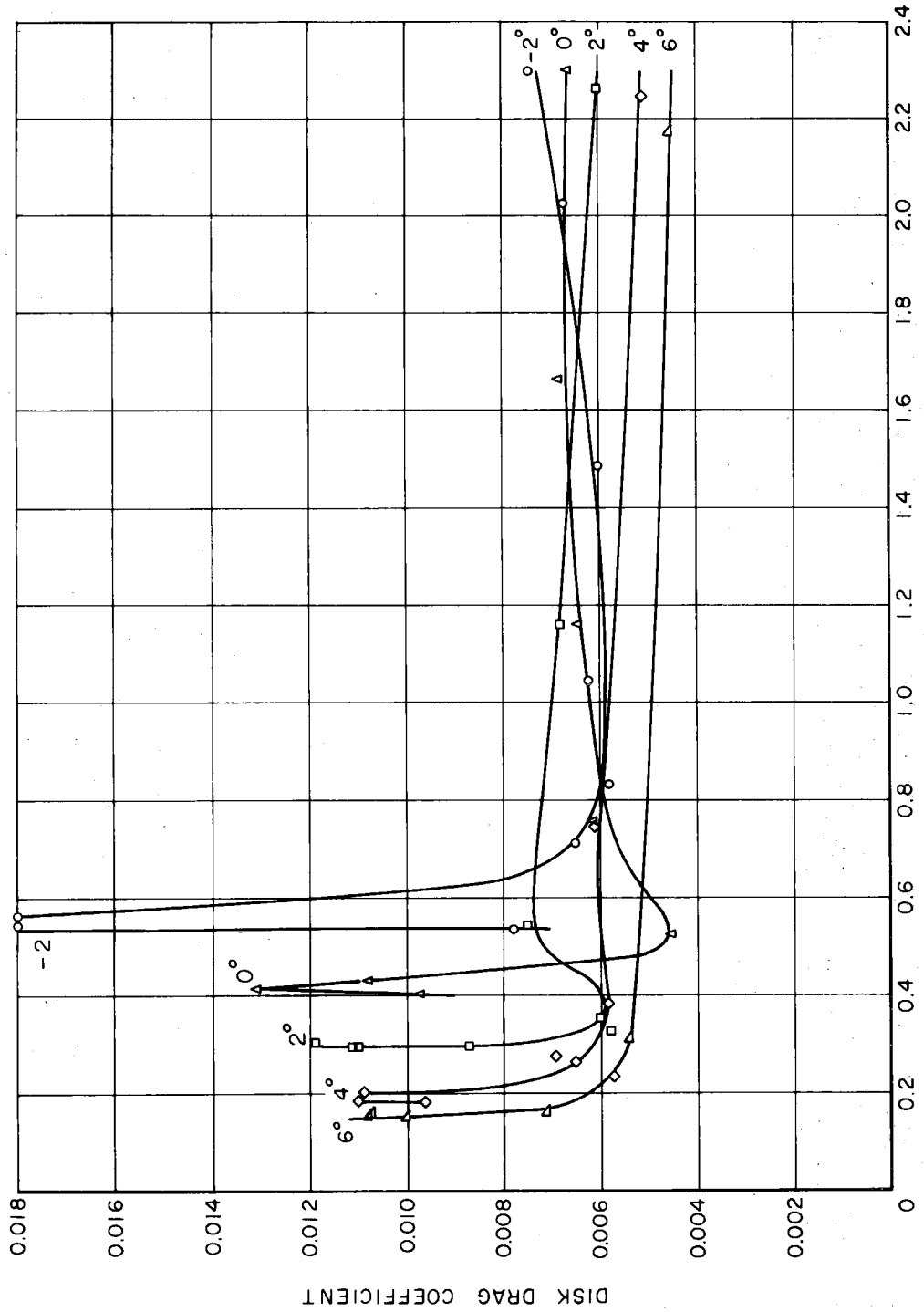

Fig. A7.2 - Tare drag coefficient on disk as a function of cavitation parameter for compressor cascade of solidity $\sigma = 1.25$.

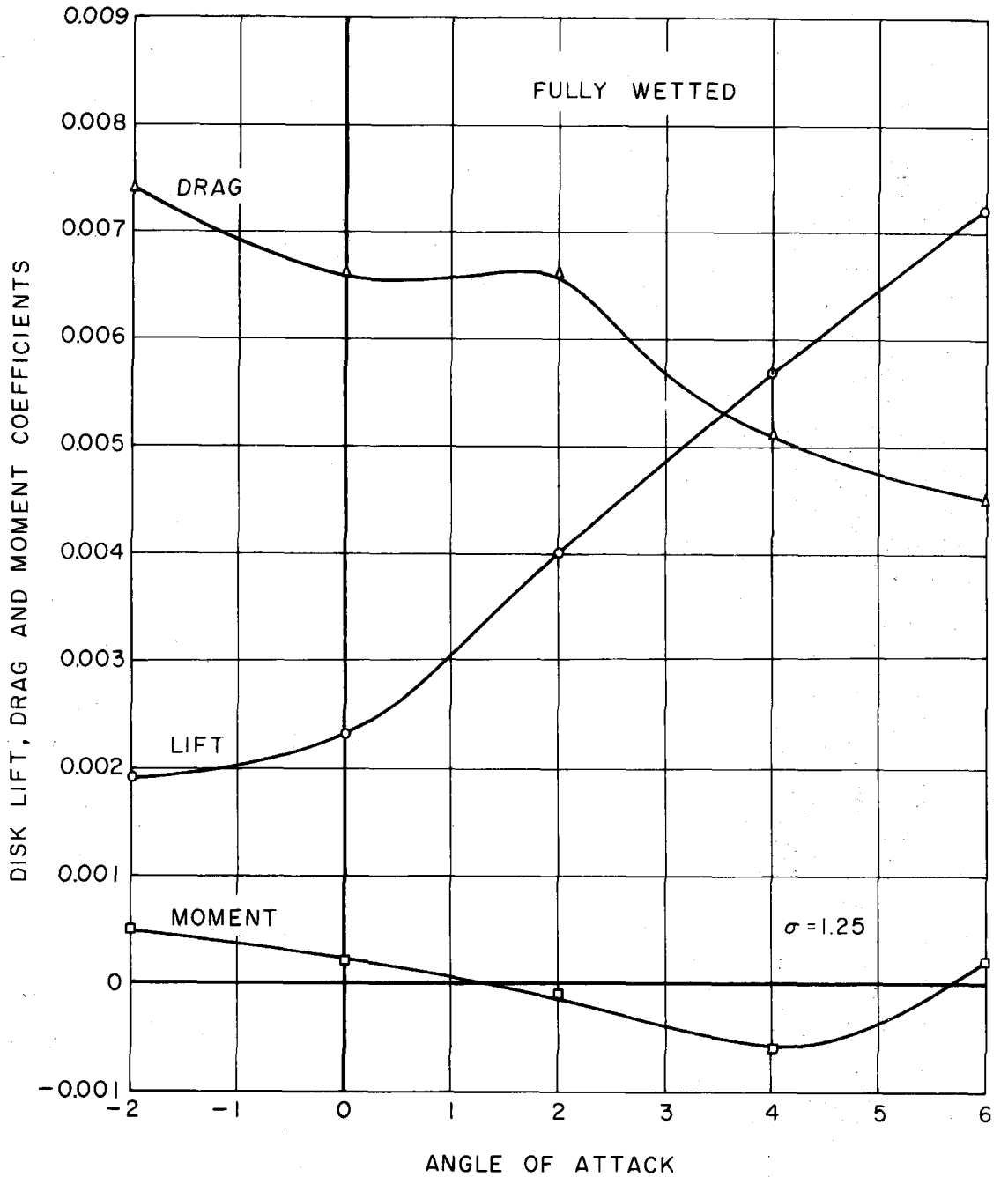

Fig. A7.3 - Tare force coefficients as functions of angle of attack for non-cavitating flow for compressor cascade of solidity $\sigma = 1.25$.

APPENDIX VIII

DATA REDUCTION FOR CASCADE TESTS

1. Calculation of Force Coefficients

Two systems of representation are used in the fully wetted data - the force coefficients based on upstream flow velocity and those based on the mean conditions. These two systems are inter-related. From Fig. 41 we obtain the following equations

$$L_m = L\cos\theta_m + D\sin\theta_m$$

$$D_m = -L\sin\theta_m + D\cos\theta_m$$

defining the lift and drag coefficient as

$$C_{Lm} = \frac{Lm}{\rho V_m^2 A/2} \quad \cdot \quad C_{Dm} = \frac{Dm}{\rho V_m^2 A/2}$$

$$C_L = \frac{L}{\rho V_1^2 A/2} \quad \cdot \quad C_D = \frac{D}{\rho V_1^2 A/2}$$

we obtain from above

$$C_{Lm} = \left[C_L\cos\theta_m + C_D\sin\theta_m\right] \frac{V_1^2}{V_m^2}$$

$$C_{Dm} = \left[-C_L\sin\theta_m + C_D\cos\theta_m\right] \frac{V_1^2}{V_m^2} \quad .$$

where L and D are the measured lift and drag from the force balance. The moment coefficient is defined as

$$C_M = \frac{M}{\rho V_1^2 Ac/2} \quad , \quad C_{Mm} = \frac{M}{\rho V_m^2 Ac/2}$$

where the same convention is used as in Part I.

The mean force coefficients can therefore be obtained from the measured ones provided θ_m and V_1/V_m can be determined experimentally.

2. Calculation of Flow Angles

From Fig. 41 we see that

$$V_1 \cos\gamma = V_2 \cos(\gamma - \theta) = V_m \cos(\gamma - \theta_m) \qquad (A8.1)$$

Further

$$V_1 \sin\gamma = 2\left[V_m \sin(\gamma - \theta_m) - V_2 \sin(\gamma - \theta)\right] + V_2 \sin(\gamma - \theta)$$

or

$$V_m \sin(\gamma - \theta_m) = \frac{1}{2}\left[V_1 \sin\gamma + V_2 \sin(\gamma - \theta)\right]$$

hence we obtain

$$\tan(\gamma - \theta_m) = \frac{1}{2}\left[\tan\gamma + \tan(\gamma - \theta)\right] \qquad (A8.2)$$

If we compare these equations with those usually used in cascade work using the angles α, α_2, α_m, and β as defined in Fig. 41, then we obtain

$$\gamma - \theta = \alpha_m + \beta$$

$$\gamma = \alpha + \beta$$

$$\gamma - \theta = \alpha_2 + \beta$$

or

$$\beta = (\gamma - \alpha); \quad \alpha_m = (\alpha - \theta_m); \quad \alpha_2 = (\alpha - \theta)$$

where α is the angle of attack. Furthermore from equation (A8.2), θ_m can be determined from the measured value of θ which is the wall angle. Hence α_m and α_2 are also determined.

3. Velocity Ratios

The velocity ratios can be obtained from equation (A8.1). They are given by

$$\frac{V_1}{V_m} = \frac{\cos(\gamma - \theta_m)}{\cos\gamma}$$

and

$$\frac{V_1}{V_2} = \frac{\cos(\gamma - \theta)}{\cos\gamma}$$

4. Cavitation Parameter

The cavitation parameter used in all of the cascade tests is based on vapor pressure and upstream velocity, i.e.,

$$K_v = \frac{p - p_v}{\rho V_1^2/2}$$

5. Unsteady Measurements

From the unsteady measurements taken in the cascade experiments it was hoped, apart from obtaining the basic frequencies of oscillation and the cavity behavior, to obtain more information concerning the influence of these oscillations on the main tunnel flow. To achieve this the outputs of the transducers were utilized. The general procedure used will now be presented.

Considering the time dependent Bernoulli equation

$$\rho \frac{\partial \varphi}{\partial t} + \frac{1}{2} \rho V^2 + p(t) = C(t),$$

and applying this equation at two points in the flow (N, H) we obtain

$$\rho \frac{\partial}{\partial t} (\varphi_N - \varphi_H) + \frac{1}{2} \rho V_N^2 \left(1 - \frac{V_H^2}{V_N^2}\right) + p_N(t) - p_H(t) = 0 \qquad \text{(A8.3)}$$

Furthermore, from the continuity equation, we have that

$$A_H V_H = A_N V_N = a(x)u(x) \qquad \text{(A8.4)}$$

where a(x), u(x) are the area and velocity at any point x in the tunnel.

Now

$$u = \frac{\partial \varphi}{\partial x}$$

or

$$\varphi = \int \varphi dx + C$$

hence

$$\varphi_N - \varphi_H = \int_H^N u dx \quad .$$

But from equation (A8.4) we have

$$u(x) = \frac{A_N}{a(x)} V_N$$

therefore

$$\varphi_N - \varphi_H = \int_H^N A_N V_N \frac{dx}{a(x)} \qquad \text{(A8.5)}$$

To evaluate this integral a plot was made of the area distribution in the modified nozzle as a function of x. This curve was then integrated numerically. This value can be expressed as

$$\varphi_N - \varphi_H = K_1 V_N \tag{A8.6}$$

Furthermore, from equation (A8.4) we have

$$\frac{1}{2}\rho\left(1 - \frac{V_H^2}{V_N^2}\right) V_N^2 = \frac{1}{2}\rho\left(1 - \frac{A_N^2}{A_H^2}\right) V_N^2 = K_2 V_N^2 \tag{A8.7}$$

where

$$K_2 = \frac{1}{2}\rho\left(1 - \frac{A_N^2}{A_H^2}\right) .$$

If we write $G(t) = p_H(t) - p_N(t)$ then equation (A8.3) can be written as

$$K_1 \frac{dV_N}{dt} + K_2 V_N^2 = G(t). \tag{A8.8}$$

As an approximate solution to this non-linear equation, we consider the velocity to be made up of a mean component $\bar{V}_N$ independent of time and a fluctuating component V_N' such that $V_N' << \bar{V}_N$. Substituting in the equation yields

$$\frac{dV_N'}{dt} + \omega^2\left[\bar{V}_N^2 + 2\bar{V}_N V_N'\right] = \frac{1}{K_1}\left[\bar{G} + G'\right]$$

where $\omega^2 = \frac{K_2}{K_1}$ and $G(t) = \bar{G} + G'(t)$.

Separating this equation into the time independent and time dependent parts, gives

$$\bar{V}_N^2 = \frac{\bar{G}}{K_2} = \overline{(p_H - p_N)} \Big/ \frac{1}{2}\rho\left(1 - \frac{A_N^2}{A_H^2}\right)$$

which is Bernoulli's equation, as expected, applied to the mean conditions. The second equation is

$$\frac{dV_N'}{dt} + 2\omega^2 \bar{V}_N V_N' = \frac{1}{K_1} G'(t) \qquad (A8.9)$$

assuming $G'(t)$ is of the form

$$G'(t) = A \cos \varphi t$$

the solution of this equation is

$$V_N' = \frac{A}{K_1 \left[\varphi^2 + (2\omega^2 \bar{V}_N)^2\right]^{\frac{1}{2}}} \cos (\varphi t + \psi)$$

where

$$\psi = \tan^{-1} \left(\frac{\varphi}{2\omega^2 \bar{V}_N} \right) \quad .$$

Hence we find that due to the oscillations in pressure between the points p_H and p_N there is a fluctuating velocity which is out of phase with the pressure field and whose amplitude is attenuated. The phase and attenuation depend on the nozzle shape.

From a Fourier analysis of the fluctuating pressures at the nozzle point and a point in the settling chamber of the tunnel, the above equations were solved for the fluctuating velocity. A typical result is given in Section IX.

APPENDIX IX

LINEARIZED THEORY OF PARTIALLY CAVITATING CASCADE OF FLAT PLATE HYDROFOILS

This appendix deals with the non-viscous steady cavitating flow through a cascade of flat plate hydrofoils in two dimensions. The usual assumptions of incompressibility and irrotationality are made. In dealing with cavitating cascade flows, hodograph methods become somewhat unwieldy, and hence linearized methods are used for solving these problems. This method, first used by Tulin (8) assumes that the cavity-body system forms a slender body and that a perturbation technique similar to that used in thin airfoil theory may be used. The use of the linearized method leads to the solution of a mixed boundary value problem.

Formulation of the Problem

As illustrated in Fig. A9.1, the cascade consists of an infinite array of flat plate hydrofoils having a stagger angle β. The chord length of each blade is c and the spacing of the hydrofoils in the direction of the stagger angle is taken as 2π. Hence the solidity, $\sigma = c/2\pi$.

The flow approaches the cascade with velocity V_1 at an angle of attack α_1. The flow is turned by the cascade so that far downstream the flow velocity V_2 is at an angle α_2 to the blade chord. The cavities spring from the leading edge and terminate on the upper surface of each

hydrofoil. In keeping with the linearized theory the thickness of the cavity is assumed small compared with the blade spacing 2π. The boundary conditions on the free streamline of the cavity are then applied along the real axis, as are the conditions on the wetted surface of the hydrofoils.

The velocity field is now considered as a perturbation about the velocity V_1. Although in the neighborhood of the cascade a more natural characteristic velocity would be the vector mean velocity V_m, it is found more convenient to adopt V_1, as V_m is undetermined a priori, since it depends on V_2. In the calculation of the lift coefficient however, the angle which the vector mean V_m makes with the blades, viz., α_m, is used so as to bring it in line with fully wetted cascade flows.

The governing parameter in cavity flows is the cavitation number K defined as

$$K = \frac{p_1 - p_c}{\frac{1}{2} \rho V_1^2} \tag{A9.1}$$

where p_1 is the pressure at upstream infinity and p_c is the cavity pressure, which is a constant. Since the velocity is defined at any point as

$$V = (u, v) = (V_1 + u', v') \tag{A9.2}$$

where u', v' are perturbation components assumed small, compared to V_1 we obtain by the use of Bernoulli's equation

$$K = \frac{V_c^2}{V_1^2} - 1 \quad .$$

However, neglecting the squares of u', v' compared with V_1^2, this becomes

$$K = \frac{2u_c'}{V_1}$$

$$u_c' = \frac{KV_1}{2}$$

On the wetted portion of the hydrofoils, $v = 0$, i.e., there is no flow through the blades. A further condition that has to be met, is the closure condition, which requires that the cavity-body system form a closed body. This condition can be expressed as

$$\int_{body} dy = 0 \qquad \text{(A9.3)}$$

The above conditions, together with the requirement that the velocity be finite at the trailing edge, enable a unique solution for the problem to be determined.

Hence the conditions to be satisfied are:

(a) $v = 0$ on the wetted portion of the hydrofoil

(b) $u_c = V_1(1 + \frac{K}{2})$ on the cavity

(c) $V = V_1 e^{-i\alpha} 1$ at upstream infinity

(d) the closure condition, viz.,

$$\int_{body} dy = 0$$

(e) V is finite at the trailing edge.

These conditions are sufficient to determine the velocity function at every point including the downstream conditions where

$$V = V_2 e^{-i\alpha_2} .$$

Before proceeding to solve the boundary value problem we derive the following simple relations from continuity considerations. The velocity triangle is as follows

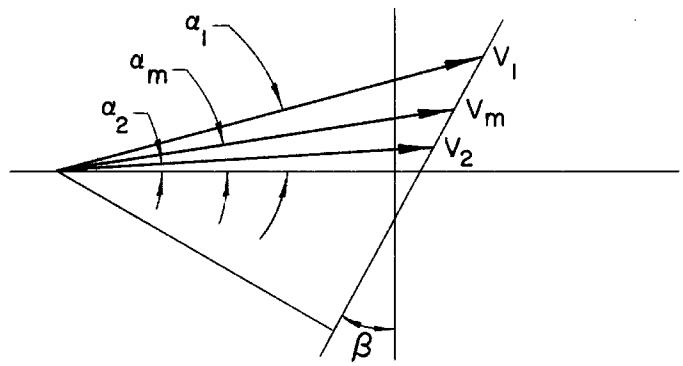

From this diagram we obtain

$$V_m \sin(\alpha_m + \beta) = \frac{1}{2}\left[V_1 \sin(\alpha_1 + \beta) + V_2 \sin(\alpha_2 + \beta)\right]$$

$$V_m \cos(\alpha_m + \beta) = V_1 \cos(\alpha_1 + \beta) = V_2 \cos(\alpha_2 + \beta) \qquad \text{(A9.4)}$$

from which we get

$$\tan(\alpha_m + \beta) = \frac{1}{2}\left[\tan(\alpha_1 + \beta) + \tan(\alpha_2 + \beta)\right] \qquad \text{(A9.5)}$$

Transformation Functions

Consider the transformation function

$$z = e^{-i\beta} \ln \frac{1 - \frac{\zeta}{\zeta_1}}{1 - \frac{\zeta}{\zeta_2}} + e^{i\beta} \ln \frac{1 - \frac{\zeta}{\zeta_1}}{1 - \frac{\zeta}{\zeta_2}} \qquad \text{(A9.6)}$$

This function maps the multiple-connected region in the z-plane onto the ζ-plane, as shown in Figs. A9.2 and A9.3. The function has branch points at ζ_1 and ζ_2 in the ζ-plane, corresponding to the points $z = \pm \infty$, respectively. There is a branch cut between ζ_1 and ζ_2. Hence when either point is encircled once, the argument of z changes by $\pm 2\pi e^{i(\pi/2-\beta)}$. The sign depends on whether the branch point is encircled clockwise or counter-clockwise. Each Riemann sheet of the ζ-plane corresponds to the flow region over a different hydrofoil. Since the flow is periodic, however, the function is continuous across the cut.

The point $\zeta = 0$ corresponds to the point $z = 0$, as seen from equation A9.6. Further, when ζ is real, z must also be real, as it consists of the sum of complex conjugates. When ζ tends to infinity, we have

$$z \longrightarrow e^{-i\beta} \ell n \frac{\zeta_2}{\zeta_1} + e^{i\beta} \ell n \frac{\bar{\zeta}_2}{\bar{\zeta}_1} \qquad \text{(A9.7)}$$

which is a real number.

Since $\zeta = 0$ is a singular point of the transformation, $dz/d\zeta = 0$ at $\zeta = 0$, i.e.,

$$e^{-i\beta} \left\{ \frac{\zeta_1 - \zeta_2}{\zeta_1 \zeta_2} \right\} + e^{i\beta} \left\{ \frac{\zeta_1 - \zeta_2}{\bar{\zeta}_1 \bar{\zeta}_2} \right\} = 0 \qquad \text{(A9.8)}$$

If we require that the trailing edge of the hydrofoil map into the point at infinity, then we must have $dz/d\zeta = 0$ at $\zeta = \infty$. However,

$$\frac{dz}{d\zeta} \text{ must} \longrightarrow 0 \quad \text{as} \quad \frac{1}{\zeta^3} \quad \text{at} \quad \zeta \longrightarrow \infty$$

This condition therefore gives

$$e^{-i\beta}(\zeta_1 - \zeta_2) + e^{i\beta}(\bar{\zeta}_1 - \bar{\zeta}_2) = 0 \qquad \text{(A9.9)}$$

Now let

$$\zeta_1 = r_1 e^{i\theta_1} = r_1 e^{i(\frac{\pi}{2} - \varphi_1)}$$

$$\zeta_2 = r_2 e^{i\theta_2} = r_2 e^{i(\frac{\pi}{2} + \varphi_2)}$$

$$\theta_1 + \theta_2 = \pi - (\varphi_1 - \varphi_2)$$

$$\theta_1 - \theta_2 = -(\varphi_1 + \varphi_2)$$

With this notation, equations A9.8 and A9.9 reduce to

$$\frac{r_1}{r_2} = \frac{\cos(\frac{\pi}{2} - \beta + \varphi_1)}{\cos(\frac{\pi}{2} = \beta - \varphi_2)} \qquad \text{(A9.8a)}$$

$$\frac{r_1}{r_2} = \frac{\cos(\frac{\pi}{2} - \beta + \varphi_2)}{\cos(\frac{\pi}{2} - \beta - \varphi_1)} \qquad \text{(A9.9a)}$$

For these two equations to be compatible, we take $\varphi_1 = \varphi_2 = \varphi$; hence

$$\theta_1 + \theta_2 = \pi$$

$$\theta_1 - \theta_2 = -2\varphi$$

With these values, either equation A9.8a or A9.9a provides an equation for r_1/r_2. Since the ratio of the moduli is the unknown, we are free to fix one of the moduli arbitrarily. Hence, we let $|\zeta_1| = r_1 = 1$ and $|\zeta_2| = r_2 = a$, where $a > 1$. Then from either A9.8a or A9.9a, we get

$$\tan \varphi = \frac{a - 1}{a + 1} \tan \beta \qquad \text{(A9.10)}$$

The transformation is now completely specified.

Since the trailing edge corresponds to the point at infinity, we get from equation A9.7

$$c = 2 \cos \beta \, \ell n \, a + 4 \varphi \sin \beta \qquad \text{(A9.11)}$$

and hence the solidity σ is given by

$$\sigma = \frac{1}{\pi} \cos \beta \, \ell n \, a + \frac{2\varphi}{\pi} \sin \beta \qquad \text{(A9.12)}$$

The point $z = \ell_c$ corresponding to the end of the cavity is mapped into a point on the positive real axis in the ζ-plane, $\zeta = \ell$. Thus, using the above notation together with equation A9.6, we get

$$\ell_c = 4 \cos \beta \ell n \left[\frac{n_1}{n_2}\right] + 2 \sin \beta \cdot \gamma \qquad \text{(A9.13)}$$

where

$$n_1^4 = 1 + \ell^2 - 2\ell \sin \varphi$$

$$n_2^4 = 1 + \ell^2 / a^2 + 2 \frac{\ell}{a} \sin \varphi$$

$$\gamma = \tan^{-1}\left[\frac{(a-1)\, \ell \cos \varphi + \ell^2 \sin 2\varphi}{a-(a-1)\, \ell \sin \varphi + \ell^2 \cos 2\varphi}\right]$$

We now transform the upper half ζ-plane into the half circle t-plane, Fig. A9.4. To achieve this, we use the well-known Joukowski transformation in the following form:

$$\left(\zeta - \frac{\ell}{2}\right) = \frac{\ell}{4}\left(t + \frac{1}{t}\right) . \qquad \text{(A9.14)}$$

In the t-plane the semi unit circle represents the constant

pressure cavity surface and the real axis outside the unit circle represents the wetted portions of the hydrofoil. The leading edge is at the point $t = -1$, and the trailing edge at $t = \infty$.

The t-plane is used, since the velocity function for the given boundary conditions shown in Fig. A9.4 can be written down by inspection.

Solution of the Boundary Value Problem

The velocity function

$$w = u - iv = \frac{A}{t+1} + \frac{B}{t-1} + C \qquad \text{(A9.15)}$$

where A, B, and C are real constants, satisfies the boundary conditions for suitable values of A, B and C. This function corresponds to sources (or sinks) placed at the leading edge and at the end of the cavity. We now apply conditions (a) through (d).

On the cavity, viz., $t = e^{i\theta}$, $(u_c, v_c) = (V_1 + u_c', v_c')$, therefore

$$u_c - iv_c = \frac{A}{2}\left[1 - i\tan\frac{\theta}{2}\right] - i\frac{B}{2}\left[\cot\frac{\theta}{2} - i\right] + C$$

hence

$$u_c = \frac{A - B}{2} + C$$

but

$$u_c = V_1\left(1 + \frac{K}{2}\right)$$

thus

$$V_1\left(1 + \frac{K}{2}\right) = \frac{A - B}{2} + C \qquad \text{(A9.16)}$$

Condition (a) is satisfied by equation A9.15 since when t is real, $v = 0$. Further, condition (e) is obviously satisfied.

To apply the remaining conditions, it is more convenient to transform equation A9.15 back into the ζ-plane, by use of the transformation function A9.14. Inverting equation A9.14 we get

$$t = \frac{2}{\ell}\left[\left(\zeta - \frac{\ell}{2}\right) + \sqrt{\zeta\,(\zeta - \ell)}\right]$$

The positive root is taken because t tends to infinity as ζ tends to infinity. On substitution of this expression into equation A9.15, one obtains

$$w(\zeta) = \frac{A - B}{2} + C + \frac{B}{2}\sqrt{\frac{\zeta}{\zeta - \ell}} - \frac{A}{2}\sqrt{\frac{\zeta - \ell}{\zeta}} \qquad \text{(A9.17)}$$

Now

$$w(\zeta_1) = V_1 e^{-i\alpha_1}$$

Applying this condition to equation A9.17, and separating the resulting expression into real and imaginary parts, gives

$$V_1 \cos\alpha_1 = \left[\frac{A - B}{2} + C\right] + \frac{\cos\frac{\psi_1}{2}}{2}\left[\frac{B}{n_1} - An_1\right] \qquad \text{(A9.18a)}$$

$$V_1 \sin\alpha_1 = \frac{\sin\frac{\psi_1}{2}}{2}\left[\frac{B}{n_1} + An_1\right] \qquad \text{(A9.18b)}$$

where

$$\psi_1 = \tan^{-1}\frac{\ell\cos\varphi}{1 - \ell\sin\varphi}$$

$$n_1^4 = 1 + \ell^2 - 2\ell\sin\varphi \qquad \text{(A9.18c)}$$

Now, applying the condition

$$w(\zeta_2) = V_2 e^{-i\alpha_2}$$

we get

$$V_2 \cos \alpha_2 = \left[\frac{A - B}{2} + C\right] + \frac{\cos \frac{\psi_2}{2}}{2} \left[\frac{B}{n_2} - An_2\right] \quad \text{(A9.19a)}$$

$$V_2 \sin \alpha_2 = \frac{\sin \frac{\psi_2}{2}}{2} \left[\frac{B}{n_2} + An_2\right] \quad \text{(A9.19b)}$$

where

$$\psi_2 = \tan^{-1} \frac{\ell \cos \varphi}{a + \ell \sin \varphi}$$

$$n_2^4 = 1 + \ell^2/a^2 + 2\ell/a \sin \varphi \quad \text{(A9.19c)}$$

We finally have the closure condition, viz.,

$$\int_{\text{body}} dy = 0$$

which reduces to

$$\text{Im pt} \frac{1}{V_1} \int_{\text{body}} w(z)dz = 0$$

Since w(z) is an analytic function in the flow region around the hydrofoils, we can deform the contour in the z-plane to the contour Γ shown in Fig. A9.5. Then, symbolically we have

$$\int_{\Gamma} w(z)dz = \int_{\text{body}} + \int_{H}^{A} + \int_{D}^{E} + \lim_{\epsilon_1 \to 0} \int_{\epsilon_1} + \lim_{\epsilon_2 \to 0} \int_{\epsilon_2} wdz = 0$$

The contributions from the other parts of the contour cancel due to the periodicity of w(z), while the contributions from the last two integrals in the above expression, are zero. Now

$$\int_{H}^{A} w(z)dz = 2\pi V_1 ie^{-i(a_1+\beta)}$$

$$\int_{D}^{E} w(z)dz = -2\pi V_2 ie^{-i(a_2+\beta)}$$

$$\text{Im pt}\frac{1}{V_1}\int_{\text{body}} w(z)\,dz = \frac{2\pi}{V_1}\left[V_2\cos(a_2+\beta) - V_1\cos(a_1+\beta)\right] = 0$$

hence

$$V_1\cos(a_1+\beta) = V_2\cos(a_2+\beta) \qquad \text{(A9.20)}$$

This is the same result as already obtained by continuity considerations in equation A9.4. Finally we have the following equations to solve:

$$\frac{A-B}{2} + C = V_1\left(1+\frac{K}{2}\right)$$

$$V_1\cos a_1 = \frac{A-B}{2} + C + \frac{\cos\frac{\psi_1}{2}}{2}\left[\frac{B}{n_1} - An_1\right]$$

$$V_1\sin a_1 = \frac{\sin\frac{\psi_1}{2}}{2}\left[\frac{B}{n_1} + An_1\right]$$

$$V_2\cos a_2 = \frac{A-B}{2} + C + \frac{\cos\frac{\psi_2}{2}}{2}\left[\frac{B}{n_2} - An_2\right]$$

$$V_2\sin a_2 = \frac{\sin\frac{\psi_2}{2}}{2}\left[\frac{B}{n_2} + An_2\right]$$

$$V_1\cos(a_1+\beta) = V_2\cos(a_2+\beta)$$

After considerable manipulation these equations reduce to the

following:

$$\left(1 + \frac{K}{2}\right) = \cos \alpha_1 + \frac{F}{D} \sin \alpha_1 \tag{A9.21}$$

$$\tan \alpha_2 = \frac{E}{G + \dfrac{D\left(1 + \dfrac{K}{2}\right)}{\sin \alpha_1}} \tag{A9.22}$$

$$\frac{V_2}{V_1} = \frac{E}{D} \frac{\sin \alpha_1}{\sin \alpha_2} \tag{A9.23}$$

where

$$D = \left[\frac{n_1}{n_2} + \frac{n_2}{n_1}\right] \sin \frac{\psi_1}{2} \cos \frac{\psi_2}{2} - \sin \psi_1 - \left[\frac{n_1}{n_2} - \frac{n_2}{n_1}\right] \sin \frac{\psi_1}{2} \sin \frac{\psi_2}{2} \tan \beta$$

$$E = \sin \psi_2 - \left[\frac{n_1}{n_2} + \frac{n_2}{n_1}\right] \cos \frac{\psi_1}{2} \sin \frac{\psi_2}{2} - \left[\frac{n_1}{n_2} - \frac{n_2}{n_1}\right] \sin \frac{\psi_1}{2} \sin \frac{\psi_2}{2} \tan \beta$$

$$F = \left[\frac{n_1}{n_2} - \frac{n_2}{n_1}\right] \cos \frac{\psi_1}{2} \cos \frac{\psi_2}{2} + \sin \psi_1 \tan \beta - \left[\frac{n_1}{n_2} + \frac{n_2}{n_1}\right] \cos \frac{\psi_1}{2} \sin \frac{\psi_2}{2} \tan \beta$$

$$G = \sin \psi_2 \tan \beta - \left[\frac{n_1}{n_2} - \frac{n_2}{n_1}\right] \cos \frac{\psi_1}{2} \cos \frac{\psi_2}{2} - \left[\frac{n_1}{n_2} + \frac{n_2}{n_1}\right] \sin \frac{\psi_1}{2} \cos \frac{\psi_2}{2} \tan \beta$$

Equation A9.21 gives us a relation between the cavitation number and the cavity length ℓ_c. If we consider the limit as the solidity tends to infinity, this equation reduces to the expression obtained by Acosta

and Hollander (38) for the case of semi-infinite flat plates. Further details are given later.

We now calculate the lift force acting on the hydrofoil. As mentioned previously, we will here adopt a slightly different perturbation procedure, so that a comparison may be made with the fully wetted case. We use the vector mean velocity V_m as reference velocity.

The element of force acting on the blade is

$$dF = (p - p_m)\, dx$$

$$F = \int_{body} (p - p_m)\, dx$$

Defining the pressure coefficient c_p as

$$c_p = \frac{p - p_m}{\rho V_m^2/2} \tag{A9.24}$$

and the lift coefficient as

$$C_L = \frac{F}{\rho V_m^2 c/2} \tag{A9.24a}$$

we obtain

$$C_L = \frac{1}{c} \int_{body} c_p dx$$

Using Bernoulli's equation, this becomes

$$C_L = -\frac{1}{c} \int_{body} \frac{2}{V_m} (u - V_m)\, dx$$

which reduces to

$$C_L = -\frac{2}{cV_m} \text{Re pt} \int_{\text{body}} w(z)\,dz$$

on the body. Carrying out the indicated procedure in an identical way as previously performed for the closure condition we obtain

$$C_L = \frac{2}{cV_m}\left[V_1 \sin(\alpha_1 + \beta) - V_2 \sin(\alpha_2 + \beta)\right]$$

By the use of equations A9.5, A9.20 and A9.23, we can eliminate α_1 and α_2 in the above expression, and deduce the following:

$$C_L = \frac{4}{\sigma} \frac{1}{\cos\beta}\left[\frac{\frac{D}{E} - 1}{\frac{D}{E} + 1}\right] \sin \alpha_m \qquad \text{(A9.25)}$$

As D, E are functions of ℓ, the cavity length in the ζ-plane, this expression can be used to obtain the limiting case for the fully wetted cascade, i.e., when ℓ tends to zero. This is carried out in a later section. The result reduces to that of the well-known, fully wetted solution, viz.,

$$C_L = \frac{4}{\sigma} \frac{1}{\cos\beta}\left[\frac{a - 1}{a + 1}\right] \sin \alpha_m \qquad \text{(A9.26)}$$

A further limiting assumption in the linearized theory is that the angle of attack α, is small. If second order powers of α are neglected, equations A9.21 through A9.24 reduce to

$$\frac{K}{2\alpha_1} = \frac{F}{D} \qquad \text{(A9.21a)}$$

$$\alpha_2 = \frac{E}{G + \frac{D}{\alpha_1}\left(1 + \frac{K}{2}\right)} \qquad \text{(A9.22a)}$$

$$V_2/V_1 = \frac{E}{D} \cdot \frac{a_1}{a_2} \qquad \text{(A9.23a)}$$

$$C_L = \frac{4}{\sigma} \frac{1}{\cos \beta} \left[\frac{\frac{D}{E} - 1}{\frac{D}{E} + 1} \right] a_m \qquad \text{(A9.25a)}$$

From these equations, the results shown in Figs. A9.6 through A9.28 were obtained.

Computational Procedure

The numerical calculations were conducted on a digital computer and the general method of computation is outlined below.

For a given cascade geometry, viz., σ and β, the value of a and φ were determined by the simultaneous numerical solution of equations A9.10 and A9.12. With these values, the functions D, E, F, and G were evaluated, for values of ℓ, ranging from zero to approximately two hundred; this latter figure giving a value of 0.99 for ℓ_c/c . The ratio ℓ_c/c can be found from equation A9.13. Having determined these quantities, the values of $K/2a_1$, a_2, V_2/V_1 and C_L are found for various angles of attack a_1. The process is repeated for various stagger angles β, holding σ constant. This final parameter σ is then varied and the above procedure repeated. The range of values considered is given below in Table A9.1.

$$\cos \psi_1 = \frac{1 - \ell \sin \beta}{n_1^2} \quad ,$$

and

$$\sin \frac{\psi_1}{2} = \frac{\sqrt{n_1^2 - 1 + \ell \cos \beta}}{\sqrt{2}\ n_1}$$

$$\cos \frac{\psi_1}{2} = \frac{\sqrt{n_1^2 + 1 - \ell \sin \beta}}{\sqrt{2}\ n_1}$$

Substituting in A9.21 gives

$$(1 + \frac{K}{2}) = \cos a_1 + \sin a_1 \quad \cdot$$

$$\frac{(n_1^2 - 1)\sqrt{n_1^2 + 1 - \ell \sin \beta} + \sqrt{2}\ \ell \sin \beta}{(n_1^2 + 1)\sqrt{n_1^2 - 1 + \ell \sin \beta} - \sqrt{2}\ \ell \cos \beta} \quad .$$

If we now change notation to that of Acosta and Hollander, such that

$$n_1 \approx \ell; \quad \ell \approx b; \quad \beta \approx \gamma; \quad a_1 \approx a$$

and we further replace

$$(1 + \frac{K}{2}) \quad \text{by} \quad \sqrt{1 + K}$$

then

$$\sqrt{1 + K} = \cos a - \sin a \frac{(1 - \ell^2)\sqrt{\ell^2 + 1 - b \sin\gamma} - \sqrt{2}\ b \sin\gamma}{(1 + \ell^2)\sqrt{\ell^2 - 1 + b \sin\gamma} - \sqrt{2}\ b \cos\gamma} \quad .$$

After some manipulation this reduces to

$$\sqrt{1 + K} = \cos a - \sin a \frac{b \cos\gamma}{\ell^2 - 1 + b \sin\gamma} \qquad X$$

$$\times \quad \frac{(1-\ell^2)\cos\gamma \; - \sqrt{2}\;\ell\sqrt{1-\dfrac{1-b\sin\gamma}{\ell^2}}\sin\gamma}{(1+\ell^2)\cos\gamma \; - \sqrt{2}\;\ell\sqrt{1+\dfrac{1-b\sin\gamma}{\ell^2}}\cos\gamma} \quad ,$$

which is the expression given by Acosta and Hollander (38).

Further, we see from equation A9.22 that since $E \longrightarrow 0$ as $\sigma \longrightarrow \infty$ we get $a_2 \equiv 0$ for all a_1.

(b) For the case when the cavity length tends to zero or equivalently $\ell \longrightarrow 0$, we can expand each term in the expressions for D and E in powers of ℓ, up to and including $0(\ell^3)$. Hence

$$\left[\frac{n_1}{n_2}+\frac{n_2}{n_1}\right] \sim 2 + \left(\frac{1}{4}+\frac{1}{2a}+\frac{1}{4a^2}\right)\sin^2\varphi\,\ell^2 + 0(\ell^4) \quad ,$$

$$\left[\frac{n_1}{n_2}-\frac{n_2}{n_1}\right] \sim -\left(1+\frac{1}{a}\right)\sin\varphi\,\ell + \left(\frac{1}{2}-\sin^2\varphi\right)\left(1-\frac{1}{a^2}\right)\ell^2 + 0(\ell^3) \quad ,$$

$$\left[\sin\psi_1\right] \sim \cos\varphi\,\ell + \sin\varphi\cos\varphi\,\ell^2 - \left(\frac{\cos^2\varphi}{2}-\sin^2\varphi\right)\cos\varphi\,\ell^3 + 0(\ell^4) \quad ,$$

$$\left[\sin\psi_2\right] \sim \frac{\cos\varphi}{a}\ell - \frac{\sin\varphi\cos\varphi}{a^2}\ell^2 - \left(\frac{\cos^2\varphi}{2}-\sin^2\varphi\right)\frac{\cos\varphi}{a^3}\ell^3 + 0(\ell^4) \quad ,$$

$$\left[\sin\frac{\psi_1}{2}\cos\frac{\psi_2}{2}\right] \sim \frac{\cos\varphi}{2}\ell + \frac{\sin\varphi\cos\varphi}{2}\ell^2 + \left(\sin^2\varphi-\frac{3}{8}\cos^2\varphi-\frac{\cos^2\varphi}{8a}\right)\frac{\cos\varphi}{2}\ell^3 + 0(\ell^4) \,,$$

$$\left[\sin\frac{\psi_1}{2}\sin\frac{\psi_2}{2}\right] \sim \frac{\cos^2\varphi}{4a}\,\ell^2 + (1-\frac{1}{a})\frac{\sin\varphi\cos^2\varphi}{4a}\,\ell^3 + 0(\ell^4) \quad ,$$

$$\left[\cos\frac{\psi_1}{2}\sin\frac{\psi_2}{2}\right] \sim \frac{\cos\varphi}{2a}\,\ell - \frac{\sin\varphi\cos\varphi}{2a^2}\,\ell^2$$

$$-(\frac{\cos^2\varphi}{8} + \frac{3\cos^2\varphi}{8a^2} - \frac{\sin^2\varphi}{a^2})\frac{\cos\varphi}{2a}\,\ell^3 + 0(\ell^4).$$

Utilizing these expressions we obtain

$$D = \left[(\frac{1}{8} + \frac{1}{4a} + \frac{1}{8a^2})\sin^2\varphi\cos\varphi + (\frac{1}{8} - \frac{1}{8a^2})\cos^3\varphi\right.$$

$$\left. + (1+\frac{1}{a})\frac{1}{4a}\sin\varphi\cos^2\varphi\tan\beta\right]\ell^3 + 0(\ell^4)$$

$$E = \left[-(\frac{1}{8a} + \frac{1}{4a^2} + \frac{1}{8a^3})\sin^2\varphi\cos\varphi + (\frac{1}{8a} - \frac{1}{8a^3})\cos^3\varphi\right.$$

$$\left. + (1+\frac{1}{a})\frac{1}{4a}\sin\varphi\cos^2\varphi\tan\beta\right]\ell^3 + 0(\ell^4)$$

therefore $\frac{D}{E} \sim$

$$a\,\frac{\left[(\frac{1}{8} + \frac{1}{4a} + \frac{1}{8a^2})\sin^2\varphi\cos\varphi + (\frac{1}{8} - \frac{1}{8a^2})\cos^3\varphi + (1+\frac{1}{a})\frac{1}{4a}\sin\varphi\cos^2\varphi\tan\beta\right]}{\left[-(\frac{1}{8} + \frac{1}{4a} + \frac{1}{8a^2})\sin^2\varphi\cos\varphi + (\frac{1}{8} - \frac{1}{8a^2})\cos^3\varphi + (1+\frac{1}{a})\frac{1}{4}\sin\varphi\cos^2\varphi\tan\beta\right]}$$

$$+ 0(\ell)$$

Now substituting for $\tan\beta = \frac{a-1}{a+1}\tan\varphi$ in the above, gives

$$\frac{D}{E} \sim a + 0(\ell) \qquad \text{as} \qquad \ell \longrightarrow 0 \quad ,$$

thus, $$C_L = \frac{4}{\sigma} \frac{1}{\cos \beta} \left[\frac{a - 1}{a + 1}\right] \sin \alpha_m \quad \text{as} \quad \ell \longrightarrow 0$$

which is the classical linearized fully wetted cascade flow result.

Now, when $\beta = 0$, $a = e^{\sigma\pi}$ then

$$C_L = 2\pi \frac{\tanh (\sigma\pi/2)}{(\sigma\pi/2)} \sin \alpha_m \quad .$$

For the isolated hydrofoil as $\sigma \longrightarrow 0$ this reduces to

$$C_L = 2\pi \alpha_m \quad .$$

Discussion of Results

Figs. A9.6 to A9.10 illustrate the relation between the cavity length and the cavitation number, for various geometries. The case of the isolated, partially cavitating flat plate is also shown on each graph. The values for this case were obtained from Reference 13. It is of interest to note that a feature of the linearized theory is the fact that after a certain value of ℓ_c/c the theory predicts two different cavity lengths for each cavitation number. This is apparent from Figs. A9.6 - A9.10. Since, in any case, the linearized assumption that the cavity-hydrofoil system forms a slender body would not be met for large values of ℓ_c/c, it is assumed that the validity of the theory only holds good for values of $\ell_c/c < \ell_c/c$ minimum.

This behavior is to be expected due to the cavity model chosen, which places a singularity at the end of the cavity. However, comparing the results with that of the isolated hydrofoil, we see that this range of validity is increased in the case of the cascade. It would seem that the cascade effect has the property of reducing the

effect of the singular behavior at the cavity end. This is further illustrated by the fact that as the solidity increases the range is extended, until at solidities greater than 0.75, a single valued function is obtained over almost the entire chord length for positive values of stagger angle. In the case of negative stagger angles, corresponding to the case of a turbine, as distinct from positive values of β which correspond to a pump, we see that there is still a region where the function is double valued. Physically, this is to be expected, since the effect of the neighboring blades is now no longer as effective near the cavity end.

It is seen that there is a large difference between the cavity geometry in cascade, compared with that of the isolated case, even for small solidities. However, this comparison is not entirely justified as the value of $K/2\alpha_1$ is based on the upstream angle of incidence. In the case of the cascade, a more natural angle to adopt is that of the mean velocity vector V_m.

Further, the curves at first glance seem to indicate that the cavity length for a given cavitation number at negative stagger angles is less than that of an isolated hydrofoil, even at low solidity. This surprising effect, however, is due once again to the choice of the upstream conditions as a reference. If the mean conditions are taken as reference, the curves for negative stagger angles will be raised above that for the isolated case and those corresponding to positive stagger angles remain below it as would be expected. If the curves are based on this angle, therefore, a better comparison is

achieved. This is clearly illustrated in Figs. A9.11 and A9.12 where the cavitation number is referred to the mean angle α_m.

There is still a significant difference for all values of β having solidities of 0.5 and greater. It therefore seems that the cascade effect is not very pronounced for solidities up to 0.5 provided the stagger angle is within the range -30° to $+60^\circ$.

Figs. A9.13 and A9.14 illustrate a further representation. Here the value of $K_m/2\alpha_m$ is plotted against ℓ_c/c, where K_m is defined as

$$K_m = \frac{p_m - p_c}{\rho V_m^2/2}$$

which to first order, reduces to

$$K_m = K + (1 + K)(\alpha_1 - \alpha_2)\tan\beta$$

with the help of Bernoulli's equation.

It is seen from these graphs, that for low solidity the curves lie very close to that of the isolated case, for all values of β. This representation, however, indicates the opposite effect to that using $K/2\alpha_1$, viz., that cavity lengths, for constant cavitation number, are longer for positive stagger angles than the isolated hydrofoil, even at low solidity. Consequently, it seems that the parameter $K/2\alpha_m$ is the most natural one to use.

A disadvantage of using these alternative forms is the fact that they depend on α_1, whereas the value of $K/2\alpha_1$ is independent of the angle of attack α_1 and thus facilitates presentation immensely.

Figs. A9.15 to A9.22 show the variation of force coefficient

with cavitation number for varying cascade geometry. It is significant that the force coefficient is little changed over the range $-30^{o} < \beta < +30^{o}$ for a constant solidity. As shown in the curves, the force coefficient for the isolated hydrofoil is approached as the solidity decreases. However, once again, we see that for solidities of 0.5 and larger, the cascade effect is prominent. The curves as plotted are terminated at the points where ℓ_c/c is a minimum.

In the remaining curves, Figs. A9.23 to A9.28, the behavior of the downstream conditions is illustrated. Here again, the curves are terminated at the point of minimum ℓ_c/c. It may be pointed out that at $\beta = 0^{o}$ the theory gives V_2/V_1 as unity, but shows that a_2 is still variable and not equal to a_1. This apparently is a violation of the continuity equation which would necessitate $a_1 = a_2$. This discrepancy is due to the linearization procedure which neglects quadratic terms.

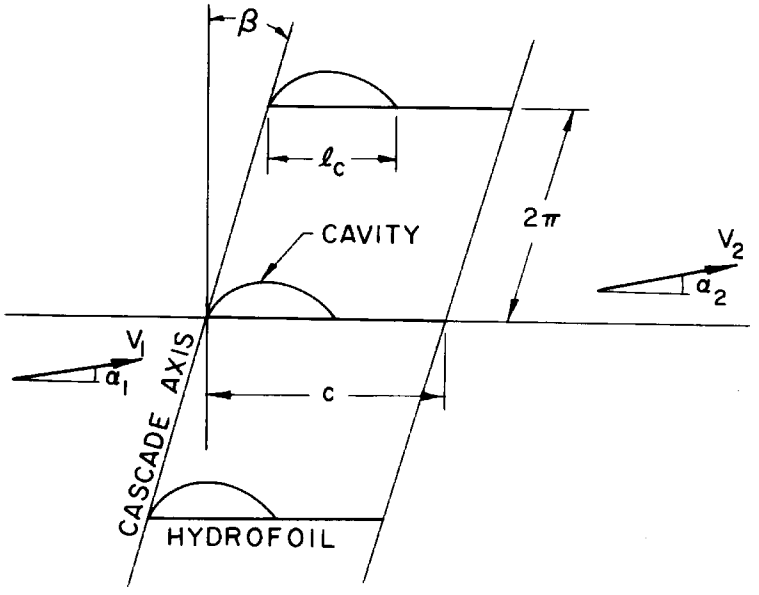

Fig. A9.1 - Partially cavitating cascade of flat plates.

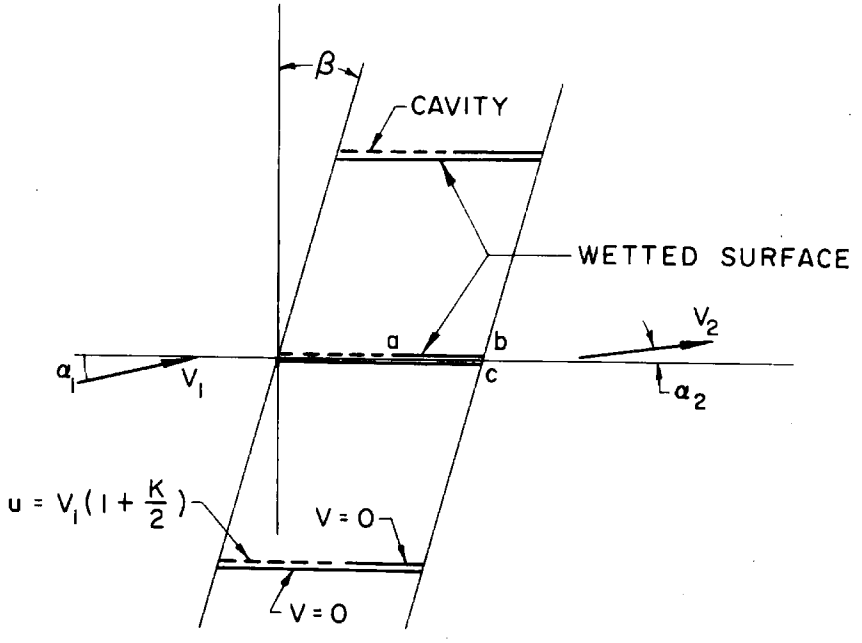

Fig. A9.2 - Linearized boundary conditions in physical z-plane.

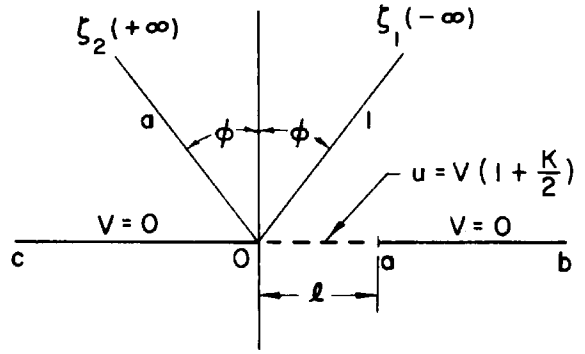

ζ - PLANE

Fig. A9.3 - Auxiliary ζ-plane.

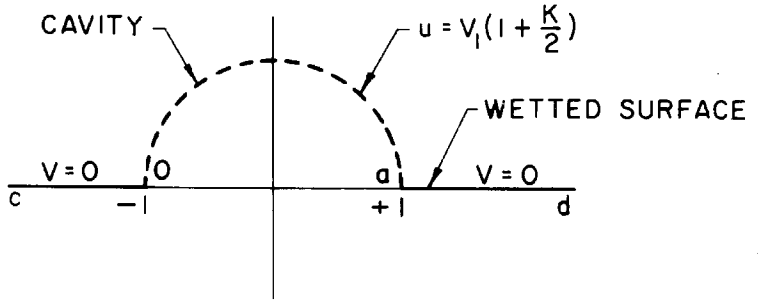

t - PLANE

Fig. A9.4 - Auxiliary t-plane

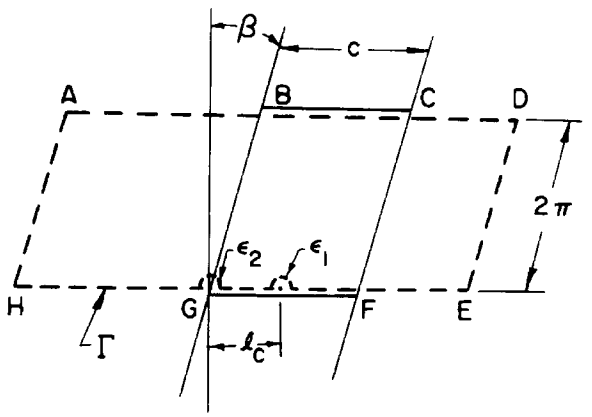

z - PLANE

Fig. A9.5 - Integration contour in z-plane.

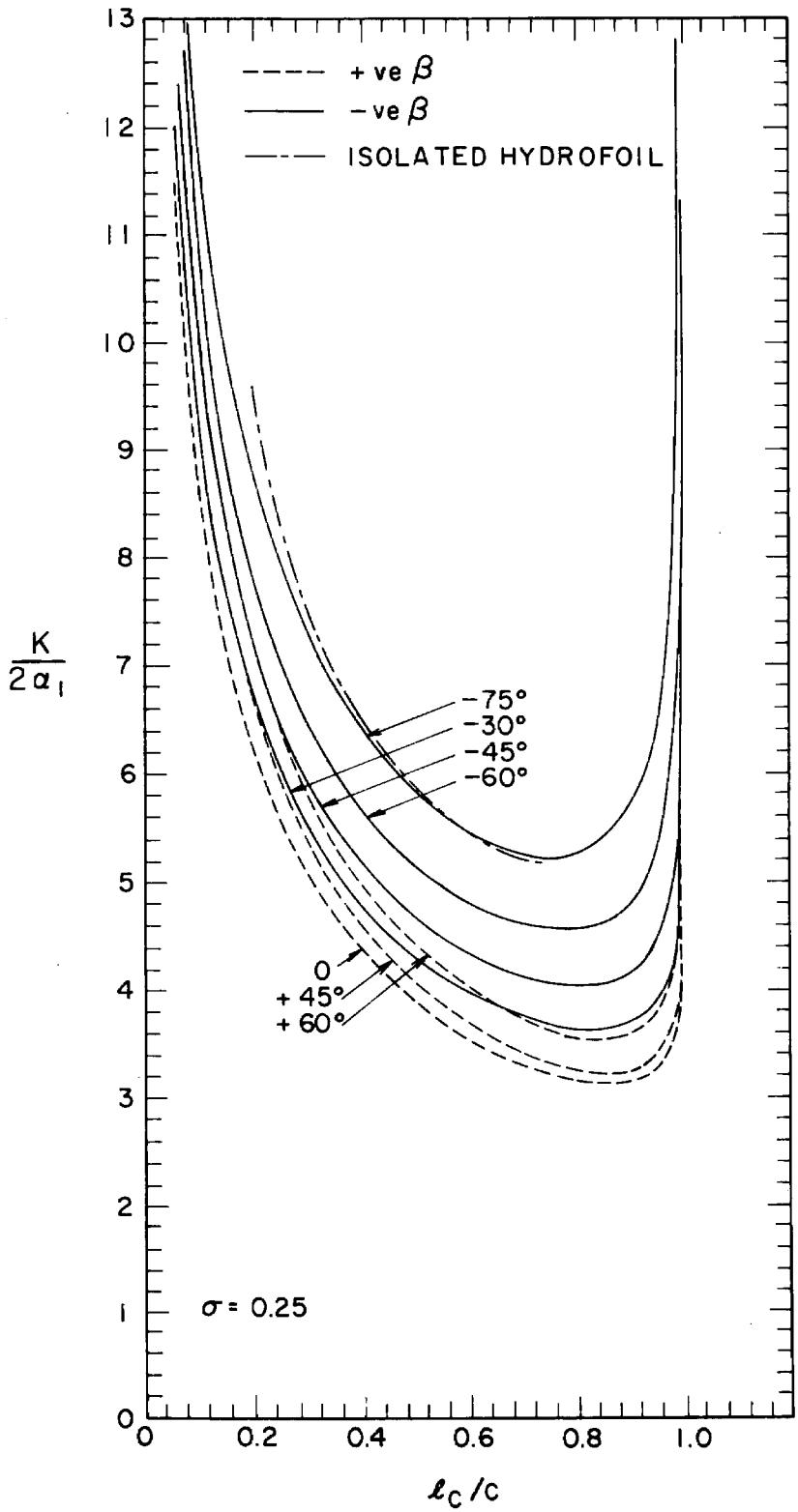

Fig. A9.6 - Ratio of cavitation number to twice inlet angle versus cavity length to chord length ratio for various stagger angles β, at a constant solidity, $\sigma = 0.25$.

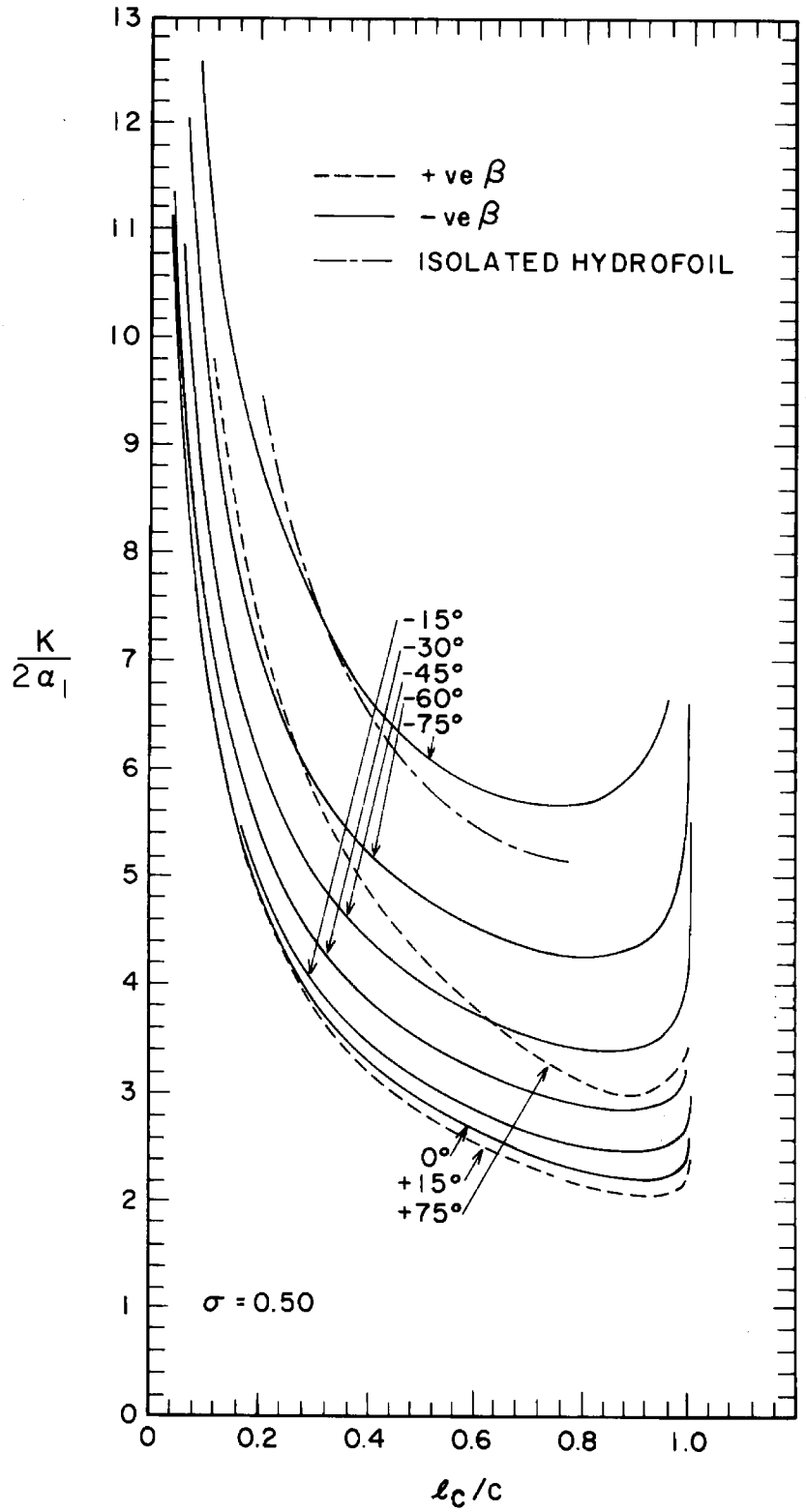

Fig. A9.7 - Ratio of cavitation number to twice inlet angle vs. cavity length to chord length ratio for various stagger angles β, at a constant solidity, σ = 0.50.

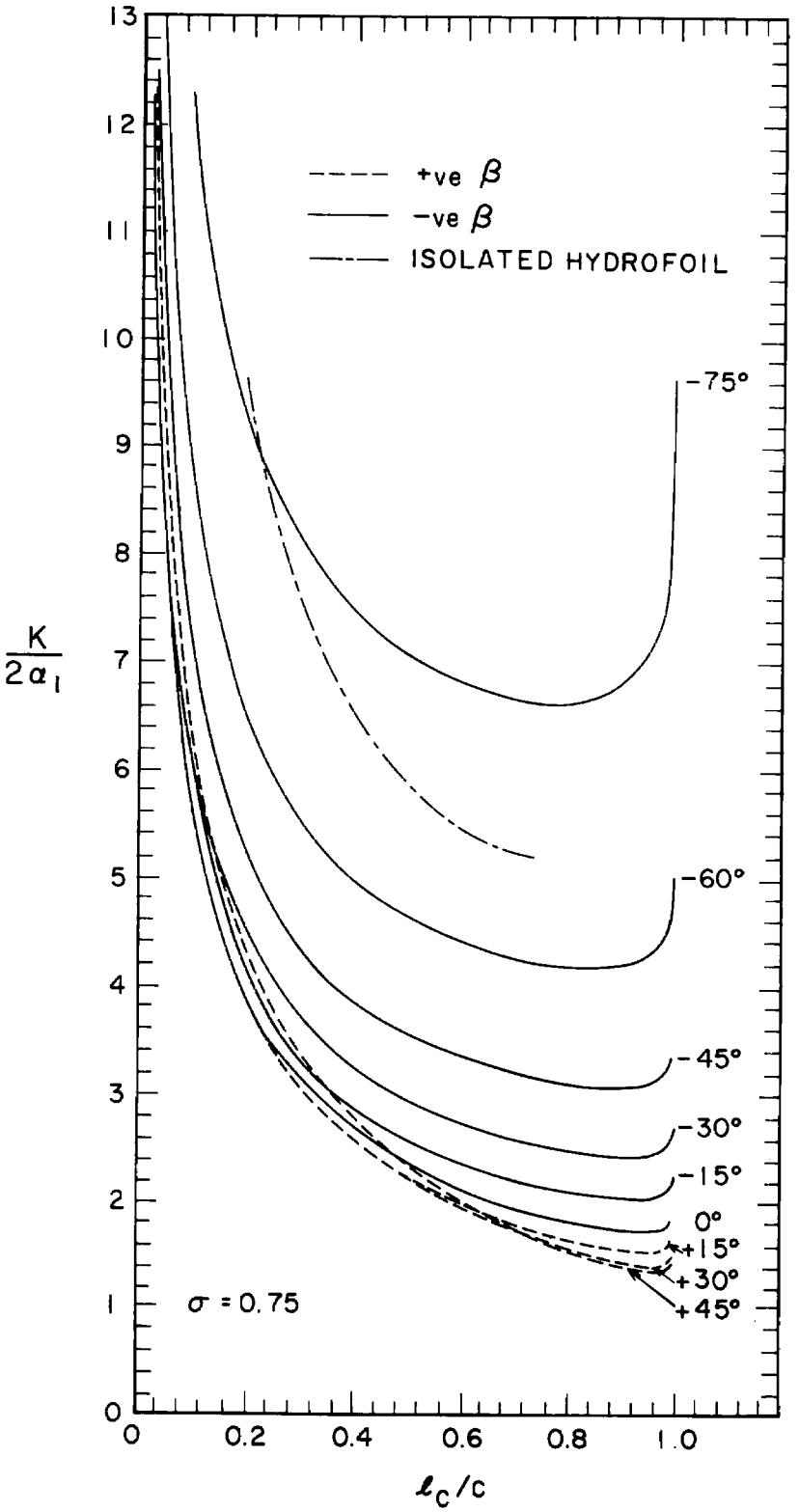

Fig. A9.8 - Ratio of cavitation number to twice inlet angle vs. cavity length to chord length ratio for various stagger angles β, at a constant solidity, $\sigma = 0.75$.

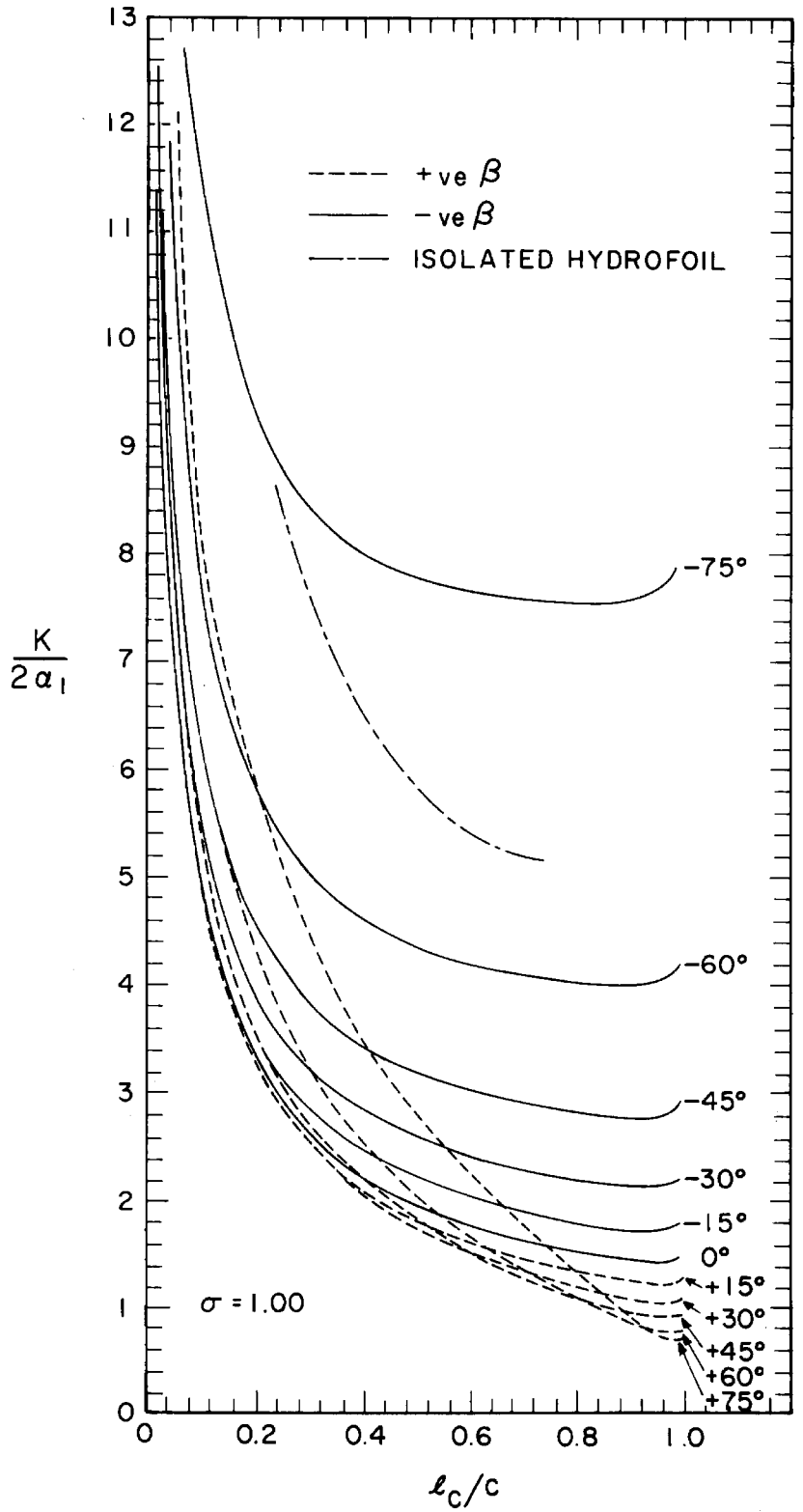

Fig. A9.9 - Ratio of cavitation number to twice inlet angle vs. cavity length to chord length ratio for various stagger angles β, at a constant solidity σ = 1.00.

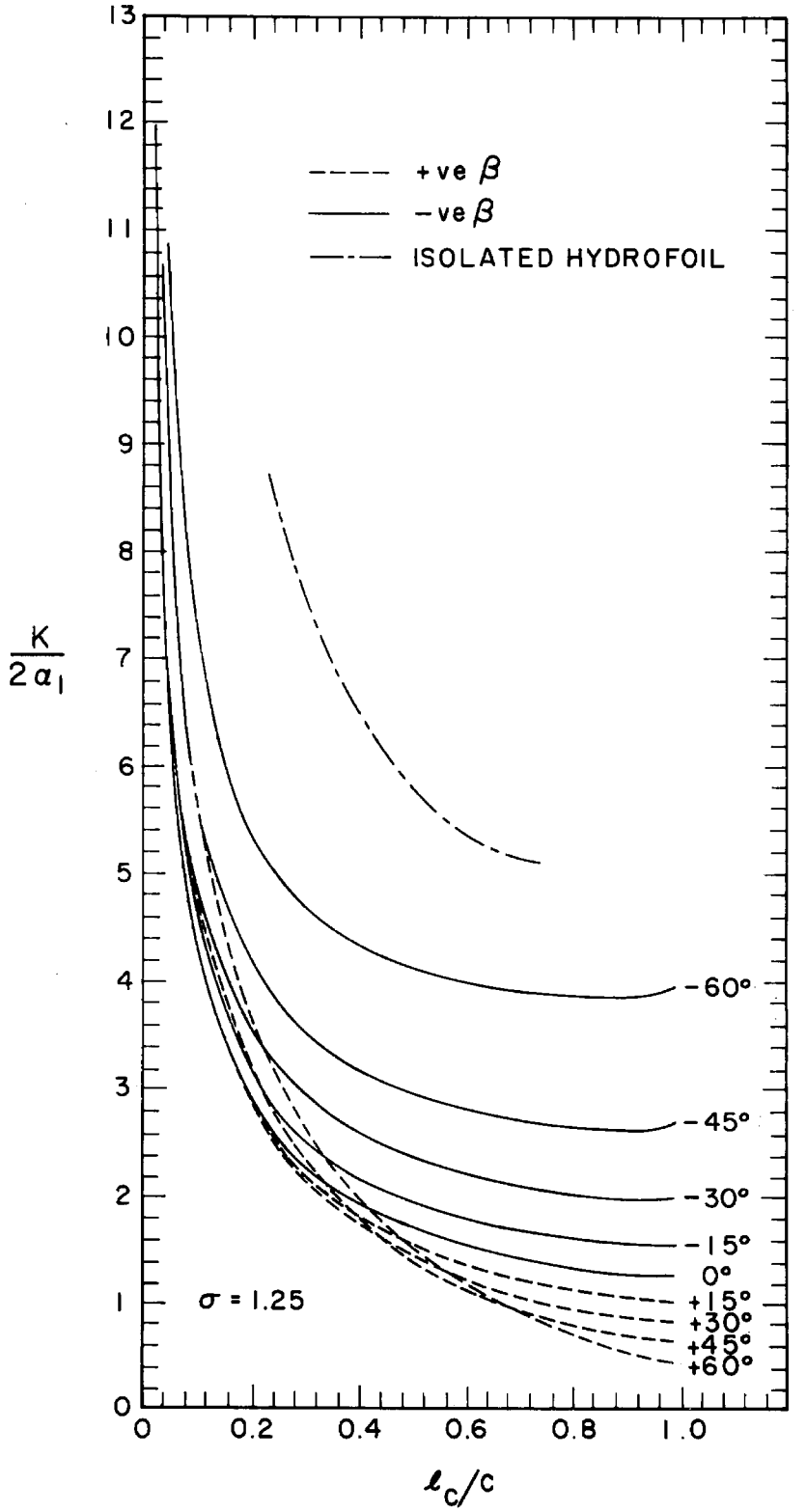

Fig. A9.10 - Ratio of cavitation number to time inlet angle vs. cavity length to chord length ratio for various stagger angles β, at a constant solidity, $\sigma = 1.25$.

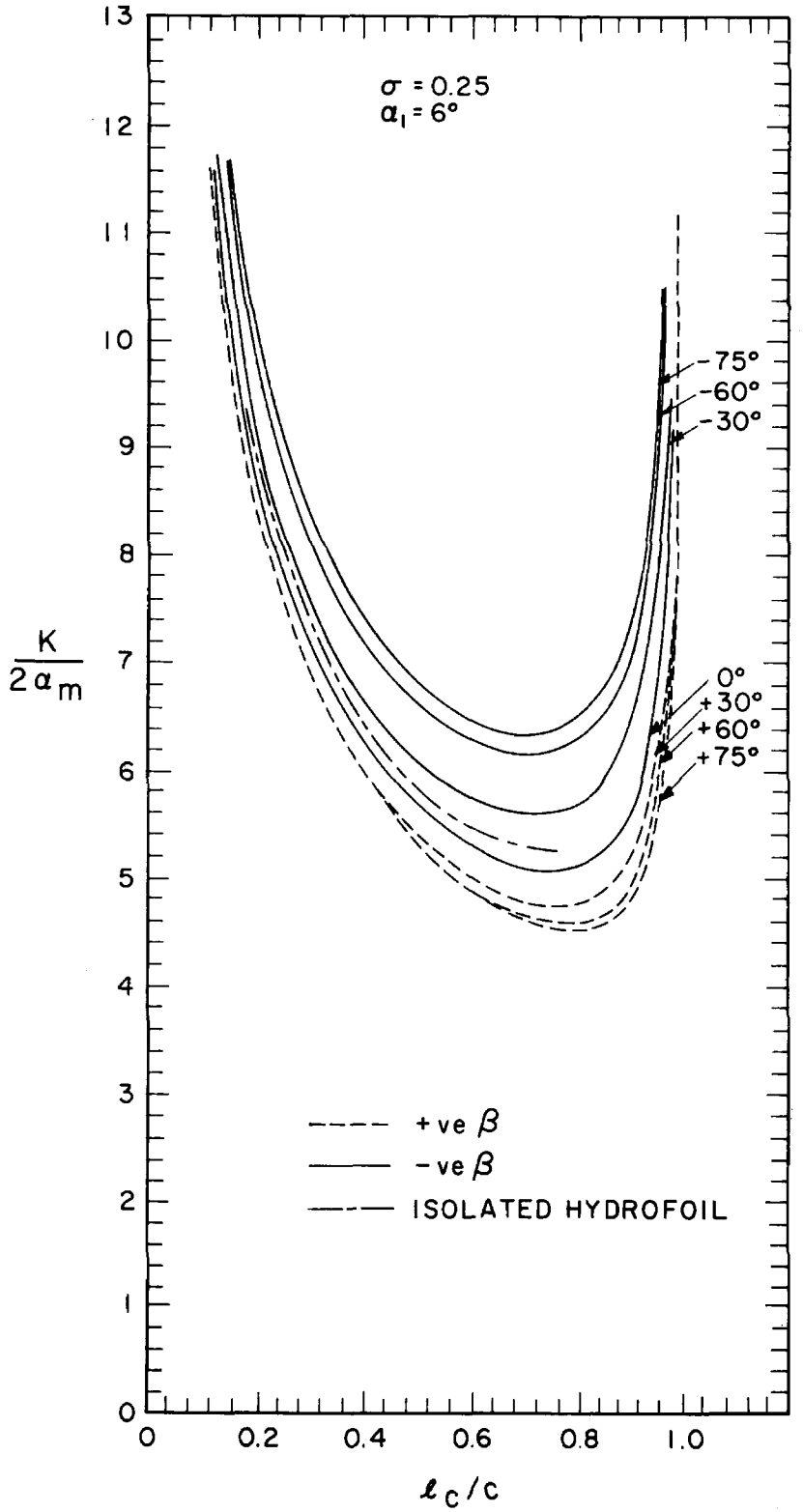

Fig. A9.11 - Ratio of cavitation to twice the mean flow angle vs. cavity length to chord length ratio for various stagger angles β, at a constant solidity σ = 0.25 and inlet angle of 6°.

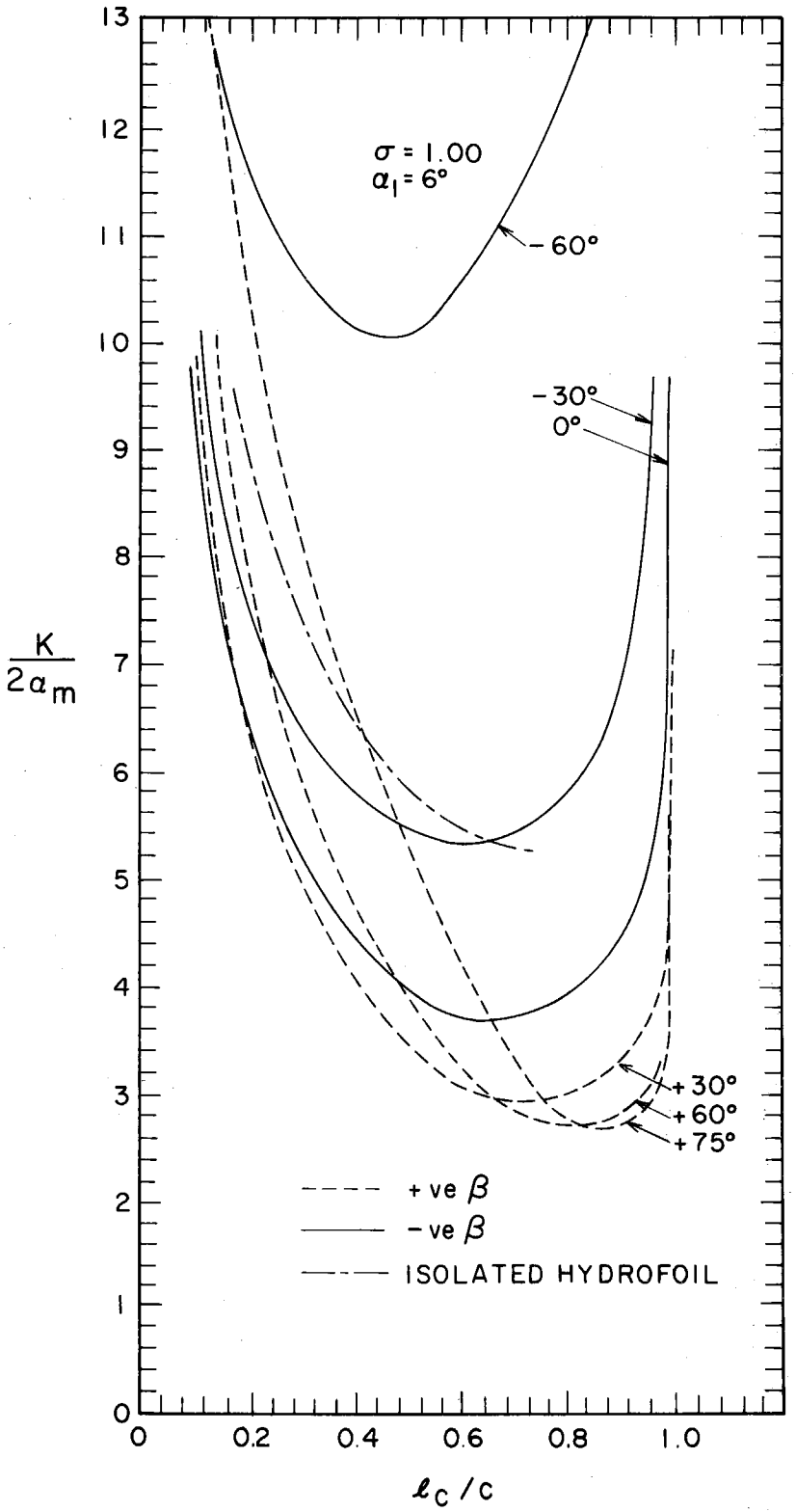

Fig. A9.12 - Ratio of cavitation number to twice the mean flow angle vs. cavity length to chord length ratio for various stagger angles β, at a constant solidity $\sigma = 1.00$ and inlet angle of 6^{o}.

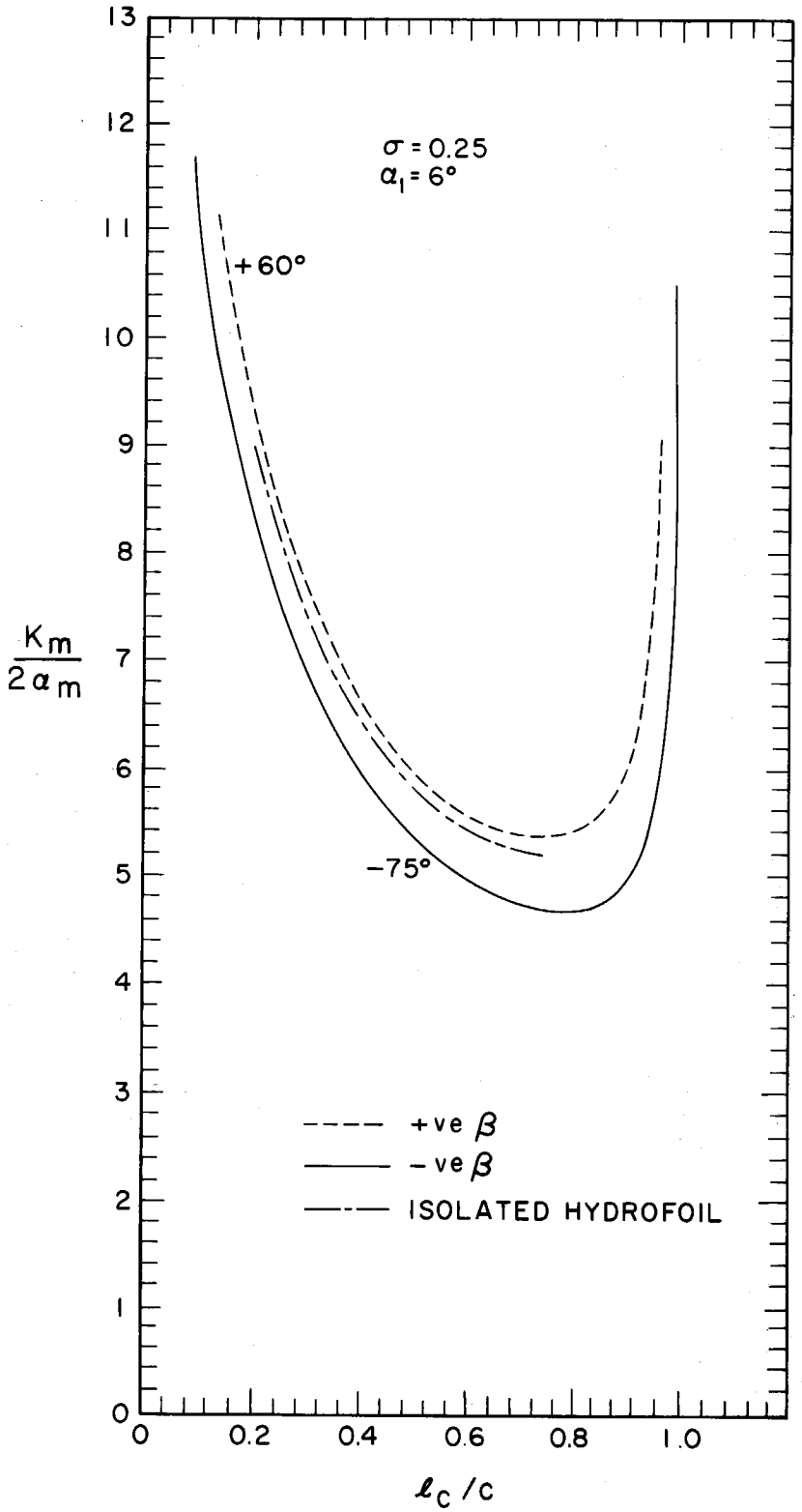

Fig. A9.13 - Ratio of mean cavitation number to twice mean flow angle vs. cavity length to chord length ratio for various stagger angles β, at a constant solidity σ = 0.25 and inlet angle of 6°.

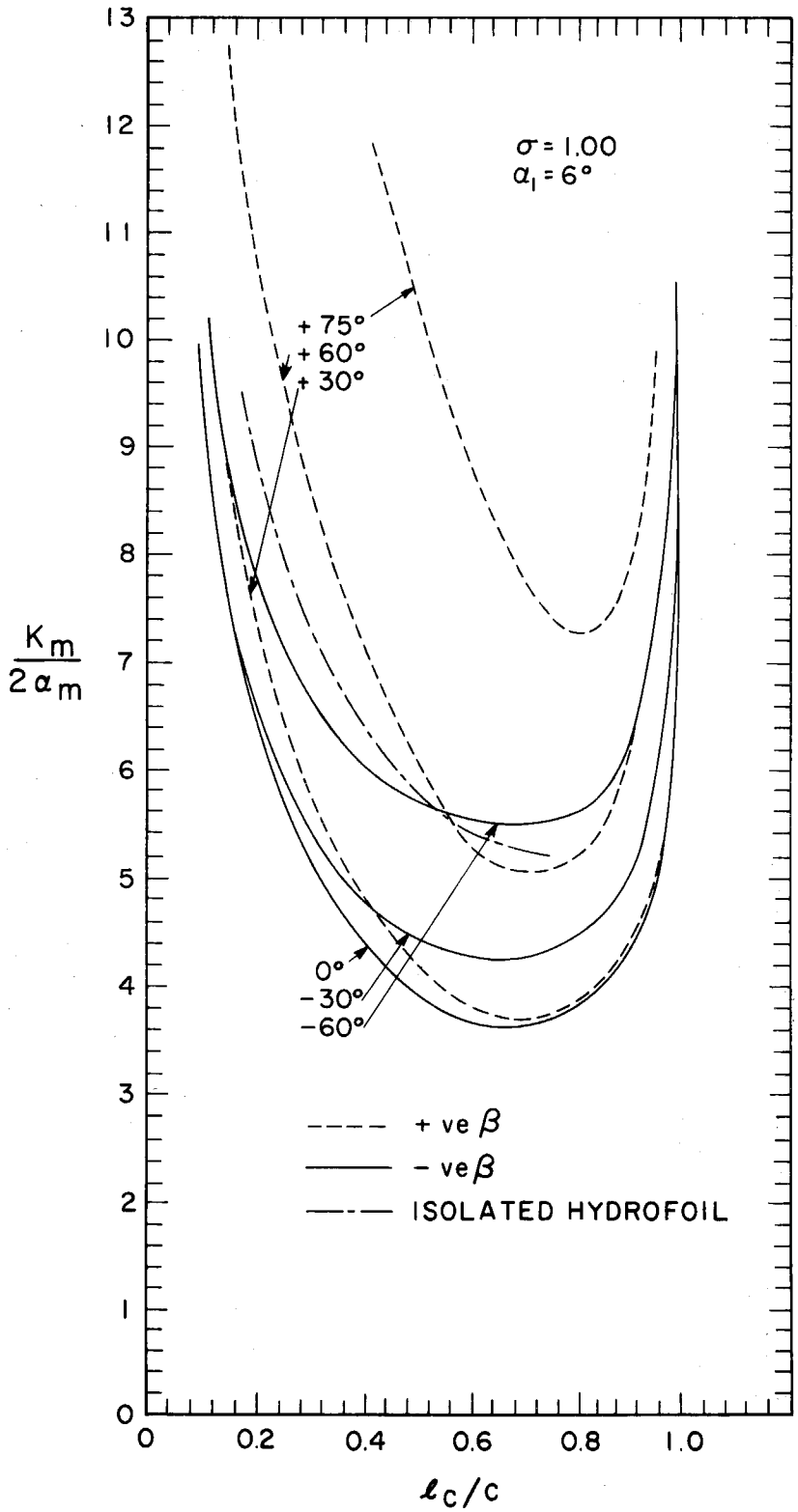

Fig. A9.14 - Ratio of mean cavitation number to twice mean flow angle vs. cavity length to chord length ratio for various stagger angles β, at a constant solidity σ = 1.00 and inlet angle of 6°.

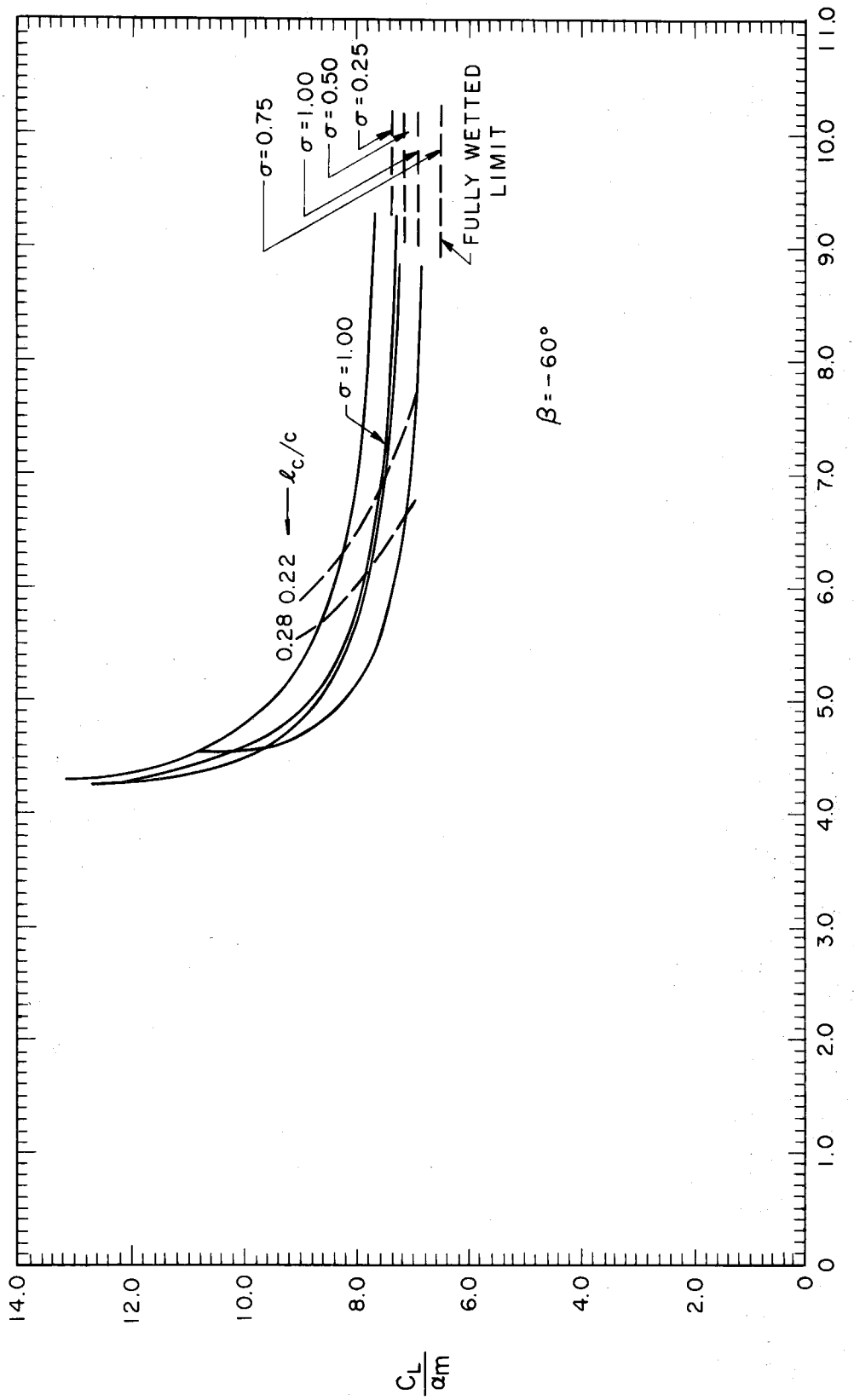

Fig. A9.15 - Ratio of lift coefficient to mean flow angle vs. ratio of cavitation number to twice inlet angle for various solidities at a given stagger angle $\beta = -60°$.

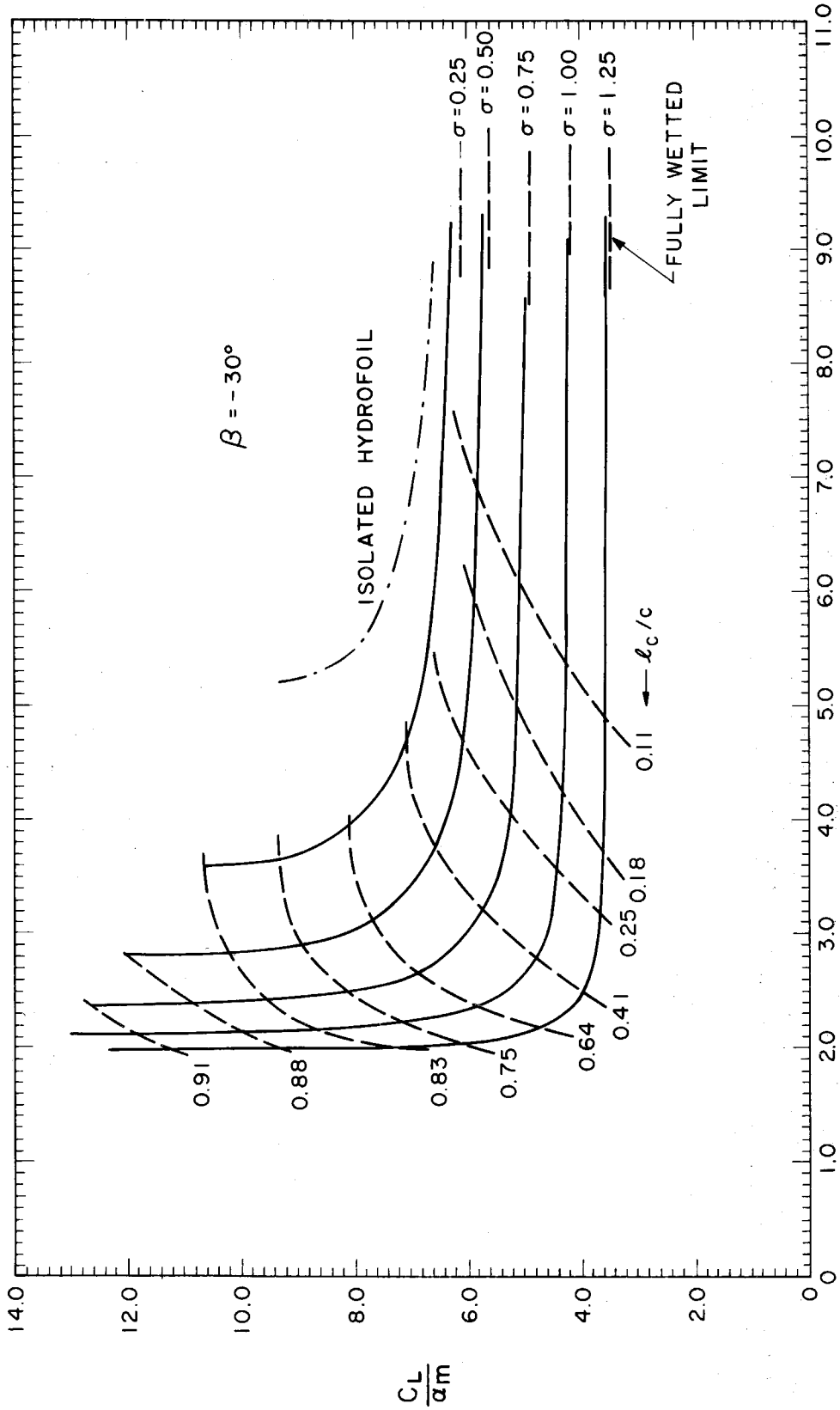

Fig. A9.16 - Ratio of lift coefficient to mean flow angle vs. ratio of cavitation number to twice inlet angle for various solidities at a given stagger angle $\beta = -30°$.

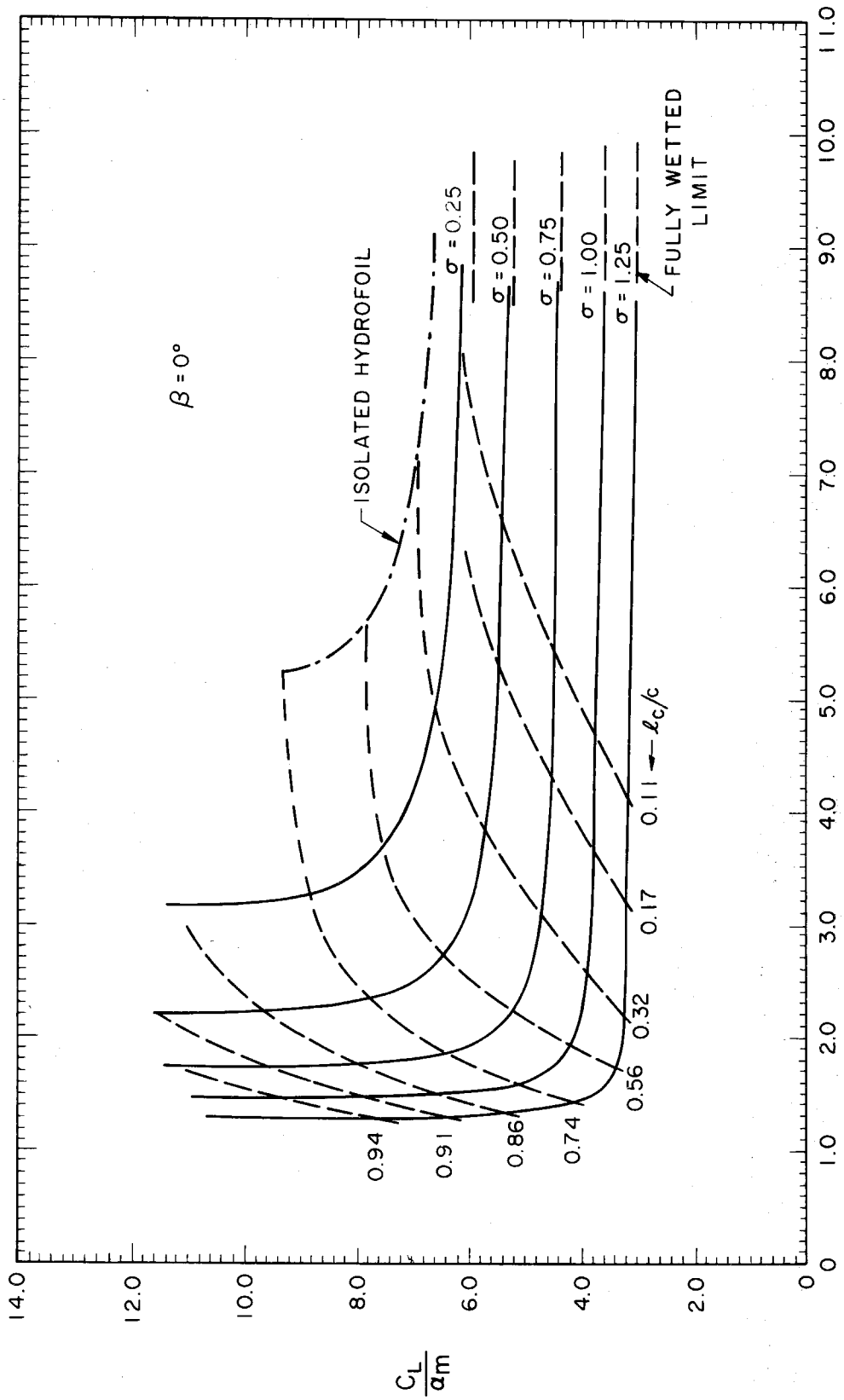

Fig. A9.17 - Ratio of lift coefficient to mean flow angle vs. ratio of cavitation number to twice inlet angle for various solidities at a given stagger angle $\beta = 0^o$.

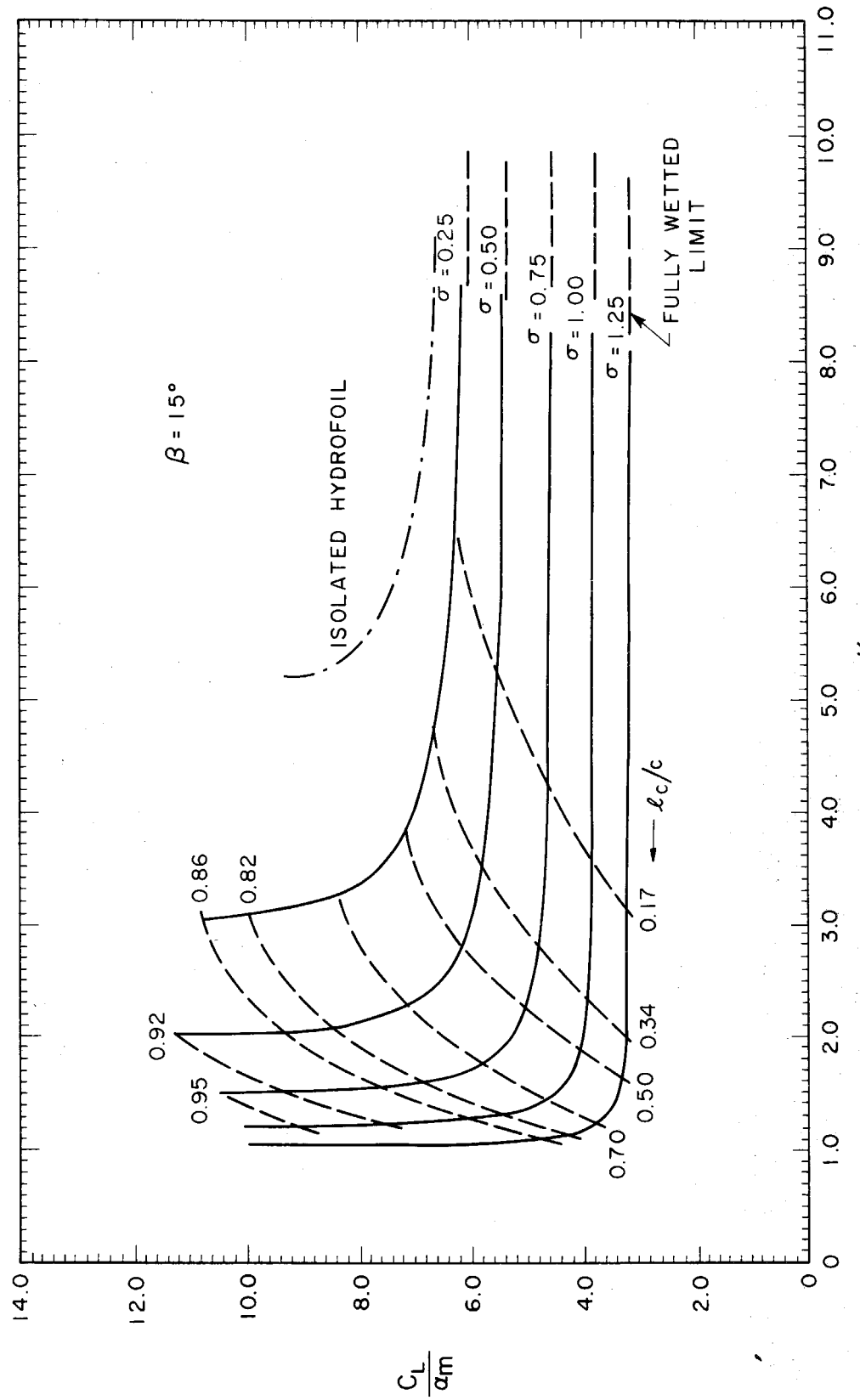

Fig. A9.18 - Ratio of lift coefficient to mean flow angle vs. ratio of cavitation number to twice inlet angle for various solidities at a given stagger angle $\beta = 15°$.

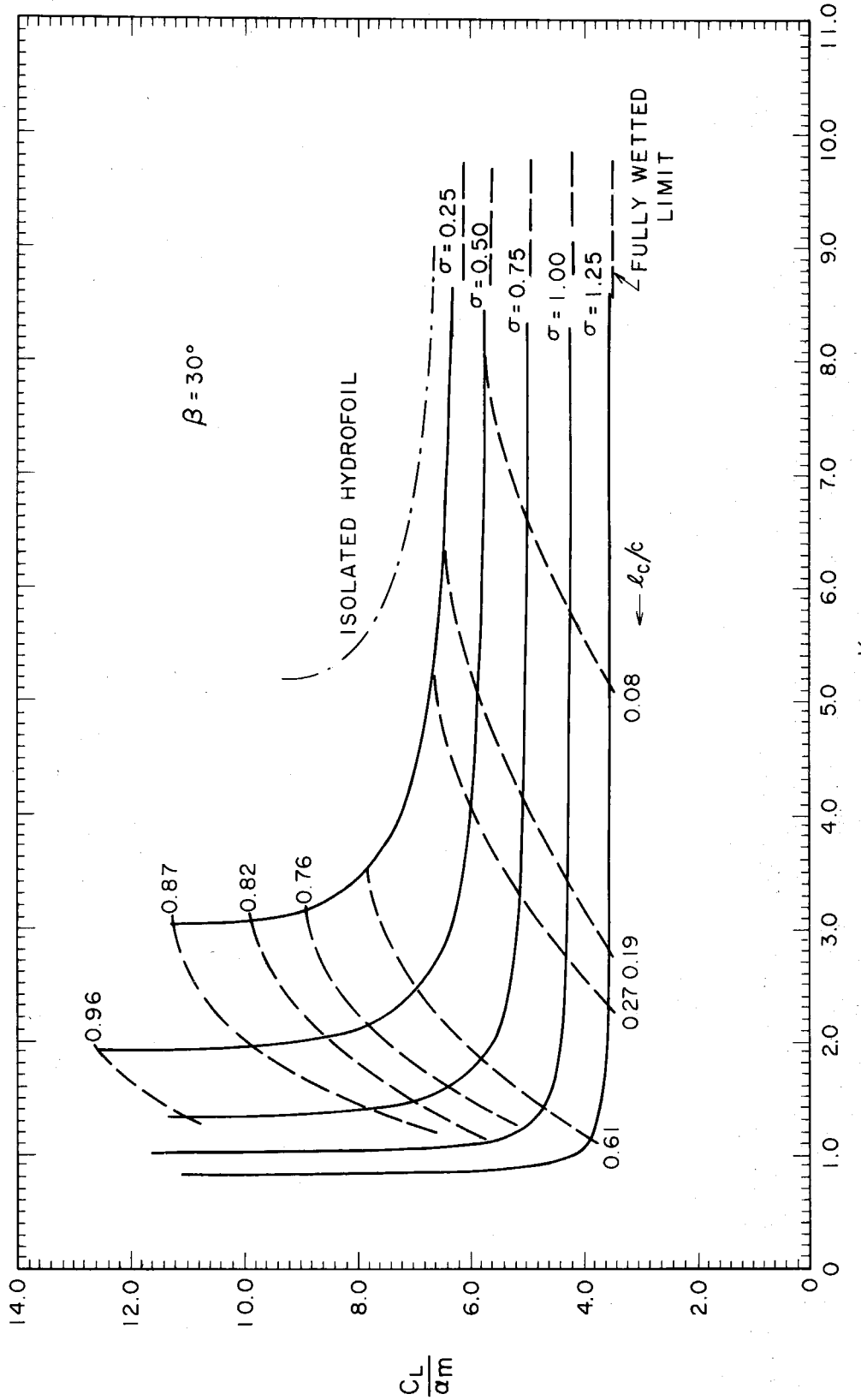

Fig. A9.19 - Ratio of lift coefficient to mean flow angle vs. ratio of cavitation number to twice inlet angle for various solidities at a given stagger angle $\beta = 30°$.

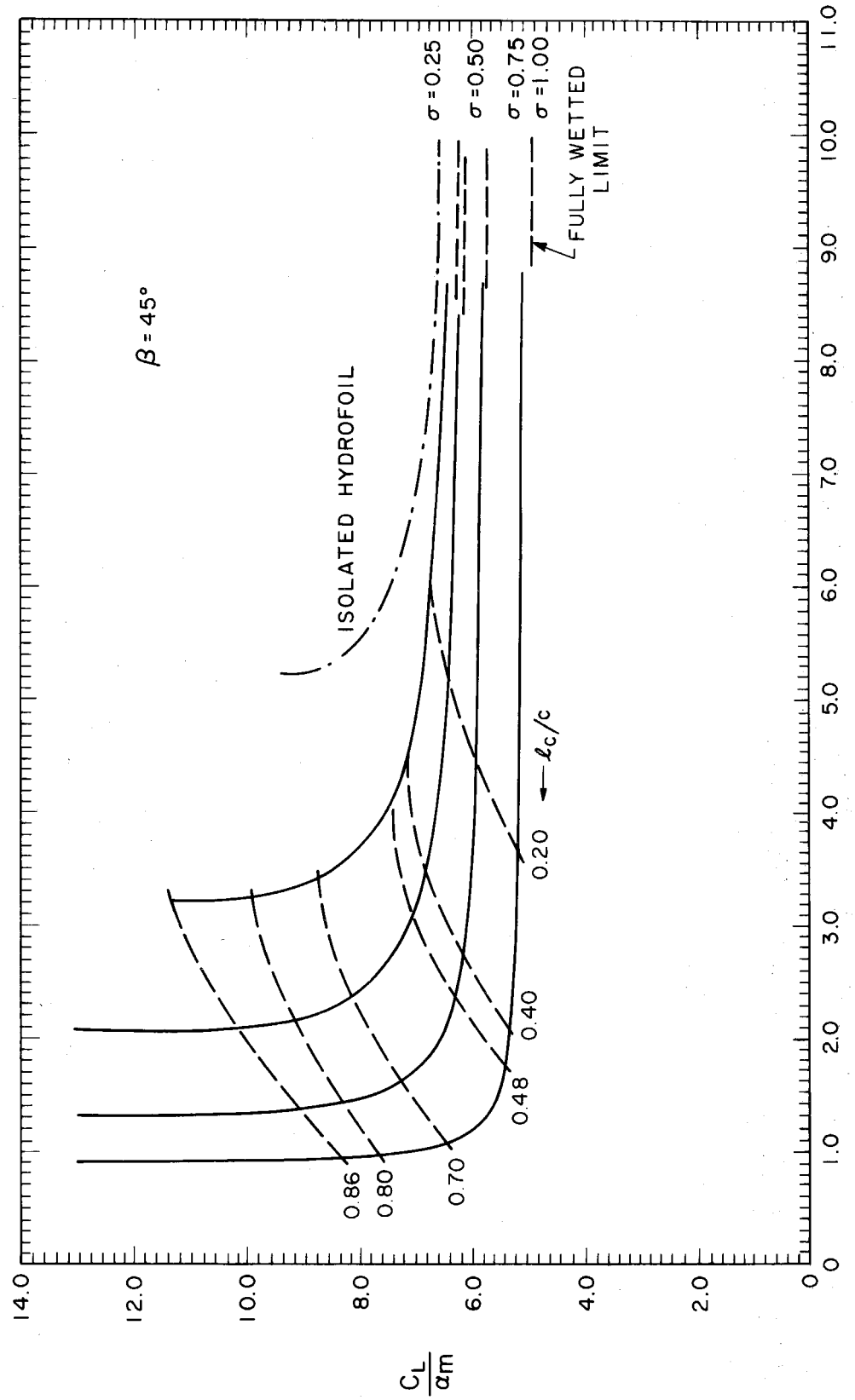

Fig. A9.20 - Ratio of lift coefficient to mean flow angle vs. ratio of cavitation number to twice inlet angle for various solidities at a given stagger angle $\beta = 45^{\circ}$.

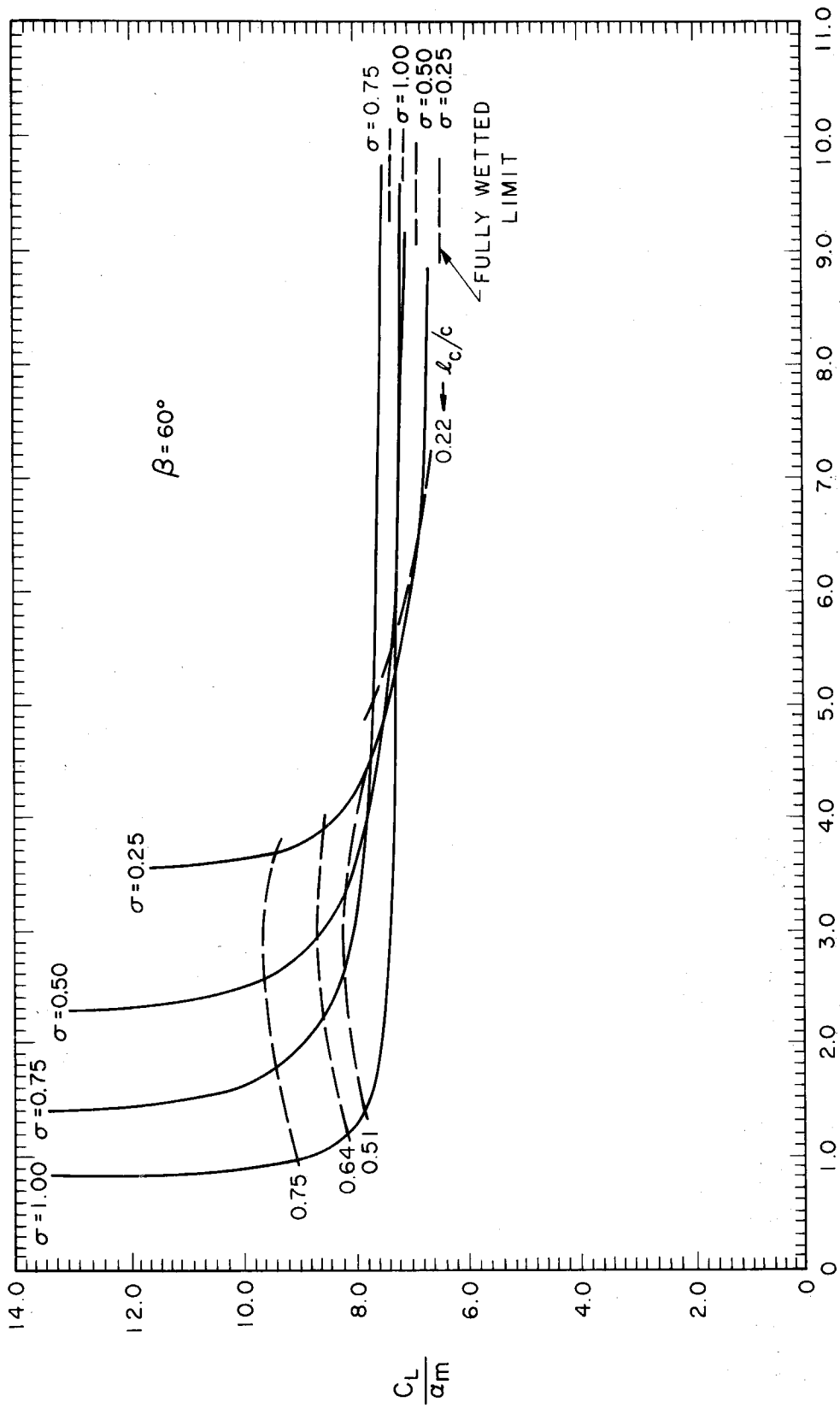

Fig. A9.21 - Ratio of lift coefficient to mean flow angle vs. ratio of cavitation number to twice inlet angle for various solidities at a given stagger angle $\beta = 60^{o}$.

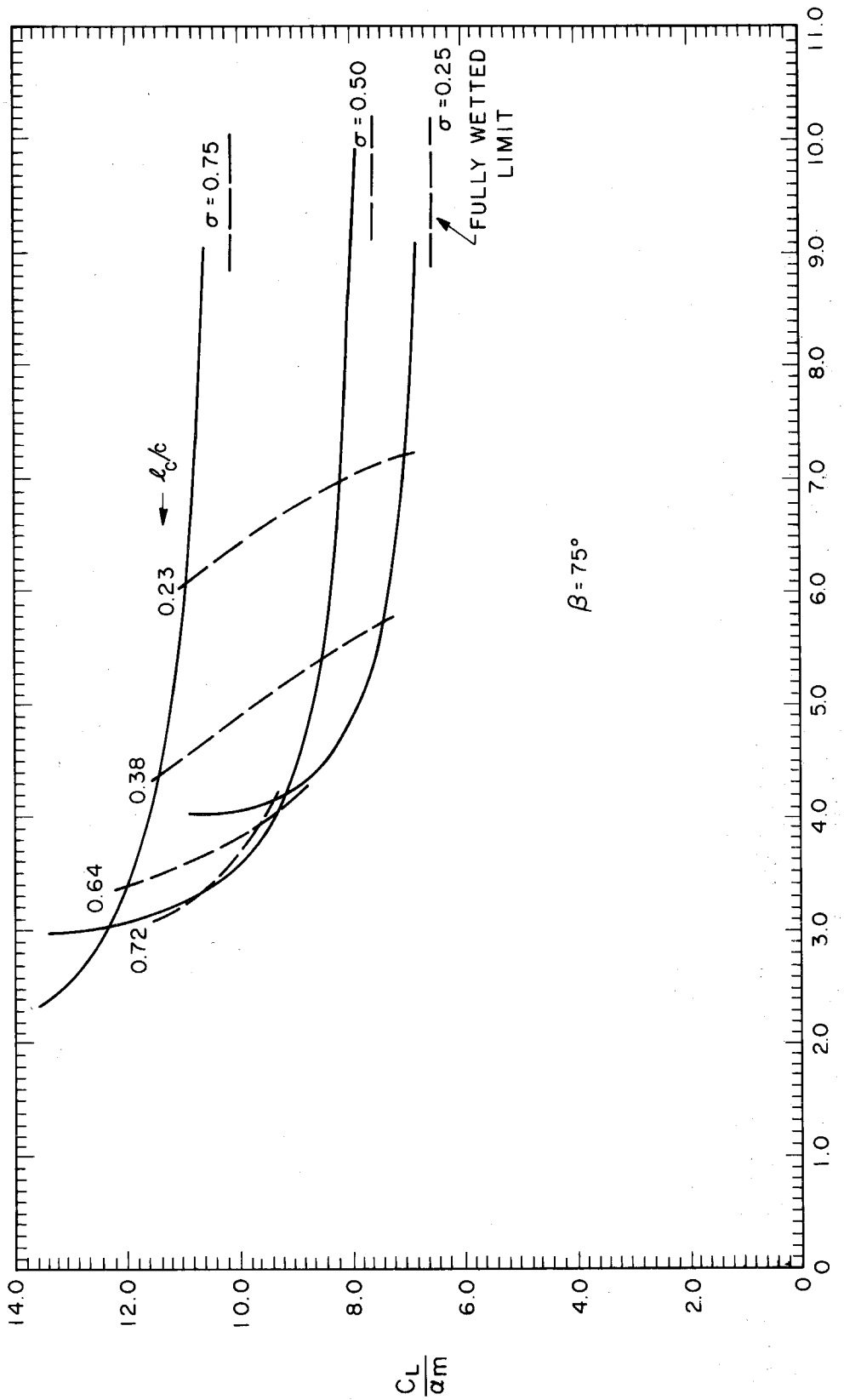

Fig. A9.22 - Ratio of lift coefficient to mean flow angle vs. ratio of cavitation number to twice inlet angle for various solidities at a given stagger angle $\beta = 75°$.

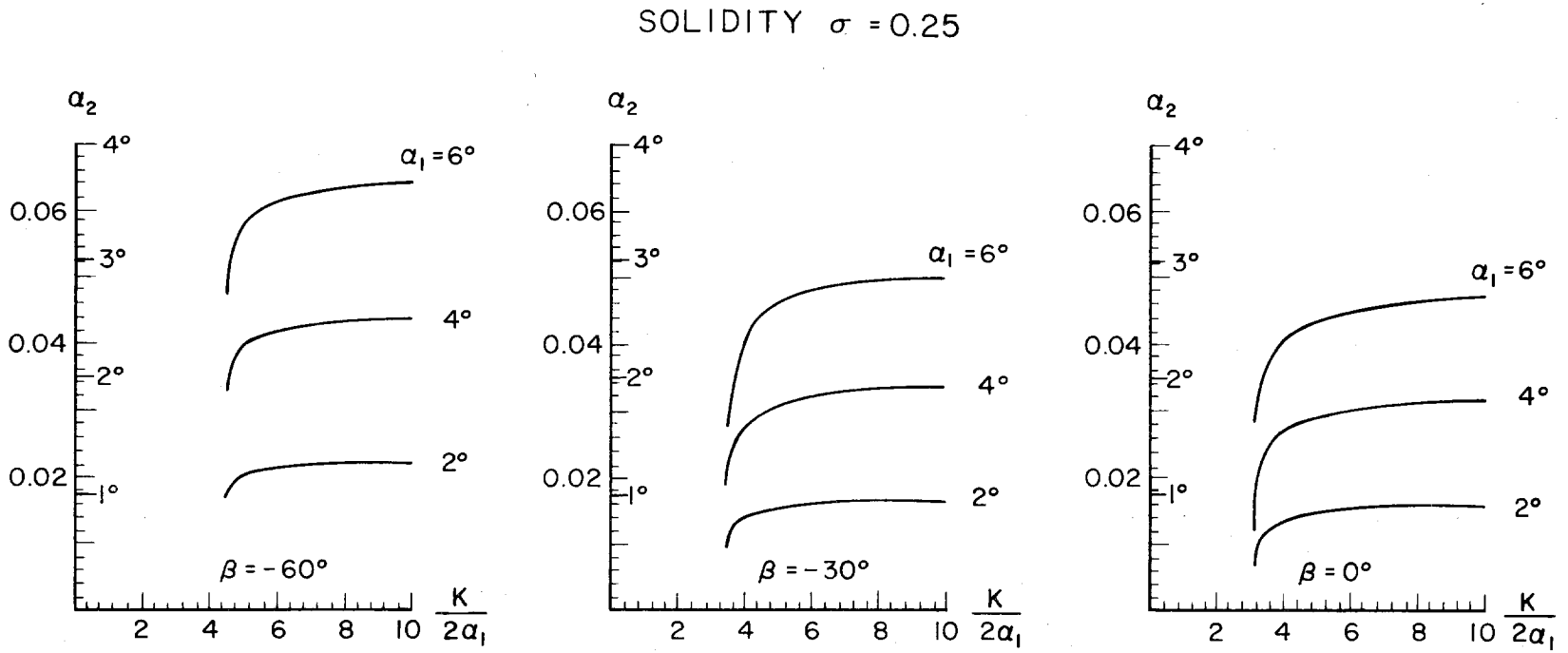

Fig. A9.23(a) - Outlet flow angle vs. ratio of cavitation number to twice inlet angle for different inlet angles, at constant stagger angle.

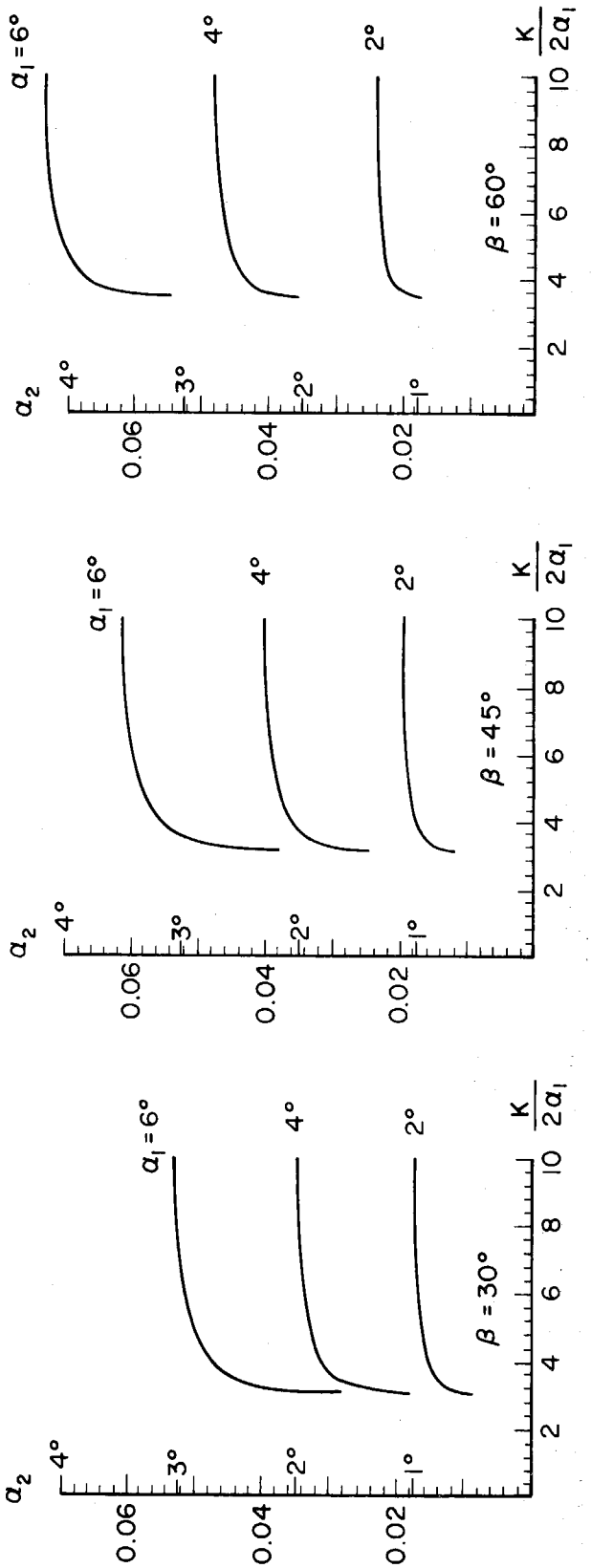

Fig. A9.23(b) - Outlet flow angle vs. ratio of cavitation number to twice inlet angle for different inlet angles, at constant stagger angle.

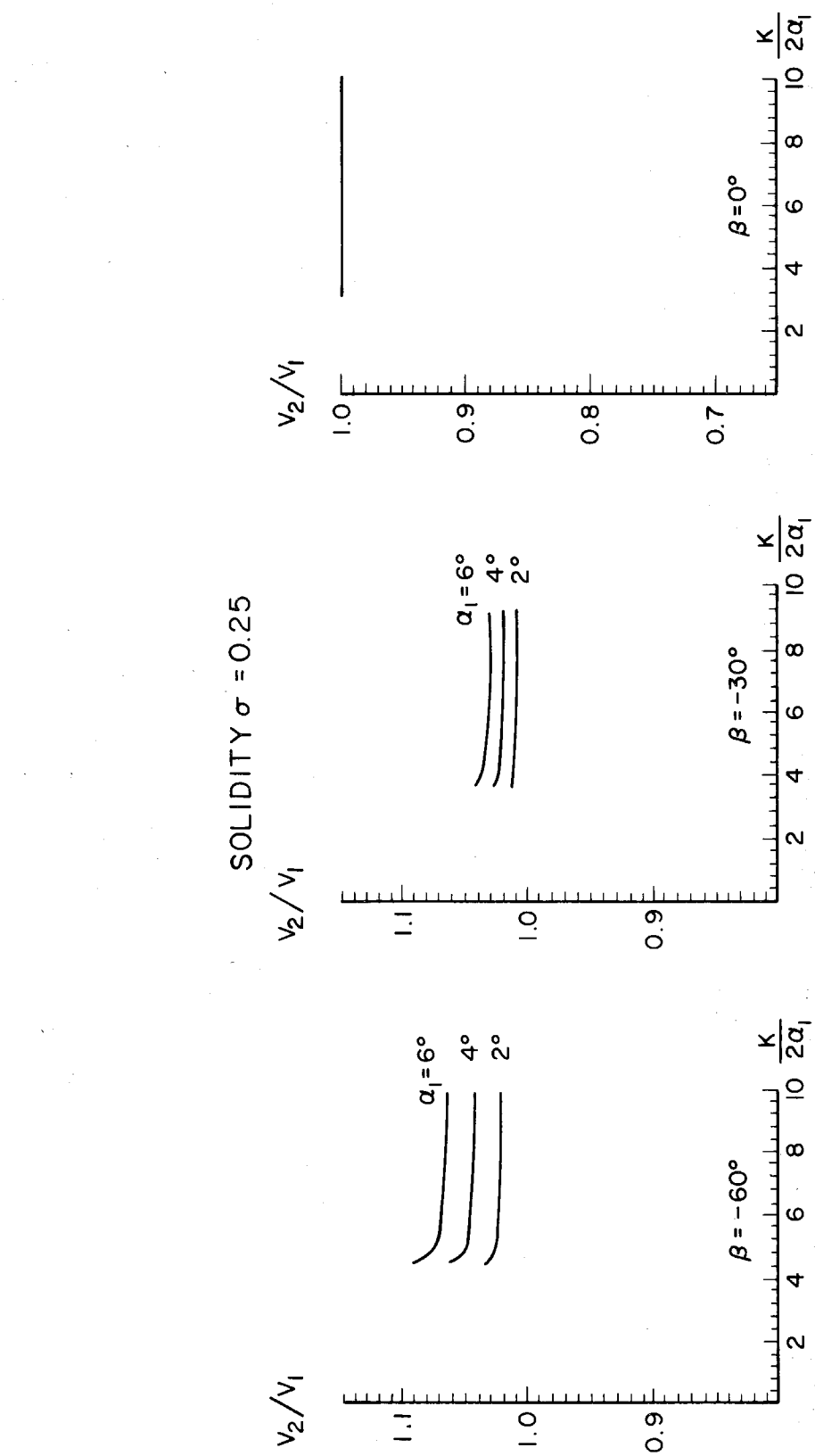

Fig. A9.24(a) - Ratio of downstream velocity to upstream velocity vs. ratio of cavitation number to twice inlet angle for different inlet angles, at constant stagger angle.

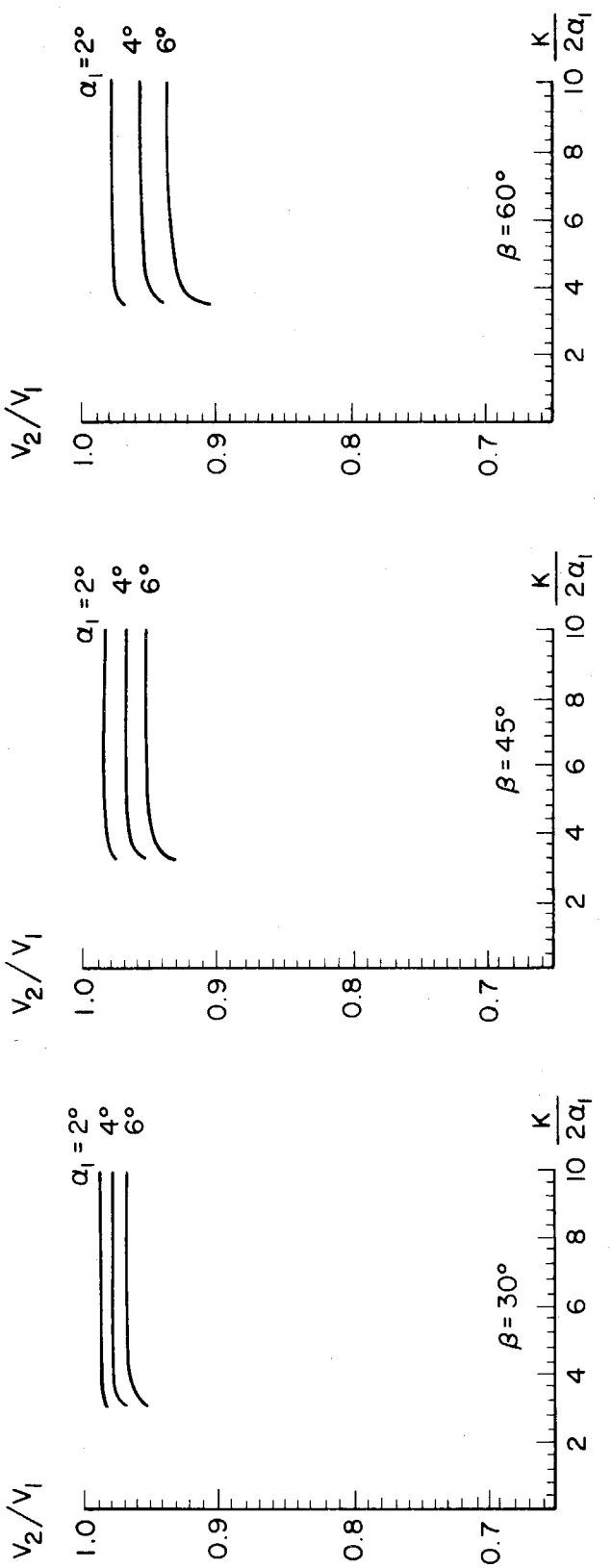

Fig. A9.24(b) - Ratio of downstream velocity to upstream velocity vs. ratio of cavitation number to twice inlet angle for different inlet angles, at constant stagger angle.

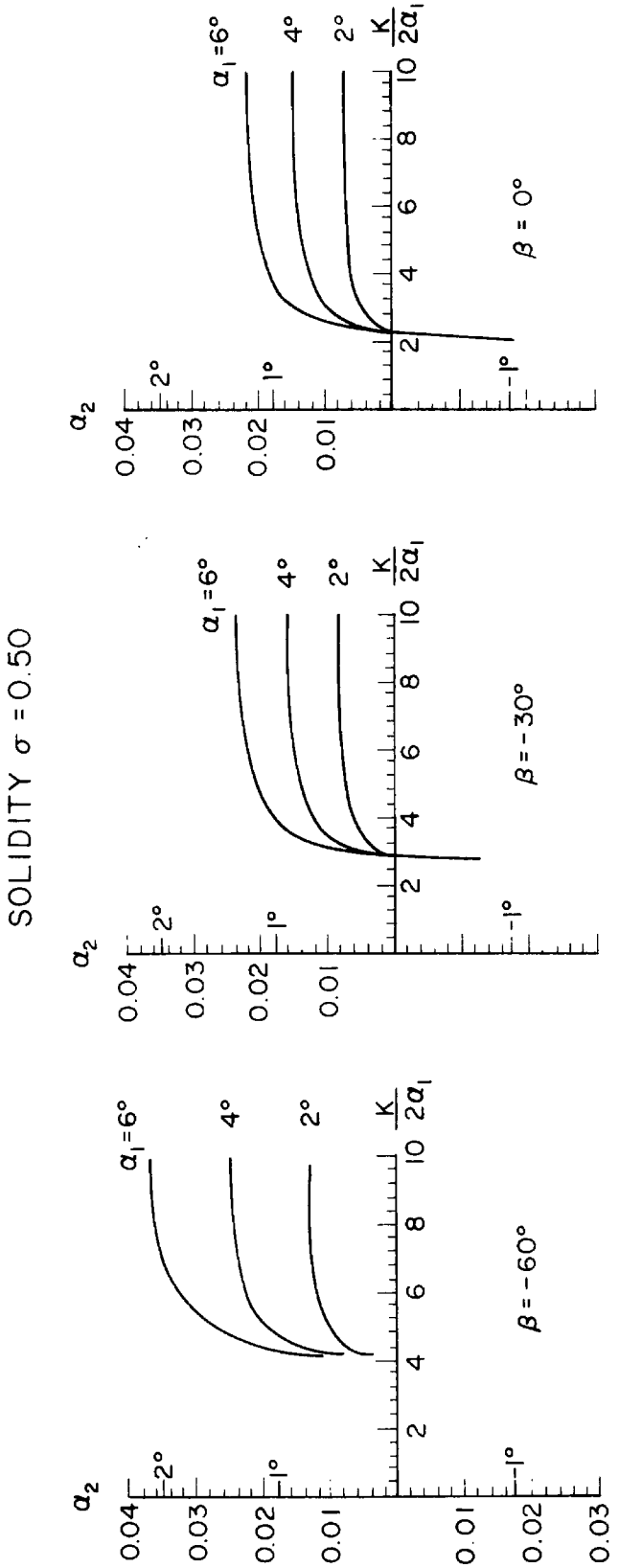

Fig. A9.25(a) - Outlet flow angle vs. ratio of cavitation number to twice inlet angle for different inlet angles, at constant stagger angle.

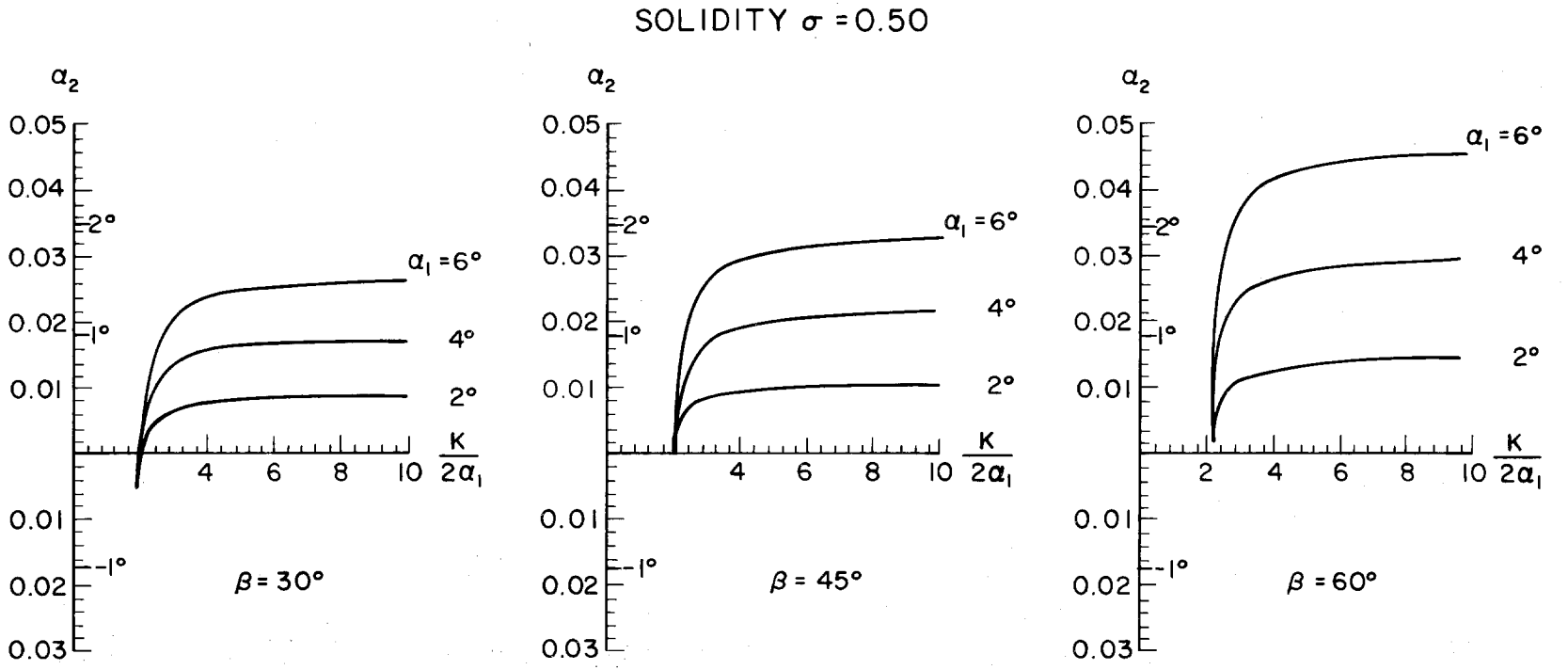

Fig. A9.25(b) - Outlet flow angle vs. ratio of cavitation number to twice inlet angle for different inlet angles, at constant stagger angle.

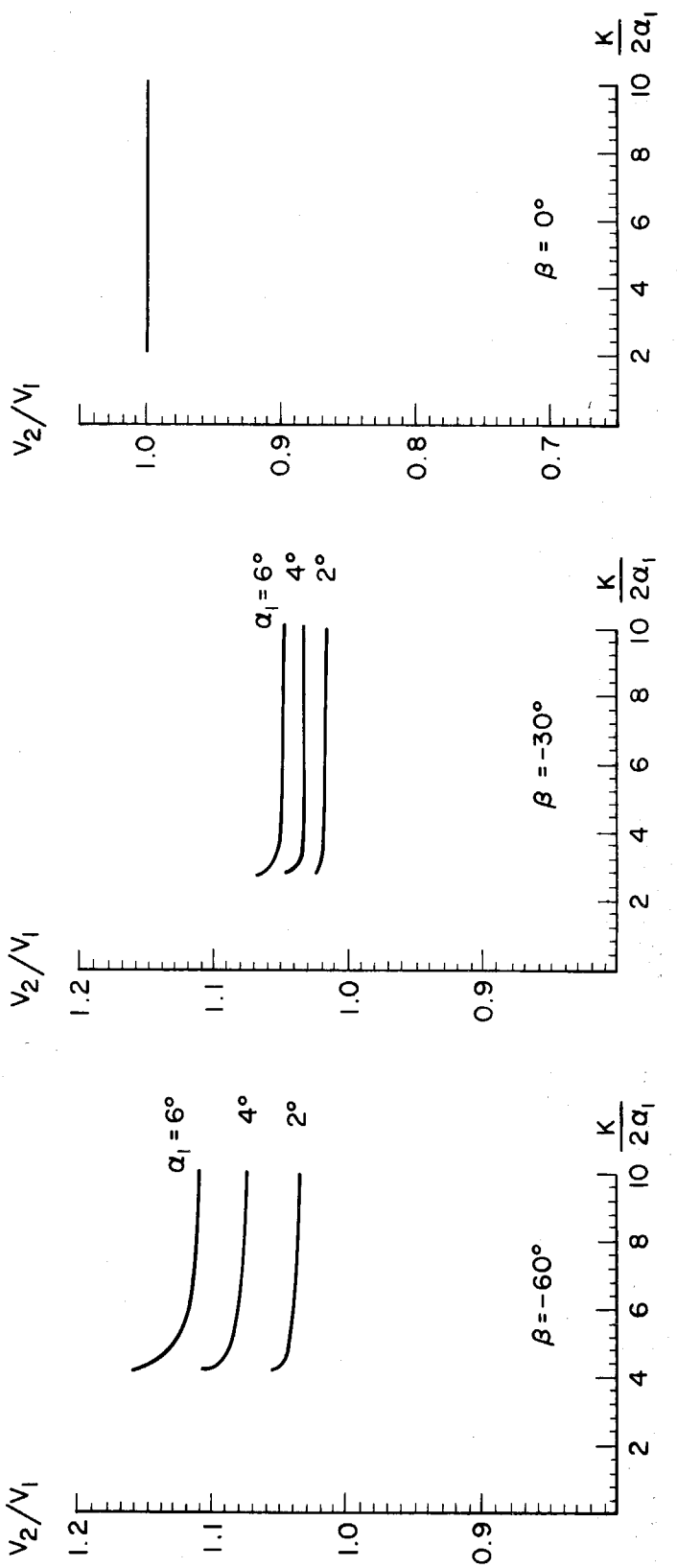

Fig. A9.26(a) - Ratio of downstream velocity to upstream velocity vs. ratio of cavitation number to twice inlet angle for different inlet angles, at constant stagger angle.

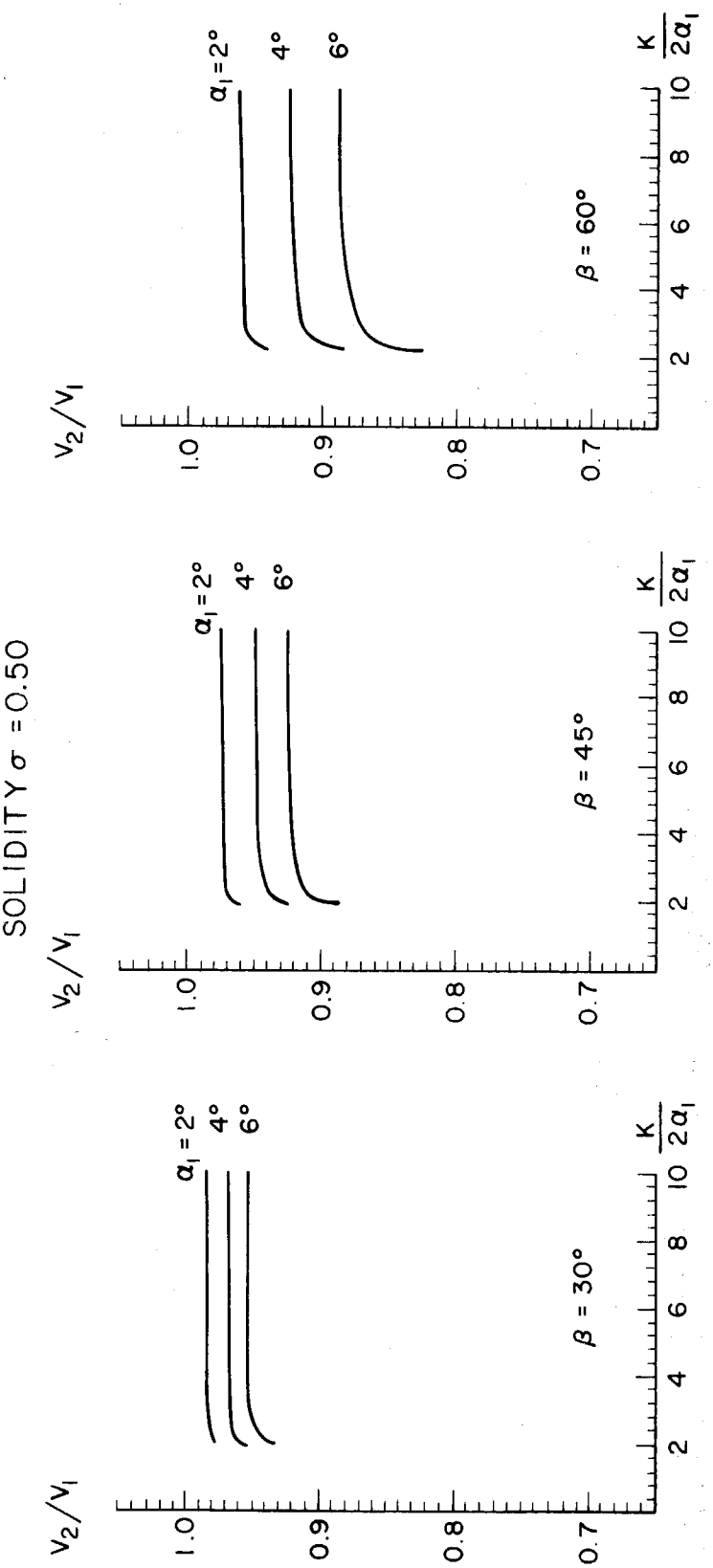

Fig. A9.26(b) - Ratio of downstream velocity to upstream velocity vs. ratio of cavitation number to twice inlet angle for different inlet angles, at constant stagger angle.

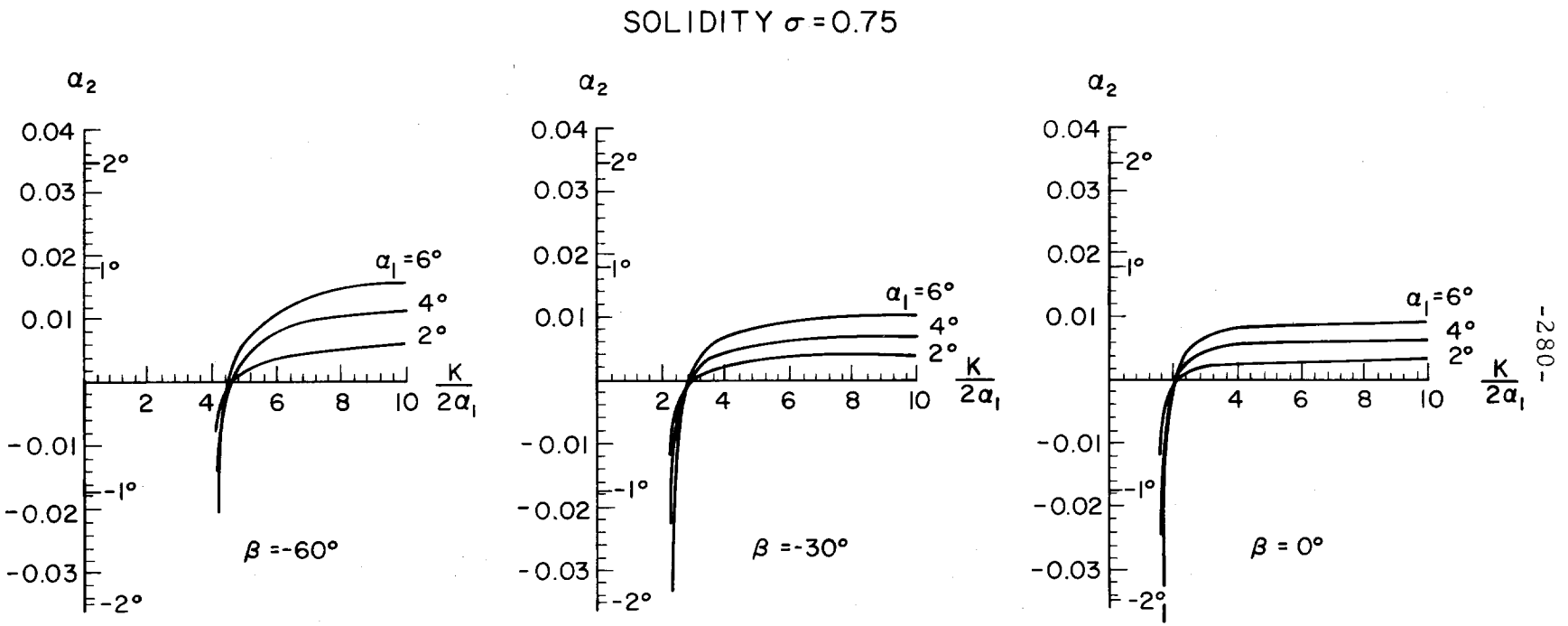

Fig. A9.27(a) - Outlet flow angle vs. ratio of cavitation number to twice inlet angle for different inlet angles, at constant stagger angle.

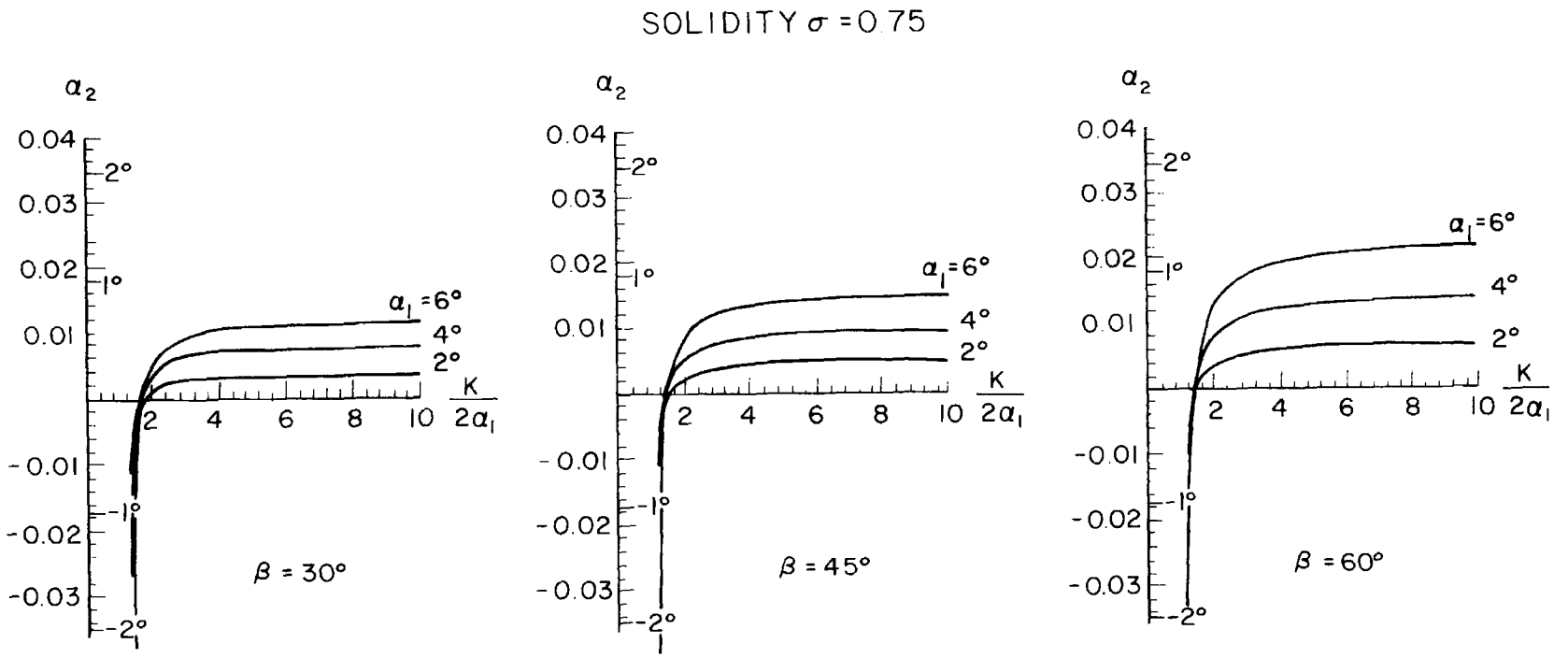

Fig. A9.27(b) - Outlet flow angle vs. ratio of cavitation number to twice inlet angle for different inlet angles, at constant stagger angle.

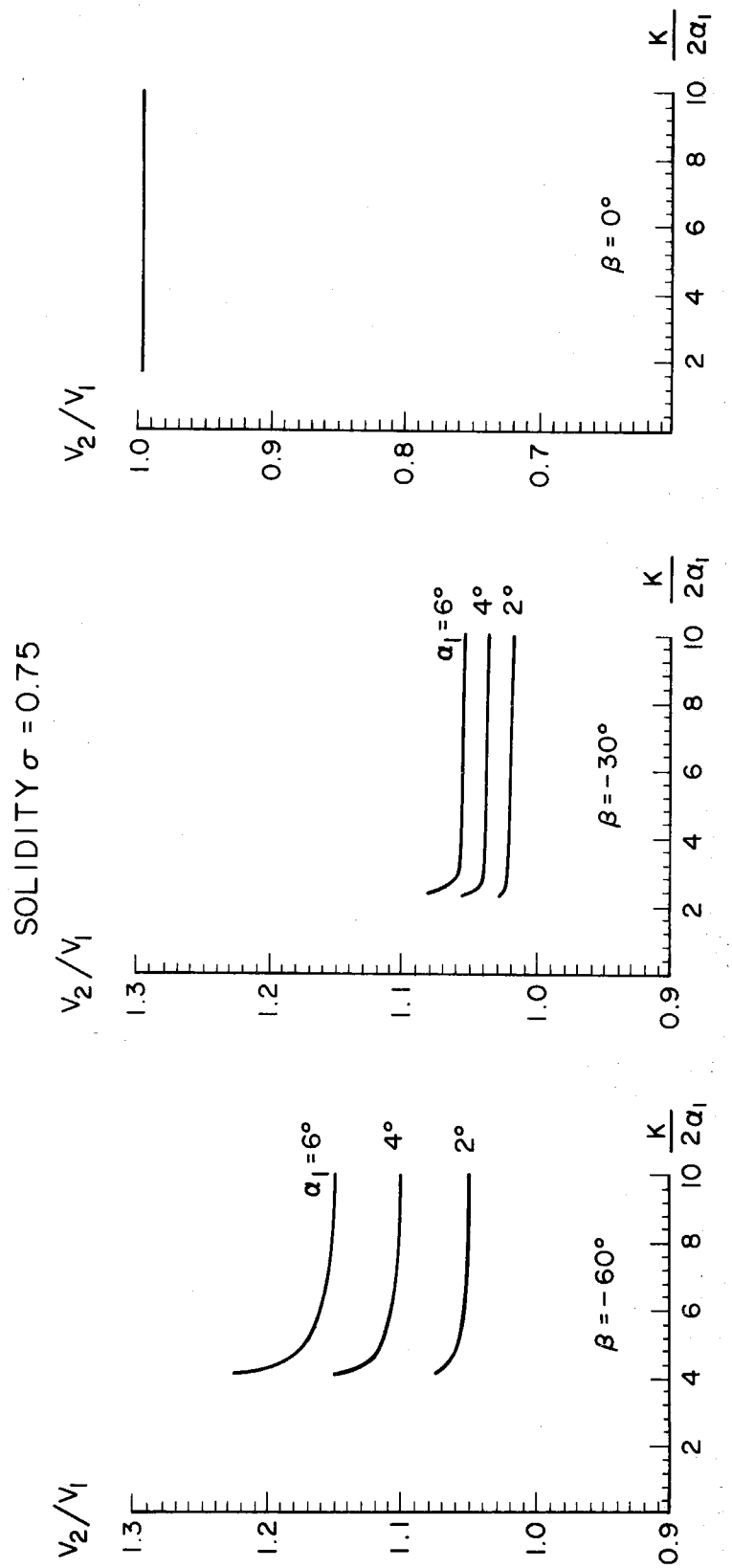

Fig. A9.28(a) - Ratio of downstream velocity to upstream velocity vs. ratio of cavitation number to twice inlet angle for different inlet angles, at constant stagger angle.

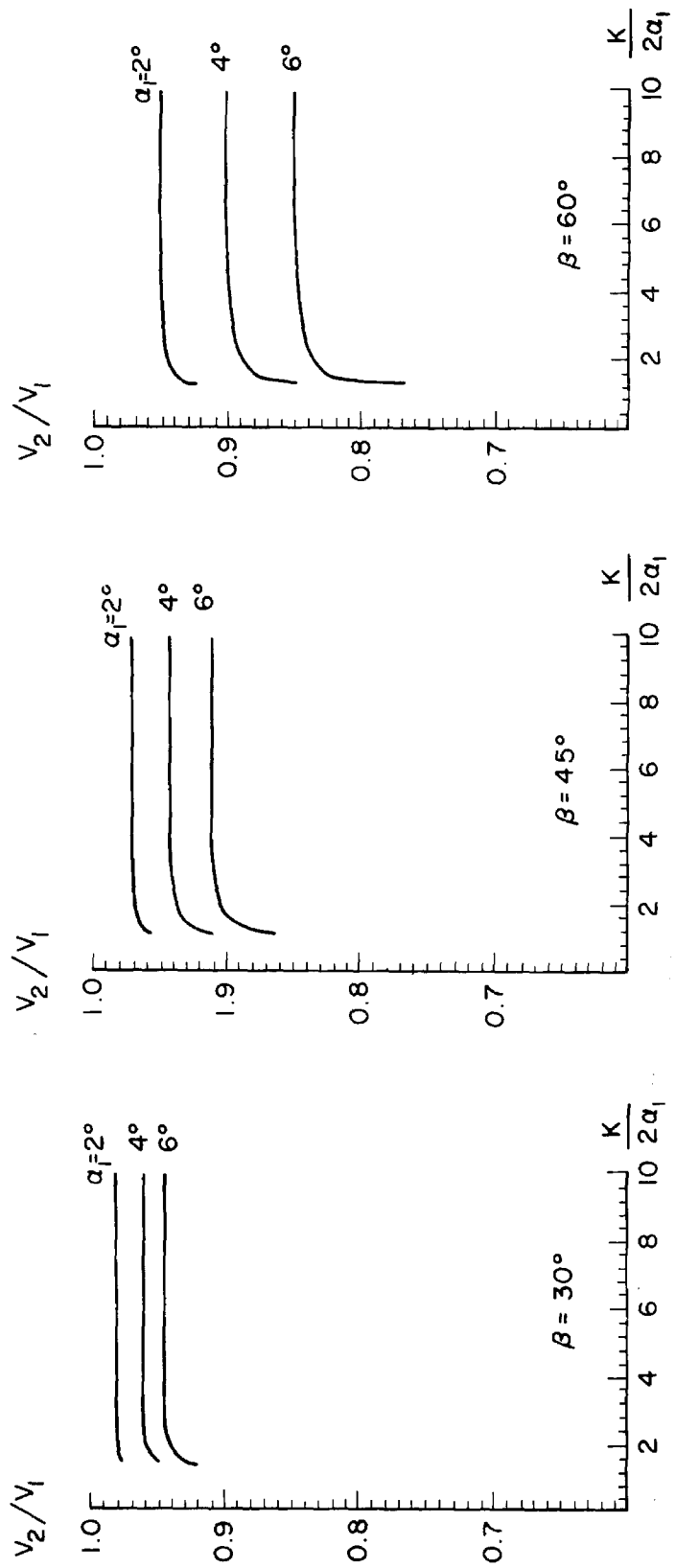

Fig. A9.28(b) - Ratio of downstream velocity to upstream velocity vs. ratio of cavitation number to twice inlet angle for different inlet angles, at constant angle.